MSc. Eng. Shivangi Sachar

Instytut Maszyn Przepływowych im. Roberta Szewalskiego
Polskiej Akademii Nauk w Gdańsku

Performance and Noise Sources of a Savonius Wind Turbine in an Urban Environment

Promotor: *Prof. dr hab. inż. Paweł Flaszyński*

Rozprawa doktorska przedłożona

Radzie Naukowej

Instytutu Maszyn Przepływowych im. Roberta Szewalskiego
Polskiej Akademii Nauk

Gdańsk, Poland
October, 2025

Acknowledgements

Completing this PhD has been an incredible journey, one that would not have been possible without the steadfast support, guidance, and encouragement of many individuals. I am deeply grateful to all who have been part of this experience, contributing both professionally and personally to my growth.

First and foremost, I extend my heartfelt gratitude to my supervisor **Prof. Pawel Flaszynski** and mentor **Prof. Piotr Doerffer**, for their invaluable mentorship. Their profound knowledge, patience, and guidance have shaped my research and broadened my perspective in ways I could never have imagined. I am truly fortunate to have learned from them.

A special mention goes to Dr Joanna Grzelak and Dr Krzysztof Doerffer whose support and insights have been instrumental throughout my research. Particular thanks are directed to Prof. Jozef Kotus for support in the area of acoustics, to Dr Michał Piotrowicz for his assistance in numerical simulations and Dr Janusz Telega for his help in wind description methods. Their encouragement and expertise have made a significant impact on my academic journey.

I would also like to express my deep appreciation to my team members, who have been more than just colleagues—they have been a family to me in an unfamiliar land. Their camaraderie, kindness, and constant encouragement have made this journey not only manageable but also truly memorable.

I am immensely grateful to **IMP-PAN (Institute of Fluid-Flow Machinery, Polish Academy of Sciences)** for providing me with the opportunity and resources to conduct my research. Additionally, my sincere thanks go to the **European Union's Horizon 2020 research and innovation programme under the Marie Skłodowska-Curie grant agreement No. 860101 – zEPHYR**, which funded this project, and to the **Computer Center-CI TASK (Gdańsk, Poland)** for their computational support.

Beyond the academic sphere, my deepest thanks go to my **parents and sister**, whose love and belief in me have been my pillar of strength. A special note of gratitude to my husband, Dr. Arjun Kalkur, whose unwavering support and motivation have been invaluable during this journey. Their encouragement has been a source of inspiration, helping me stay focused and determined through every challenge.

This thesis is a testament not only to my efforts but also to the collective support of all these incredible individuals. I am profoundly grateful to each one of you.

Abstract

The ever-existing source of energy, based on wind, has undergone significant practical development in the past century. Two principal zones of application can be distinguished. The first concerns high-power output systems, which have converged towards a single solution: the three-bladed horizontal-axis rotor. This approach, however, is accessible only to highly developed industries and requires substantial financial resources. The second zone of interest involves small-scale turbines, which have been developed intensively in recent decades. While initially implemented for individual use, such systems are now increasingly being deployed in densely populated urban environments. Unlike large-scale wind energy, this sector has not converged to a single technological solution. Instead, there is a wide spectrum of approaches, reflecting various technical, environmental, and social considerations that must be carefully analyzed. The present work addresses this challenge by formulating the following hypothesis:

The integration of wind energy into urban environments necessitates specific wind turbine characteristics that must be addressed to ensure their acceptance from both environmental and social perspectives.

In order to test this hypothesis, the research explores urban wind energy as a promising yet underexplored area of sustainable power generation. With the increasing global demand for renewable energy and the urgent need to reduce reliance on fossil fuels, wind energy presents a compelling, environmentally friendly solution. Historically, deployment and research have been dominated by large-scale installations in rural or offshore locations, where steady and unobstructed wind flows are available. By contrast, urban wind energy has received comparatively little attention, despite its considerable potential for decentralized energy production in cities where demand is concentrated.

This work therefore investigates the feasibility and performance of Savonius-type vertical axis wind turbines (SVAWTs), which are particularly suited to turbulent and multidirectional wind conditions in urban areas. The central research question is: *How applicable and efficient are Savonius wind turbines in urban settings, considering both their power generation capabilities and acoustic impact? To address this question, the study combines experimental, computational, and analytical methods.

The main objectives include assessing the suitability of different wind turbine technologies for urban deployment, analyzing wind energy potential at multiple sites across two countries, and conducting detailed aerodynamic and acoustic investigations of Savonius turbines. Experimental studies in wind tunnels and on rooftop prototypes are complemented by CFD simulations to capture performance under both controlled and real-world conditions. Acoustic measurements, carried out using single microphones and microphone arrays, enable the identification of noise sources and mechanisms. This understanding is essential for evaluating the acoustic impact of Savonius turbines in urban environments, ensuring regulatory compliance and minimizing disturbance to residents.

An innovative contribution of this work is the study of a twin-rotor Savonius configuration, designed to improve power output while maintaining scalability and cost-effectiveness for urban applications. Furthermore, by systematically examining the relationship between power generation and acoustic emissions, the research establishes optimal operating parameters that balance efficiency with noise reduction—an important step toward socially acceptable wind energy in cities.

The thesis is organized into five parts: the introduction and problem statement; theoretical foundations; performance analyses of SVAWTs through experiments and simulations; detailed acoustic studies; and finally, the integration of turbines within urban environments, including wind pattern analysis and site-specific assessments.

In summary, this research makes a significant contribution by advancing practical and scalable solutions for harvesting wind energy in cities. By addressing both technical performance and acoustic challenges, it supports the development of turbine designs that can operate harmoniously within densely populated areas. In doing so, it demonstrates how tailored turbine characteristics can enable the wider acceptance of urban wind energy, thereby validating the central hypothesis.

Streszczenie

Energia wiatru, jako nieprzerwanie dostępne źródło energii, w ciągu ostatniego stulecia znalazła się w obszarze coraz większego zainteresowania i praktycznego znaczenia. Można wyróżnić dwie zasadnicze sfery jej zastosowania. Pierwsza odnosi się do systemów wielkoskalowych, które zbieżnie doprowadziły do ustandaryzowanego rozwiązania w postaci trójłopatowego wirnika o poziomej osi obrotu. Rozwiązanie to jest jednak dostępne wyłącznie dla wysoko rozwiniętych gospodarek i wymaga znacznych nakładów finansowych. Druga sfera obejmuje turbiny małej skali, których rozwój w ostatnich dekadach nabrał szczególnej dynamiki. Początkowo wykorzystywane głównie do celów indywidualnych, współcześnie są coraz częściej wdrażane w gęsto zaludnionych obszarach miejskich. W odróżnieniu od systemów wielkoskalowych, sektor ten nie wykształcił jednolitego rozwiązania technologicznego. Zamiast tego charakteryzuje się szerokim spektrum podejść, wynikających z różnorodnych uwarunkowań technicznych, środowiskowych i społecznych, które wymagają pogłębionej analizy. W niniejszej rozprawie przyjęto hipotezę:

Integracja energetyki wiatrowej w środowisku miejskim wymaga uwzględnienia specyficznych właściwości turbin, których dostosowanie jest warunkiem akceptacji zarówno z perspektywy środowiskowej, jak i społecznej.

W celu weryfikacji hipotezy badania koncentrują się na wykorzystaniu energii wiatru w miastach, rozpatrywanym jako obszar obiecujący, lecz wciąż niedostatecznie eksplorowany w kontekście zrównoważonej produkcji energii. W obliczu rosnącego globalnego zapotrzebowania na źródła odnawialne oraz pilnej potrzeby ograniczenia zależności od paliw kopalnych, energetyka wiatrowa jawi się jako szczególnie atrakcyjne rozwiązanie niskoemisyjne. Dotychczas rozwój badań i wdrożeń był zdominowany przez instalacje wielkoskalowe, lokowane na terenach wiejskich bądź morskich, gdzie dostępne są stabilne i niezakłócone przepływy powietrza. W przeciwieństwie do tego, wykorzystanie energii wiatru w środowisku miejskim pozostawało marginalne, mimo istniejącego potencjału dla zdecentralizowanej produkcji energii w miejscach o największej koncentracji zapotrzebowania.

Przedmiotem badań jest analiza przydatności i efektywności turbin wiatrowych typu Savoniusa o pionowej osi obrotu (SVAWT), które ze względu na swoją konstrukcję wykazują szczególną odporność na turbulentne i wielokierunkowe przepływy powietrza charakterystyczne dla obszarów miejskich. Sformułowano główne pytanie badawcze: W jakim stopniu turbiny Savoniusa są przydatne i efektywne w warunkach miejskich, z uwzględnieniem zarówno ich potencjału produkcji energii, jak i oddziaływania akustycznego? W celu udzielenia odpowiedzi zastosowano metody eksperymentalne, obliczeniowe i analityczne.

Cele szczegółowe obejmują: ocenę przydatności różnych technologii turbin wiatrowych w środowisku miejskim, analizę potencjału energetycznego wiatru w wybranych lokalizacjach w dwóch krajach oraz przeprowadzenie szczegółowych badań aerodynamicznych i akustycznych turbin Savoniusa. Badania eksperymentalne, realizowane

w tunelach aerodynamicznych oraz na prototypach dachowych, zostały uzupełnione symulacjami CFD, umożliwiającymi analizę wydajności zarówno w warunkach laboratoryjnych, jak i rzeczywistych. Równolegle prowadzono pomiary akustyczne z wykorzystaniem pojedynczych mikrofonów i macierzy mikrofonowych, co pozwoliło na identyfikację źródeł oraz mechanizmów emisji hałasu. Analiza ta jest kluczowa dla oceny oddziaływania akustycznego turbin w środowisku miejskim, zapewnienia zgodności regulacyjnej oraz minimalizacji uciążliwości dla mieszkańców.

Innowacyjnym elementem rozprawy jest analiza konfiguracji Savoniusa z podwójnym wirnikiem, której celem jest zwiększenie wydajności energetycznej przy zachowaniu skalowalności i opłacalności w zastosowaniach miejskich. Ponadto, poprzez systematyczne badanie relacji pomiędzy generacją mocy a emisją hałasu, określono optymalne parametry

eksploatacyjne, umożliwiające równoważenie efektywności z ograniczeniem oddziaływań akustycznych — co stanowi istotny krok w kierunku społecznie akceptowalnej energetyki wiatrowej w miastach.

Rozprawa została podzielona na pięć części: wprowadzenie i sformułowanie problemu badawczego; podstawy teoretyczne; analizy wydajności turbin Savoniusa oparte na eksperymentach i symulacjach; szczegółowe badania akustyczne; oraz integrację turbin w środowisku miejskim, obejmującą analizę wzorców wiatrowych i oceny lokalizacyjne.

Podsumowując, praca wnosi istotny wkład w rozwój praktycznych i skalowalnych rozwiązań dla pozyskiwania energii wiatrowej w środowisku miejskim. Poprzez równoczesne uwzględnienie zagadnień technicznych i akustycznych, wspiera proces projektowania turbin zdolnych do harmonijnego funkcjonowania w gęsto zaludnionych obszarach. W ten sposób potwierdzono zasadność hipotezy o konieczności dostosowania charakterystyk turbin do specyfiki środowiska miejskiego w celu umożliwienia szerszej akceptacji społecznej energetyki wiatrowej.

Contents

Nomenclature

Greek Symbols	
α	Surface roughness exponent
μ	Dynamic viscosity of air (Pa·s) / location parameter (log-normal, GEV)
$\mu_{\log}$	Mean of associated normal distribution (log-normal)
ρ	Air density (kg/m^3)
σ	Standard deviation of wind speed (m/s)
ν	Viscosity
$\Gamma(x)$	Gamma function
$\gamma(a, z)$	Lower incomplete gamma function
τ	Torque
ω	angular velocity
Latin Letters	
c	Scale parameter of Weibull distribution (m/s)
c_h	Scale parameter of Weibull distribution at hub height (m/s)
C_p	Power coefficient
E_D	Energy density (kWh/m^2/year)
E_{pf}	Energy pattern factor
F	Cumulative distribution function (CDF)
$f(v)$	Probability density function (PDF) of wind velocity
$f(x; k, c)$	PDF of gamma distribution
$F(x; k, c)$	CDF of gamma distribution
k	Shape parameter of Weibull distribution
k_h	Shape parameter of Weibull distribution at hub height
$k_{\log}$	Shape parameter of log-normal distribution
P_h	Average power density at hub height
$\bar{P}_h$	Mean power density at hub height
$\mathcal{T}$	Duration of measurement (s, h, or year)
T	Temperature
Z	Reference height of wind measurement (m)
Z_h	Hub height of wind turbine (m)
v	Wind speed (m/s)
v_h	Wind speed at hub height (m/s)
$\bar{v}$	Mean wind speed (m/s)
v_m	Mean wind speed for Rayleigh distribution (m/s)
v_i	Wind speed at instant i (m/s)
x	Random variable (gamma distribution)
m_1, m_2	First and second moment estimators (Method of Moments)
Acronyms / Abbreviations	
HAWT	Horizontal Axis Wind Turbine
MAPE	Mean Absolute Percentage Error

MLM	Maximum Likelihood Method
MMLM	Modified Maximum Likelihood Method
MOM	Method of Moments
PDF	Probability Density Function
PDM	Power Density Method
RMSE	Root Mean Square Error
SVAWT	Savonius Vertical Axis Wind Turbine
TSR	Tip Speed Ratio
VAWT	Vertical Axis Wind Turbine
SBL	Surface Boundary Layer
GEV	Generalized Extreme Value distribution
KDE	Kernel Density Estimation
WPD	Wind Power Density
HFN	High Frequency Noise
LFN	Low Frequency Noise
SPL	Sound Pressure Level
CDF	Cumulative Density Function
WPD	Wind Power Density
CFD	Computational Fluid Dynamics
OR	Overlap Ratio
CSM	Cross Spectral Matrix
PSF	Point Spread Functions
ROI	Region of Interest
SPI	Source Power Integration
AR	Aspect Ratio
GCI	Grid Convergence Index
BR	Blockage Ratio
TI	Turbulence Intensity
OSPL	Overall Sound Pressure Level
Units / Others	
m/s	meters per second
rpm	Revolutions per minute
K	Kelvin (temperature)
X_{obs}	Observed value
X_{pre}	Predicted value
χ^2	Chi-square error
R^2	Coefficient of determination / variance error
$E(v)$	Wind energy

List of Figures

List of Tables

Part 1

INTRODUCTION

Chapter 1.1

Introduction and Background

1.1.1 Motivation

The rising global energy demand has spurred research across various domains, including the exploration of wind energy as a viable power source [1]. Over recent decades, extensive studies have been conducted in the field of wind energy, reflecting the increasing interest in harnessing this renewable resource [2]. With urban areas experiencing a surge in population, there is a growing need for power generation solutions [3]. In this context, the potential utilization of safe, quiet, and renewable energy sources holds significant promise [1, 2]. The presence of advanced technology and the accessibility of wind energy in urban settings have attracted researchers' attention toward wind turbines (WTs) [4–6]. This interest is fueled by several factors, including the reduction in energy transportation distances, increased power source availability, enhanced energy efficiency, and minimized transmission losses [4, 7]. Additionally, the intricate layouts of buildings and their configurations impact local wind patterns, with reduced spacing between buildings resulting in accelerated wind velocities, particularly dependent on wind direction [8, 9].

Wind characteristics play a crucial role in determining the suitability of turbine types and installation sites [10]. This data, which includes variables such as surface type, wind speed, site temperature, measurement device height, air density, and turbulence [11–13], is vital for designing robust turbines capable of withstanding harsh environmental conditions while maximizing energy production and minimizing maintenance costs. Furthermore, wind energy analysis assists in evaluating the potential environmental impact of wind energy projects, considering factors like noise pollution [14], visual aesthetics, and effects on local wildlife [15, 16]. By examining these factors, projects can be developed to mitigate adverse environmental and community impacts. Given the fluctuating nature of wind patterns governing energy output, it is essential to employ optimal analysis techniques. Various distributions have been developed over the years to predict wind probability density, as evidenced by studies [10, 17–22]. The insights gained from the literature have been applied in this thesis to study wind patterns and select the type of turbine and its installation locations.

Despite their high efficiency in open environments, HAWTs (Horizontal Axis Wind Turbines) are generally unsuitable for urban applications because their large size and spatial requirements hinder integration into densely built areas, limiting their contribution to cost-effective urban wind energy solutions [23]. Conversely, Small VAWTs (Vertical Axis Wind Turbines) demonstrate superior performance in urban environments due to their compatibility with complex flows and lower noise levels compared to HAWTs [7, 9, 24–26]. Many urban wind projects offering aesthetic wind energy conversion have been seen in the last few years [27–29]. These smaller turbines offer advantages such as ease of installation, grid integration, and the provision of backup power during grid outages, thereby enhancing urban resilience [30]. Notably, the Savonius-type VAWTs present additional appealing features such as low wind start-up and simplified maintenance.

Furthermore, the inherent stability of Savonius-type VAWTs in high winds protects the rotor against damage caused by centrifugal forces, making them particularly suitable for urban environments characterized by variable wind patterns and turbulence intensities [31]. By delving into their design intricacies, performance characteristics, and optimization strategies, researchers can contribute significantly to advancing renewable energy technologies and addressing pressing global energy challenges. Thus, within the context of this thesis, studying Savonius wind turbines emerges as a crucial avenue for advancing our understanding and application of sustainable energy solutions.

The performance attributes of a Savonius wind turbine are influenced by various factors, such as the overlap ratio of the curved blades, segmentation, blade count, twisted blades, inclusion of end plates, bucket spacing, and aspect ratio [32–38]. Consequently driving extensive research efforts aimed at enhancing their effectiveness through blade modifications and optimization strategies [33, 39–47]. However, the impact of rotor segmentation remains uncertain, with contradictory findings in the literature [18, 33, 35, 48, 49]. Based on the literature review, extensive experiments were conducted to analyze Savonius wind turbines. Numerical simulations were conducted on a standard Savonius rotor in both open-field and wind tunnel conditions, with results compared to experimental data from wind tunnel tests. Given the conflicting findings in existing literature on rotor segmentation, efforts were made to investigate this aspect further.

As mentioned before, an important reason of selecting a savonius type rotor is the less noise produced. Noise is a critical concern in the wind power sector, with potential impacts including irritation, sleep disturbances, and hearing impairment from prolonged exposure to high noise levels [50–52]. High-frequency noise may induce headaches, fatigue, and vascular constriction, weakening the immune system [53–55]. Residents near wind power plants may experience annoyance, resulting in reduced daily productivity. Thus, it is imperative to investigate wind turbine noise to develop effective mitigation strategies and enhanced designs. More details can be found in Chapter 1.3.5.

In contrast, VAWTs are designed with the driving mechanism situated closer to the ground, reducing mechanical noise transmission [56]. Operating at lower TSR (Tip Speed Ratio) compared to HAWTs, VAWTs exhibit lower aerodynamic noise levels [34, 57, 58]. However, decreasing the turbine's rotational speed by reducing the TSR directly reduces noise, albeit at the cost of energy generation, with an estimated 1 dB SPL (Sound Pressure Level) reduction accompanying 2-4% annual energy loss [59]. Despite advancements in urbanwind turbine installations, detailed analysis of power production and acoustics remains limited [24, 28, 29, 34].

To optimize energy production while minimizing noise, understanding the relationship between noise and turbine efficiency is crucial. Numerous investigations have used computational methods to model aerodynamic noise [60–63], indicating that VAWTs produce less noise than their horizontal counterparts [62, 63]. However, available experimental data on this topic is somewhat limited [24]. Furthermore, most literature focuses on the Darrieus WT, with limited information available on Savonius VAWTs, despite their growing popularity for small-scale applications in populated areas.

The literature discussed above served as inspiration for the research goals outlined in this thesis, which are elaborated upon in Section 1.4.1.

1.1.2 Wind Energy and its Evolution

Wind energy is a by-product of the solar energy. Due to the sunlight radiation, the surface of the earth gets heated to different temperatures at varying locations. This is due to various factors such as cloud cover, surface roughness, material of the ground (soil, cemented, etc). This difference in the temperature leads to a differential pressure over the surfaces. This causes the movement of air from high pressure regions to low pressure regions, resulting in the generation of wind. This pressure gradient also leads to the bending of air from its trail, as witnessed by an onlooker. This drift is caused by the rotation of the earth and is called the Coriolis force.

The Coriolis force affects the global winds in the sense that when the air from the equator rises towards the higher atmospheric layers of the northern and southern hemispheres, this force restricts the air travel after a certain latitude due to high-pressure regions and causes the air to sink down. The wind near to the surface of the earth is different than these global winds and is largely affected by the surface roughness, presence of obstacles, etc up to an approximate height of 100 m above the ground.

The local winds are largely dependent on the parameters of the particular region. The presence of a water body, next to land causes high winds. This can be attributed to the fact that the land masses get heated at a higher rate than the water bodies, causing a large differential pressure. During the night time, the areas around a water body are often more calm as compared to the day time.The presence of mountains leads to an interesting pattern of wind flow. With the the differential density caused of irregular heating, the air ascends or descends. This pattern is reversed during night time. These winds flowing down the leeward side of the valleys are often very powerful.

The wind as discussed above, contains energy which is directly proportional to the mass contained in the wind. The idea of harnessing wind energy is to convert the kinetic energy present in the air to electrical energy.

1.1.3 Types of Rotors

With peaking interest in the field of wind energy, a number of mechanical equipment were developed to harness it. These machines are now referred to as wind turbines. These are rotating machines which convert the kinetic energy present in moving air into electrical energy to be later distributed or used at the moment of its generation. Over the years, several wind turbines came into existence as a joint and individual effort of many countries, as seen in Fig. 1.1.1 [64].

The wind turbines, can be characterised based on a number of parameters, typically, this classification is done on the basis of the axis of rotation, direction of wind propagation, number of blades, type of aerodynamic force and the location where it is installed. In addition to the conventional designs which have been widely accepted by industries, a number of innovative designs are also under research to be launched into the market. In this section, some of these classifications will be discussed.

Axis of Rotation

Considering the axis of rotation, a wind turbine can mainly be classified as a VAWT and HAWT. Further, these horizontal and vertical axis turbines can be categorised under drag-type and lift-type turbines, depending on the component of the force being used for torque production. The blades of the turbines that use lift force, move faster than the wind speed and have slim blades, whilst the turbines that use the drag force rotate at a velocity lower than that of the wind, and thus, require large blades in order to

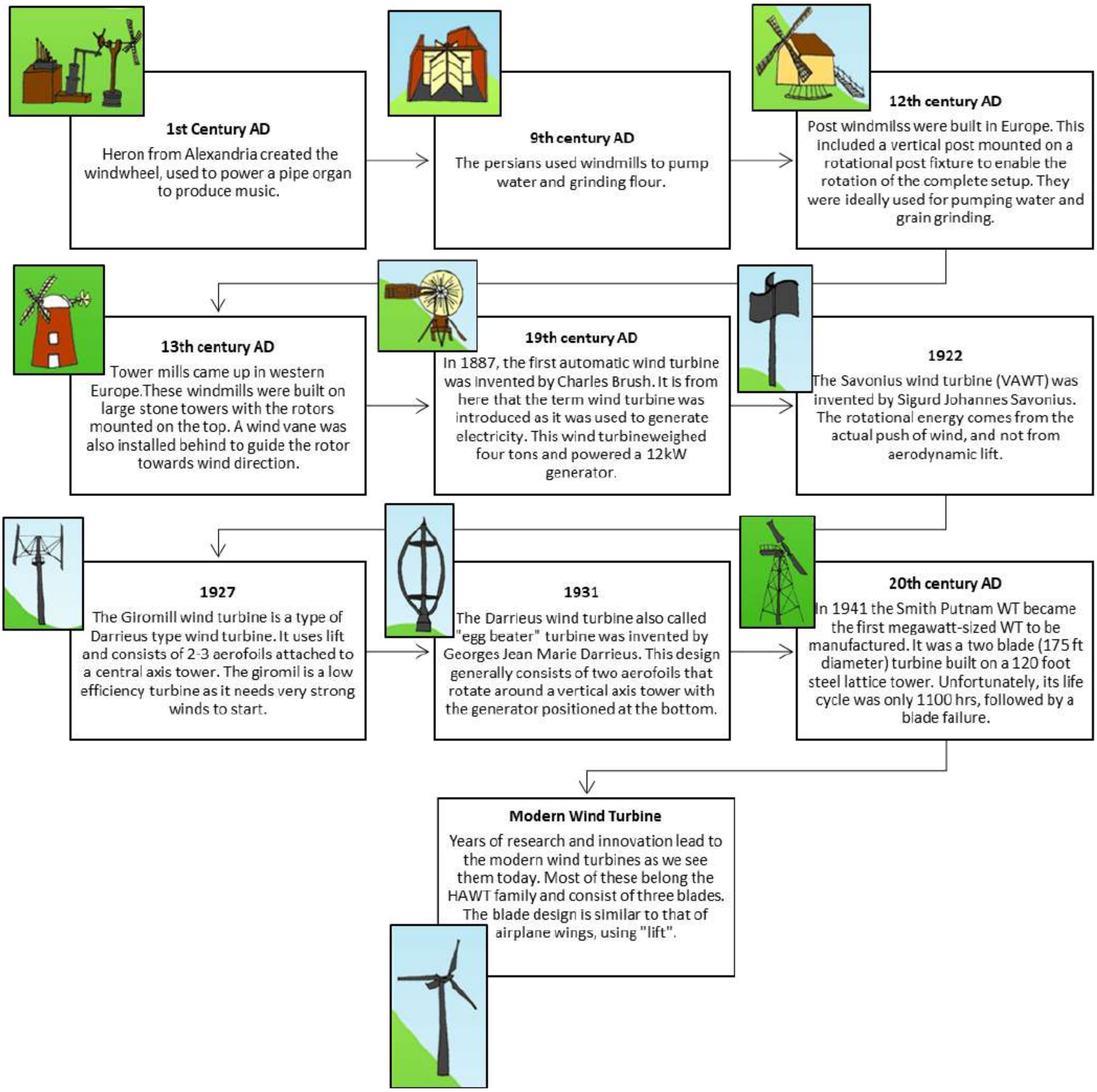

Figure 1.1.1: Evolution of wind turbine over the years [64].

increase the force acting on the rotor. It can be seen in the Fig. 1.1.2 [7] that these types of turbines cover almost the entire rotor projection area. A comparison, weighing the disadvantages and advantages of both types of turbines (HAWT's & VAWT's) will also be summarised in the following subsections.

Vertical Axis Wind Turbine

The vertical axis wind turbines are characterised by the main rotor shaft positioned vertically to the ground. This machine can be further categorised as either lift-based or drag-based. These Wind Turbines are gaining popular interests by many individuals and industries to be implemented in urban areas as they show better results in turbulent environments. A key advantage of this type of machine is that it can harness power

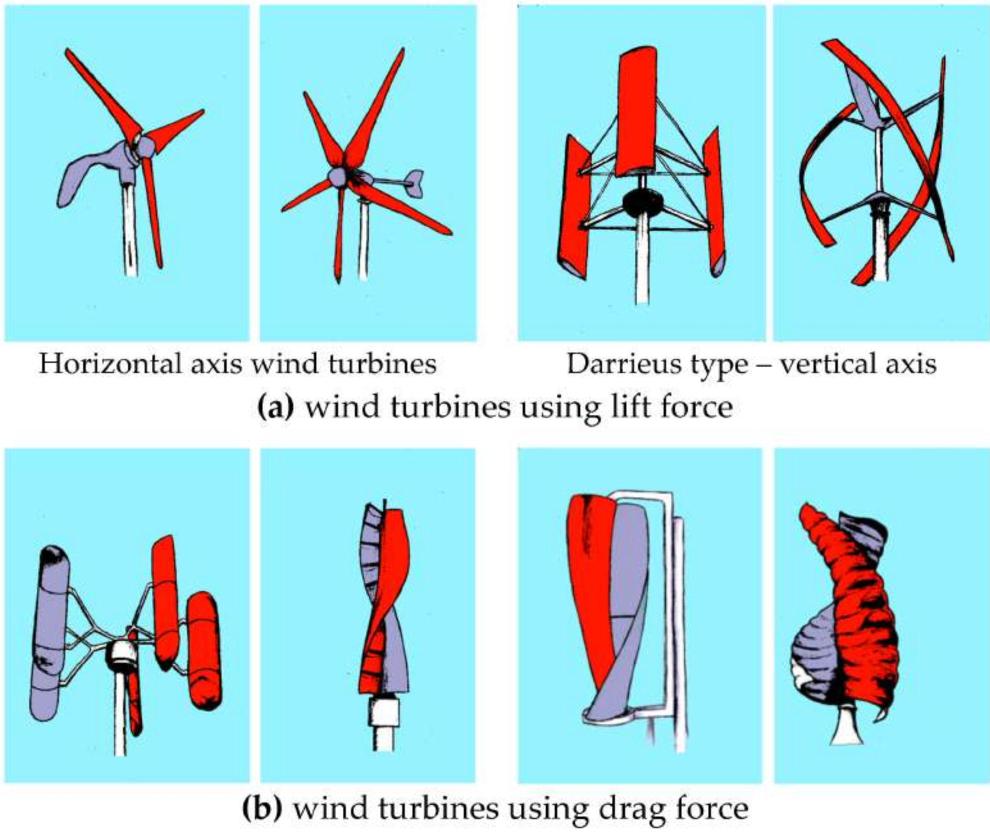

Figure 1.1.2: Different types of wind turbines [33].

from the wind, irrespective of its direction. Many new designs of VAWT's have come into development based on various blade designs; however, the most widely used still remain Darrieus and Savonius types of rotors, sometimes with additional modifications.

Darrieus type

A Darrieus rotor is principally a lift-based WT and has a design consisting of a frame or tower, with curved aerofoils (giving it the appearance of an eggbeater) or straight aerofoils mounted on its side. Over the years, these designs have seen various developments, a detailed timeline of which can be found in [65]. A typical problem with this type of rotor is that the angle of attack of the airfoils changes as they rotate, resulting in the maximum torque being generated at two locations(the position of the rotor facing the wind direction and another position at 180 degrees from the wind direction). Due to this, a pulsating power is produced, which further complicates the design.

Even though this type of wind turbine offers more efficiency than the Savonius type WT, it poses a major challenge in the form of its inability to self-start. A lot of research is being put into the improvement of its designs, however, the main advancements have been observed in the optimization of the design to be more efficient. Owing to the design of the blades, it experiences less drag in comparison to a savonius type of turbine and can rotate faster than wind.

Savonius type

A Savonius wind turbine is typically the simplest form of WT, consisting of a vertical mast, on which 2 half-cylinders facing opposite sides are mounted, forming an S shape. This is illustrated in Fig. 1.1.3. The flowing wind exerts forces on the concave and convex sides of the turbine. The differential force between the two sides results in the rotation of the turbine and thus the generation of electricity. During this, the reverse side of the blades experiences drag, which means that there is always an opposing force. Due to this, this rotor can not rotate higher than that of the wind speed.

This kind of rotor can self-start and offer a large torque, but it works at a low TSR and delivers a comparatively low power coefficient. The noise generated during operation is very low compared to other types of industrial turbines, making it suitable for urban installations. This type of wind turbine is the main focus of analysis for the presented manuscript and is detailed in subsequent sections.

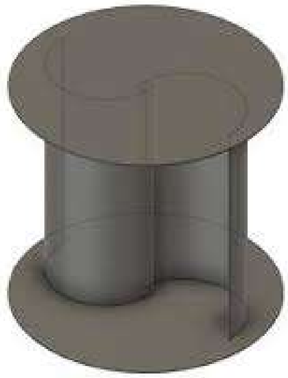

Figure 1.1.3: Typical Savonius type rotor [66].

Hybrid Darrieus and Savonius type

The drag-type Savonius rotor and lift-type Darrieus rotors are the major wind turbines being used in the urban environment. While the Savonius wind turbines offer a simple design and self-starting capabilities at low wind speeds, the Darrieus rotor has a more complicated design and uses the lift force for its operation, resulting in low torque. Thus, it requires an additional system to provide the initial starting torque at low wind speeds. In terms of wake generation, the Darrieus rotor achieves smaller wakes in contrast to the Savonius rotor.

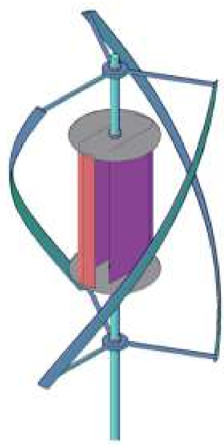

Figure 1.1.4: Combined Savonius-Darrieus wind turbine

Various attempts have been made to combine these two turbines to gain the benefits of both rotors. After several studies, the designs which have proved to be the most promising consist of the Darrieus rotor in the upper portion and the Savonius part in the lower region, and a Savonius rotor, encircled with Darrieus blades as shown in Fig. 1.1.4 [67].

[68] Analysed the two configurations as shown in Fig. 1.1.5. The configuration consisting of a Savonius rotor in the center, surrounded by Darrieus blades shows that there is a reduced cut in velocity as compared to only Darrieus rotor. In addition, the performance of the combined system is always greater than that of a Savonius rotor but lower than that of a Darrieus turbine alone due the the airflow interference. Although it results in significant development in performance at low TSR regimes.

In actual wind conditions, it was observed that for net power output, type B is more competent. However, for conditions where wind blew for a short duration, a reduction in electric power coefficient was observed for this design, and the former design proved to be more viable.

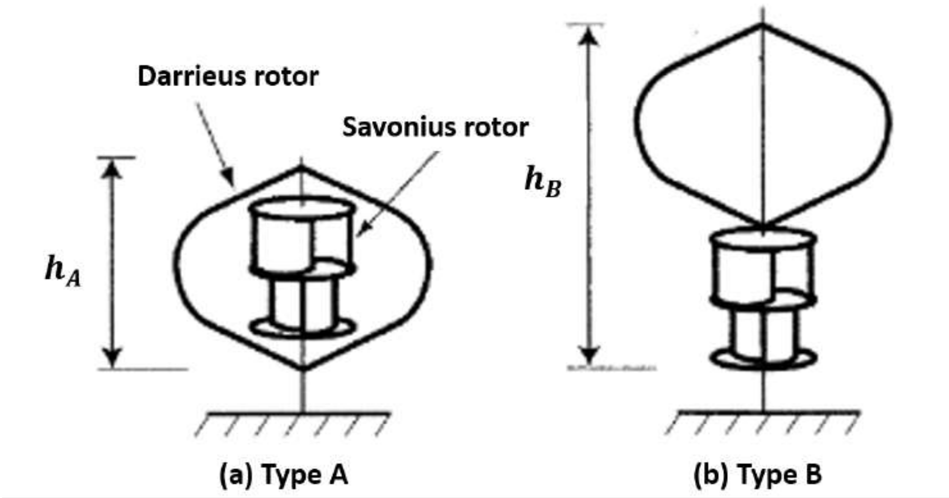

Figure 1.1.5: Two different hybrid savonius-darrius hybrid configurations

These results pave the way for future investigations in the field by taking into consideration such as the number of blades in each type of turbine, the design and arrangement of the Darrieus counterpart needs to be examined to diminish the aerodynamic interference to further improve the performance.

Horizontal Axis Wind Turbine

As the name suggests, a HAWT is one where the main shaft on which a propeller-type rotor is mounted is parallel or with little inclination to the ground (Fig. 1.1.6). These types of turbines are most widely used for large-scale power production and industrial purposes to be connected to the grid lines. Quite a lot of research is being conducted in developing HAWTs for urban environments, which will be discussed later in detail. These rotors generally have 2 or 3 blades and function at high tip speed ratio. Similar to aircraft airfoils, these also use lift as the driving aerodynamic force for the rotation of the blades.

Further classification of this WT can be done on the basis of the face of hub relative to the direction of wind - upwind and downwind (Fig. 1.1.6). Upwind rotors are characterized by the wind hits the turbine blades before reaching the mast. Currently, only

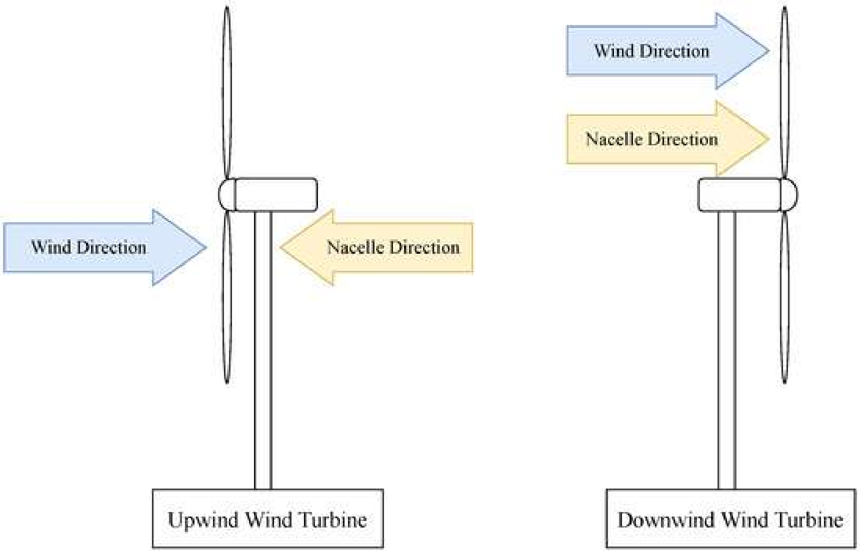

Figure 1.1.6: A typical HAWT with different rotor orientation with respect to wind direction. [69]

this type is in use, as opposed to downwind rotors, where the blades are located on the side of the mast that is shielded from the wind.

Table 1.1.1 provides a concise overview of the main differences between horizontal-axis and vertical-axis aiding in understanding their suitability for various applications.

Feature	HAWT	VAWT
Design Orientation	Rotor shaft aligned with wind direction	Rotor shaft perpendicular to wind
Common Types	Three blade, two blade	Savonius, Darrieus
Efficiency	High, especially at optimal TSR	Moderate
Wind Direction Sensitivity	Requires yaw mechanism to align with wind	Omni-directional operation
Noise Levels	Can be high due to blade movement	Generally low
Maintenance	Moderate to high	Low
Installation Location	Typically onshore or offshore	Suitable for urban and rural areas
Power Output	High (up to several MW)	Low to moderate
Cost	High initial investment	Lower initial investment
Scalability	Suitable for large-scale applications	Limited scalability

Table 1.1.1: Overview: Comparison of different wind turbines

Chapter 1.2

Fundamentals of Wind Turbine

1.2.1 Power available in wind

The kinetic energy (E) present in the moving air is proportional to the air mass (m) and wind velocity (v) in m/s. In the Eq. form, it is written as:

$$\begin{aligned} E &= \frac{1}{2}(mv^2) \\ &= \frac{1}{2}(\rho V v^2) \end{aligned} \tag{1.2.1}$$

Where ρ is the density of air and V is the volume of the air available to the rotor.

The wind that flows over the rotor per unit time has an area equal to that of the rotor cross-sectional area A (m^2), exposed to the incoming wind, then Eq. 1.2.1 can be changed and expressed in terms of power in watts as:

$$P = \frac{1}{2}(\rho A v^3) \tag{1.2.2}$$

Fig. 1.2.1 shows the area considered for calculating the energy in wind passing through the rotor. The area considered for savonius wind turbine is the projected area of a cylinder, i.e.: the product of the diameter (D) and height (H) of the rotor.

The air density is highly influenced by the air constituents, temperature, pressure of the atmosphere, and the coordinates of the location. Dry air can be assumed to be an ideal gas. According to the law of ideal gas:

$$pV_g = nRT \tag{1.2.3}$$

where p is the pressure, V_g is the gas volume, n is the amount of substance(in kmol), R is ideal gas constant and T is temperature. Air density is defined by the ratio of the mass of air (1 kmol) and its volume, and can be written as:

$$\rho_a = \frac{m}{V_g} \tag{1.2.4}$$

Equations 1.2.3 and 1.2.4 can be combined to give:

$$\rho = \frac{mp}{RT} \tag{1.2.5}$$

The relationship between the altitude Z, T and the air density at a location is written as:

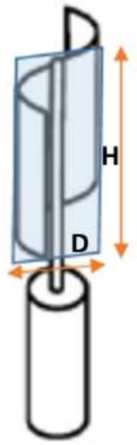

(a) Vertical Axis Wind Turbine- Savonius Turbine.

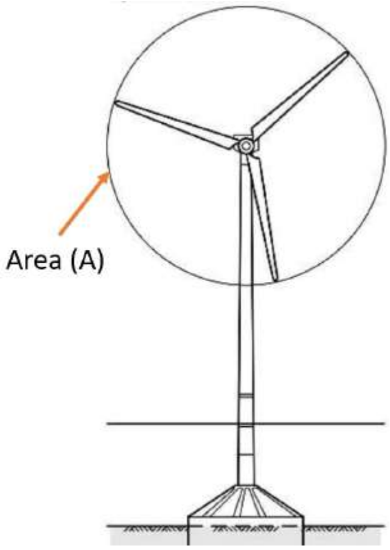

(b) Horizontal Axis Wind Turbine [70].

Figure 1.2.1: Wind passing through rotor.

$$\rho = \frac{353.049}{T} e^{-0.034 \frac{Z}{T}} \tag{1.2.6}$$

Altitude and temperature have an inverse effect on the air density, as explained in detail in [71]. This means that the air density decreases with an increase in atmospheric temperature and elevation of the site. The value of air density is typically considered as 1.225 kg/m^2 as measured at sea level and 15℃. Due to this small value of air density and thus, very large wind turbines often need to be manufactured for notable power production.

Velocity is a very important factor for retrieving energy from wind. If the wind speed doubles, the power available increases by eight times. Therefore, it can be implied that for the same power, the rotor size can be decreased by eight times. Thus, it is very important to do a proper study of the wind patters of the location where the wind turbine is to be installed.

1.2.2 Wind Rotor Flow Dynamics

As wind flows through a wind turbine rotor, it transfers part of its kinetic energy to the rotor, resulting in a reduction of wind speed. This interaction causes the streamtube—the imaginary tube formed by streamlines encompassing the airflow through the rotor—to expand downstream, as the air slows down and its pressure adjusts. To conserve mass flow rate, the cross-sectional area of the streamtube increases after passing through the rotor. This phenomenon is illustrated in Fig. 1.2.2.

In practice, the rotor begins to influence the airflow even before the wind reaches the rotor plane, causing a deflection of the streamlines. Not all of the wind's energy can be extracted by the rotor, as the air must retain some velocity to continue flowing downstream. If the air were brought to a complete stop, it would accumulate behind the rotor, causing an unrealistic and unsustainable increase in the downstream cross-sectional area ($A2$). This limitation is consistent with the Betz limit as explained in Section 1.2.3.1.

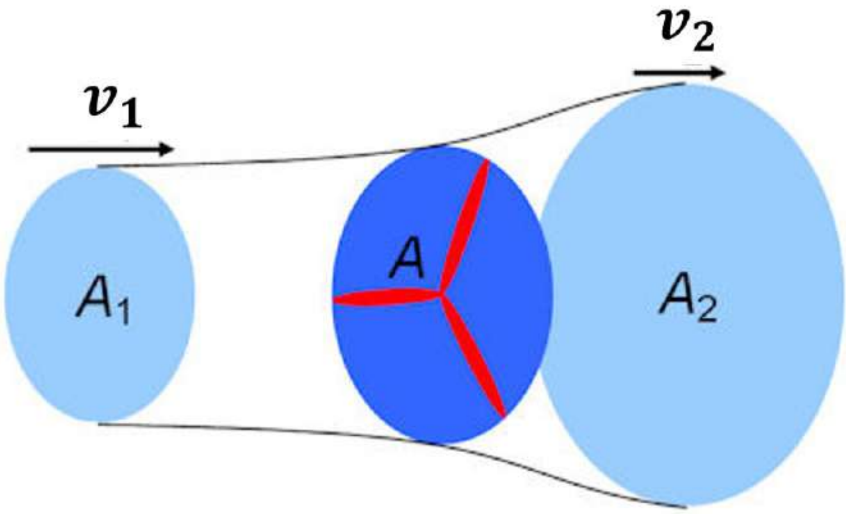

Figure 1.2.2: Flow of wind across rotor [72]

Fig. 1.2.3 shows the variation of the local wind pressure before and after the wind passes through the rotor (in green lines). As the wind advances towards the rotor from the left, an increase in air pressure is observed, as the rotor serves as an obstruction to the incoming air. It should also be noted that the pressure drops immediately after the wind passes by the rotor and then eventually increases to become equal to the local air pressure.

When the wind moves further downstream from the rotor, the decreased wind velocity gradually becomes equal to the local wind velocity. This is because of the presence of high turbulence behind the rotor. The wind shade behind the rotor also decreases as we go farther away from the turbine.

1.2.3 Wind turbine performance

1.2.3.1 Betz Law

When extracting energy from the wind, the objective is to capture as much kinetic energy as possible. However, attempting to extract all the energy would result in the wind coming to a complete stop after passing through the rotor. This cessation would

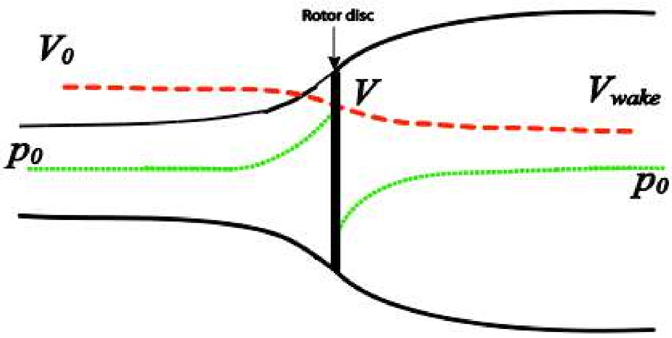

Figure 1.2.3: Deflection of wind across rotor [73]

prevent further airflow into the rotor plane, effectively halting energy production. Conversely, if the wind passes through the rotor without any reduction in velocity, no energy is extracted. Therefore, an optimal balance must be achieved to maximize energy conversion while maintaining continuous airflow.

This balance is described by Betz's Law, formulated by German physicist Albert Betz in 1919. The law states that no wind turbine can capture more than 59.3% (or 16/27) of the kinetic energy in the wind (Fig. 1.2.4). This theoretical limit arises because extracting more energy would reduce the downstream wind speed to zero, preventing further airflow through the turbine. Thus, the geometry of the turbine and the flow dynamics impose inherent constraints on its efficiency.

In practice, modern wind turbines operate at efficiencies ranging from 60% to 80% of the Betz limit, depending on design and operational conditions. These efficiencies are influenced by factors such as blade design, aerodynamics, mechanical losses, and control systems. Understanding and applying the principles encapsulated in Betz's Law are crucial for optimizing wind turbine performance within the physical constraints imposed by the conservation of mass and momentum. To prove the law, some assumptions need to be made:

- an ideal rotor with an infinite number of blades and no drag
- absence of hub from the rotor
- incompressible flow of the wind
- velocity and pressure are uniformly distributed across the rotor disc
- the flow across the rotor is axial, and the volume of air entering and leaving the rotor is conserved
- the average wind speed across the rotor is an average of the wind speed entering (v_1) and leaving (v_2) it, i.e. $(v_1 + v_2)/2$

The mass flow rate of the wind stream ($\dot{m}$) can be written as Eq. 1.2.7, and the power converted from air to useful mechanical energy (represented as 'P') is as shown in Eq. 1.2.8 (using Newton's second law).

$$\dot{m} = \frac{1}{2}\rho A(v_1 + v_2) \tag{1.2.7}$$

$$P = (1/2)\dot{m}\left(v_1^2 - v_2^2\right) \tag{1.2.8}$$

Substituting Eq. 1.2.7 in Eq. 1.2.8, we get Eq. 1.2.9

$$P = (P/4)\left(v_1^2 - v_2^2\right)(v_1 + v_2)\,A \tag{1.2.9}$$

Eq. 1.2.10 gives the power available in the wind that can be derived for useful purposes.

$$P_0 = (P/2)v_1^3 A \tag{1.2.10}$$

The ratio of the power being extracted to the power available in the wind is called the Coefficient of performance and is detailed in the next section. This value is calculated as:

$$(P/P_0) = (1/2)\left(1 - (v_2/v_1)^2\right)(1 + (v_2/v_1)) \tag{1.2.11}$$

Plotting P/P_0 as a function of v_2/v_1 results in a curve as shown in Fig. 1.2.4. It can be observed that the curve reaches a maximum value of 0.59 or 16/27 for the power that can be extracted from the wind.

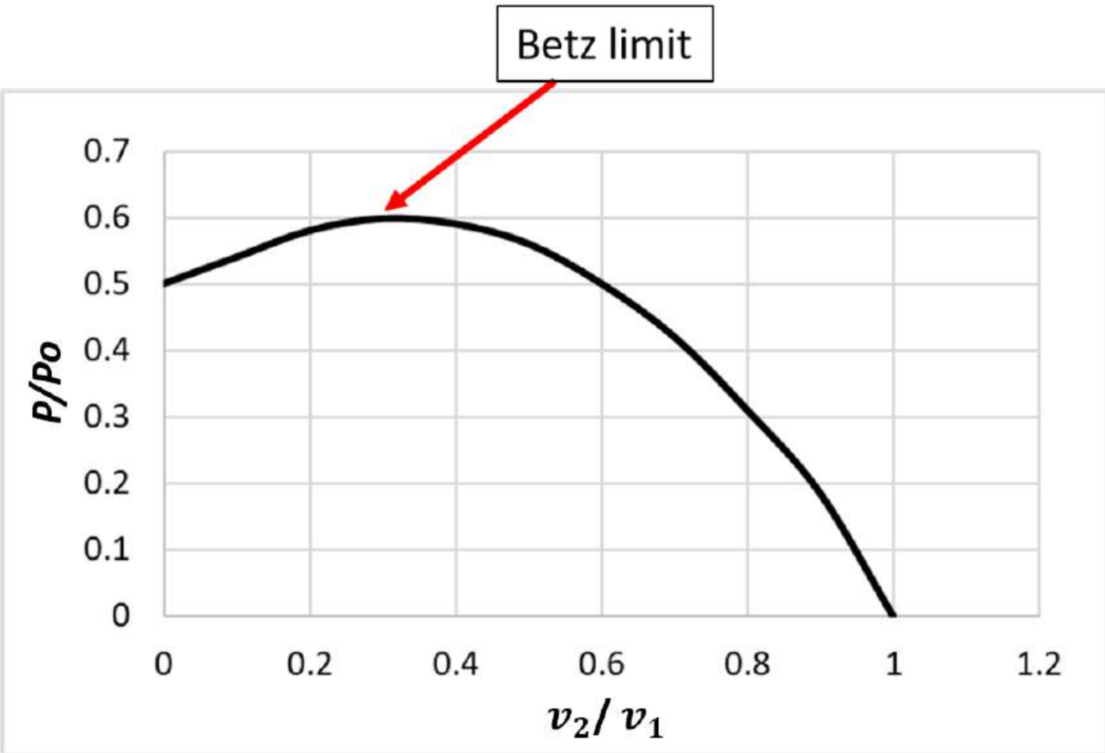

Figure 1.2.4: Betz Law

1.2.3.2 Coefficient of Performance C_p

The performance coefficient of a wind turbine is typically defined as the ratio of the actual power output of the turbine to the maximum possible power output based on the available wind energy. The performance coefficient, denoted as C_p, can be calculated using the following Eq.:

$$C_p = \frac{P}{P_0} = \frac{P}{\frac{1}{2}\rho A V^3} \tag{1.2.12}$$

This is a very important aspect used in the industry as it gives information about the performance of a particular turbine at a particular site. As explained in section 1.2.3, Betz law, this value can not exceed 0.593.

1.2.4 Tip Speed Ratio

The TSR is a key parameter to wind turbine design and is defined by the ratio of the speed of the rotor blade tip to speed of the free-stream wind [Eqs. 1.2.13 and 1.2.14]. If the speed of the rotor blade is very slow, most of the wind will escape through it. Thus generating very little or no power. Alternatively, if the rotor blade is rotating at a very high speed, it will act as a pseudo-solid wall to the incoming wind.

$$\text{TSR}(\lambda) = \frac{\text{blade tip speed}}{\text{wind speed}} \tag{1.2.13}$$

$$\text{blade tip speed (m/s)} = \frac{\text{rotational speed (rpm)} \times \pi \times D}{60} \tag{1.2.14}$$

Where, D= diameter of rotor (m).

The torque coefficient C_t of a wind turbine is defined as:

$$C_t = \frac{\text{Torque produced by the turbine}}{\text{Available torque from the wind}}$$

The power extracted by the wind turbine is given by:

$$P = \frac{1}{2}\rho A v^3 C_p$$

The mechanical power on the turbine shaft can also be expressed as:

$$P = T\omega$$

where:

- τ is the torque,
- ω is the angular velocity of the rotor.

Since $\omega = \frac{v\lambda}{r}$, where r is the radius of the turbine blade, we can rewrite the power Eq. as:

$$P = \tau \left(\frac{v\lambda}{r}\right)$$

Rearranging for τ and substituting P from the wind power Eq.:

$$\tau = \frac{\left(\frac{1}{2}\rho A v^3 C_p\right) r}{v\lambda}$$

The torque coefficient C_t is defined as:

$$C_t = \frac{\tau}{\frac{1}{2}\rho A v^2 r}$$

Substituting τ from the above expression:

$$C_t = \frac{\frac{1}{2}\rho A v^2 r \frac{C_p}{\lambda}}{\frac{1}{2}\rho A v^2 R}$$

Therefore:

$$C_t = C_p \cdot \lambda$$

As wind turbine blades rotate, they generate turbulent airflow in their wake. This turbulence can lead to aerodynamic inefficiencies, increased structural fatigue, and potential reductions in energy capture—ultimately affecting overall efficiency. These effects highlight the importance of optimizing turbine design to maximize energy conversion while minimizing the impact of wake-induced turbulence.

Higher TSR values are associated with increased WT rotational speed, which can enhance the overall performance. However, excessively high TSRs introduce several aerodynamic and structural challenges. Elevated blade tip velocities result in increased aeroacoustic emissions, which can be significant in noise-sensitive environments. Additionally, higher centrifugal forces at elevated TSRs impose greater mechanical loads on the rotor blades, necessitating the use of high-strength materials and leading to increased fatigue and maintenance demands. From an aerodynamic point of view, high TSRs intensify wake turbulence, which can reduce the performance due to increased flow unsteadiness and energy dissipation. These aerodynamic losses are also observed in the case of low TSR when the flow separation is high, thereby resulting in high turbulence. In the case of Savonius-type turbines, a TSR exceeding unity indicates that the blade tips are moving faster than the freestream velocity, potentially causing the rotor to transfer energy to the flow, thereby reducing net power extraction efficiency.

1.2.5 Performance comparison for various wind turbines

The coefficient of performance and the TSR are two important parameters used to assess the performance of wind turbines. However, the specific values of C_p and TSR can vary significantly depending on the design and specifications of different wind turbine types.

Fig. 1.2.5 [74] shows the comparison of the variation of C_p with the TSR for different wind turbines.

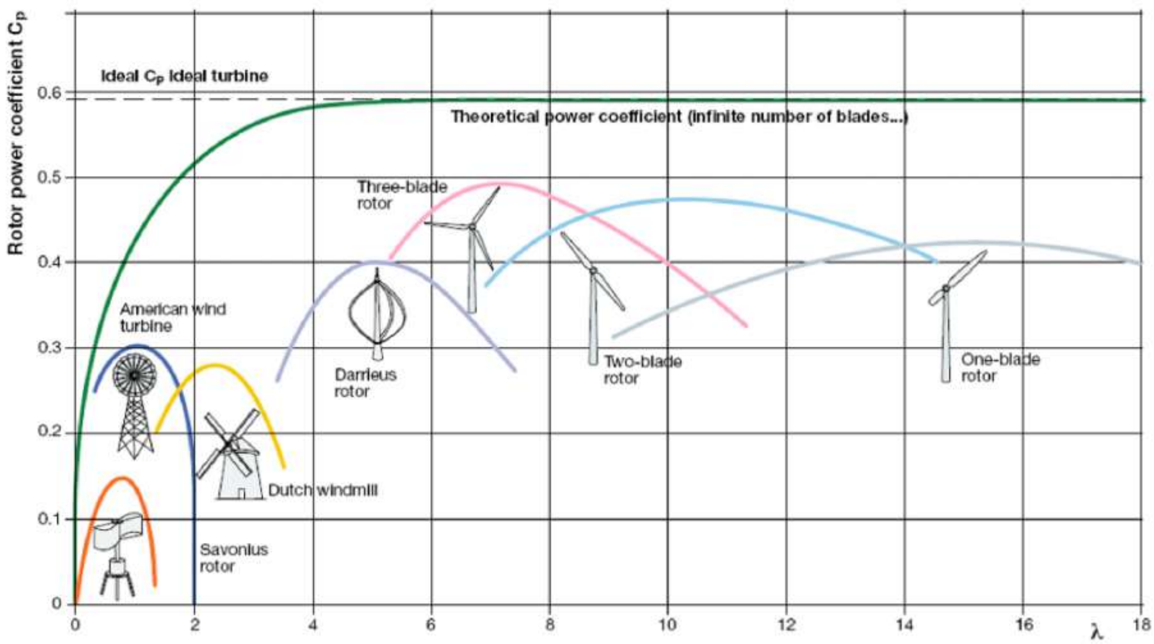

Figure 1.2.5: Variation of C_p with Tip Speed Ratio (λ) [74]

As shown, the three-bladed HAWT delivers the highest power output among all types, typically operating efficiently within a TSR range of 5 to 11. Although the two-bladed and single-bladed VAWTs can function at higher TSRs, their performance is lower compared to the three-bladed HAWT.

The Darrieus turbine operates efficiently at TSR values between 3 and 7 and achieves a higher power coefficient compared to traditional Dutch windmills, which operate at lower TSRs ranging from 1 to 3, prioritizing robustness and specific applications such as drainage, which results in lower aerodynamic efficiency and power output. The Savonius rotor typically operates within a TSR range of 0 to 2, which indicates that it functions efficiently even at low wind speeds. In contrast to other wind turbines it produces maximum torque at low TSR, hence it starts much quicker than other rotors, making it particularly well-suited for areas where wind conditions are generally mild or inconsistent. Due to these characteristics, the **Savonius rotor** presents a practical and reliable solution for harnessing wind energy in such environments. **This specific type of vertical-axis wind turbine forms the central focus of this thesis, and its design, working principles, and performance characteristics have been examined and discussed in detail throughout the study.**

Chapter 1.3

Urban Wind Power: Outline

1.3.1 Analysis of wind characteristic in urban environment

The surface roughness in an urban setting significantly influences the wind flow features, such as the turbulence intensity, surface drag, speed of wind and its profile [75]. Detailed and accurate measurements of these characteristic is therefore required to predict the urban wind performance [76]. At present, three principal methods are being used to make such measurements, including Davenport roughness classification [77], morphometric and micrometeorological methods [76]. The surface type classification-Davenport is given according to various surface roughness estimates that are based on high quality readings. Even though this method considers an extensive array of surfaces, it is not highly effective to define urban permeability in densely populated cities. The morphometric methods, in comparison with the micrometeorological technique, evaluates the aerodynamic properties by making use of empirical relations [78].

This surface roughness layer runs from the surface to a height where the wind flow becomes homogeneous, which is about 2-5 times the height of a typical canopy element [79]. Specific building arrangements affect the local airflow patterns and consequentially result in complicated features adjacent to the urban canopy elements present in this layer [80]. The different sub-layers of the urban Atmospheric Boundary Layer (ABL) are shown in Fig. 1.3.1. To better understand the urban environment, the effects of certain large-scale urban features, such as lakes, parks, and the seaside, must be studied [81].

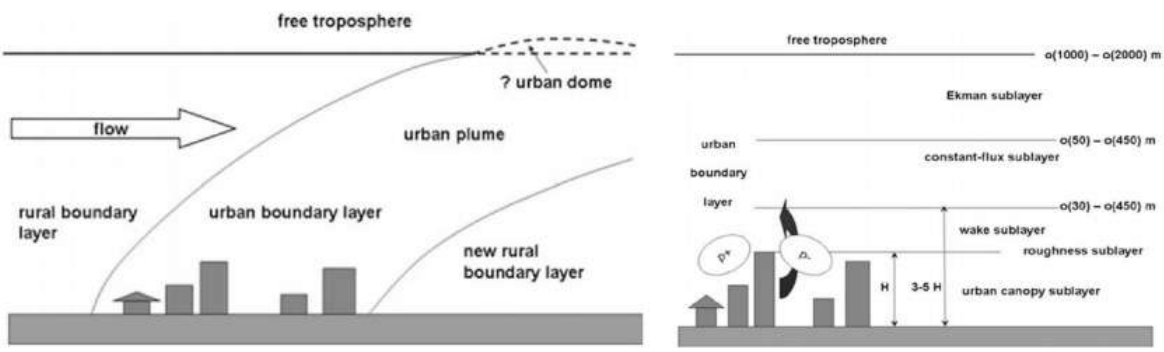

Figure 1.3.1: Comparison of the rural and urban ABL. The urban ABL comprises of the urban canopy sublayer and the wake sublayer created by the urban canopy [82].

1.3.2 Wind Potential Availability: Insights and Trends

An important source of information when making a decision on the type of turbine and its installation location is the wind characteristics of the region. It provides information on the environmental conditions that the turbines will be exposed to, such as wind speed and turbulence [10]. This data is critical in designing turbines that can withstand harsh weather conditions, optimize energy production, minimize maintenance costs ([11], [12], [13]), and help predict their energy output. The total energy output is influenced by various factors, some of them being site temperature, type of surface, wind speed, height of measurement device, air density, etc. [83]. Wind energy analysis also helps to evaluate the potential environmental impact of a wind energy project [15]. It takes into account factors such as noise pollution [14], visual impact, and the effects on local wildlife [16]. By studying these factors, experts can design projects that minimize their impact on the environment and local communities.

Recent years have seen a growing interest among researchers in exploring wind power potential in urban areas, driven by the proliferation of high-rise buildings to accommodate urban population growth. Turbine deployment in such areas presents challenges due to unpredictable and turbulent wind patterns, compounded by heterogeneous terrain and evolving architectural plans. This underscores the need for focused studies on local wind dynamics. Juan et al. [3] provide insightful analysis, demonstrating the impact of varying building width, height, and spacing on dimensionless power density, alongside detailed examinations of wind velocity fluctuations influenced by adjacent building heights.

Due to the fluctuating nature of wind patterns that govern the energy output at any given location, it is imperative to find an optimal analysis technique. Over the years, many distributions have been developed to predict the probability density of wind velocity(details can be found in Section 2.1.1.5). Studies demonstrated in [17] compare the Wakeby distribution function, Beta distribution function, Pert distribution function, Generalized Pareto distribution function, Gamma distribution function, Generalized Gamma function, and the Johnson SB distribution function. It was concluded that the Wakeby method outperformed the other functions used in the study, with a good agreement between the predicted and recorded data. Some of the other distribution functions are the inverse Gaussian distribution, the generalized normal, the log-normal distribution, the three-parameter log-normal, the kappa, the normal two-variable distribution, the normal square root of the wind speed distribution, and hybrid distributions. Wind speed at the airport in Dolný Hričov was modeled using the Lognormal, gamma, and Weibull probability density distributions, with the Weibull prediction outperforming the others [84]. Through a comparative analysis of probability density distributions for the Mediterranean coast of Turkey over a one-year period utilizing Rayleigh and Weibull predictions, it was determined that the Weibull model offered a better fit and superior probability density estimates for the entire duration of the study [85].

Kernel Density Estimation (KDE), a flexible method in wind potential analysis, is gaining popularity for its non-parametric approach [19,86]. However, its accuracy may be affected by factors like kernel selection, sample size, and bandwidth [87,88]. While KDE primarily estimates probability density functions, it can complement other models for predictive purposes [89,90]. For wind speed prediction, machine learning algorithms and memory networks offer greater flexibility and capability in capturing complex patterns, albeit requiring more data and computational resources [91,92]. The Weibull distribution function is extensively discussed here due to its ability to satisfactorily estimate skewness, maintain consistency in velocity distributions, and enable simple estimation of total Wind Power Density (WPD) and its standard deviation [93].

The Weibull distribution is a flexible distribution that can fit a wide range of data. This distribution is used in reliability engineering to model the failure rates of devices and systems over time. It is also used in other fields, such as finance, engineering, and environmental science, meteorology, business, social science, hydrology, and biology to model the distribution of data. For the purpose of this study, the discussions are restricted to its usage in the wind energy industry where it has been widely used for site assessment, turbine design, and wind power forecasting. Many methods such as the Inverse Gaussian, Extreme Value, Lognormal, etc., are used to estimate the wind distribution [20], however, the Weibull distribution is utilized vastly. The shape and scale parameters defining the shape and location of the probabilistic curve on the plot can be calculated using various methods [21] [22] [94]. Many investigations have been carried out to find the accuracy of the methods available to perform such calculations, and many new ones have been developed as well.

In conclusion, a thorough investigation of wind characteristics at specific locations is imperative for informed decision-making in turbine selection and deployment. Understanding the unique wind patterns, environmental conditions, and potential impacts allows for optimized turbine design, efficient energy production, and minimization of environmental disturbances. Failure to conduct detailed assessments tailored to individual sites can lead to inaccurate predictions and suboptimal performance, underscoring the critical importance of site-specific wind analysis in wind energy projects.

1.3.3 Wind Turbines in the Urban Environment

The presence of buildings, trees and other obstacles in urban areas causes a significant change in wind profiles, giving rise to turbulent and chaotic flows, as compared to remote areas where the flow is more uniform. This poses challenges in the development of an urban wind energy system, although the availability of faster computing resources has been a boon in such an endeavour. Nowadays, the key approach being followed to incorporate wind turbines in urban surroundings is to locate a wind energy farm in the vicinity of an urban setting or install wind turbines on building rooftops. Even though this approach has helped to overcome many challenges, such as noise pollution, turbulence, visual impression of the city, and the need for space, it is accompanied by an additional cost of a grid network to transmit the generated power to distant electrical loads [95].

One of the major goals after analyzing the optimal wind resource available is to check the type of wind turbine to be installed. A variety of wind turbines are available in the market and can be selected based on the purpose of interest. The selection of the wind turbine is dependent on various factors [96] [97] [34], such as:

- Wind speed: Different turbines are designed to operate at different wind speeds, and an optimal selection is required based on the wind potential assessment of the area.

- Power output: The amount of power production decides the specifications of the wind turbine. For small-scale production, like to power a small home, a smaller turbine is required than to power a farm or other large property.

- Tower height: The higher the wind turbine is installed, the more wind it will capture. However, taller towers also increase the cost of installation and maintenance. Other limitations include the regional government laws and the strength of the base on which the turbine is mounted, such as the ground or the roof.

- Noise: This is a very important aspect that needs to be taken into consideration during WT installation and has been discussed in detailed in Sections: 1.3.5, 4.1 and 4.2.

Other factors also include the cost of purchase and maintenance, selection of appropriate grid connections in case of plans to transfer power to the grid, or electrical connections and storage for the usage of the installation for charging cars, powering street lamps, heating system for a household or small community, etc.

Many wind turbine designs are industrially available and development is still underway to come up with unique solutions to harness wind energy in urban areas. Wind turbines can be potentially incorporated into urban areas to harness as:

- installing wind turbines on existing buildings
- complete integration of wind turbines with architectural form
- wind turbines mounted on the highway, driven by the atmospheric wind and high-speed vehicles passing by [98, 99].

(a) (b) (c)

Figure 1.3.2: Possible installations of BIWT: (a) The Bahrain World Trade Center, with three 225 kW turbines on bridges spanning the twin towers [100]. (b) Strata SE1 with three wind turbines rated at 19 kW. (c) Adventure Aquarium in Camden, New Jersey, featuring eight 0.4 kW and four 1 kW AeroVironment turbines [100].

A considerably new wind turbine attracting researchers as a substitute for micro-scale energy generation is a Building Integrated Wind Turbine (BIWT). At present, two possible arrangements of these types of turbines are available. Comparatively large-sized wind turbines mounted on the rooftop, positioned between two adjacent buildings (Fig. 1.3.2b or structural openings inside the buildings (Fig. 1.3.2a); small-sized wind turbines or an arrangement of small wind turbines spread over the roof or along the height of the building Fig. 1.3.2c. Despite the fact that this approach excludes the need of high voltage electricity networks for power transmission to the required area, it poses contests such as reduced wind turbine power output, shadow flicker and adds up to a certain amount of vibrations and noise related problems in the building [101].

A very good example of this is the skyscraper in London: Fig. 1.3.2b [102], which has been stationary for a long time due to excessive noise and vibration issues faced by the residents of the building. Furthermore, it also necessitates thorough planning and designing so that this system can be exploited to its maximum benefit.

1.3.4 Wind Turbines suitable for Urban Environment

Small wind turbines are designed to generate electricity for residential or small commercial use, and they are typically less than 100 ft in height. They are designed to operate at lower wind speeds and can be installed on rooftops or other small areas, making them ideal for urban environments. Vertica-axiss wind turbines, on the other hand, have a unique design that allows them to capture wind from any direction, which is particularly useful in urban environments where wind direction can change quickly and unpredictably due to buildings and other structures [103] [104]. They are also quieter than horizontal axis wind turbines, making them more acceptable to the neighborhood [105, 106]. These can also be installed closer to the ground, making them a good option for rooftops and small urban spaces, also allowing for easy access to the equipment parts for maintenance. Thus, it can be inferred that a combination of both the above-mentioned types of rotors, i.e. a small VAWT is a good choice for the case study under consideration. VAWT's can again be classified as Darrieus and Savonius-type rotors.

A Darrieus rotor offers advantages in terms of power coefficient resulting from high operational rotational speeds, whereas an SVAWT can self-start, even at very low wind speeds. An examination of diverse published works, encompassing experimental, theoretical, or numerical studies on Savonius turbines foresees this VAWT as a compelling technological substitute for traditional wind turbines [24]. It consists of a simple and compact design, making it easier to repair, maintain, and manufacture. In Savonius rotors, safety is a major benefit, as these rotors do not overspin at high wind speeds. Moreover, due to its low operational rotational speed, it produces less overall noise. Therefore, the choice between Savonius and Darrieus turbines depends on specific requirements, site conditions, wind resources, and other factors that must be considered in the context of the intended application.

Various simulations and experiments investigate the impact and arrangement of multiple Savonius rotors in wind farms [107]. Research reveals distinct behaviors among different rotor arrangements, with counter-rotating configurations exhibiting superior performance, reclaiming wind stream velocity efficiently. VAWT wind farms, though inherently less efficient than HAWTs, benefit from closer turbine placement [108]. Studies modeling arrays of 2-16 Savonius rotors indicate increased efficiency with closely positioned turbines, emphasizing the importance of turbine number and proximity [109]. Analysis of wake interactions underscores the downstream effects on rotor performance, highlighting optimal turbine spacing for enhanced power output. Investigation of various wind farm configurations suggests an optimal rotor gap for maximizing power generation [110]. Overall, leveraging Savonius-type turbines in wind farms offers promising energy production with minimal land requirements, particularly in urban environments. This study includes diverse Savonius rotor designs, aiming to advance both standalone and wind farm installations, supported by comprehensive numerical and experimental analyses.

1.3.5 Wind Turbine Noise

Noise generation is one of the key factors when it comes to the wind power industry. Moreover, wind turbines located in residential areas can have a significant impact on the quality of life of nearby residents, leading to complaints about noise pollution. Wind turbine noise can be classified based on its frequency as tonal or broadband [111]. Another classification is based on the noise source, namely aerodynamic and mechanical. The measure of noise given by the level of sound pressure is the sum of aerodynamic and mechanical noises.

The acoustic disturbance generated by wind turbines can be essentially divided into two parts: Low Frequency Noise (LFN) and High Frequency Noise (HFN). The HFN ranges from about 250 Hz- 20 kHz and correspond to less audible distance from the source, but are are however,more audible to an ordinary human ear. These sounds can be perceived as can be described as a high-pitched whine or screech and leading to a higher irritation and disturbance. Long term exposure to these sounds can cause serious auditory damage along with the health affects associated with LFN.

On the other hand, the dominant range of LFN is associated with frequency ranges from 20 Hz - 250 Hz [112], however, infrasound (1-20 Hz) are also studied commonly due to its impact on nearby inhabitants. A low frequency noise is often described as a low-level humming or rumbling sound and can be difficult for people to hear, but can travel long distances. In theory, non physical health effects such as headache, difficulty sleeping, nausea, vertigo, irritation, lack of concentration, inability to do everyday work with full efficiency, tinnitus, panic attacks and memory issues can be linked to low frequency infrasonic sounds [113, 114]. Some other biological effects from LFN include cognitive alterations [115, 116], the development of cardiovascular diseases [53, 54, 117], increased blood pressure [55], and, more recently, the effects of on dental wear [118], [119].

However, wind turbines are not the sole reason for such health issues. It should also be noted that a number of factors alter the propagation of noise from the wind energy generation equipment, some of them include temperature of air, humidity, obstacles, reflection and the material of the ground surface. Background noise is another key factor, mainly including noise produced by cars, railways, industries, aircraft, machinery, including air conditioners, compressors, mining equipment, etc [120] and [121]. Considering these facts, it can be said that the health distress faced by the residents in the vicinity of wind turbines can not be entirely associated with wind turbines but also the annoyance caused by visual impact and a negative attitude towards wind turbines [122–124]. To mitigate the impact of wind turbine noise, developers and manufacturers are researching and designing quieter turbines.

In order to restraint the noise levels, the government and medical associations have come up with certain recommendations and measurement standards. They have suggested to have a minimum distance between the wind turbine power plant. Alternatively, a maximum limit to the noise generated (dbA levels) has been given, which can be heard from the closest inhibiting locality. These values differ for different localities and countries. Thus, a suitable precedent should be taken into account while installing a wind turbine, along with other local considerations such as the ground roughness, obstacles, etc. Upwind turbines, which are also more dominant than the downwind turbines produce less low-frequency noise. An improved blade design is one of the key aspects in reducing the noises generated by leading edge, trailing edge, vortex shedding noise, etc. These are explained in detail in section 1.3.5. A lot of studies are being conducted to reduce the noise by improving the blade geometry and adding serrations. Reducing wind turbine noise can also improve public perception of wind energy and increase community acceptance of wind turbines. The concerning research is one of the main goals of the project zEPHYR, Horizon 2020.

Noise from Different Wind Turbines

Considering the reasons explained above, it is apparent that it is necessary to investigate the noise from wind turbines to find suitable mitigation strategies and improved designs.

HAWTs, typically comprising three blades, are prevalent for wind energy extraction, boasting efficiencies nearing 35% for megawatt-scale turbines. However, at the prosumer level, their efficiency is reduced due to the inaccessibility of mechanisms such as rotor yaw and blade pitch adjustments, rendering them less cost-effective [125,126]. Additionally, HAWTs are constrained by drawbacks including their large dimensions, intricate yaw systems, and increased maintenance requirements.

In contrast, VAWTs employ a design where the driving mechanism is situated closer to the ground, thereby reducing mechanical noise transmission [56]. Operating at lower TSRs as compared to HAWTs, VAWTs exhibit diminished aerodynamic noise levels [34, 57, 58, 127]. Thus, reducing the turbine's rotational speed, by reducing the TSR, is a direct method to reduce noise, often followed during nighttime. However, this reduces energy generation, with an estimated 1 dB SPL reduction accompanying 2-4% annual energy loss [59].

In recent years, wind energy research has focused on urban integration and regulatory compliance, driven by environmental goals [27–29]. The Savonius VAWT emerges as a compelling option when factors such as noise emission, turbine maintenance expenses, or reliability take precedence [24]. SVAWTs, with their potential for aesthetic designs and compact installations, are increasingly favoured for urban projects [27–29]. Despite advancements in VAWT technology, detailed analysis of their power production and acoustics is lacking [24, 27–29, 34].

To achieve optimal energy production while minimizing noise, investigating the relationship between noise and turbine efficiency is imperative. Several investigations have been conducted to model the aerodynamic noise through computational techniques [60–63], with findings indicating that VAWTs generate less noise compared to their horizontal counterparts [62, 63]. Nonetheless, the available data regarding such experiments is somewhat limited [24]. Moreover, most of the literature available is concentrated on Darrieus VAWTs (DVAWT), and very little information is available on SVAWTs, despite their increased popularity for small-scale production in populated regions. Moreover division of Savonius rotors into segments, along with the non-uniform inflow conditions typically encountered in urban environments, has a significant impact on the development of flow structures, the strength and evolution of vortices, and the wakes downstream of the blades and the entire rotor assembly. These intricate details of flow structures not only influence the performance of wind turbines but also contribute to the generation of noise. Therefore, conducting acoustic analysis and investigating noise sources within the Savonius rotor domain, particularly in the context of acoustic mitigation, is essential for its successful integration into urban environments and for gaining public acceptance.

Typical Noise Sources

Concerning wind turbine noise [128, 129], a distinction can be drawn between two sources: mechanical noise (see Fig. 1.3.3a) originating from components within the hub, such as the gearbox, generator, or cooling system within the nacelle, and aerodynamic noise (see Fig. 1.3.3b) resulting from the interaction between the incoming flow

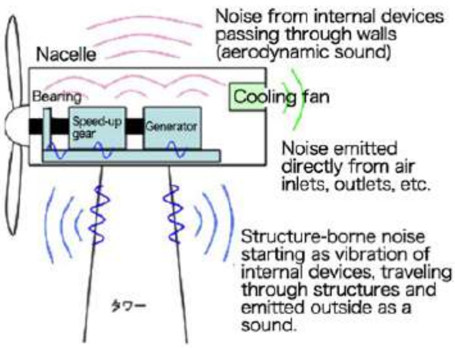

(a)

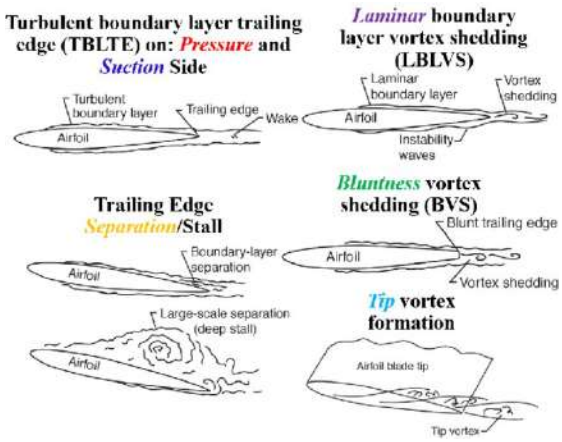

(b)

Figure 1.3.3: Noise sources in a typical Horizontal Axis Wind Turbine. (a)Mechanical noise sources of HAWT [133]. (b)Aerodynamic noise sources of HAWT [134].

and the tower and rotor blades. While the first type of noise can be effectively attenuated through the use of sound-absorbing materials [130], mitigating aerodynamic noise proves challenging since the sound sources are situated on the rotor blades. Consequently, aerodynamic noise takes precedence as the primary noise source in modern wind turbines. As explained by Brooks [131], airfoil noise generation mechanisms can be categorized into two main types: inflow turbulence noise and airfoil self-noise. Inflow turbulence noise occurs due to the interaction between incident eddies and the airfoil surface, making it contingent on the local atmospheric conditions. However, this mechanism generally has only a minor impact on the overall sound emission in wind turbines [132]. The main sources of airfoil self noise are as illustrated in Fig 1.3.3b include:

- **Trailing-edge Vortex Shedding**: One of the dominant noise sources is the shedding of vortices at the trailing edge of the airfoil. As the boundary layer separates from the airfoil surface, vortices are formed and periodically shed into the wake region. These vortices interact with the surrounding flow, creating fluctuations in pressure and velocity, which generate noise.
- **Turbulent Boundary Layer Interaction**: The turbulent boundary layer flowing over the airfoil interacts with the trailing edge, resulting in complex flow patterns. The irregular mixing of turbulent eddies in the wake leads to pressure fluctuations and noise generation.
- **Trailing edge bluntness noise**: If the thickness of the trailing edge exceeds a certain threshold value, von Kármán vortex streets may develop in the airfoil's wake, leading to periodic pressure fluctuations. This can generate tonal noise with a frequency determined by the airfoil's bluntness. Careful airfoil design or the use of splitter plates can help avoid this noise mechanism [135].
- **Separation and stall noise**: At angle of attack (AOA) greater than a specific threshold, flow separation occurs at the suction side, creating a large recirculation bubble of unsteady flow. This generates broadband noise due to the shedding of vorticity [132]. Further increasing α can lead to deep stall, causing large-scale vortex shedding and increased low-frequency noise emissions [131]. Careful selection of the airfoil's operation conditions or the installation of vortex generators can prevent separation and stall noise.

- **Tip noise**: The finite length of wings or blades results in pressure differences between the pressure and suction sides, potentially creating a strong vortex at the tip and causing flow separation. However, in modern wind turbine blades, the contribution of this mechanism to overall noise emissions is typically negligible [130].

Despite numerous studies and detailed data available on wind turbine noise, the work is mostly focused on HAWT's. This manuscript aims to address the gap in research by focusing on the noise characteristics of Savonius turbines specifically in urban settings. Understanding the noise emissions from Savonius wind turbines is crucial, particularly in the context of their potential application in urban environments. Given their vertical-axis configuration, small size, and increased safety, Savonius turbines offer promise for energy generation in densely populated areas where noise pollution is a significant concern. By investigating noise emissions from Savonius turbines, we aim to assess their suitability for urban environments, ensure regulatory compliance with noise regulations, and provide a basis for future design optimization. Detailed analysis can be found in Chapters 4.1 & 4.2

Chapter 1.4

Thesis Contents

1.4.1 Research Objectives

With the increasing demand for energy and the necessity to reduce dependence on non-renewable resources, there is a growing interest in harnessing wind energy, an environmentally friendly resource. While much research has focused on exploiting wind energy in vast open lands, there is a recent shift towards exploring its potential in urban areas where it often goes untapped.

In this thesis, a comprehensive investigation is conducted on the Savonius-type vertical-axis wind turbine, with a focus on its applicability and efficiency in urban environments despite its inherent limitations in effectiveness. Through rigorous analysis and experimentation, several key findings are established. The thesis demonstrates the feasibility of implementing an effective strategy for localizing wind energy sources within urban settings, thus highlighting the potential for harnessing renewable energy in densely populated areas. Additionally, the development of simple and reliable experimental setups is presented, facilitating the thorough examination of Savonius rotor characteristics, thereby enhancing our understanding of its operational dynamics. Moreover, the significance of segmentation in Savonius rotor design is elucidated, revealing its pivotal role in optimizing power production and mitigating noise generation, thus offering valuable insights for improving rotor performance.

Additionally, this thesis offers a comprehensive analysis by precisely identifying noise sources, thereby addressing gaps in existing literature and previous studies. This information is valuable for optimizing turbine design and improving overall performance in the future. Furthermore, the establishment of a relationship between power generation and noise emission demonstrate the optimal operating parameters that balance energy efficiency with acoustic considerations. Such insights can inform the development of strategies to optimize turbine performance while minimizing noise pollution in urban environments.

Lastly, the thesis investigates an innovative twin rotor vertical axis wind turbine design, showcasing its operational viability and potential to replace large single Savonius rotors at reduced investment costs, thereby addressing scalability concerns in urban wind energy systems. Through these investigations, this thesis aims to contribute to the advancement of urban wind energy technology by providing practical solutions and novel insights into the utilization of Savonius type wind turbines in urban environments.

The presented thesis consists of:

1. **Literature Review and Suitability Assessment:** Conduct a comprehensive review of available wind turbines and assess their suitability for urban environments.

2. **Wind Turbine Placement and Energy Potential:** Analyze wind turbine siting and assess wind potential for seven different locations across two countries.

3. **Aerodynamics Analysis:**

   a) Perform experimental aerodynamic analysis of a typical Savonius wind turbine within a controlled environment, such as a wind tunnel.

   b) Experimentally compare the operational characteristics of a typical Savonius wind turbine with its segmented counterparts across the complete operational range.

   c) Perform numerical analysis to predict the performance of a typical Savonius turbine in a wind tunnel or controlled environment to find input variables for matching efficiency in free field conditions.

4. **Experimental Acoustic Analysis of a Savonius Wind Turbine:**

   a) Compare overall noise generated by a typical Savonius rotor with one incorporating segments.

   b) Analyze the noise sources for a typical Savonius rotor for possible further improvements.

   c) Investigate the correlation between power generation and noise emission across the entire operational spectrum to identify optimal operating parameters.

5. **Study of Wind Turbines in Complex Urban Environments:**

   a) Conduct an in-depth analysis of a novel Twin-rotor Savonius wind turbine in real conditions using a small prototype mounted on the roof of the building-Institute of Fluid Flow Machinery, Polish Academy of Sciences (IMP-PAN) to study its operation in complex urban conditions.

   b) Analyze a full-size power plant based on the twin-rotor concept.

1.4.2 Thesis outline

The thesis delves into an extensive analysis of a specific wind turbine, utilizing both field experiments and numerical simulations. This investigation encompasses the examination of operational characteristics in controlled environments, such as wind tunnels, and in real-world scenarios, along with acoustic measurements to gauge the overall noise emitted by Savonius rotors with single and five segments. To facilitate comprehension, the thesis is structured into six main sections, each aligned with the initial research objectives.

The first part offers a thorough literature review, exploring the historical evolution of wind turbines and assessing the suitability of contemporary designs for urban settings.

Following this, the second part introduces wind regimes and conducts case studies to illustrate the wind potential across diverse European locales.

Subsequently, the third part undertakes an aerodynamics analysis, including numerical simulations and experimental studies, to dissect the power characteristics of the focal Savonius rotor across its operational spectrum. Additionally, this part examines the performance disparities among differently segmented Savonius rotors.

Part four transitions to an aeroacoustic analysis, addressing the fundamental principles of noise emission and conducting comparative studies on the overall noise output of varied Savonius rotor configurations. Furthermore, this part investigates the sources of noise in single-segment Savonius wind turbines and explores the intricate relationship between noise generation and power production.

Part five pivots towards practical applications in urban contexts, particularly focusing on a novel twin-rotor Savonius design. It presents two models—an experimental prototype installed on a building roof amidst urban structures and an extended prototype situated on a small ski hill—to underscore the viability and challenges of implementing Savonius wind turbines in complex urban landscapes.

Finally, the thesis culminates in a comprehensive conclusion, synthesizing the research findings and offering insights into the implications for future studies and practical applications.

Part 2

METHODS UTILIZED IN THIS THESIS

Chapter 2.1

Wind Dynamics and Wind Turbine Site Selection

Wind velocity is the most crucial factor that significantly impacts the power generation of a wind energy conversion system. Wind exhibits stochastic behavior, with its speed and direction randomly varying over time at a specific location. In addition to daily and seasonal fluctuations, the wind pattern can also change from year to year. Therefore, it is crucial to conduct a comprehensive analysis and understanding of the wind behavior at a potential site. Due to the exponential relationship between velocity and power, even slight variations in wind speed can lead to substantial changes in power output. Since wind velocity and power vary across different locations, the first step in wind energy project planning involves identifying a suitable site with consistent and robust wind characteristics.

Such understanding is essential for turbine designers to align their designs and components with the expected wind characteristics at the site. Similarly, project developers can assess the energy potential of their projects by considering the characteristics of the wind regime. Average wind velocity provides an initial indication of a site's wind energy potential. However, for detailed planning, it is important to consider not only the average strength of the wind spectra but also their distribution. Statistical models are commonly employed to define the distribution of wind velocity within a regime over a given time period.

Once the wind velocity and its distribution at a prospective site are known, further assessment of the energy potential can be conducted. One of the initial questions to address is the energy available per unit area of the rotor. Other factors of interest include the percentage of time the wind falls within a useful velocity range, the most frequent wind velocity, and the velocity that contributes the maximum energy to the regime. Additionally, identifying the possibility of extremely high winds at the site is crucial for safe structural design.

This chapter aims to discuss the fundamental characteristics of wind, along with methods for measuring its strength. It also introduces statistical models typically employed for wind resource analysis, highlighting their application in wind energy conversion.

2.1.1 Analysis of wind data

2.1.1.1 Weibull Distribution: Describing the Variation of Wind

Weibull distribution is a continuous probability distribution that is used in many different fields such as engineering, reliability analysis and quality control. It is popular because of its flexibility and ability to model a wide range of data sets. The advantages of using the Weibull distribution include its ability to easily fit data with varying shapes, its wide range of applications, and its ability to estimate parameters from a limited sample size. Additionally, it can be used for predicting future behavior based on past data. With the use of the Weibull distribution, engineers and scientists can gain valuable insights into their designs and processes. A detailed study on this topic is presented in section 5.1.1.

The information related to the variation of wind is required in industry, especially by the wind turbine designers, in order to optimise the design and reduce the related costs. When the wind speeds are measured over the period of a year, very strong gusts are uncommon. Whilst mild and slow winds are more prevalent. The Weibull distribution is used to find the probability of a certain wind speed occurring as an application to the wind energy industry. This distribution can be plotted in two ways:

- Probability Density Function(PDF)
- Cumulative Density Function (CDF)

A probability density distribution is plotted with the wind speeds on the horizontal axis and the frequency of the wind speed repetitions on the vertical axis. The consequent function is given by $f(v)$ and signifies the percentage of time for which the wind is flowing at a velocity v.

$$F(v) = \frac{k}{c}\left(\frac{v}{c}\right)^{k-1}.e^{(\frac{-v}{c})^k}, k > 0, v > 0, c > 1 \tag{2.1.1}$$

Where k is the shape parameter and c(m/s) is the scale parameter. CDF is given by the integral of Weibull PDF as the cumulative relative frequency of every speed band; this is represented by Eq 2.1.1. The Weibull shape parameter characterizes the behaviour of wind as per its value, i.e, small value of k means weak wind speeds, and large values signify even number of weak and strong wind speeds. While a high value of scale parameter c, leads to an increase in the scatter of the values about the mean wind speed. Commonly, the considered area have a shape factor of 2.

$$F(v) = \int_0^v f(v)dv = 1 - e^{(\frac{-v}{c})^k} \tag{2.1.2}$$

There are many methods available for calculating the values of k and c. Some of these values include:
(a) Graphical Method (GM)
(b) Standard Deviation method (STDM)
(c) Method of Moments (MOM)
(d) Equivalent Energy Method (EEM)
(e) Power Density Method (PDM)
(f) Maximum Likelihood Method (MLM)
(g) Modified Maximum Likelihood Method (MMLM)

Graphical Method

This method is also called the linear regression method, least squares fit method, or least squares regression method [136]. Taking natural log of Eq. 2.1.2 twice for simplification, we get:

$$\ln[-\ln(1 - F(v))] = k\ln(v) - k\ln(c) \tag{2.1.3}$$

where $\mathrm{i} = 1, 2, 3 \ldots, \mathrm{n}$.

Eq. 2.1.3 can be represented in linear form as:

$$Y = mX + b$$

where,

$$Y = \ln\left[-\ln\left(1 - F(v)\right)\right], \quad X = \ln(v), \quad \text{with slope } k, \quad \text{and intercept } -k\ln(c)$$

Standard Deviation Method

Using this method, the shape and scale factor can be calculated using Eq.2.1.4 and Eq. 2.1.5.

$$k = \left(\frac{\sigma}{\bar{v}}\right)^{-1.086} \tag{2.1.4}$$

$$c = \frac{\bar{v}}{\Gamma\left(1 + \frac{1}{k}\right)} \tag{2.1.5}$$

where, $\bar{v}$ is the mean wind speed, $\Gamma(x)$ is the gamma function and σ is the standard deviation of wind speed for a given time. These can be calculated as [137]:

$$\bar{v} = \frac{1}{n}\sum_{i=1}^{n} v_i \tag{2.1.6}$$

$$\Gamma(x) = \int_0^{\alpha} \exp(-u)u^{x-1}dx \tag{2.1.7}$$

where, $x = \left(\frac{v}{c}\right)^k$ and $\frac{v}{c} = x^{y-1}; y = 1 + \frac{1}{k}$

By performing further calculations, this can be transformed into:

$$\bar{v} = c + \Gamma\left(1 + \frac{1}{k}\right) = 0.8525 + 0.0135k + e^{-[2+3(k-1)]} \tag{2.1.8}$$

Once we have the value of $\overline{v}$, σ for the given test sample can be simplified and is written as:

$$\sigma = \left[\left(\frac{1}{n-1}\sum_{i=1}^{n}(v - \bar{v})^2\right)\right]^{1/2} \tag{2.1.9}$$

Method of Moments

The method of moments was put forward by a British statistician, Karl Pearson, in the early 19th century and involves the calculation of the probability distribution parameters [138] and was introduced in the field of wind pattern study by Justus and Mikhail in the later half of the 19th century [139].

This technique can be used as a substitute for MLE, as it allows comparatively easy determination of the Weibull parameters. If the numbers $v_1, v_2 \ldots, v_n$ represent a data set, then an unbiased estimator for the nth origin moment is given by:

$$\widehat{m_n} = \frac{1}{n}\sum_{i=1}^{n} v_i^n$$

, representing estimation of m_{n}

Eq. 2.1.1 provides a direct method to determine the nth moment in a Weibull distribution. By utilizing the Gamma function $\Gamma(x)$ (Eq. 2.1.7), the average wind speed can be expressed as a function of parameters c and k as :

$$\mu_n = \left(\frac{1}{c^n}\right)^{-\frac{n}{k}} \Gamma\left(1+\frac{n}{k}\right) \tag{2.1.10}$$

From Eq. 2.1.10 the first and second moments can be found as:

$$m_1 = \widehat{\mu_n} = \left(\frac{1}{c}\right)^{\frac{1}{k}} \Gamma\left(1+\frac{1}{k}\right)$$
$$m_2 = \widehat{\mu_n^2} + \widehat{\sigma_n^2} = \left(\frac{1}{c}\right)^{\frac{2}{k}} \left[\Gamma\left(1+\frac{2}{k}\right) - \left\{\Gamma\left(1+\frac{1}{k}\right)\right\}^2\right]$$

Dividing the square of m_2 by m_1, we get the expression:

$$\sigma = c\left[\Gamma\left(1+\frac{2}{k}\right) - \Gamma^2\left(1+\frac{1}{k}\right)\right]^{1/2}$$
$$\frac{\sigma}{\bar{v}} = \sqrt{\frac{\Gamma\left(1+\frac{2}{k}\right)}{\left[\Gamma\left(1+\frac{1}{k}\right)\right]^2} - 1}$$

Simplifying these equations we get the value of 'k' and 'c' as: Equations 2.1.1.1 and 2.1.1.1.

$$k = \left(\frac{0.9874}{\frac{\sigma}{\bar{v}}}\right)^{1.0983} \tag{2.1.11}$$

$$\bar{v} = c\Gamma\left(1+\frac{1}{k}\right) \tag{2.1.12}$$

Power Density Method

The calculation of the Weibull parameters is performed using the equations (2.1.1.1) and (2.1.1.1).

$$k = 1 + \frac{3.69}{E_{\text{pf}}^2} \tag{2.1.13}$$

$$c = \frac{\bar{v}}{\Gamma\left(1+\frac{1}{k}\right)} \tag{2.1.14}$$

A new term called the Energy Pattern Factor (E_{pf}) is introduced in this method. This factor is determined by taking the ratio of the total wind power available to the power calculated using cube of mean wind speed [140].

$$E_{\text{pf}} = \frac{\frac{1}{n}\sum_{i=1}^{n} v_i^3}{\left(\frac{1}{n}\sum_{i=1}^{n} v_i\right)^3} = \frac{\overline{v^3}}{(\bar{v})^3} = \frac{\Gamma\left(1+\frac{3}{k}\right)}{\Gamma^3\left(1+\frac{1}{k}\right)} \tag{2.1.15}$$

Where Γ is the gamma function, calculated using Eq. 2.1.7.

Maximum Likelihood Estimation or Maximum Likelihood Method

MLE is one of the most extensively used Weibull distribution estimation techniques. Estimation of parameters is carried out by maximizing the likelihood function, resulting in their most probable evaluation. The likelihood estimation function was proposed by Fisher [141] and extended for application in wind data analysis by Stevens and Smulders [142]. The Weibull distribution is represented as Eq. (2.1.16). Performing further evaluation results in Eq. (2.1.17). Therefore, finding the most likely value of k, an iteration needs to be performed by considering an initial value of the shape factor.

$$L\left(v_i, k, c\right) = \prod_{i=1}^{n} \left\{ \left(\frac{k}{c}\right) \left(\frac{v_i}{c}\right)^{k-1} \exp\left[-\left(\frac{v_i}{c}\right)^{k}\right] \right\} \tag{2.1.16}$$

$$k = \left[\frac{\sum_{i-1}^{n} v_i^k \ln\left(v_i\right)}{\sum_{i=1}^{n} v_i^k} - \frac{\sum_{i-1}^{n} \ln\left(v_i\right)}{n}\right]^{-1} \tag{2.1.17}$$

$$c = \left(\frac{1}{N} \sum_{i=1}^{N} v_i^k\right)^{1/k} \tag{2.1.18}$$

where v_i is the wind speed at an instant i.

This method can be further extended to the Modified Maximum Likelihood Method (MMLM). This method is similar to MLE, with the addition that the observed data is arranged according to the wind speed bins. The frequency of each bin formed within a specific range of wind speeds, corresponds to its probability [143].

$$k = \left[\frac{\sum_{i=1}^{n} v_i^k \ln\left(v_i\right) f\left(v_i\right)}{\sum_{i=1}^{n} v_i^k f\left(v_i\right)} - \frac{\sum_{i=1}^{n} \ln\left(v_i\right) f\left(v_i\right)}{f(v \geq 0)}\right]^{-1}, c = \left[\frac{1}{f(v \geq 0)} \sum_{i=1}^{n} v_i^k f\left(v_i\right)\right]^{1/k} \tag{2.1.19}$$

2.1.1.2 Other Probability distributions

Rayleigh distribution

The reliability of Weibull distribution in wind regime analysis depends on the accuracy in estimating k and c. For the precise calculation of k and c, adequate wind data, collected over shorter time intervals are essential. In many cases, such information may not be readily available. The existing data may be in the form of the mean wind velocity over a given time period (for example daily, monthly or yearly mean wind velocity). Under such situations, a simplified case of the Weibull model can be derived, approximating k as 2. This is known as the Rayleigh distribution. Taking $k = 2$ in Eq. 2.1.5 we get

$$v_m = c\Gamma\left(1 + \frac{1}{2}\right) \tag{2.1.20}$$

Evaluating the above expression and rearranging:

$$c = 2v_m\sqrt{\pi} \tag{2.1.21}$$

Substituting for c in Eq. 2.1.2, we get

$$f(v) = \frac{\pi}{2v_m v_m} e^{-\left(\frac{\pi^2}{4}\right)\left(\frac{v}{v_m}\right)^2} \tag{2.1.22}$$

Similarly, the cumulative distribution is given by:

$$F(v) = 1 - e^{-\left(\frac{\pi^2}{4}\right)\left(\frac{v}{v_m}\right)^2} \tag{2.1.23}$$

Thus, we can calibrate the probability density and cumulative distribution functions of wind on the basis of its average velocity. The validity of the Rayleigh distribution in wind energy analysis has been established by comparing the Rayleigh-generated wind pattern with long-term field data. Under the Rayleigh distribution, the probability of wind velocity to be between v_1 and v_2 is:

$$P(v_1 < v < v_2) = e^{-\left(\frac{\pi^2}{4}\right)\left(\frac{v_1}{v_m}\right)^2} - e^{-\left(\frac{\pi^2}{4}\right)\left(\frac{v_2}{v_m}\right)^2} \tag{2.1.24}$$

The probability of wind to exceed a velocity of v_x is given by:

$$P(v > v_x) = 1 - \left(1 - e^{-\left(\frac{\pi^2}{4}\right)\left(\frac{v_x}{v_m}\right)^2}\right) = e^{-\left(\frac{\pi^2}{4}\right)\left(\frac{v_x}{v_m}\right)^2} \tag{2.1.25}$$

In addition, other distribution functions are used to predict wind potential. These are explained in the following subsections.

Gamma distribution

The gamma distribution is a versatile probability distribution frequently used to model positively skewed data. PDF of gamma distribution is given by:

$$f(x; k, c) = \frac{1}{\Gamma(k) \cdot c^k} \cdot x^{k-1} \cdot e^{-\frac{x}{c}} \tag{2.1.26}$$

where $x \geq 0$, $k > 0$, and $c > 0$. Here, $\Gamma(k)$ represents the gamma function.

The cumulative distribution function (CDF) of the gamma distribution can be expressed as:

$$F(x; k, c) = \frac{1}{\Gamma(k)} \cdot \gamma\left(k, \frac{x}{c}\right) \tag{2.1.27}$$

where $\gamma(a, z)$ is the lower incomplete gamma function.

The gamma distribution is often used to model variables such as waiting times, durations, and rainfall amounts. It provides flexibility in capturing different shapes of skewed data depending on the values of the shape and scale parameters.

Log-normal distribution

The log-normal distribution is often used to model variables that are positively skewed and have a logarithmically transformed distribution. It is characterized by two parameters: the location parameter, μ, and the shape parameter, k. The probability density function (PDF) of the log-normal distribution is given by:

$$f(x) = \frac{1}{xk\sqrt{2\pi}} \exp\left(-\frac{(\ln x - \mu)^2}{2k^2}\right), \quad x > 0 \tag{2.1.28}$$

where x represents the random variable. The cumulative distribution function (CDF) of the log-normal distribution is given by:

$$F(x) = \frac{1}{2} + \frac{1}{2}\text{erf}\left(\frac{\ln x - \mu}{k\sqrt{2}}\right), \quad x > 0 \tag{2.1.29}$$

where $\mathrm{erf}(z)$ denotes the error function. The mean ($\mu_{\log}$) and standard deviation ($k_{\log}$) of the associated normal distribution are related to the parameters of the log-normal distribution as follows:

$$\mu_{\log} = \ln\left(\frac{\mu^2}{\sqrt{k^2+\mu^2}}\right) \quad \text{and} \quad k_{\log} = \sqrt{\ln\left(\frac{k^2}{\mu^2}+1\right)} \tag{2.1.30}$$

Genextreme and Gumble distributions

The following methods belong to the family of Generalized Extreme Value (GEV) distribution, which is a statistical approach commonly used to analyze extreme events, such as extreme wind speeds or rainfall amounts. The GEV distribution is characterized by three parameters: location parameter (μ), scale parameter (c), and shape parameter (k). These parameters determine the position, spread, and shape of the distribution, respectively.

The probability density function (pdf) of the Genextreme distribution is given by:

$$f(x;\mu,c,k) = \begin{cases} \frac{1}{c}\left[1+k\left(\frac{x-\mu}{c}\right)\right]^{-\frac{1}{k}-1} \exp\left[-\left(1+k\left(\frac{x-\mu}{c}\right)\right)^{-\frac{1}{k}}\right] & \text{if } k \neq 0 \\ \frac{1}{c}\exp\left[-\exp\left(-\frac{x-\mu}{c}\right)\right] & \text{if } k = 0 \end{cases} \tag{2.1.31}$$

where $-\infty < x < \infty$, $c > 0$, and $-\infty < k < \infty$. The parameter k determines the shape of the distribution: $k > 0$ corresponds to a distribution with a right tail, $k < 0$ corresponds to a distribution with a left tail, and $k = 0$ corresponds to the Gumbel distribution.

Estimating the parameters of the GEV distribution involves fitting the model to the observed data. Various methods can be used for parameter estimation, such as MLE or MOM. The MLE method is commonly used due to its desirable statistical properties, similar to those of the Weibull distribution.

Wind Power Density and Energy Density

The Wind Power Density (WPD) as calculated from the Weibull parameters can be given as 2.1.32.

$$\text{WPD}(v) = \frac{1}{2}\rho c^3 \Gamma\left(1+\frac{3}{k}\right) \tag{2.1.32}$$

and the WPD (average) of the recorded wind sample can be presented as:

$$\text{WPD}(v) = \frac{1}{2}\rho \overline{v}^3 \tag{2.1.33}$$

The value of air density ρ is assumed to be 1.225 kg/m^3 and $\overline{v}$ is the mean velocity of the sample for the purpose of the calculations included in this paper. The Wind Energy Density (WED) can be calculated by multiplying the WPD by the time over which the data has been sampled. EPD is generally expressed in terms of kg/m^3.

2.1.1.3 Interdependence of "k" and "c"

Plots represented in Fig.2.1.1 show how the Weibull distribution changes with the different values of k and c. With a scale factor constant, increasing shape factor signifies

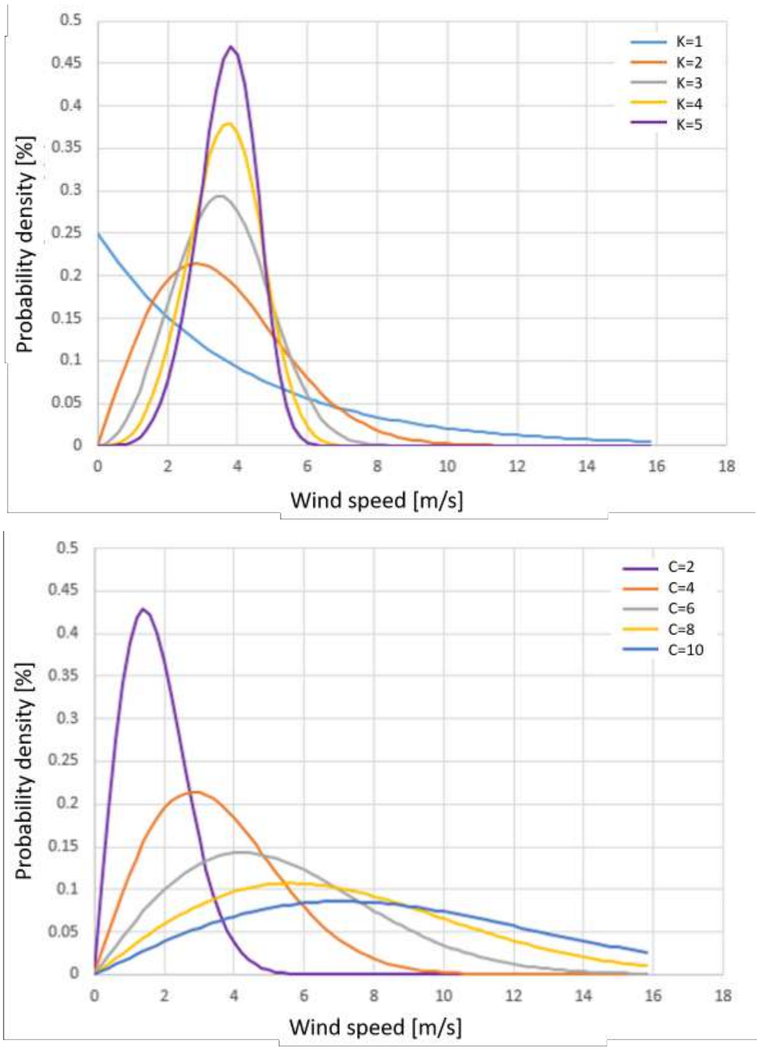

Figure 2.1.1: Changing Weibull parameters. a) Changing the value of k with a constant c value of 4. b) Changing the value c with a constant value of k as 2.

more uniform wind over the period of study while with shape factor constant, an increasing scale factor demonstrates an increase in the value of mean velocity with a reduction in the frequency of the wind speeds.

2.1.1.4 Wind distribution at height

An additional important factor to be taken into account when performing the wind analysis is the height at which the wind velocities have been recorded. This needs to be adjusted according to a reasonable height at which the wind turbine needs to be mounted. Equations (12.1.35) to (2.1.39) can be used to calculate the Weibull parameter values, the energy and power density values for a desired height. The power law given by Eq. (2.1.34) is used to extrapolate the wind velocity recorded at height 'Z' to the height of interest $'Z_h'$ (hub height) [144]. The surface roughness given by α can be calculated according to the conditions mentioned in table 2.1.1.

$$V = V_h \left(\frac{Z}{Z_h} \right)^{\alpha} \tag{2.1.34}$$

$$k_h = \frac{k}{\left[1 - 0.0881 \ln\left(\frac{z_h}{z_{\text{ref}}}\right)\right]} \tag{2.1.35}$$

$$c_h = c\left(\frac{z_h}{z_{\text{ref}}}\right)^n \tag{2.1.36}$$

$$v_h = c_h \Gamma\left(1 + \frac{1}{k_h}\right) \tag{2.1.37}$$

$$\bar{P}_h = \frac{1}{2}\rho\bar{v}_h^3 = \frac{1}{2}\rho\bar{v}_h^3 \frac{\Gamma\left(1+\frac{3}{k_h}\right)}{\Gamma^3\left(1+\frac{3}{k_h}\right)} = \frac{1}{2}\rho c_h^3 \Gamma\left(1 + \frac{3}{k_h}\right) \tag{2.1.38}$$

$$E_D = \frac{1}{2}\rho c_h^3 \Gamma\left(1 + \frac{3}{k_h}\right)\mathcal{T} \tag{2.1.39}$$

In the above equations, the Weibull parameters at a height $'h'$ are described as k_h and c_h. The velocity is given by v_h, average power density as $\bar{P}_h$, duration of measurement $'\mathcal{T}'$ and the energy density as E_D.

LOCATION	SURFACE ROUGHNESS(α)
Unstable air above open water surface:	0.06
Neutral air above open water surface	0.10
Unstable air above flat open coast	0.11
Neutral air above flat open coast	0.16
Stable air above open water surface	0.27
Unstable air above human inhabited areas	0.27
Neutral air above human inhabited areas	0.34
Stable air above flat open coast	0.40
Stable air above human inhabited areas	0.60

Table 2.1.1: Surface roughness values given by Qblade [145].

2.1.1.5 Statistical Tools for Wind Distribution Evaluation

Several statistical tools are available to calculate the error between data sets. By comparing different statistical tools for comparison of errors, we can gain a more complete understanding of the strengths and limitations of each tool and make more informed decisions about which tool to use in a given context. This can help to ensure that the analysis is accurate and meaningful, and can help to avoid potential pitfalls or misinterpretations that can arise from using a single tool in isolation. Details of the methods used for calculating the errors between the predicted function and observed data set for the cases under consideration is presented in this section.

Mean Absolute Percentage Error

$$\text{MAPE} = \frac{1}{N}\sum_{i=1}^{N}\left|\frac{X_{\text{pre}} - X_{\text{obs}}}{X_{\text{obs}}}\right| \times 100 \tag{2.1.40}$$

Root Mean Square Error

$$\text{RMSE} = \sqrt{\frac{\sum_{i=1}^{N}\left(X_{\text{obs}} - X_{\text{pre}}\right)^2}{N}} \tag{2.1.41}$$

Variance Error (R^2)

$$R^2 = \frac{\left(\sum_{i=1}^{n}\left(X_{\text{obs}} - \overline{X_{\text{obs}}}\right) \times \left(X_{\text{pre}} - \overline{X_{\text{pre}}}\right)\right)^2}{\sum_{i=1}^{n}\left(X_{\text{obs}} - \overline{X_{\text{obs}}}\right)^2 \times \sum_{i=1}^{n}\left(X_{\text{pre}} - \overline{X_{\text{pre}}}\right)^2} \tag{2.1.42}$$

Chi Square Error(χ^2)

$$\chi^2 = \frac{\sum_{i=1}^{N}\left(X_{obs} - X_{pre}\right)^2}{X_{pre}} \tag{2.1.43}$$

Where N=no. of observations,
X_{pre} is predicted values from the probability distribution
X_{obs} is observed values from the data set
$\overline{X_{pre}}$ is mean of the predicted values from the probability distribution
$\overline{X_{obs}}$ is mean of the observed values from the probability distribution

MAPE gives the mean absolute value between the predicted terms from the Weibull distribution and the values calculated from the collected data sample. RMSE is essentially the standard deviation of the predicted errors. The predicted errors (residual) signify how far the data points are from the regression curve. It can also be explained as how spread the data is about the best-fitting line [146]. R^2 illustrates the fraction of variance of the true value recorded by the regression model, in contrast to the residuals, as in the case of RMSE. A value of R^2 close to 1 is considered preferable to determine the goodness of the fit [147]. Even though this model is simple to use, it can not completely take into account the effect of the theoretical distribution, thus, it is recommended to use it in conjunction with other methods [148]. χ^2 is another test used to determine the closeness of the predicted data to the observed data. This is a non-parametric tool, i.e. it is distribution-free and can be used to compare groups with different sample sizes. In addition, this study provides information about how each compared group affected the complete study, making it one of the significant tools [149].

The probability distribution methods defined above were utilized to compare the wind potential at different locations. By applying these methods, we were able to generate statistical representations of wind speed data, which provided insights into the wind characteristics of each site. These statistical representations were then analyzed and ranked using the statistical tools described earlier, such as mean, variance, and goodness-of-fit tests. This approach enabled us to identify the most suitable distribution method, ensuring an accurate and reliable comparison of wind potential. Ultimately, this comprehensive analysis facilitates informed decision-making in selecting optimal sites for wind energy development. For detailed analysis, refer Chapter 5.1.

Chapter 2.2

Numerical Analysis

2.2.1 Governing equations

The motion of a compressible fluid can be mathematically described using the Navier-Stokes equations.

Mass conservation equation:

$$\frac{\partial \rho}{\partial t} + \nabla \cdot (\rho \mathbf{v}) = 0 \tag{2.2.1}$$

Momentum conservation equations (vector form - 3 scalar equations):

$$\rho \frac{d\mathbf{v}}{dt} = \rho \mathbf{f} - \nabla P - \nabla \left(\frac{2}{3} \mu \nabla \cdot \mathbf{v} \right) + \nabla \cdot (2\mu \mathbf{D}) \tag{2.2.2}$$

Energy conservation equation:

$$\frac{d(\rho E)}{dt} = \dot{T}_{\text{sm}} + \frac{P}{\rho} \frac{d\rho}{dt} + \lambda \nabla T \tag{2.2.3}$$

This particular system consists of a set of 5 equations involving 7 unknowns (v_x, v_y, v_z, P, T, E, ρ).

The governing equations consist of mass conservation, momentum conservation, and energy conservation equations, with additional equations of state for pressure and temperature. Together, these equations define the behavior of the fluid and its thermodynamic properties. In the calculations presented in the thesis, a calorically perfect gas model is employed, assuming negligible intermolecular forces and constant specific heat with respect to temperature.With such an assumption, additional equations presenting the relation between the unknowns can be written as:

$$P = \rho R T \tag{2.2.4}$$

$$E = cvT \tag{2.2.5}$$

Considering the temperature range studied, the viscosity relationship with temperature can be represented by Sutherland's law:

$$\mu_l = \frac{C_1 + T^{\frac{3}{2}}}{T + C_2} \tag{2.2.6}$$

where, $C_1 = 1.458 \times 10^6 kg/m.s\sqrt{^\circ\text{K}}$, and $C_2 = 110.4K$.

Turbulence

When a fluid flows at low velocities, its streamlines remain parallel and layered without any random mixing between layers, resulting in a laminar flow. However, at higher velocities, the flow undergoes stochastic lateral mixing, known as turbulent flow. Turbulent flow occurs due to inertial forces prevailing over viscous forces. The Reynolds number (Re, Eq.2.2.1) was introduced to quantify the relationship between inertial and viscous forces, enabling the determination of whether the flow is laminar or turbulent.

$$Re = \frac{\rho v L}{\mu} \tag{2.2.7}$$

2.2.1.1 General CFD Setup

In CFD (Computational Fluid Dynamics) simulations, an essential aspect of accuracy and stability lies in the choice and quality of the computational mesh. Meshes can broadly be categorized as structured or unstructured. Structured meshes consist of regular grid patterns with logically ordered cells, often yielding better numerical accuracy and easier implementation of boundary layers. Unstructured meshes, made of irregular cells such as triangles or tetrahedra, provide greater flexibility to model complex geometries but may require more careful mesh quality control to avoid numerical errors.

A critical parameter in turbulent flow simulations involving walls is the dimensionless wall distance, y^+, which quantifies the non-dimensional thickness of the first cell adjacent to the wall. The value of y^+ is used to ensure that the near-wall mesh resolution is adequate to capture the boundary layer behavior accurately. For example, a y^+ value close to 1 allows the use of low-Reynolds number turbulence models resolving the viscous sublayer directly, while higher y^+ values often require wall function approaches. Proper y^+ control is fundamental in achieving reliable results, especially in simulations involving wall-bounded turbulence.

Boundary conditions define how the flow interacts with the computational domain boundaries and significantly influence solution fidelity. Common boundary conditions include velocity inlets, pressure outlets, walls, and symmetry or slip boundaries. Slip walls assume no friction between the fluid and the surface, effectively modeling frictionless boundaries or symmetry planes, reducing computational complexity where viscous effects are negligible. In contrast, no-slip walls impose zero fluid velocity at the surface, capturing viscous boundary layers essential in many aerodynamic and hydrodynamic applications.

When modeling rotating machinery or moving parts, sliding mesh interfaces are often employed to allow relative motion between different mesh zones, such as between a rotor and its surrounding environment. This approach enables accurate capture of transient flow features and interactions across rotating and stationary domains by dynamically exchanging flow information at the mesh interfaces, essential for unsteady simulations of turbomachinery, propellers, or rotors.

Complete details of the mesh design, y^+ values, boundary condition specifications, and sliding mesh implementation used in this thesis are presented in Chapter 3.2.

2.2.2 Used Numerical Approach

The Navier-Stokes equations, being non-linear, are generally unsolvable analytically for most cases. Hence, numerical methods have been developed to address fluid mechanics problems. CFD methods enable complex flow calculations in various geometries, providing insight into every region of the flow.

This approach is fast, allowing for quick model modifications to obtain results, making it suitable for prototyping and cost-effective initial calculations for test section design.

Several numerical methods can be utilized, each having distinct advantages, limitations, and accuracy. Notably, two main approaches are the mesh-based and mesh-free methods. The latter includes Smoothed Particle Hydrodynamics (SPH) and Lattice-Boltzmann method (LBM), which operate on particles instead of fixed fluid elements/volumes.

The mesh-based approach involves dividing the flow field into small volumes, forming a mesh (grid). This representation simplifies the governing equations into multiple solvable equations. There are three primary simplification methods: Finite Element Method (FEM), Finite Difference Method (FDM) and Finite Volume Method (FVM).

- **Finite Elements Method:** Approximates variables in each cell using shape functions, solving the problem by minimizing error.
- **Finite Difference Method**: Approximates derivatives by differences between neighboring points, typically used on structured grids.
- **Finite Volume Method**: It consists of splitting the domain into small volumes. This method integrates governing equations over the volumes' surfaces, balancing fluxes with sinks and sources within each volume due to mass, momentum, and energy conservation. Iterative solutions are obtained step by step until a low difference between subsequent steps is achieved.

  Most commercial codes used for fluid mechanics problems adopt FVM, including its use within this thesis.

2.2.3 Turbulence Models

The flows encountered and discussed in this thesis, are turbulent flows. In CFD, three main strategies are employed to address turbulence, involving different levels of explicit resolution and modeling of turbulence scales.

Direct Numerical Simulation (DNS): solves the full Navier-Stokes equations, resolving all turbulence scales without any modeling, but is computationally prohibitive for most engineering applications.

Large Eddy Simulation (LES): resolves the large turbulent scales explicitly and models only the smaller scales, offering a balance between accuracy and computational cost.

Reynolds Averaged Navier Stokes (RANS): in this thesis, the RANS methodology has been employed, utilizing turbulence models to represent the stochastic components of the flow. RANS allows for steady-state calculations using relatively coarse grids. However, these turbulence models are often calibrated for specific conditions and may lack validation across a wide range of cases. Nevertheless, RANS calculations yield satisfactory overall results and are commonly used in engineering applications due to their computational efficiency.

The Navier-Stokes equations can be averaged to separate mean and fluctuating parts, where variables are described as the sum of their mean and fluctuating components (Eq. 2.2.3 & 2.2.3). For compressible flows, Favre averaging is employed, considering variable density.

One outcome of Reynolds averaging is the emergence of the Reynolds stress tensor (Eq. 2.2.3) in the momentum equation, introducing additional unknowns to the system. To address this, the Boussinesq hypothesis (Eq. 2.2.3) assumes a linear relationship between Reynolds stresses and the mean rate of strain via turbulent viscosity. This forms the basis for RANS turbulence models used in this thesis, with different formulations to calculate turbulent viscosity.

$$\phi(x) = \bar{\phi}(x) + \phi'(x) \tag{2.2.8}$$

$$\bar{\phi}(x) = \lim_{T_0 \to \infty} \frac{1}{T_0} \int_t^{t+T_0} \phi dt \tag{2.2.9}$$

$$\tau^R = -\rho \left(\overline{v'v'}\right) \tag{2.2.10}$$

$$\tau^R = -\rho \left(\overline{v'v'}\right) = 2\mu_i \bar{D}^R - \frac{2}{3}\rho\kappa I \tag{2.2.11}$$

where: D is mean strain tensor, I identity matrix, μ_t is turbulent viscosity, κ is turbulent kinetic energy, τ^R is Reynolds stress tensor,and ϕ is field.

Despite the benefits of CFD simulations in resolving fluid dynamics, it's crucial to acknowledge their limitations. CFD simulations are approximations based on simplified mathematical models and numerical methods, introducing errors and reliance on idealized boundary conditions. The choice of models and case definitions significantly impacts solution quality. Experimental validation is generally recommended for comparing numerical results and gaining deeper insights into the flow. This thesis combines numerical and experimental approaches to leverage the strengths of both methods.

There are several types of RANS turbulence models, each with its own level of complexity and suitability for different flow scenarios. Discussed below are some of the commonly used RANS turbulence models:

k-omega (M-SST)

The Wilcox $k-\omega$ turbulence model is a hybrid two-equation model, offering high accuracy and robustness near solid walls. To tackle these issues, a blended model was proposed. This blended approach allows for the utilization of the Wilcox $k-\omega$ model near solid walls and the standard $k-\varepsilon$ model, formulated in a $k-\omega$ manner, in freestream regions. However, some drawbacks cause challenges in predicting the asymptotic behavior of turbulence eddy viscosity and reproduce DNS profiles of k and ε in the boundary layer. More details about this model can be found in [150, 151].

The numerical method used within this thesis was selected based on the initial tests, specific software capabilities and experience. Simulations were conducted using the unsteady RANS method. In this thesis, the k-omega (M-SST) turbulence model has been chosen based on an extensive review of literature concerning comparable numerical simulations. Further details regarding the application of this model within the context of the thesis can be found in Chapter 3.2.

Chapter 2.3

Wind Turbine Noise

2.3.1 Noise Measurements Using a Single Microphone

Wind turbine noise measurement is a crucial aspect of assessing the environmental impact of wind energy projects and ensuring compliance with noise regulations. While various advanced methods, such as microphone arrays and sound power level measurements, are commonly employed for comprehensive noise assessment, there is growing interest in exploring the effectiveness of simpler measurement techniques utilizing a single microphone.

The use of a single microphone for wind turbine noise measurement offers several advantages. Firstly, it is a cost-effective solution, requiring fewer resources compared to complex microphone arrays. This affordability makes it accessible for smaller-scale wind energy projects and research endeavors with limited budgets. Additionally, the setup process for a single microphone is relatively straightforward, requiring less time and expertise, thus increasing its practicality for field measurements in diverse environmental settings. Moreover, the portability of a single microphone setup enables flexibility in deployment, allowing noise measurements to be conducted at various locations around wind turbine sites, including remote or challenging terrain.

Despite its simplicity, wind turbine noise measurement with a single microphone provides valuable insights into the overall noise emissions of wind turbines. By capturing noise data from a single point, this method allows for the assessment of noise levels at specific distances and directions from the turbine, aiding in understanding the spatial distribution of noise and its potential impact on nearby communities, wildlife, and ecosystems. Furthermore, single microphone measurements facilitate continuous monitoring of noise levels over time, enabling the identification of temporal variations and trends in noise emissions under different operating conditions, weather patterns, and wind speeds.

However, it is essential to acknowledge the limitations of using a single microphone for wind turbine noise measurement. This approach may not capture the full spatial complexity of noise fields around turbines, particularly in complex terrain or in the presence of multiple turbines generating overlapping noise patterns. Additionally, single microphone measurements may be susceptible to background noise interference, requiring careful consideration of ambient conditions and noise sources in data analysis and interpretation. Another significant limitation is the inability to localize noise sources accurately. Unlike microphone arrays, which can provide detailed spatial information about noise distribution, a single microphone setup captures overall noise levels without discerning specific sources. This limitation hinders the identification of individual noise contributors and may limit the effectiveness of targeted noise mitigation efforts.

In the next section, strategies and methodologies for overcoming this limitation and enhancing the accuracy of wind turbine noise measurement and source localization using microphone arrays is presented.

2.3.2 Acoustic imaging

2.3.2.1 Basics of beamforming

To provide a foundational understanding of acoustic imaging algorithms, this section explains the delay-and-sum method [152–154] as an illustrative technique. Operating in the time domain, this algorithm relies on time delays and pressure amplitudes captured by microphones in an array.

In practical scenarios, sound source locations are not known beforehand, necessitating a scan grid encompassing all potential source positions. Fig. 2.3.1 depicts an example application of delay-and-sum beamforming. Consider a single sound source situated at scan point ξ_j and a linear array of N microphones. Due to the microphone positions relative to the sound source, the sound arrives earlier at the nearest microphones.

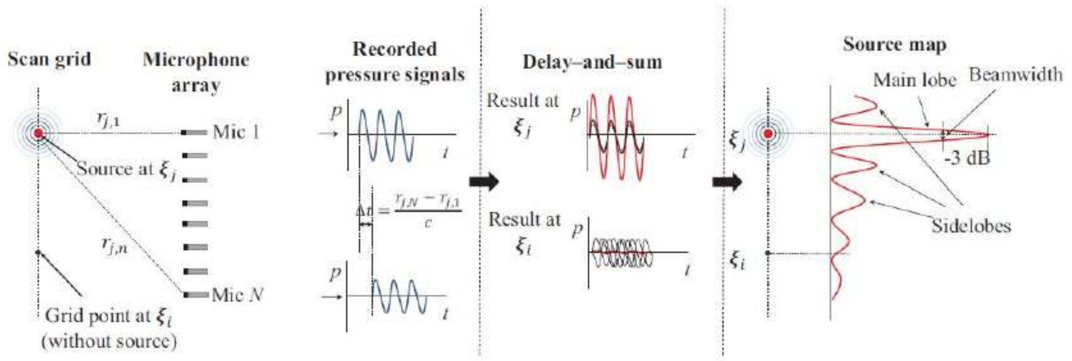

Figure 2.3.1: Diagram explaining the performance of delay–and–sum beamforming in the time domain and spatial resolution [155].

For instance, microphone 1 receives the sound signal first, while microphone N receives it last ($r_{j,1} < r_{j,N}$, where $r_{j,n}$ is the distance between the j^{th} grid point and the n^{th} microphone). The time delay between both microphones is determined by the travel distances from the source to each microphone $\Delta t = (r_{j,1} - r_{j,N})/C$. Additionally, the pressure amplitude detected by microphone N exhibits a slight decrease compared to that registered by microphone 1, owing to the greater travel distance.

The exhaustive search process involves evaluating every scan grid point, where microphone time signals are shifted to account for the relative time delays Δt and the amplitude losses caused by sound spreading [156]. Subsequently, the corrected time signals from all microphones are added for that grid point. If a sound source is present at the considered location (e.g.: ξ_j in Fig.2.3.1), the sum of the signals will be in phase, resulting in a high amplitude. Conversely, if no sound source is present at the grid point (e.g.: ξ_i in Fig. 2.3.1), the summed signals will exhibit a random phase, leading to low amplitude. Thus, it can be concluded that the phased microphone array amplifies sound from the grid point under consideration compared to sound coming from other directions [156].

If the squared pressures of each grid point are plotted (usually in logarithmic scale in dB, i.e., L_p, see Appendix A.3, a source map (also known as a beamform plot) is obtained, as shown in the right part of Fig. 2.3.1. This plot displays the beamwidth

(BW), main lobe, and sidelobes, which determine the concepts of spatial resolution and sidelobe level (SL)(detailed in section 3.2 of thesis [155]). To quantify the strength of the sound source, the summed signal needs to be averaged by the number of microphones N.

More sophisticated time-domain techniques have been previously devised [157–159], including methods specifically customized for moving sources [160], particularly focusing on rotating sources like wind turbines or propellers. Some of these techniques include CLEAN-SC [161], orthogonal beamforming [162, 163], functional beamforming [164, 165], wavenumber beamforming, DAMAS [166], Linear programming deconvolution,Robust adaptive beamforming [167, 168], etc. Details of additional methods can be found in the thesis [155].

2.3.3 Conventional Frequency Domain Beamforming (CFDBF)

Transferring the delay–and–sum beamforming method (Section 2.3.2.1 to the frequency domain results in CFDBF [153, 154]. This method has gained popularity in the field owing to its robust, fast and intuitive properties. However, this algorithm suffers from certain limitations [169] and exhibits a notable elevation in sidelobe level, particularly noticeable at higher frequencies (see Fig. 2.3.1). In CFDBF, the recorded pressures in each of the N microphones of the array $(\tilde{p}_n)$ are considered as an N-dimensional vector $\boldsymbol{p}(f) \in \mathbb{C}^{N\times 1}$ in the frequency domain, where (f) denotes the frequency:

$$\boldsymbol{p}(f) = \begin{pmatrix} \tilde{p}_1(f) \\ \vdots \\ \tilde{p}_N(f) \end{pmatrix}. \tag{2.3.1}$$

Considering only a single sound source at the scan point ξ_j, the received signal is modeled as $s_j\, g_j$, where s_j represents the source strength, and $g_j \in \mathbb{C}^{N\times 1}$ is the steering vector. The steering vector comprises N components, $g_{j,n}, n \in [1, \ldots, N]$, representing the modeled pressure amplitudes at the microphone locations for a sound source with unit strength at that grid point [170].

Various steering vector formulations exist in the literature [171, 172], each with distinct advantages and limitations. For simplicity, monopole sources are typically considered, although dipoles and other sources can also be accounted for [173]. In the case of a stationary point source, the steering vector is derived from the free-field Green's function of the Helmholtz Eq. [174]:

$$g_{j,n} = \frac{\exp\left(-2\pi i f \Delta t_{j,n}\right)}{4\pi \left\|x_n - \xi_j\right\|} = \frac{\exp\left[\frac{-2\pi i f \left\|x_n - \xi_j\right\|}{C}\right]}{4\pi \left\|x_n - \xi_j\right\|}, \tag{2.3.2}$$

where $i^2 = -1, \boldsymbol{x}_n = (x_n, y_n, z_n) \in \mathbb{R}^{N\times 3}, n = 1, \ldots, N$ are the locations of the N microphones, and $\Delta t_{j,n}$ is the time delay between the emission at ξ_j and the signal's reception by the observer at position x_n.

$\left\|x_n - \xi_j\right\|$ represents the distance between the j^{th} grid point and the n^{th} microphone, often referred to as $r_{j,n}$.

In the case of moving sources, an expression of Eq.2.3.3 can be derived [155, 156, 160] taking into consideration the source movement [175]. The estimation of the source autopower, A, at a source located at grid point ξ_j, involves minimizing the difference between the recorded pressure vector, p, and the modeled pressures for a source at that grid point $\xi_j, s_j g_j$, in a least-squares sense [156].

$$A\left(\xi_j\right) = \frac{1}{2}\frac{g_j^* \langle pp^* \rangle g_j}{\left\|g_j\right\|^4} = w_j^* C w_j. \tag{2.3.3}$$

In Eq. 2.3.3, $(\cdot)^*$ represents the complex conjugate transpose, $\langle\cdot\rangle$ denotes the time average of several snapshots, and w_j is the weighted steering vector, which has various formulations in the literature [171]:

$$w_j = \frac{g_j}{g_j^* g_j} = \frac{g_j}{\left\|g_j\right\|^2}, \tag{2.3.4}$$

while C is the $N \times N$ Cross-Spectral Matrix (CSM) of the measured pressures, obtained by averaging the Fourier-transformed sample blocks over time (for more details refer to source [155]). The CSM is Hermitian (i.e., conjugate symmetric) and positive-semidefinite:

$$C = \langle pp^* \rangle . \tag{2.3.5}$$

In the realm of CFDBF, a source map, also referred to as a beamform plot or acoustic image, is constructed by summing the Point Spread Functions (PSFs) of the actual sound sources. Given that the strengths of these sources are inherently positive due to the positive-definiteness of C, and taking into account the presence of noise in real-world scenarios, the resulting source plot tends to overestimate the actual source levels when multiple sound sources coexist.

2.3.3.1 Background noise suppression

For measurements in environments with strong wind noise or turbulent boundary layer noise, such as in closed-section wind tunnels [152, 170], the flow-noise signals can be approximated as independent stationary stochastic processes [176]. When a sufficiently long averaging time is employed, the flow noise mainly contributes to the main diagonal of the averaged Cross-Spectral Matrix (CSM), lacking phase information, which is non-critical for array performance. The main diagonal elements of C normally have much higher levels than the cross-powers, and they influence the beamforming results at each grid point, leading to a noise floor that hampers the source identification process [156].

To address the incoherent noise contribution from all array microphones, the main diagonal of C can be removed (converted to zeros). However, caution is necessary with Diagonal Removal (DR) as it no longer confirms C as a positive-definite matrix, resulting in negative eigenvalues in C. This can lead to unphysical negative values in the PSF and the potential masking of weaker sources by the negative sidelobes of strong sources in certain situations [156]. This issue affects all methods relying on the CFDBF algorithm [156].

2.3.3.2 Integration methods

The CFDBF technique accurately provides correct source sound pressure levels L_p when dealing with well–separated monopole sources, as evident from the peak levels in the source map [156]. However, in practical scenarios, this ideal situation is not typical. Challenges arise when the main lobes of closely–spaced sound sources overlap, leading to a deterioration in the source map due to sidelobes. Moreover, the spatial distribution of sound sources, such as in trailing–edge noise, further complicates matters. In such cases, the peak levels obtained from CFDBF may correspond to erroneous source levels. Additionally, when coherence loss [177] comes into play, the main lobe

(a) (b)

Figure 2.3.2: (a) Example of the application of the SPI technique: Experimental distributed sound source and (b) simulated point source. The dashed black rectangle denotes the ROI, and the white + marker the location of the simulated point source [178].

broadens and experiences a reduction in strength. To address these complexities, different integration methods have been proposed. There are many algorithms available to perform such integration, namely Extension to line sources (SPIL) [155, 156, 178], Inverse SPI (ISPI) [178], and Source Power Integration (SPI). For the analysis performed in this thesis, SPI method has been used and is described as below.

Source Power Integration (SPI)

To reduce the impact of the array's PSF, the Source Power Integration (SPI) technique was proposed [170]. The SPI method entails integrating the source power over a predefined Region Of Integration (ROI) and considering it as a simulated unit monopole. A scaling factor is determined to normalize the total source power to a unit monopole source within the ROI. This scaling factor represents the overall sound power present in the ROI.

In Fig. 2.3.2a, an experiment yields an arbitrarily distributed sound source. At the j^{th} grid point, the estimated source power is denoted as $A_{j,exp}$. Employing the SPI method, the source powers from j grid points within ROI enclosed by dashed lines are aggregated and represented as a simulated monopole source at the K^{th} grid point, as depicted in Fig. 2.3.2b. The location of this simulated monopole is typically defined at the center of the ROI. In contrast to $A_{j,exp}$ in Fig. 2.3.2a, $A_{j,sim}$ in Fig. 2.3.2b provides the source power of the simulated monopole's PSF at the j^{th} grid point within the ROI.

The ROI should include the entire sound source (as shown in Fig. 2.3.2a and have sufficient size to account for potential broadening of the main lobe due to coherence loss [156]. However, it is crucial to ensure that the ROI consistently captures the variations in main lobe width across all considered frequencies. Additionally, the selection of the ROI should avoid contributions from other sound sources and sidelobes, as well as the noise floor from the source map [156]. This integration approach has proven successful in various wind-tunnel experiments [155, 156, 170] and aircraft flyover measurements [155], producing accurate sound pressure levels, even in scenarios with coherence loss [156].

In conclusion, this section explores the noise sources of a typical HAWT, acknowledging the limited literature available and underscoring the significance of examining SVAWTs, particularly in urban environments, which is the primary focus of this thesis. It presents methods for noise measurement and acoustic imaging, specifically emphasizing CFDBF and the SPI technique. The thesis follows a systematic approach, commencing with individual microphone assessments to evaluate overall noise from various Savonius rotors. It then advances to the use of microphone arrays for precise noise source localization through CFDBF and SPI integration methods, aiming to fill the gaps in the literature concerning VAWTs.

Part 3

PERFORMANCE ANALYSIS: SAVONIUS WIND TURBINES

Chapter 3.1

Literature Review and Analysis of Characteristics

3.1.1 Comprehensive Analysis of Existing Research

An overview of the key characteristics of the typical Savonius rotor is presented in Fig. 3.1.1. The power characteristics obtained with the change in torque are presented in Fig. 3.1.1b. Power generation is observed to follow distinct patterns within three TSR ranges. For TSR values up to 0.7, the produced power increases with the rise in TSR, corresponding to an increase in the rotor's rotational speed. In the range of 0.7 < TSR < 1.2, the power production undergoes a significant transformation, reaching its maximum power coefficient. For TSR values exceeding 1.2, further increases in TSR and rotational speed lead to a considerable decline in power generation, reaching C_p = 0 at approximately TSR $\approx$ 1.8. This characteristic behavior is likely to have an impact on the noise generation mechanism as discussed in detail in chapter 4.1 and 4.2.

The 'torque on the rotor axis', refers to the rotational force that acts on the turbine's rotor, causing it to spin around its central axis. This exhibits a linear dependence on the TSR. This correlation is illustrated in Fig. 3.1.1a.

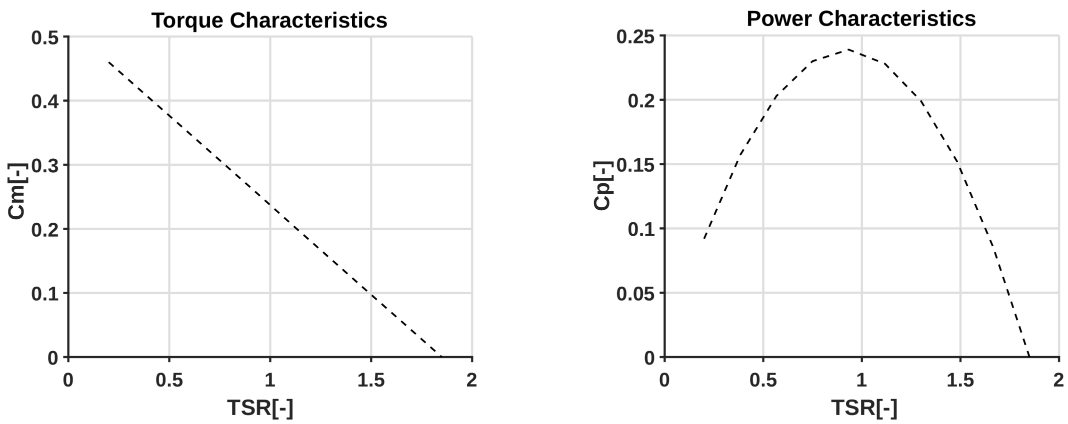

(a) Torque variation with TSR. (b) Performance variation with TSR.

Figure 3.1.1: Characteristics of a typical Savonius rotor.

The power and torque characteristics of a Savonius wind turbine depend on a number of factors including, but not limited to, the overlap ratio of the two blades/buckets, the number of segments (Fig. 3.1.4), the number of blades, blades twist, the effect of the end plates, and the aspect ratio (height/width). Thus, a suitable combination of these aspects needs to be taken into consideration while designing a wind turbine.

Many authors have performed research to focus on improving the efficiency of Savonius wind turbines by taking into consideration augmentation methods such as parametric analysis and multi-staging [39]. The key aspect for many of the studies was the conventional S-shaped blades. Advancements have also been made by investigating the wind turbine performance using helical blades, which have proved to reduce the torque fluctuation on the rotor axis. However, this results in an increase in the overall cost and complexity of the wind turbine system [40]. The accommodation of features such as deflector plates, guiding vanes, or curtains in the wind turbine leads to the enhancement of performance characteristics and torque characteristics. Conversely, it resulted in a direction dependency and more complicated design [39].

In addition, the effects of TSR, rotor's speed of rotation, the wind velocity and thrust load on the rotor are also being studied to get optimum power. The impact of various modifications on Savonius wind turbines has been demonstrated, highlighting the benefits of these transformations. [41]. An experimental investigation was conducted to compare different geometries of SVAWT, aiming to define the optimal operating parameters [42]. The static torque was measured for each individual rotor at distinctive wind speeds and it was observed that the blade had higher efficiency as compared to the three and four blade rotors. It was also concluded that rotors with mounted end plates were more efficient in comparison to those without end plates. Single-segment rotors show better performance than the dual-segment rotors.

The Overlap Ratio (OR), defined as the ratio of the distance by which the two semi-cylindrical blades overlap to the diameter of the blades, is a critical parameter influencing the aerodynamic performance of Savonius wind turbines. An appropriate overlap allows wind to pass through the gap between blades, reducing negative torque and enhancing the turbine's ability to start rotating at lower wind speeds. Studies have shown that an inward overlap ratio of 0.2 can lead to higher power coefficients across various wind speeds, indicating that rotors with an overlap ratio exhibit better operational characteristics than those without [179–181]. However, an excessive overlap ratio can create vortices in the overlap region, leading to increased drag and reduced torque, thereby decreasing overall efficiency [182]. Additionally, increasing the aspect ratio has been found to result in an increased power coefficient.

15 different arrangements of a Savonius rotor were tested and reported by Sheldahl et al. [43]. It was concluded that a two-blade rotor demonstrated a higher aerodynamic performance when compared to a three-blade rotor. Studies conducted contributed to the investigation of the optimal number of Savonius rotor blades and yielded similar results [44, 45].

A comparison of various helical angles was made for a rotor with and without an inner shaft. The helical rotors with shaft indicated a lower performance when compared to a rotor without a shaft. Aerodynamic performance research was carried out by Anbarsooz [46], including numerical and experimental studies on a helical Savonius rotor with a twist angle of 30° and 45°. It was established that the conventional rotors deliver a higher power coefficient as compared to the helical rotor, whilst the latter exhibits more uniform time variations of the torque coefficient.

Experiments performed by Patel et al. [47] summarised that the power coefficient increases with an increase in Aspect Ratio (AR). Investigation concerning AR = 0.5-5.0 was conducted by Sobczak [32] for a classic two-blade Savonius rotor. The agreement between the numerical simulations and experiments suggested that an increase in the aspect ratio could directly be linked with an improvement in the power coefficient [183].

The effect of the rotor segmentation was investigated and presented in [33]. The segmentation of Savonius rotors is a recognized topic in the literature [34]. Most typically, the height of a segment is equal to one or two rotor diameters. There is not much information on the effect of this rotor aspect, as it requires experiments [35, 36] or fully three-dimensional unsteady numerical simulations [37, 38, 184].

The information available in the literature on segmented rotors is sometimes contradictory. The material found in the literature does not allow unequivocal conclusions. Utilizing a multi-segment rotor leads to smoother torque distribution compared to a single-segment rotor, as demonstrated by experimental findings [48]. However, research indicates that increasing the number of segments might lead to a decrease in the power coefficient, with varying outcomes. Previous studies have reported power coefficients of 0.17 for a single-segment rotor and 0.14 for a two-segment design [35], 0.16 for a single-segment rotor and 0.12 for a three-segment rotor [18], and an increase in the power coefficient from 0.18 for a single-segment rotor to 0.29 for a two-segment rotor, followed by a decline to $C_{p,\max} = 0.23$ with three segments [49]. The reason for the performance increase in the two-segment configuration remains uncertain. Experimental analysis suggests that a single-segment rotor performs better than its four-segment counterpart, though the performance difference diminishes with increasing wind speed [33]. To address the ambiguity surrounding the impact of rotor segmentation, comprehensive experiments have been conducted to assess power characteristics across the operational range for single and five-segment rotors.

In Fig.3.1.2 the maximum effectiveness C_p is plotted against wind velocity [33]. The plot shows clearly the higher effectiveness of the single-segment rotor in the whole range of the considered wind velocities. The difference between the rotors becomes really significant at low wind velocities. At higher velocities, the difference becomes much smaller.

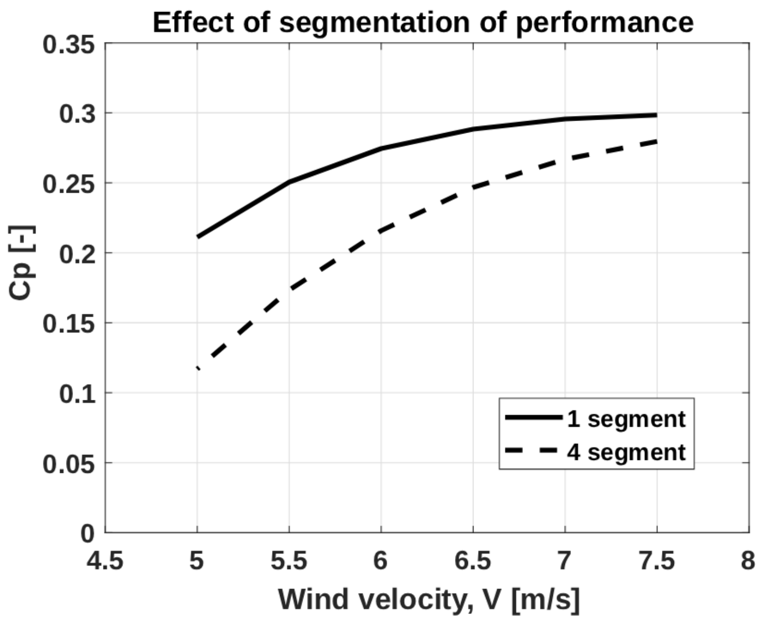

Figure 3.1.2: Effectiveness (Cp) for 1-segment and 4-segment rotors [33].

Since the available data on the impact of rotor segmentation is ambiguous, extensive experiments have been conducted by the author of this thesis to examine the power characteristics and noise generation across the entire operational spectrum for both single and five-segment rotors. A comprehensive analysis is presented in Chapters 3.3 and 4.1.

Novel SVAWT designs in urban environment

In recent years, extensive research efforts have been directed towards harnessing wind energy in urban environments, driven by the need to meet new regulatory requirements. The European Union's Green Deal has set forth a compelling objective: a mandatory reduction of CO2 emissions by 55% by the year 2030 along with the Paris Climate Agreement, which focuses on enhancing Environmental, Social, and Governance (ESG) performance. Within this context, SVAWT present an intriguing opportunity to incorporate aesthetically pleasing wind turbine designs, thereby enhancing its acceptance for integration in urban settings by people.

SVAWT, being an optimal choice for such installations has found use in many such projects. SVAWT in the form of tulip-shaped [27] structures has already been implemented in some parking lots in the Netherlands, serving the purpose of powering phone charging stations and night lamps. Additionally, innovative companies like New World Wind have introduced SVAWT designs that mimic the appearance of wind trees [28], with the potential for combined wind and solar energy exploitation.

Another noteworthy advancement in this field is the Power Nest technology [29], which integrates both Darrieus and Savonius VAWTs for use on building rooftops. However, detailed analysis of such wind turbines in terms of their power production and aeroacoustics is still not available extensively.

3.1.2 Savonius Wind Turbine Under Consideration

The dimensions of the wind turbine used at IMP-PAN for the purpose of the experiments performed as a part of this thesis are detailed in Table 3.1.1, and the basic geometry of the wind turbine is shown in Fig. 3.1.2

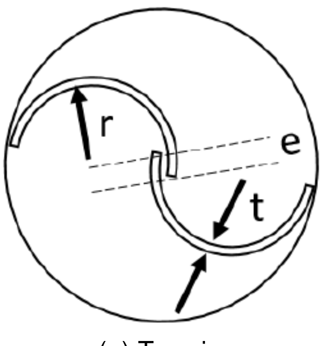

(a) Top view

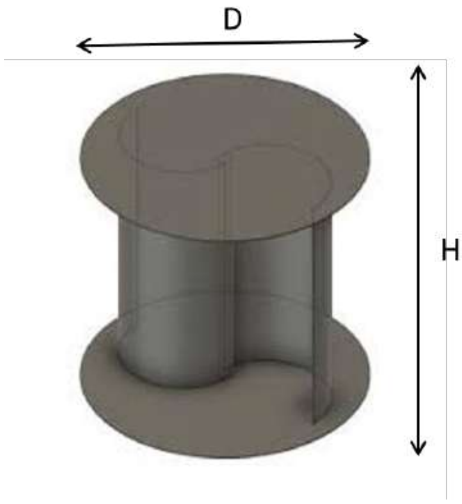

(b) Front view

Figure 3.1.3: Dimensions of Savonius rotor under study

Radius of curvature 'r'	Diameter 'D'	Thickness of blades 't'	Height 'H'	Overlap ratio 'e'
0.135 m	0.5 m	2 mm	2.2 m	10% of D

Table 3.1.1: Dimensions of Savonius wind turbine used for experiments at IMP-PAN.

For the purpose of this study, two rotors were considered: one consisting of a single segment and the other of five segments. The basic dimensions of both turbines, such as diameter, radius of curvature, blade thickness, and overall height (H), are the same. The five-segment rotor was obtained by stacking five individual single-segment rotors, arranged vertically with a phase difference of 90°. The individual height of each segment is approximately $\mathrm{H}/5$, which corresponds to an aspect ratio of AR = 1 for each segment. The effect of the aspect ratio is therefore represented by these two cases: a single-segment rotor with AR = 5 and a five-segment rotor with AR = 1 per segment.

The choice of these two configurations was guided by both structural and aerodynamic considerations. The single-segment rotor has a high eigenfrequency (around 4000 rpm), which provides a robust structure and enables safe operation at higher wind speeds by avoiding resonance. In contrast, the five-segment rotor has a lower eigenfrequency (around 800 rpm) and a comparatively heavier structure due to the inclusion of plates and stiffeners, which improves its rigidity. The segmented design allows valuable flexibility for aerodynamic and acoustic optimization.

This selection is also consistent with findings from previous studies on such rotors [185]. Prior research has shown that the power coefficient increases with aspect ratio, with the most significant improvements occurring at low aspect ratios, while further increases yield diminishing gains. Although simulations indicate that performance could continue to improve at aspect ratios greater than 5, practical and structural limitations make such designs challenging. Therefore, including both a five-segment rotor (with AR = 1 per segment) and a single-segment rotor (with AR = 5) provides a meaningful basis for performance comparison while maintaining consistent rotor dimensions. These configurations are illustrated in Fig. 3.1.4.

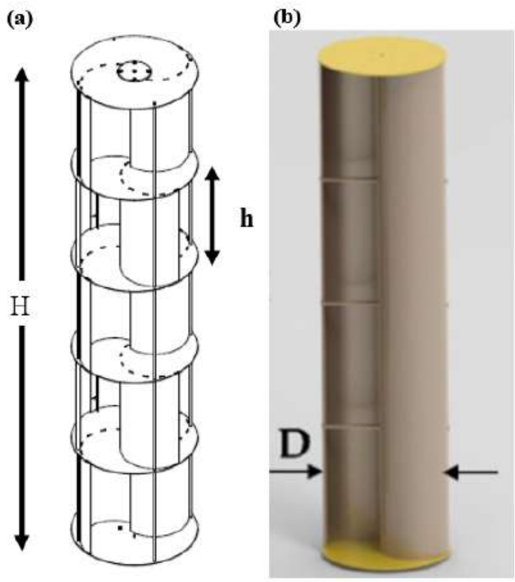

Figure 3.1.4: (a) Five-segment rotor (b) Single-segment rotor

Comparitive studies related to the performance characteristics and acoustics were performed for these rotors and have been detailed in Chapter 3.3 and 1.3.5.

Chapter 3.2

Numerical Simulations of Savonius Rotor

The main idea behind this study is to analyze the performance and torque characteristics over the complete operational range of TSR's. The study is divided into two parts. The first part of the study consists of numerical simulations to verify and validate the numerical model with experimental results. The second part of the study details the behavior of characteristics of the savonius rotor when tested in a test section (open wind tunnel), when the rotor is placed at different distances from the jet stream outlet. The ideology behind such simulations is to check the optimal distance in this test section, which can give similar results to those of free stream conditions. These simulations will be beneficial to explain the effect of different testing facilities on flow physics behind the savonius rotor experiments, with special attention to the test section at IMP PAN (refer Appendix B).

3.2.1 Geometry

The wind turbine model used for the purpose of simulations is a single-segment rotor. More details about this can be found in Section 3.1.2. The test section used for the second part of the study has been detailed in AppendixB.

3.2.2 Performance Characteristics: Freestream

3.2.2.1 Domain and mesh

Fig. 3.2.2 demonstrates the domain and mesh configuration for the single-segment rotor in freestream. Part A of the Fig. shows the simulation domain, part B demonstrates the rotor top view, and part C illustrates the mesh refinement at blade edges. The following mesh was created using Cadence (formerly Numeca) software HEXPRESS. The domain length is 90D, and the width is 40D, where the diameter ('D') of the rotor is 0.5m. These large distances for the side walls and inlet/outlet are selected to avoid the influence of the side walls on the results. The rotor center was set at the coordinates (0,0). The number of cells in the given mesh was $\approx$ 70k. The mesh was constructed in two parts, the domain without the rotor($\approx$ 45k cells) and the rotor($\approx$25 k cells), refined close to the blades in order to keep $y^+ \approx 1$. The two parts of the mesh consist of a 'sliding mesh' interface (rotor–stator interface) with non-matching connections. The mesh is also refined downstream of the rotor (Fig. 3.2.2).

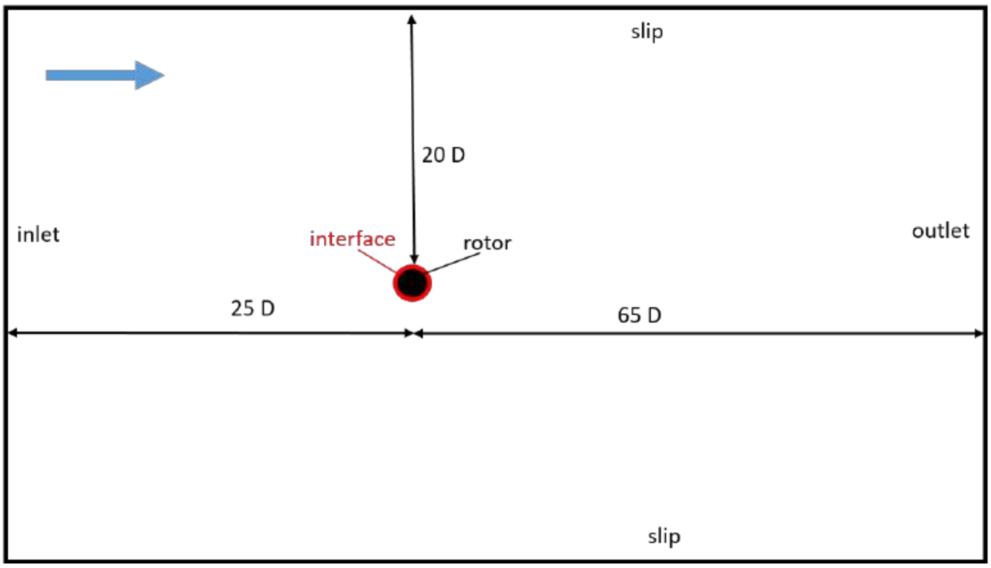

Figure 3.2.1: Domain for Savonius rotor simulations in free-stream

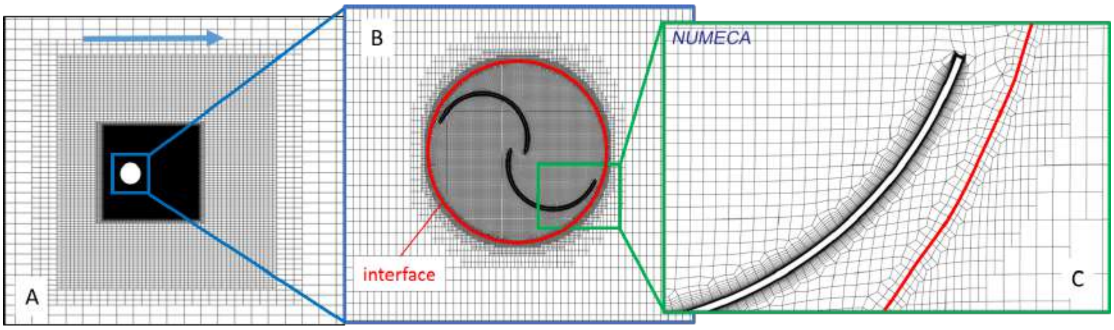

Figure 3.2.2: Domain and mesh for Savonius rotor simulations in free-stream

3.2.2.2 Numerical Model

Unsteady simulations were performed using Fine/OPEN software from Cadence. The flow model used was Reynolds-averaged Navier Stokes with the turbulence model as k- Omega SST.

The boundary conditions (BC) include an inlet velocity of 12 m/s and a static temperature of 293 K. At the outlet, a static pressure of 100 kPa was specified, while other flow variables were solved by the code. The fluid was considered a perfect gas. This setup corresponds to the standard velocity-inlet and pressure-outlet configuration commonly used in CFD when inlet flow parameters are known and a reference pressure is defined at the outlet. These boundary conditions were defined based on the options available in the software used. The speed of rotation was changed by keeping the velocity normal to the inlet constant for selected TSR's between 0.4 and 1.6 (increments of 0.2). A second-order central discretization scheme was used, and the CFL number was set to 1 and a full multigrid strategy was implemented to improve the convergence rate. The time step was set to correspond to 2 degrees of the complete rotation. The physical time step varied for different TSR. To determine the optimal number of revolutions for future simulations using the same model, multiple simulations were conducted with varying revolution counts. This study demonstrated that simulating 10 full revolutions of the rotating component is sufficient to capture the system's performance characteristics. This duration allows the flow field and performance metrics to reach a periodic steady state, beyond which additional revolutions yield negligible changes.

Within each time step of the simulation, the solver performs multiple internal iterations to converge the solution. Testing has indicated that 25 internal iterations per time step are adequate, as increasing this number further results in less than 0.5% changes in the results. This balance ensures computational efficiency without compromising accuracy.

The blade surfaces were subjected to a no-slip condition, meaning that the fluid velocity at the wall is zero. This condition is essential for accurately modeling viscous flows near solid boundaries, as it governs the development of boundary layers and shear stresses, which are critical for the performance of rotating machinery.

3.2.2.3 Grid Convergence Analysis

An assessment of grid convergence was conducted to analyze how the calculated rotor torque is influenced by variations in grid resolution. The validation calculations were performed for an input velocity of $v = 12$ m/s and TSR $= 1.0$, corresponding to 458.4 rpm. The quantity of elements for each distinct computational domain, along with the torque results and GCI (Grid Convergence Index) values, is presented in Table 3.2.1. The mesh density was adjusted by modifying the cell size within the rotor region, while the mesh size in the stator region resulted from maintaining the same resolution on the rotor–stator interface to minimize inaccuracies arising from interpolation across this interface.

Mesh	**Rotor cells**	**Stator cells**	**Total cells**	**Torque [Nm]**	**GCI (Relative difference to Medium) [%]**
Coarse	11,606	18,536	30,142	2.48	-5.7
Medium	24,582	44,494	69,076	2.62	–
Fine	32,934	66,098	99,032	2.64	0.6

Table 3.2.1: Grid Convergence Analysis for Rotor Torque

Torque increases with mesh refinement, but the difference between medium and fine is only 0.6%, indicating that the solution is close to mesh-independent. The coarse mesh shows a larger deviation of 5.7% compared to Medium. Based on the GCI assessment, the Medium mesh was selected for further simulations, balancing accuracy and computational cost.

Using the GCI technique (refer to [186] for details), an extensive examination of the mesh was conducted exclusively within the rotor domain, focusing on torque monitoring. When considering the outcomes of the Medium mesh as a benchmark, the disparity between the Coarse and Fine meshes was found to be 5.7% and 0.6%, respectively. Given the minimal distinction between the Medium and Fine mesh outcomes, the decision was made to employ the Medium mesh for subsequent simulations to conserve computational resources and reduce computing time.

3.2.2.4 Results and Discussion

Plots in Fig. 3.2.3 demonstrate the torque and performance characteristics obtained from the 2D simulations (marked as violet dashed line). The performance of the single-segment rotor simulated in free-stream was then verified using existing experimental data by Blackwell [66]. This data was obtained by wind tunnel tests and was later corrected to match freestream results.

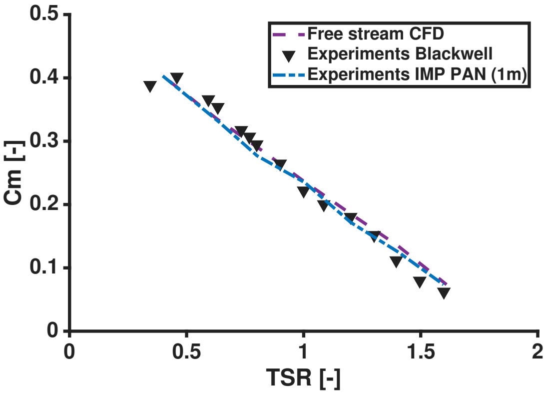

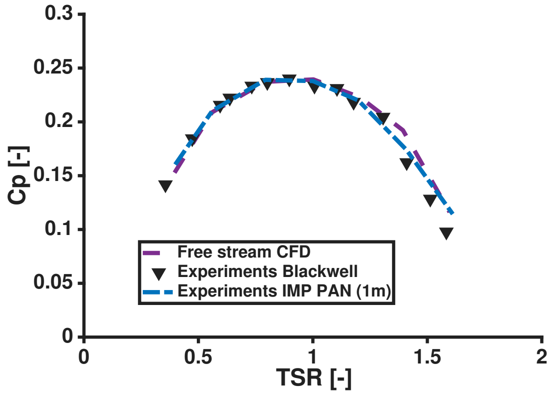

(a) Coefficient of torque variation with TSR. (b) Performance coefficient variation with TSR.

Figure 3.2.3: Characteristics of a typical Savonius rotor in comparison with freestream CFD and experiments performed in the lab when the rotor is placed at a distance of 1m from the test section outlet.

Based on the results presented, it can be concluded that a good agreement was observed between the simulated and the experimental results. Thus, the model stands validated. This allowed for further analysis to simulate the flow with a wind tunnel. This has been detailed in Section 3.2.3.

3.2.3 Performance Characteristics: Rotor Location in Test Section

The subsequent phase of the study entailed analyzing the rotor performance positioned at varying distances from the test section outlet. This approach was adopted to replicate the real-wind operating performance of the rotors as closely as possible, thereby ensuring the experimental results closely reflect practical performance.

The cases were undertaken for the analysis at varying distances, X measured between the rotor axis and the test section outlet (jet outlet).

- Case 1: X= 1 m, also referred to as position 1.
- Case 2: X= 0.5 m, also referred to as position 2.
- Case 3: X= 0.28 m, also referred to as position 3.

The domain layout for this study is shown in Fig. 3.2.4.

3.2.3.1 Domain and Mesh

The domain used in the previous study 3.2.1 was later modified for the purpose of numerical studies to incorporate test section/open jet wind tunnel studies. This new domain is shown in Fig. 3.2.4. The mesh was regenerated, maintaining the same resolution on the rotor-stator interface. The mesh was as seen in Fig. 3.2.5. In part A of the Fig. 3.2.5, the red box marks the location of the rotor and the test section outlet, which can be seen in more detail in Fig.3.2.5.B. Just like the previous case, the mesh was again made in two parts, consisting of the rotor and the domain with the test section. Part C of the Fig. illustrates the mesh for the connection and the blades in detail; the rotor mesh was not changed. Part D demonstrates the wall edge of the test section fluid flow outlet. Changes in X in different cases resulted in minor variations of the mesh, with the number of cells varying from 102k for case 1 to 106k for case 3.

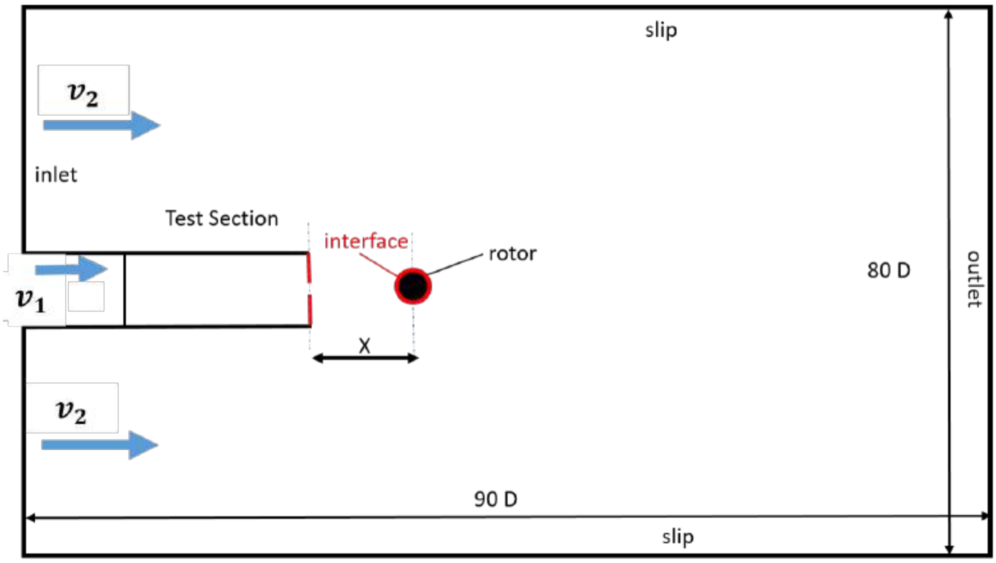

Figure 3.2.4: Domain for Savonius rotor simulations with test section

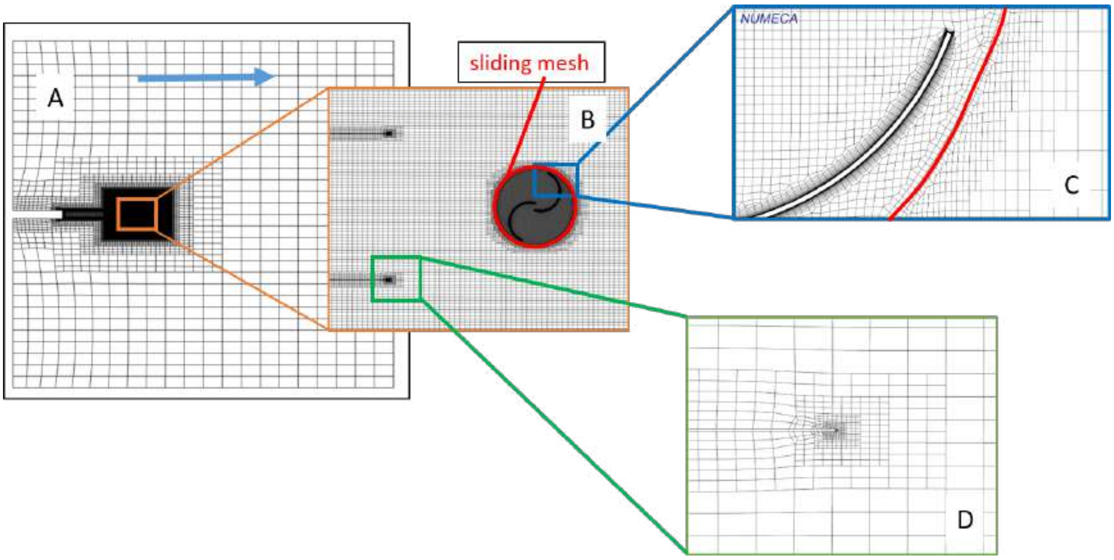

Figure 3.2.5: Domain and mesh for Savonius rotor simulations with test section.

3.2.3.2 Numerical Settings

The numerical model followed was similar to the one described in Section 3.2.2.2, except for the boundary conditions.For the three cases under consideration, the inlet velocity at the test section (v_1) was given as 12 m/s, and v_2 was given as 1 m/s (as seen in Fig. 3.2.4). The reason was to avoid the formation of re-circulation zones and secondary flows at the side of the test section walls. Slip conditions were maintained at the side surfaces and inlet nozzle surfaces (Fig. 3.2.5).

3.2.3.3 Results and discussion

The results obtained from test section simulations suggest the distance of the center of the rotor from the test section outlet for which the results are similar to a rotor under free stream conditions.

Overall, the curves presented in Fig. 3.2.6 are observed to match or, in some cases, exceed the typical performance characteristics of a Savonius rotor, approaching the Betz limit in certain instances. This dependence of rotor performance from the distance to wind tunnel exit reflects the intensity of interaction between the rotor and wind tunnel.

It was observed that the power characteristics for position 1 were in close agreement with the free-stream simulations as demonstrated in Fig. 3.2.3 and thus also with the experiments by Blackwell et. al. [66].

Despite the shape of the characteristics obtained for all cases being similar to a typical Savonius rotor (refer to Fig.3.1.1, the C_p and C_m are very high, with the turbine efficiency reaching up to $\approx 59\%$ (the Betz limit). Thus, it is imperative to study flow physics in detail to understand the reason for these abnormally high values. It can thus be suggested that there is a need to make some manipulations in the flow velocity used for simulations in the cases discussed above to have results similar to real testing conditions. An in-depth experimental analysis has been detailed in Chapter 3.3.

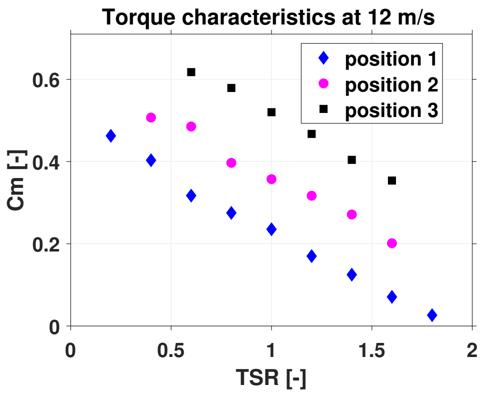

(a) Torque variation with TSR.

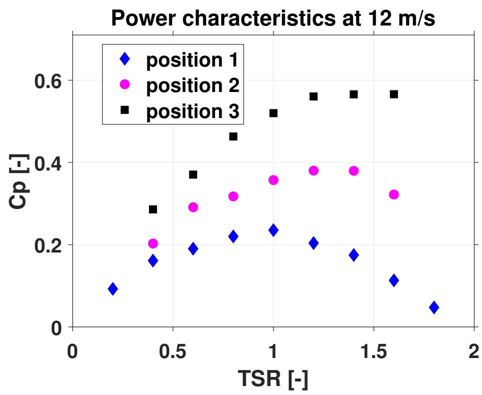

(b) Performance variation with TSR.

Figure 3.2.6: Characteristics of a typical Savonius rotor.

During wind tunnel testing, particularly within the test section, the proximity of the tunnel walls can restrict the natural expansion of airflow around the rotor. This confinement leads to an effect known as solid blockage. As airflow is constrained, it accelerates around the rotor to maintain mass continuity, resulting in a localized increase in velocity. According to Bernoulli's principle, this acceleration corresponds to a decrease in static pressure, creating a pressure gradient. This altered pressure distribution can lead to an increase in the measured aerodynamic forces, such as drag, on the rotor. The solid Blockage Ratio (BR) is the ratio of the solid body projected area (rotor) and the jet outlet cross-section. The flow acceleration at a local level also exerts an impact on the boundary layer encircling the rotor, causing an augmentation in the thickness of this boundary layer alongside the rotor blades. Additionally, the formation of a viscous wake downstream of the rotor further constrains the effective cross-sectional area of the tunnel and creates an extra flow acceleration. This occurrence is related to object blockage, contributing to an uneven pressure gradient and a corresponding increase in drag. In this case, the rotor acts as the obstruction for the jet flow and the change in rotor position results in similar results as changing the blockage effect. When the fluid encounters an obstruction, its velocity decreases locally at the centre while it increases at the walls of the nozzle as the flow diverts around the obstacle. This phenomenon leads to changes in pressure distribution, velocity profiles, and turbulence characteristics in the flow field. Consequently, since the power output of the wind turbine is directly linked to the cube of the wind speed, any modifications in wind acceleration induced by blockage effects distinctly influence the overall performance of the wind turbine and thus the overestimated C_p values in our case.

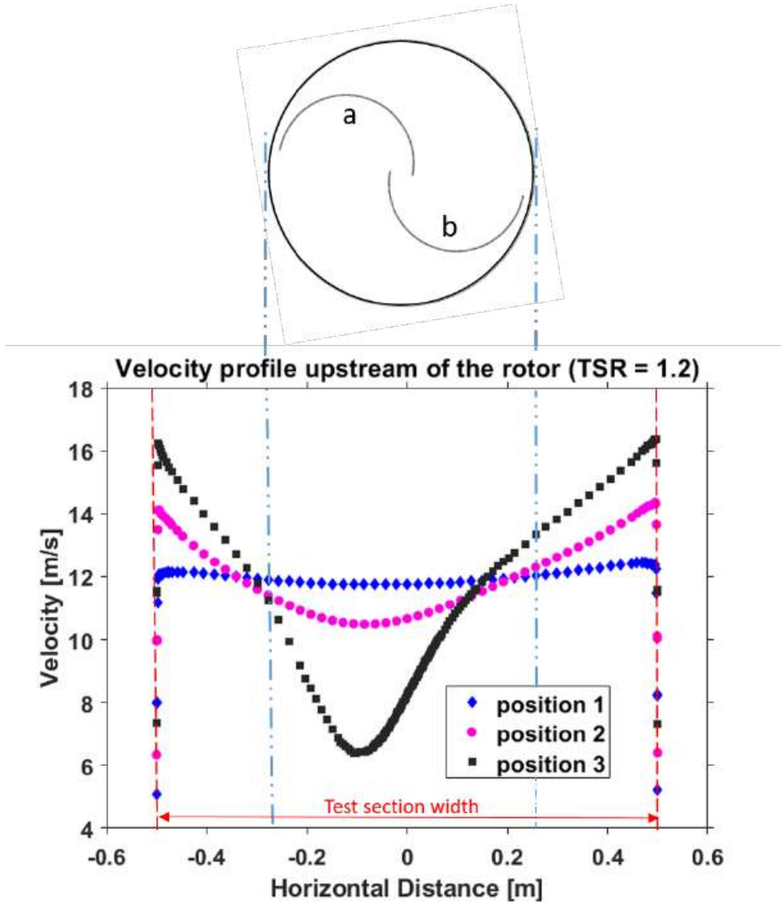

Figure 3.2.7: Time averaged variation of velocity along the test section outlet (horizontal cross-section, as marked in red vertical line in Fig. 3.2.4) for different cases at TSR=1.2.

Fig. 3.2.7 shows the time-averaged velocity perpendicular to the stream direction (span direction) for TSR = 1.2 at the test section outlet- upstream of rotor. The maximum difference (decrease) in velocity from reference velocity is seen for position 3, followed by Positions 2 & 1 (Fig. 3.2.7 & 3.2.8) when measured along the center of the rotor. In addition, an increase in acceleration around the nozzle (test section) edges is observed for these cases as highest for Position 3 and the lowest for Position 1. Thus, it can be said that the influence of reducing the distance $_1X$ can be interpreted in terms of the blockage effect: a shorter distance produces flow conditions comparable to those of a higher blockage ratio, thereby leading to an increase in Turbulence Intensity (TI), which can distort performance. The pressure variation in the flow is illustrated in the contour plots (Fig. 3.2.8). As the rotor position shifts from 3 to 1, a progressive pressure drop is observed on the side of the retreating blade (marked as blade 'a' in Fig. 3.2.7). Conversely, the red regions in the plots indicate an increase in pressure acting on the surface of the approaching blade (marked as blade 'b' in Fig. 3.2.7), highlighting the asymmetric loading of the rotor with decreasing distance from the outlet. This leads to an increase in velocity (or flow acceleration) on the retreating blade side of the test section, explaining the shift of velocities from the center of the rotor (refer to Fig. 3.2.7). The dip in velocities with a reduction in distance $_1X$ is also justified by an increase in the pressure on the approaching blade from position 1 to 3.

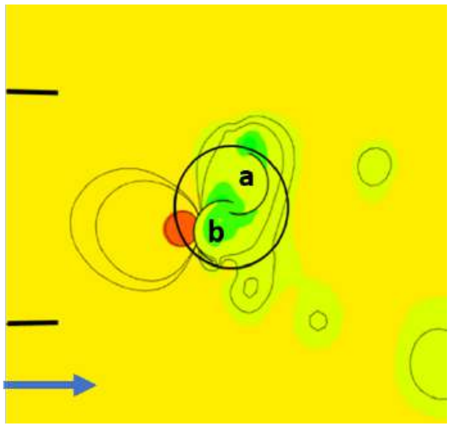

(a) Position 1

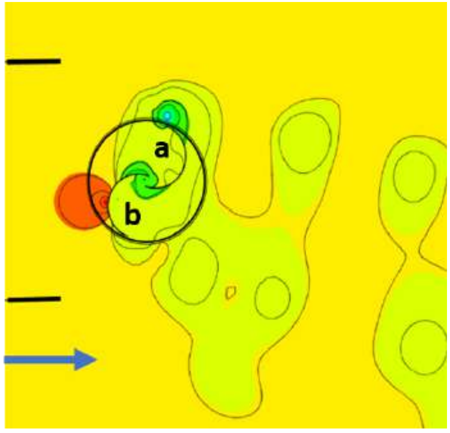

(b) Position 2

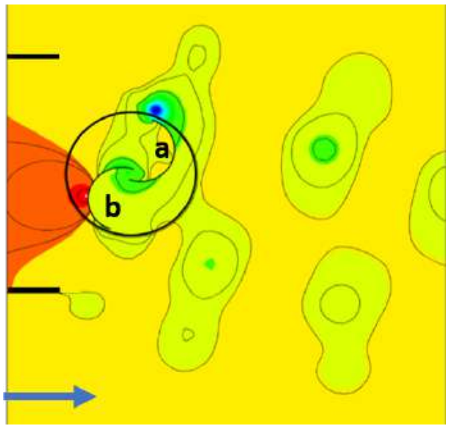

(c) Position 3

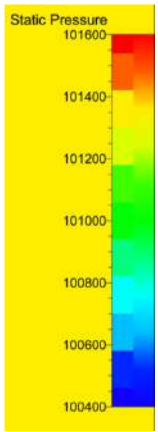

Figure 3.2.8: Variation of static pressure for different cases at TSR=1.2 (specific time step).

3.2.4 Summary: Numerical Analysis

A numerical analysis model was developed to perform unsteady, two-dimensional RANS simulations of the operational characteristics of a typical Savonius turbine. The study was carried out in two stages: first, free-stream simulations of the rotor were performed and validated against available experimental data; subsequently, the model was adapted to simulate rotor performance within an open-jet test section.

The results demonstrated that the axial position of the rotor relative to the test section outlet (X) is a critical parameter that influences the measured power coefficient. As shown in Fig.3.2.6, C_p reaches its expected maximum of 0.23 at position 1, confirming agreement with typical Savonius rotor performance. Positions closer to the outlet, however, exhibited significantly higher C_p values, in some cases appearing to approach the Betz limit. It must be emphasized that this does *not* indicate exceptionally high rotor efficiency, but rather reflects an artifact of the interaction between the turbine and the test section, combined with the difficulty of defining a representative reference velocity under such conditions. These factors lead to artificially elevated efficiency estimates.

This interpretation is supported by the velocity and pressure field analyses in Figs. 3.2.7 and 3.2.8. The time-averaged velocity distribution perpendicular to the flow direction (for TSR = 1.2) shows the largest velocity deficit at the test-section outlet for position 3, with progressively smaller deficits for positions 2 and 1. Correspondingly, flow acceleration near the blade tips follows an inverse pattern—highest for position 1 and lowest for position 3—indicating that reducing X produces flow conditions analogous to an increased BR and TI. The pressure contours reveal a localized drop on the retreating blade side and an increase on the approaching blade side, which drives asymmetric velocity distribution across the rotor and shifts the velocity maxima away from the rotor centerline.

These findings clarify that the observed overestimation of performance for small X values results from a combination of blockage-like effects and the inherent simplifications of two-dimensional modeling. Extending the analysis to fully three-dimensional unsteady simulations would capture additional flow features and improve agreement with wind tunnel measurements. Such investigations are recommended for future work.

Chapter 3.3

Experimental Evaluation of Performance Characteristics and Rotor Segmentation

The findings showcased in 3.2.3 lacked reliability in their original form. Hence an effort was made to introduce specific modifications in the experimental segment elaborated in Appendix B. The updated design of this test section included the ability to change the position of the rotor axis from the jet stream outlet, referred to as 'distance' from here onwards. Other features of this test section remained unaltered. For the purpose of experiments, this distance was kept similar to that of its simulations counterpart 3.2.3.

This experimental study was extended beyond the traditional single-segment rotor (discussed in chapter 3.2), and included an evaluation of performance characteristics for a five-segment wind turbine. The analyzed rotors were identical to those discussed in section 3.1.2.

3.3.1 Operational conditions and setup

These tests were conducted at a variable wind speed from about 5 m/s to 12 m/s. This was adjusted by controlling the frequency of the test section fans. The velocity of the flow field mentioned in this chapter was recorded individually for every case by a fixed probe present at the center of the test section (Fig. B.4 in Appendix B.1). As explained in chapter 3.2.3, the blockage effect along with reverse flow at the vicinity of rotor tips, results in a varying velocity distribution along the test section outlet, even when considering the same flow velocity at different locations. This phenomenon was also observed in the experiments detailed in this chapter.

The tests were performed for the same cases (distance from test section outlet) as the numerical simulations performed (refer to Chapter 3.2). The rotor characteristics were recorded by changing the load on the rotor with the help of a loading device. The rotor was left to stabilise for at least two minutes each time the loading conditions were changed. The data consisting of the voltage, current, torque and speed of rotation was then recorded for a period of 100 seconds, with a time step of one second. An average was then taken over this time frame, resulting in the operational characteristic for the particular setting. This was repeated for all cases and over the complete operational range of the wind turbines.

3.3.2 Results and discussion

The results obtained for these experiments are compared for both types of rotors at the same distance. In section 3.2.6, the deviation of characteristics from the typical behaviour of a Savonius rotor has been attributed to an effect similar to the Blockage Ratio (BR). The blockage effect, in the context of fluid dynamics and aerodynamics, refers to the alteration of a fluid flow pattern caused by the presence of an obstacle or barrier in the flow path and is a typical behaviour of a closed test section. The effects of this phenomenon are detailed in section 3.2.3.3.

The effect of these blockages can be accommodated by most conventional correction methodologies [187–189]. However, the available relations are applicable to the closed test section (wind tunnel). The challenge in the presented study is the addition of the changing distance between the jet outlet and obstruction to the BR, not allowing for the application of simple corrections. Also, the introduction of segments in the rotor further complicates the process of converting the measured values to match freestream conditions.

As expected, the power characteristics of the rotor are highly dependent on the flow velocity. For plots specific to a single-segment rotor, it can be concluded that for most of the cases presented, the operating TSR is higher than that of its five-segment counterpart (Figs. 3.3.2,3.3.2 and 3.3.2). Both rotors achieve maximum efficiency for the values of TSR between 0.8 and 0.9 for a distance of 0.5 m and 1 m (Fig.3.3.2 & 3.3.2). When each rotor is positioned at a distance of the rotation axis of 0.28 m from the outlet, the maximum of the function moves closer to TSR = 1 (Fig. 3.3.2).

The rotor efficiencies at a distance of 0.28 m are higher than expected for this type of rotor construction (typically with a coefficient of performance, C_p, around 0.2). For the single-segment rotor, the efficiency is approximately 35%, while for the five-segment rotor, it is around 30% (Fig. 3.3.2). At a distance of 1 m, the efficiency appears slightly lower than anticipated (Fig. 3.3.2). In all configurations, both rotor types exhibit significantly lower efficiencies at the lowest incoming air stream speeds.

Considering the overall performance of the two turbine structures, it is evident that the five-segment rotor exhibits lower efficiency when compared to its single-segment counterpart. This difference in efficiency can be attributed to the additional aerodynamic losses associated with the five-segment rotor. These losses stem from the formation of extra boundary layers on the walls of the supplementary middle plates added to create the segments. The multiple plates result in the generation of additional vortices, creating complex three-dimensional flow structures. Furthermore, the five-segment rotor was heavier than its single-segment counterpart due to the added components. This increased weight caused greater dynamic losses, which reduced the rotor's rotational speed and allowed more time for the formation of these turbulent flow structures. Consequently, the single-segment rotor outperforms the five-segment rotor in terms of efficiency, highlighting that more segments do not necessarily lead to better performance in this specific setup. Thus, despite the potential benefits of adding more segments, the simpler design of the single-segment rotor proves to be more efficient in this case.

3.3.3 Summary: Experimental Analysis of Rotor Performance

The experimental investigations conducted in this study underscore the significant influence of both streamwise placement within the test section and rotor segmentation on the aerodynamic performance of Savonius wind turbines.

Initially, the rotor's axial position relative to the test section outlet was found to crit-

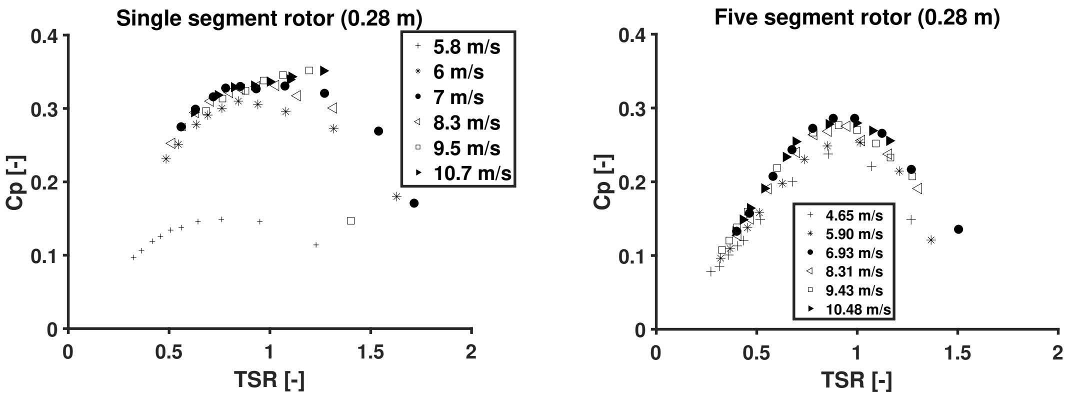

(a) (b)

Figure 3.3.1: Performance characteristics for distance = 0.28m

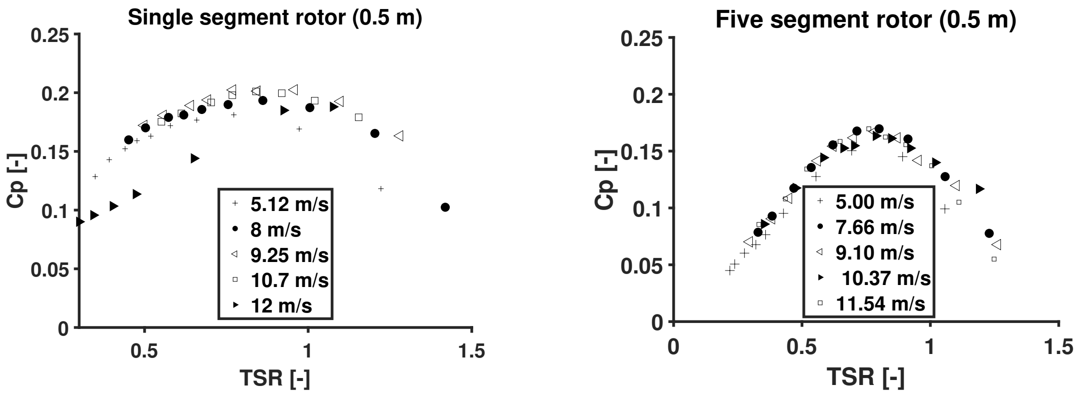

(a) (b)

Figure 3.3.2: Performance characteristics for distance = 0.5m

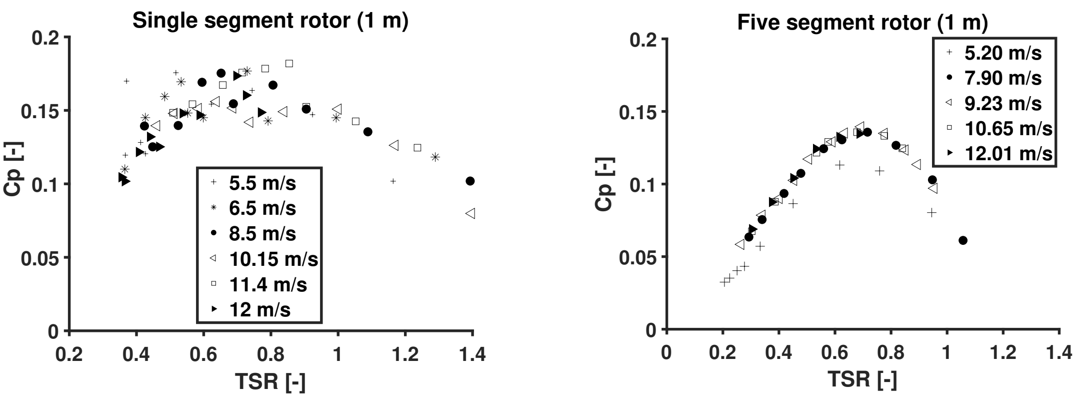

(a) (b)

Figure 3.3.3: Performance characteristics for distance = 1m

ically affect performance measurements. The highest power coefficient ($C_p = 0.33$) was recorded when the rotor was positioned 0.28 m from the outlet, whereas under free-stream conditions this value was approximately 0.23. A progressive decline in efficiency was observed as the rotor was moved further downstream, with maximum C_p values reducing to 0.2 and 0.18 at distances of 0.5 m and 1 m, respectively. These results highlight the necessity of carefully selecting the rotor placement to minimize artificial flow acceleration effects and ensure representative performance data.

Furthermore, comparative testing between single-segment and five-segment Savonius rotors revealed notable differences in efficiency. While both rotor types achieved peak performance at similar tip speed ratios (TSR $\approx$ 0.8–0.9), the single-segment rotor consistently exhibited superior efficiency across multiple test distances. The reduced performance of the five-segment rotor is attributed to increased aerodynamic losses from the additional middle plates and higher dynamic losses resulting from its greater mass, which collectively led to lower rotational speeds. These findings indicate that increased structural complexity does not inherently yield performance benefits, and in some cases, may be detrimental.

Overall, the study provides key insights into the interplay between test configuration and rotor design, emphasizing that accurate performance assessment requires careful control of both experimental setup and design parameters. These conclusions contribute to a more informed approach to the development and testing of vertical-axis wind turbines, particularly in small-scale and urban applications.

3.3.4 Conclusion: Numerical Modeling and Experimental Validation

This study evaluated the performance of SVAWTs through a combination of numerical simulations and experimental investigations. Due to the computational complexity and resource demands associated with modeling multi-segment rotors—particularly the five-segment configuration, which requires detailed 3D CFD—the comparative numerical analysis was limited to single-segment rotors. This approach allowed a focused investigation of fundamental aerodynamic behaviors while maintaining manageable computational resources.

The experiments and CFD simulations were conducted at different rotor locations to better replicate realistic operational conditions. Initial experiments at the fixed position (position 3, 0.28 m) showed efficiency values slightly higher than typical for standard Savonius rotors. This discrepancy led to further simulations concentrated on the test section, which revealed significantly inflated performance predictions at that location, emphasizing the limitations of current numerical models to fully capture the complex flow dynamics near the test section outlet. To address these issues, additional experimental tests at multiple rotor positions were carried out to evaluate the agreement between simulation and measurement data. This iterative process helped identify rotor positions that closely matched the characteristic performance of Savonius turbines under free-stream conditions, enhancing the reliability of the results.

The maximum C_p and corresponding TSR obtained from both simulation and experimental investigations at three different rotor positions are summarized in Table 3.3.1.

The data show a variation in the maximum power coefficient between rotor positions in both simulation and experimental results. In particular, the highest simulated C_p was observed for position 3 with a value of 0.56 at TSR 1.0, seemingly approaching the theoretical Betz limit of approximately 0.59. However, it must be emphasized that the velocity at the inlet was used as the reference for calculations, rather than the velocity directly in front of the rotor. When the rotor is placed too close to the jet outlet, the local velocity can be significantly higher due to interaction effects between the rotor and the inlet flow. For this reason, several rotor positions were investigated to estimate the location that best represents freestream conditions, and position 3 was identified as providing the most reliable comparison. This clarifies that the apparent proximity to the Betz limit is not indicative of an unusually efficient rotor, but rather a result of test-section interactions and reference velocity definition.

Table 3.3.1: Maximum C_p and corresponding TSR at different rotor positions for simulation and experimental results.

position	**Simulation C_p**	**Simulation TSR**	**Experimental C_p**	**Experimental TSR**
1	0.23	1.0	0.18	0.85
2	0.38	1.2	0.22	0.9
3	0.56	1.0	0.36	1.0

In contrast, the experimental C_p values at position 3 remain significantly lower at 0.36, reflecting more realistic aerodynamic losses and operational factors present in physical testing. This difference highlights the importance of validating numerical predictions with experimental data.

Experimental C_p values are consistently lower than simulation results across all positions, but both datasets show an increasing trend in C_p from position 1 to position 3, indicating rotor placement influences turbine performance. The TSR values corresponding to peak C_p vary slightly between simulation and experiment but remain close to unity. Minor differences in TSR likely result from flow disturbances and mechanical losses encountered during physical testing.

Overall, the strong correlation between rotor position and performance metrics highlights the critical importance of rotor placement in optimizing turbine efficiency. While position 3 appears aerodynamically favorable, the proximity of simulated C_p to the Betz limit warrants cautious interpretation. Further investigation is necessary to validate these findings and understand the flow dynamics influencing turbine operation. The reasonable agreement in trends between simulation and experiment supports the utility of the numerical model as a predictive tool while underscoring the need to consider experimental limitations and real-world complexities in performance assessment.

Experiments were also performed on both single-segment and five-segment rotors at the same streamwise locations to directly compare their aerodynamic performance. The single-segment rotors consistently outperformed the five-segment counterparts, achieving higher C_p and operating efficiently at greater TSR. This performance difference is attributed to the increased boundary layer development on the additional plates of the five-segment rotor, which generates complex flow structures that negatively impact aerodynamic efficiency. Additionally, a comparison of noise emissions between the two rotor types was conducted; this will be discussed in detail in later chapters.

Overall, this study emphasizes the challenges and intricacies involved in accurately predicting the aerodynamic performance of Savonius turbines in realistic settings, particularly due to complex geometries and proximity effects. These observations highlight the need for more refined, higher-fidelity simulation models that incorporate unsteady flow features and can accurately replicate experimental conditions. Although improving the numerical model fidelity to better predict real-world performance of Savonius VAWTs was recognized as a valuable direction for future research, this aspect was beyond the scope of the current study due to time limitations. Moreover, the findings support the ongoing design optimization of multi-segment rotors to achieve scalable and efficient solutions suitable for deployment in densely populated urban areas.

Part 4

EXPERIMENTAL ACOUSTICS ASSESSMENT OF SAVONIUS VAWT

Chapter 4.1

Effect of Rotor Segmentation on Acoustics and its Performance

The division of rotors into segments is a widely discussed topic in the literature concerning the optimization of SVAWTs efficiency. However, existing data are constrained and somewhat unclear, as elaborated in Section 3.1.1. The division of Savonius rotors into segments, along with the non-uniform inflow conditions typically encountered in urban environments, has a significant impact on the development of flow structures, the strength and evolution of vortices, and the wakes downstream of the blades and the entire rotor assembly. These intricate details of flow structures not only influence the performance of wind turbines but also contribute to the generation of noise. Therefore, conducting acoustic analysis and investigating noise sources within the Savonius rotor domain, particularly in the context of acoustic mitigation, is essential for its successful integration into urban environments and for gaining public acceptance. Consequently, the author opted to conduct experiments to gain deeper insights into the correlation between wind turbine noise and energy output for both segmented and non-segmented rotors under consideration. More details of this study can be found in the article [190].

4.1.1 Experimental setup

For this experimental campaign, the rotors discussed in Section 3.1.1 were mounted in the test section detailed in Appendix B. The steps followed for the noise measurements are as shown in Fig. 4.1.2. The measurements were done by first selecting a rotor from the single-segment and five-segment options. This was followed by placing microphones outside the jet. The microphone was placed at half the height of the rotor at a distance of 0.7 m from the rotor axis. This arrangement can be seen in Fig.4.1.1. A windscreen for the microphone was also used. The noise measurements were made for four different cases, while the velocity of the test section was fixed at 8.5 m/s:

- Case 0: Only fan noise (no rotor mounted in test section).
- Case 1: Rotor at stopped position, used as a reference case.
- Case 2: Loaded condition, when the rotor is loaded for maximum efficiency.
- Case 3: No load condition, when the rotor was lead to run freely.

It should be noted that the ‘load’ corresponds to the torque on the rotor axis, which is linearly dependent on the TSR.

The data analysis was done using the Constant Percentage (CPB) analyzer. The data was treated with 1/12 octave band analysis in contrast to the popular 1/3 octave

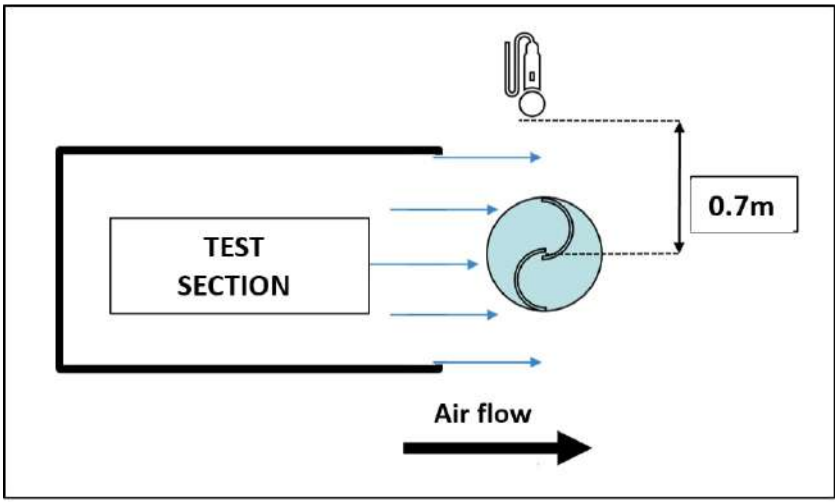

Figure 4.1.1: Experimental setup for measurements at IMP-PAN.

band analysis. With its finer frequency resolution, 1/12 octave analysis can more accurately capture the spectral content of low-frequency sounds, allowing for a more detailed understanding of sound characteristics and behavior. The measurements were made three times for each of the cases stated above and then averaged.

However, it's important to note that the precision of any frequency measurement depends on various factors, such as the accuracy of the measuring equipment, the frequency range of the equipment, and the quality of the signal being measured. To ensure reliable results, high-quality equipment with proper calibration was used. The measurements were performed using SVAN 979 sound level meter, which allows for sound measurements at frequencies as low as 3.5 Hz. This is a class 1 'precision' grade meter in accordance with IEC 61672-1. This was accompanied by G.R.A.S. measuring microphone type 40AE equipped with SV 17 preamplifier. The sound level meter was checked before and after the measurements using the acoustic calibrator SV 36. During the noise measurements, the raw data was also recorded for future analysis. The SVANPC++ version 3.4.4. software was used for this purpose. The above measurements were made for both rotors and all three cases under the same conditions. The data was finally compared for the given cases.

At the same time, measurements were conducted to analyze the rotor performance characteristics and establish the relationship between the C_p, TSR and rotational speed. These experiments were carried out under the same conditions as the noise measurements. The test section's fan frequency was set to 35 Hz, equivalent to a wind velocity output of 8.5 m/s. The rotor load was incrementally increased to obtain the discussed plots. Three individual measurements were performed for each of the cases, and the averaging was done using Eq. A.6.

In this study, Z-weighting frequencies were employed to compare the relative actual noise production between the considered rotors. The study presented in this section of the thesis solely discusses the relative noise production between the single and five-segment rotor configurations. It is crucial to emphasize that this comparison does not represent the noise produced by the individual rotors in a real-life environment. Factors such as inlet turbulence, temperature, humidity, and shear are significant contributors to altering noise levels in practical applications.

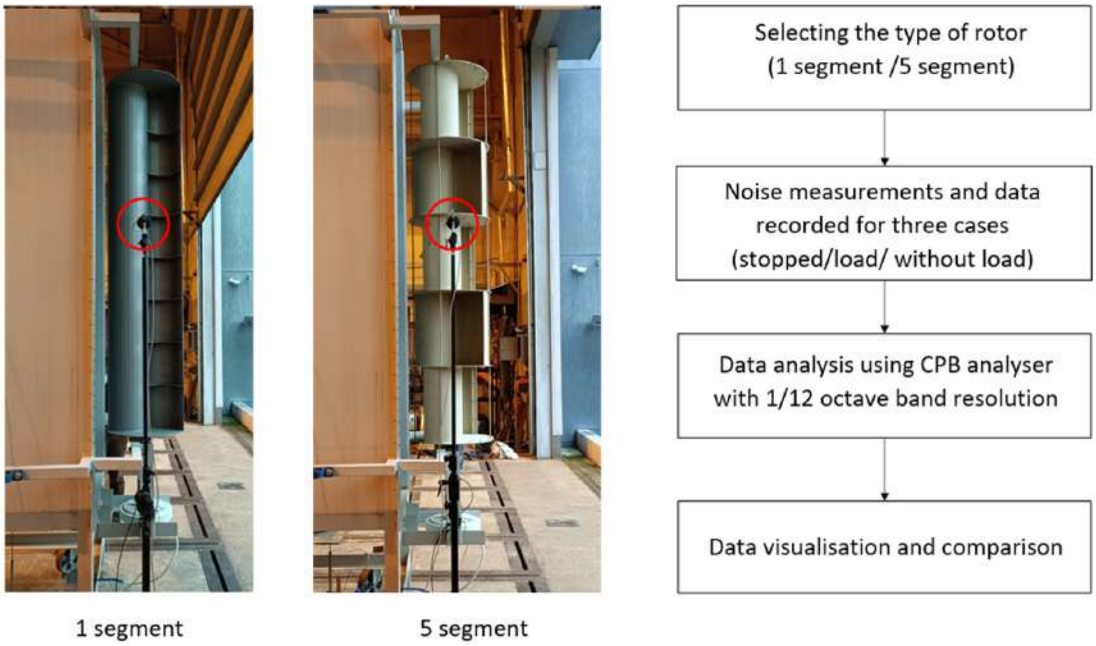

Figure 4.1.2: Algorithm followed for the noise measurements and analysis.

4.1.2 Results and discussion

4.1.2.1 Noise power spectrum

The results obtained from testing a single and five-segment rotor are depicted in Fig. 4.1.3 within this section. The wind velocity generated by the fans corresponds to a frequency of 35 Hz and is represented by a dashed vertical line in the plots. It is essential to acknowledge that the fans emitted a substantial amount of acoustic energy; therefore, the focus should be on comparing the difference in Sound Pressure Level (SPL) between the two rotors rather than their absolute values.

As depicted in the Fig. 4.1.3a, both segments exhibit similar noise level outputs for case 1, allowing for a direct comparison for cases 2 and 3 (see Fig. 4.1.3b and 4.1.3c). It is worth mentioning that the stopped rotor's angular position relative to the wind direction did not affect the results. The rpm of the rotors serve as the reference value for each scenario, and the corresponding frequencies and recorded sound energy (dB) are provided in Tables 4.1.1 and 4.1.2.

The important frequency peaks observed correspond to the cases studied are as follows :

- Case 2: With a rotor speed of 300 rpm for the single-segment rotor (corresponding to a frequency of 5 Hz) and 250 rpm for the five-segment rotor (corresponding to a frequency of 4.17 Hz).
- Case 3: Rotor without loading, with rotor speeds of 500 rpm for the five-segment rotor (corresponding to a frequency of about 8.5 Hz) and 575 rpm for the single-segment rotor (corresponding to a frequency of 9.55 Hz).

The acoustic energy distribution differences for the considered rotors are primarily noticeable in the low-frequency range (1 Hz up to 51 Hz), as depicted in Fig. 4.1.3b and 4.1.3c. Notably, the single-segment rotor generates significantly higher acoustic energy in this frequency range compared to the five-segment rotor. When considering

1 segment	**Frequency (Hz)**	**4.78**	**9.55**	**19.1**	**38.2**
	Noise (dB)	83.26	107.80	84.20	79.90
5 segment	**Frequency (Hz)**	**4.25**	**8**	**16.10**	**32.20**
	Noise(dB)	74.58	98.77	73.68	80.70

Table 4.1.1: Noise production and corresponding frequencies- loaded rotor (Case 2).

1 segment	**Frequency (Hz)**	**4.78**	**9.55**	**19.10**	**38.20**
	Noise (dB)	70	86.10	107.8	91.7
5 segment	**Frequency (Hz)**	**4.25**	**8**	**16.10**	**32.20**
	Noise (dB)	66.5	92.49	88.70	91.50

Table 4.1.2: Noise production and corresponding frequencies- no load (Case 3)

the entire frequency spectrum, differences in energy distribution are observed around 1000 Hz, with the single-segment rotor producing higher sound levels than the five-segment rotor under specific conditions (Fig. 4.1.3c). The acoustic energy analysis for this study involves summing values for 75 sub-bands from 1 Hz to 51 Hz. The difference in SPL between the stopped rotors (case 1) is negligible (approximately -1 dB), whereas, under no loading (case 3), the single-segment rotor produces 11.2 dB higher SPL than the five-segment rotor, indicating its higher acoustic energy production (Fig. 4.1.4). Similar differences are observed for loaded rotors (case 2), with the single-segment rotor generating 13.8 times more acoustic energy than the five-segment rotor.

Moreover, it was observed that the five-segment rotor exhibited shifting noise peaks toward broadband frequency with faster damping, attributed to enhanced mixing and coherence pattern breakage. Evaluating the two cases, it becomes evident that the unloaded rotor generates higher noise than its loaded counterpart (Fig. 4.1.4).

,

4.1.2.2 Noise and rotor efficiency

The subsequent section of the findings, pertaining to the impact of segmentation on efficiency relative to noise, is depicted in Fig.4.1.5. Evidently, the single-segment rotor exhibits higher C_p across the range of rpm or TSR considered. It is noteworthy that both cases show maximum efficiency at a TSR value of approximately 1. The single-segment rotor achieves a maximum efficiency of 33.15%, whereas the five-segment rotor attains 26.45%. The segmented rotor exhibits a relative decrease of 20% in efficiency compared to the conventional Savonius rotor.

In the case of segmented rotor, additional plates are inserted (Fig.3.1.4). These plates introduce additional surface on which boundary layers are formed, inducing viscous losses in the rotor. Moreover, it can be assumed that the boundary layers that develop on the highly curved surfaces of the blades generate pressure gradients perpendicular to the blade surface. Such pressure gradients induce transverse flows within the boundary layers, leading to the formation of complex three-dimensional flow structures. These 3D flow structures can further disrupt the aerodynamic performance of the rotor by enhancing flow separation and increasing energy losses. These two reasons become a source of increased losses at the segmented rotor.

4.1.2.3 Psychoacoustics

For the subsequent phase of the study, psychoacoustics related to sound quality were investigated based on the studies presented in [191, 192]. Figure 4.1.6 illustrates

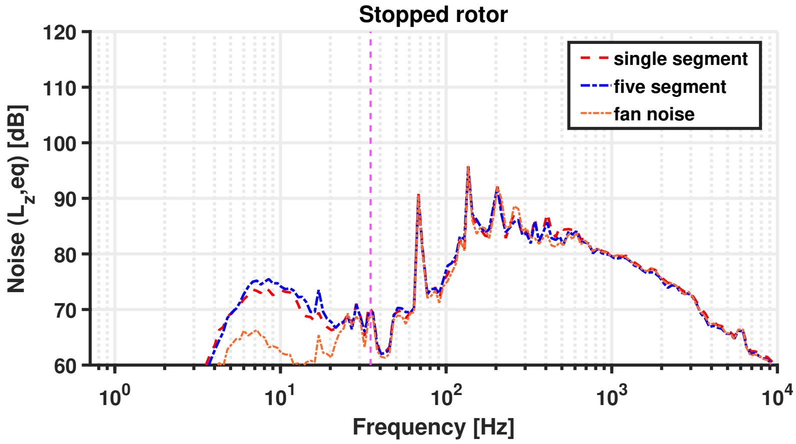

(a) Case 1

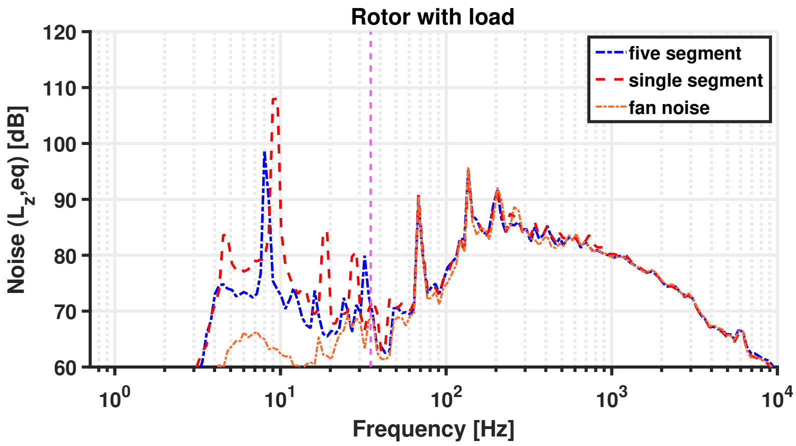

(b) Case 2

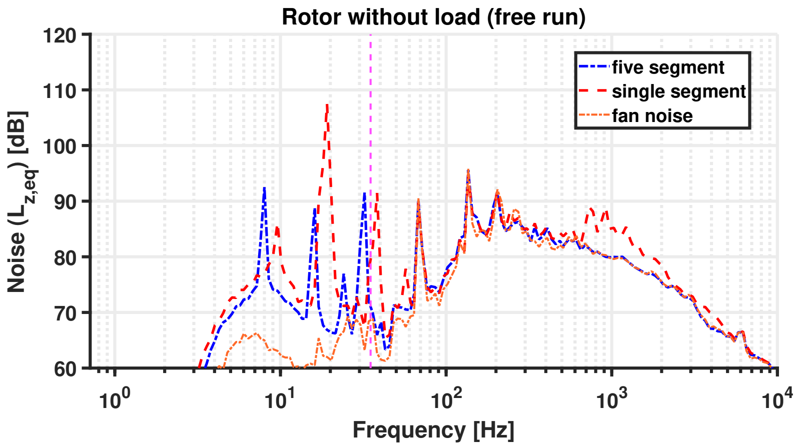

(c) Case 3

Figure 4.1.3: Noise measurements for single and five-segment rotor- over complete frequency range

the variations in different sound parameters under examination. Notably, fluctuation strength, indicative of sound modulation, peaks around a frequency of approximately 4 Hz.

Fluctuation strength is the perception of slow changes in loudness, typically between 0.5 and 20 Hz, creating a sense of rhythmic modulation. Roughness refers to the sensation of rapid, irregular amplitude variations between 20 and 300 Hz, giving a

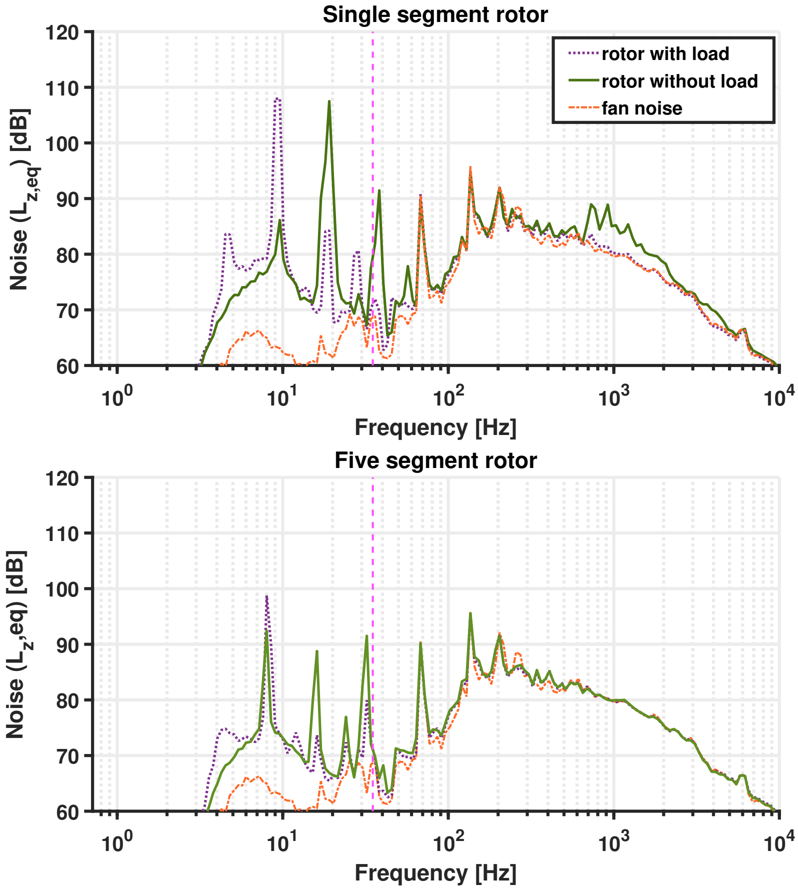

Figure 4.1.4: Comparison of noise measured for different rotors- over selected frequency range.

sound a harsh or grating quality. Sharpness is the perception of high-frequency dominance in a sound, making it seem bright, piercing, or shrill.

Higher fluctuation strength draws greater attention and may cause heightened irritation. As indicated in Table 4.1.1, a peak related to BPF (Blade Passing Frequency) occurs around this frequency when the rotor operates under maximum loading, as also evident in Figure 4.1.6. Another consideration is sound roughness, which reaches its maximum around 70 Hz. As expected from power spectrum plots, sharpness, reflecting the pleasantness of sound perception, is mainly influenced by higher frequencies and remains consistent across all cases.

4.1.3 Conclusion

The study demonstrates that wind turbine noise is significantly influenced by operational parameters, including rotor design. By comparing a single-segment rotor with a five-segment rotor, the research identifies optimal operating conditions and rotor configurations that minimize noise while maximizing efficiency. The findings suggest that rotor segmentation can impact aerodynamic noise generation, and selecting the appropriate rotor design is crucial for achieving a balance between low noise emissions and high performance. From the results obtained, it is thus inferred that:

- The five-segment rotor produces less overall acoustic energy compared to that produced by a single-segment rotor. The changing phase of the segments breaks

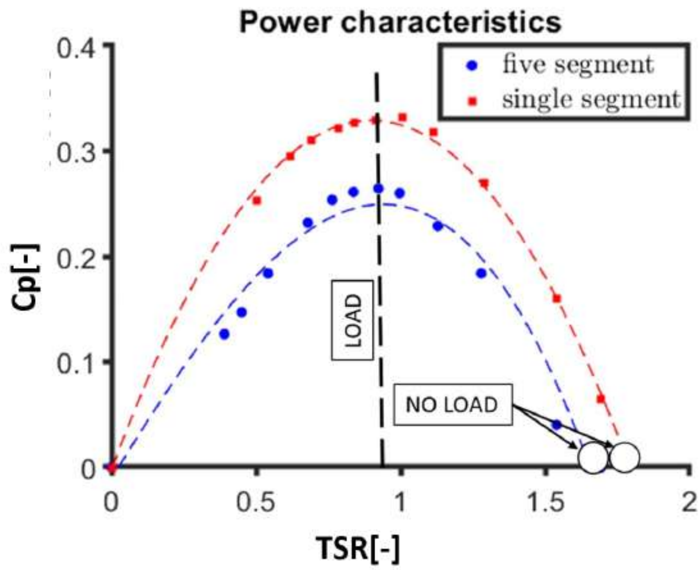

Figure 4.1.5: Performance characteristics with respect to TSR.

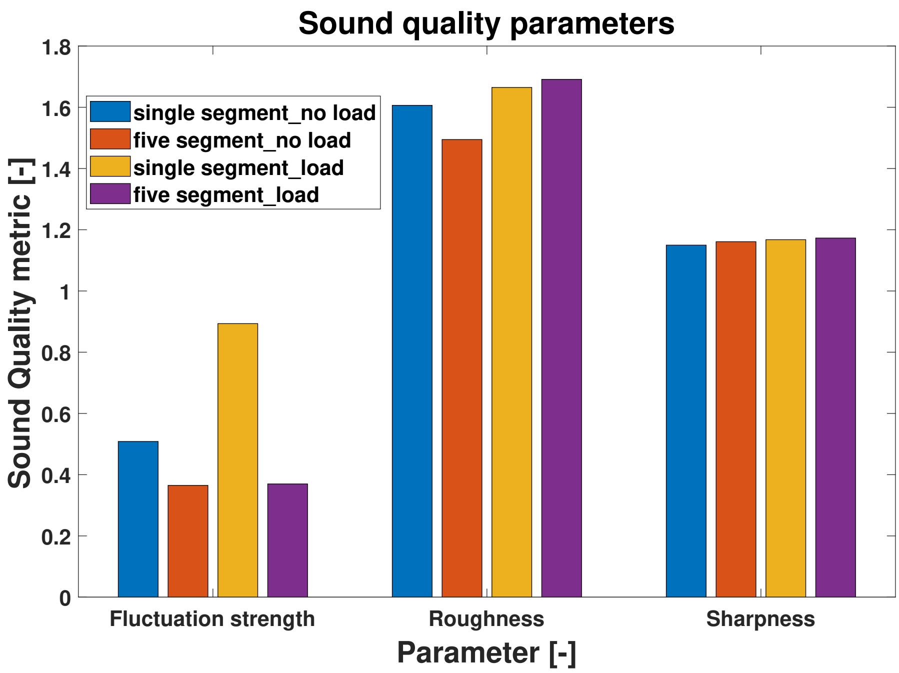

Figure 4.1.6: Information about sound quality for single and five-segment rotor under different operational conditions

the coherence of the flow and shifts the noise energy content to higher frequency spectra, where the dissipation rate is faster.

- The amount of acoustic energy produced decreases as the load increases, peaking when the rotor is spinning without any external load.
- The greatest differences in noise emissions between considered types of rotors concern low-frequency noise.
- Under the test conditions specified at a wind speed of 8.5 m/s, the single segment rotor demonstrates greater efficiency compared to the five segment rotor, achiev-

ing a maximum performance efficiency of 32% as opposed to 26.5% for the five segment rotor.

The analysis of the sound quality measures indicated that the metrics as roughness and sharpness, for both rotors are similar. Significant differences were observed between the examined rotors for fluctuation strength. The greater value of this metrics occurred for single-segment rotor. For 5-segment rotor, the SQ metric values were similar for all conditions (free run and with load) to the values obtained for fan noise.

Very practical conclusions can be drawn from the analysis: If minimizing noise is a critical requirement—such as in residential or noise-sensitive areas—the five-segment rotor is advisable due to its lower acoustic emissions. Conversely, if maximizing energy efficiency is the primary goal, the single-segment rotor is preferable, despite its higher noise output.

The single-segment rotor design offers higher efficiency but also generates more noise. To optimize this design for reduced noise without compromising performance, a detailed analysis of its noise sources in a controlled, quiet environment is essential.

A detailed analysis was thus required in order to predict the noise sources not only at low narrowband frquencies but also at high broadband frequencies. The beamforming technique has proved to be quite useful in such situations. Measurements were carried out in collaboration with the Technical University of Delft the use of a microphone array to identify the noise sources at high frequencies. This has been discussed in detail in Chapter 4.2

Chapter 4.2

Noise Source Localization

As demonstrated in Chapter 4.1, the noise levels and performance attributes of Savonius-type rotors are contingent upon rotor segmentation. The findings from these investigations serve as the rationale behind the selection of the single-segment rotor configuration under examination in this section of the thesis. This choice aims to facilitate a more comprehensive examination of the noise generation phenomenon, laying the groundwork for future work.

To address the research gap outlined in Section 1.3.5, a systematic experimental approach involving extensive wind tunnel measurements was adopted. The presented work establishes a correlation between the generated noise and power output across the entire operational range of the single-segment rotor. Subsequently, an extensive analysis of noise source localization utilizing beamforming methods is performed. Given the inadequacy of data in the literature on this subject, these findings offer a valuable foundation for future advancements in the field of mitigation strategies and turbine design improvements for urban environments.

4.2.1 Experimental Setup

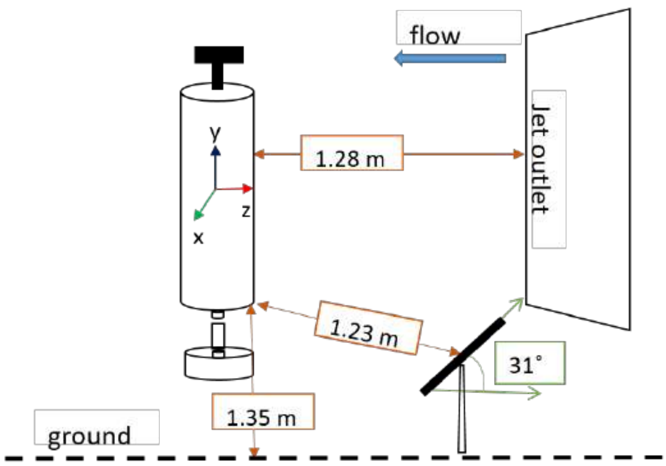

Figure 4.2.1: Experimental setup in the Open Jet Facility, TU Delft.

The aeroacoustic measurements were performed in the Open Jet Facility (OJF) wind tunnel at Delft University of Technology (TU Delft), the Netherlands. This facility is contained inside a large room of 13 m in width and 8 m in height. The flow velocity in the OJF is controlled by a fan powered by a 500 kW electric engine. In the test section, the maximum flow velocity that can be reached is approximately 35 m/s. More details about this test section can be found in [193, 194].

4.2.1.1 Apparatus configuration

The single-segment Savonius rotor described in Section 3.1.2 was employed for the investigation detailed in this chapter.

The positioning of the rotor, along with the coordinate system, is depicted in Fig. 4.2.1. In this study, the coordinate system originates from the center of the rotor. The axes labeled y and z, respectively, represent the axis of rotation of the rotor (spanwise direction) and the streamwise direction (aligned towards the microphone array). The x-axis is perpendicular to the yz plane and parallel to the outlet cross-section of the nozzle.

Placed within the open jet at a distance of 1.28 m from the nozzle outlet plane (refer to Fig. 4.2.1), the SVAWT model had its center (in width) aligned with the jet axis. When observed from the direction of the incoming flow, the SVAWT exhibited clockwise rotational movement, as depicted in Fig. 4.2.2.

The rotor was affixed with bearings using an external small shaft, secured to base discs positioned at the top and bottom, as illustrated in Fig. 4.2.2b. The wind turbine was supported by an additional structure, bolted onto a movable testing table of adjustable height. A torque meter was installed between the two couplings at the bottom, with a sensor placed near the upper coupling to monitor the wind turbine's rotational speed. A 1 kW generator was then connected to the bottom coupling to facilitate the extraction of generated energy. This assembly, including a loading device for controlling the generator's load and converting electrical energy into thermal energy, is depicted in Fig. 4.2.2b.

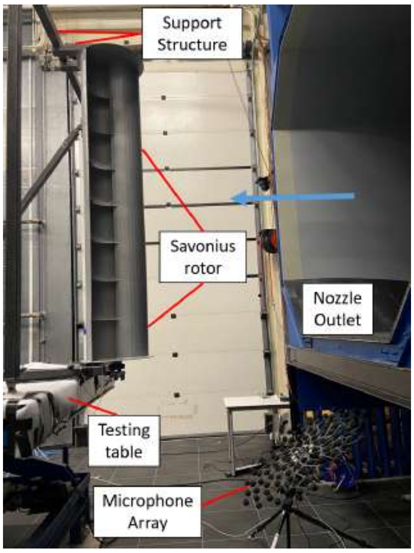

(a) Experimental setup.

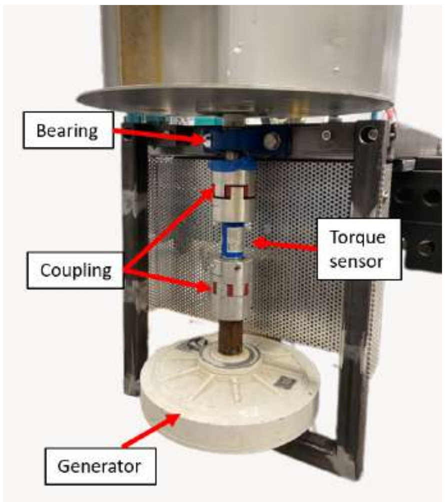

(b) Lower part of the rotor assembly.

Figure 4.2.2: Setup for the experiments performed.

4.2.1.2 Acoustic measurements

Acoustic measurements were conducted using a Bionic M-112 microphone array manufactured by CAE Systems, as depicted in Fig. 4.2.3. This array features a diameter of 1m and comprises 112 MEMS microphones boasting a resolution of 24 bits, a sampling

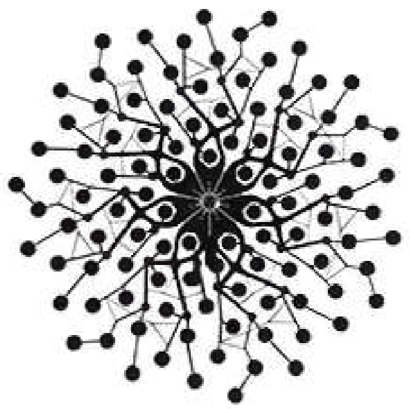

Figure 4.2.3: Microphone array distribution.

rate of 48 kHz, and a frequency range spanning from 10 Hz to 24 kHz. Further specifications of this device can be found in [195]. To prevent undesired flow interactions with the microphones, the array was positioned outside the jet, directly beneath the outlet nozzle, inclined at an angle of 31.1° relative to the floor (refer to Fig. 4.2.1). Data were recorded for each test case over a duration of 30 s. The distance between the rotor axis and the jet outlet was 1.28 m, while the distance between the center of the inclined microphone array and the bottom plate of the SVAWT was 1.23 m.

4.2.1.3 Experimental conditions

Urban environments are typically characterized by low wind speeds in the order of 6 m/s [196]. In the experiments presented in this paper, the variation of the noise emissions with respect to the changing torque (loading) throughout the operational range was investigated. Thus, the study was divided into two parts, consisting of the effect of loading and free run. Wind velocities up to 15 m/s were employed to account for atypical conditions in windy regions, e.g. gusts.

Case 1: Dependence of noise on rotor loading

To study the performance characteristics and relative noise produced, over the operational range with wind velocities of 6 m/s and 8 m/s were considered. For both settings, the wind turbine was subjected to a varying load, establishing the power characteristics. Acoustic microphone-array measurements were also performed simultaneously for every load point, corresponding to a different TSR value. It should be noted that the 'load' corresponds to the torque on the rotor axis, which is linearly dependent on the TSR (refer Section 3.1.1, Fig. 3.1.1a). As discussed in Section 3.1.1, up to TSR < 0.9, the produced power increases with an increase in TSR, hence with increasing speed of rotation. Around TSR $\approx$ 0.9, maximum power is achieved. For TSR > 0.9, the increase of TSR, and hence the speed of rotation, is linked to a significant drop of power, down to $C_p = 0$ at TSR $\approx$ 1.8. These characteristic features may be expected to influence the noise generation mechanisms.

Case 2: Detection of maximum noise emissions - dependence of noise emissions on wind speed

The generator, torque meter, and loading device were detached from the rotor assembly, and the rotor was allowed to run freely without any load, i.e., no power being withdrawn. The wind-velocity range for this case was set between 6 m/s to 15 m/s, corresponding to rotational speeds between 340 RPM and 1020 RPM. Acoustic measurements were also performed for noise source localization. This scenario exemplifies a situation where the electrical system becomes detached from the rotor, either due to an electrical malfunction or adverse operational circumstances within the wind turbine assembly.

4.2.2 Methodology

The performance of the SVAWT throughout its entire operational spectrum was evaluated by monitoring torque, rpm, and power output. Initially, tests were conducted under the conditions outlined in Case 1. The wind tunnel's velocity was adjusted to attain a speed of 6 m/s at the nozzle exit. Data on rotational speed and torque were gathered for varying load conditions. The initial reference point corresponded to the maximum TSR value with no load applied to the rotor. Subsequent increases in load were introduced, with data recorded until the rotor halted rotation at TSR = 0.0, resulting in zero power output (refer to Fig. 3.1.1b) and maximum torque on the rotor axis (refer to Fig. 3.1.1a). This procedure was repeated for each wind velocity scenario.

Following this, adjustments were made to the configuration to align with Case 2, which included the elimination of the generator, coupling, and torque meter. Subsequently, a comparative investigation was carried out across the complete range of velocities under consideration. Additional insights into the examination of acoustic sources are provided in Section 4.2.3.

Beamforming analysis

Conventional acoustic beamforming methods typically assume the presence of point sound sources at each scan point within a designated grid [152, 153, 197]. However, in practical scenarios, noise sources often extend across larger areas, such as along the edges of wind turbine blades [170, 198–200]. In such cases, conventional beamforming methods may lack accuracy in determining the emitted sound levels, particularly when considering peak levels in the source map. To address this limitation, the Source Power Integration (SPI) technique was used [170, 201]. SPI sums and scales the results obtained from an acoustic source map across a specified portion of the scan grid. The objective is to derive a single value representing the source level of the distributed source, thus enabling a more accurate assessment of noise levels from extended noise sources. Information regarding the fundamentals of beamforming has been elaborated on in Section 2.3.2.1.

Each measurement utilized a sampling frequency of 48 kHz and recorded data for 30 s. Acoustic data were averaged in time blocks of 8192 samples (corresponding to 170.67 milliseconds) and windowed using a Hanning weighting function with a 50% data overlap, following Welch's method. With these parameters, the frequency resolution was approximately 5.86 Hz. The frequency range of interest for this study spanned from about 600 Hz to 6 kHz.

For the beamforming analysis, a scan grid covering a region from x = - 1 m to x = 1 m and from y = - 1.5 m to y = 1.5 m was employed, with a spacing between grid points of 0.1 m. The Region of Interest (ROI) considered for the SPI method is depicted as a dashed cyan rectangle with dimensions of width = 1 m and length = 1.75 m, symmetrically placed with respect to the x-axis. This ROI was selected to avoid including the noise source from occurring at the junction between the SVAWT and the testing table due to the flow interaction. The rotor shape is represented by a green solid rectangle as seen in Figs. 4.2.8- 4.2.11.

4.2.3 Results and Discussion

The acoustic analyses reported in the literature by various authors [34, 202] infer that, for a Savonius-type rotor, two noise components are typically identified in the noise spectrum. The former consists of the narrow energy bands seen at low frequencies, typically at the BPF, while the latter represents the harmonic components whose fundamental frequency exceeds that of BPF. Detailed investigations of these High-Frequency Harmonics (HFH) are presented in the following sections to characterize the potential noise sources at various operating conditions.

4.2.3.1 Effect of Loading

In this section, the outcomes for Case 1 are presented. Fig. 4.2.4a illustrates the power coefficient (C_p) values recorded for each TSR, adjusted by varying the load imposed on the rotor. Notably, the maximum TSR value observed at $Cp = 0$ is diminished compared to the reference shown in Fig. 3.1.1b, attributed to differences in the manner of data presentation. While Fig. 3.1.1 portrays pure rotor characteristics, Fig. 4.2.4a illustrates electrical power inclusive of rotor losses. Additionally, the corresponding Overall Sound Pressure Level (OSPL) is plotted as a function of TSR in Fig. 4.2.4b.

A comparison of these plots leads to the observation that OSPL levels remain relatively stable within the TSR range up to approximately 0.8, corresponding to the maximum C_p value, followed by a sharp escalation. In essence, rotor noise is notably high when minimal or no load is applied. Conversely, under conditions of maximal power extraction, noise levels are considerably lower. The plots in Fig. 4.2.4 substantiate that an increase in wind speed alters power characteristics toward a higher maximum power and an increased maximal rotation speed during load alleviation. However, this elevated power output leads to amplified noise across the entire TSR range.

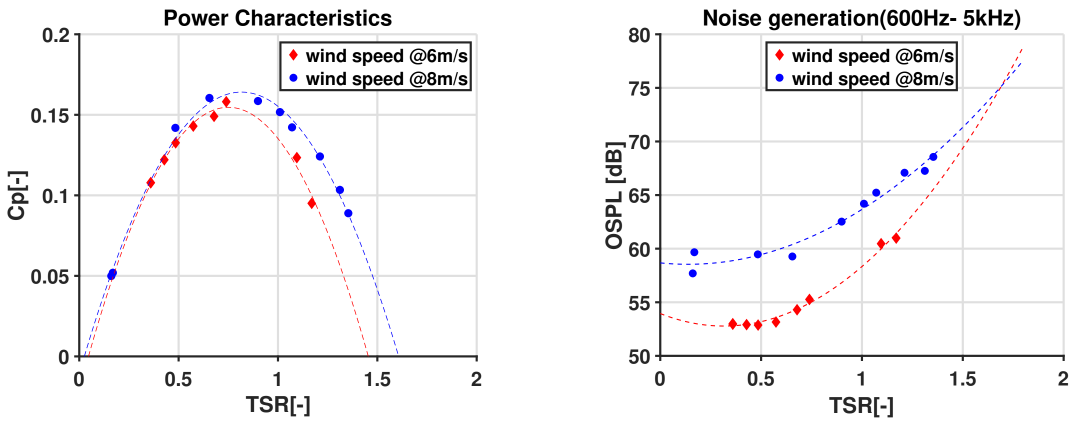

(a) Power Characteristics

(b) Loaded Noise

Figure 4.2.4: Noise and performance characteristics inter-dependency.

4.2.3.2 Dependence on wind speed

As detailed in Section 4.2.1.3, the experiments were carried out for wind speeds between 6 m/s to 15 m/s in increments of 1 m/s. This enabled the assessment of noise levels during high wind gusts or technical failures when the turbine was disconnected from the rotor. Acoustic imaging techniques were applied to localize the dominant noise sources, providing valuable insights for future design enhancements to achieve desired operational conditions.

A similar trend of the power spectrum with an upward shift was observed with increasing wind speeds in all cases under consideration. In order to study the difference in the sound pressure level (Lp) of the extreme cases taken into consideration, a graphical representation has been demonstrated in Fig. 4.2.7a and 4.2.7b. The plots also provide details about the background noise, integrated over the complete sound recorded without the application of the beamforming technique.

The plots indicate that rotor noise is dominating up to about 2 kHz. At higher frequencies, rotor noise is embedded in the background noise. This domination range is increasing with the wind velocity. In general, the sound level is increasing with wind velocity in the whole considered frequency range. It can also be observed that the ratio of rotor noise to background noise is significantly reduced for higher wind velocities.

The broadband noise is caused by the turbulent flow separation due to the interaction of the cylindrical body with the turbulent flow. This interaction leads to a fraction of turbulent energy being transferred to noise, which can be modeled using acoustic dipoles [203].

When the produced eddies are larger than the characteristic length l of the source sound, the acoustic wavelength $l/\lambda << 1$, and the noise source is assumed to be acoustically compact. Then, the noise source is proportional to the sixth power of the flow velocity [204], i.e., $p^2 \propto v^6$. However, for practical cases, the size of eddies is small, i.e., $l/\lambda >> 1$ [132], and the noise source is assumed to be non-compact. The eddies thus produce fluctuating pressure locally, with sound being scattered at the trailing edge. For a non-compact regime, the acoustic intensity can be approximated to a semi-infinite plate as $p^2 \propto v^5$, where the high-frequency noise can be modeled as a cardioid, with maximum radiation direction towards the leading edge [132, 205]. The in-depth research presented in [206] suggests that, at low Mach number, the noise scales to a power of four to five.

Fig. 4.2.5 shows the SPL (x-axis) to the wind velocity in log scale (y-axis). An increasing trend of noise production with the wind velocity is observed. Previous research works justify that, for such measurements recorded in a wind tunnel, the SPL scales to the wind velocity to an approximate order of four [207–209]. For the experimental study presented in this article, a similar trend between the noise and flow velocity has been established, with the scaling factor being approximated as 3.8. A detailed Power Spectral Density (PSD) over the entire range of frequencies is demonstrated in Fig. 4.2.6 in relation to the noise dependency on the power of wind velocity.

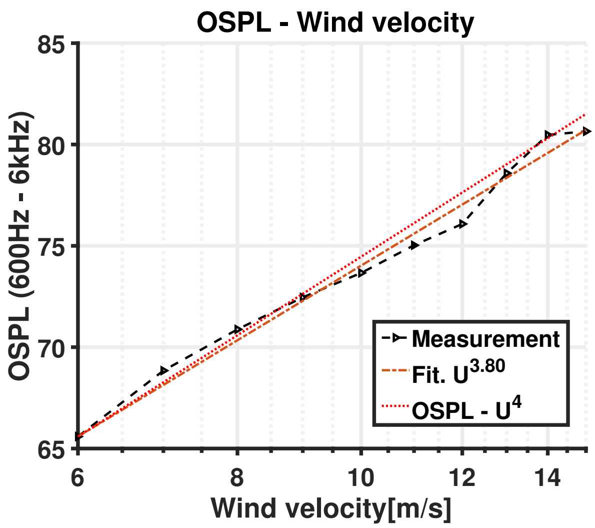

Figure 4.2.5: Aerodynamic noise radiated from a VAWT with increasing wind speed

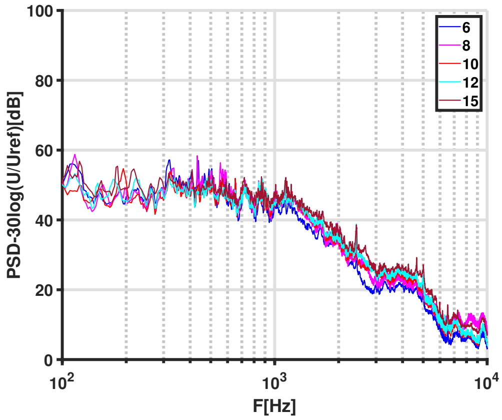

(a)

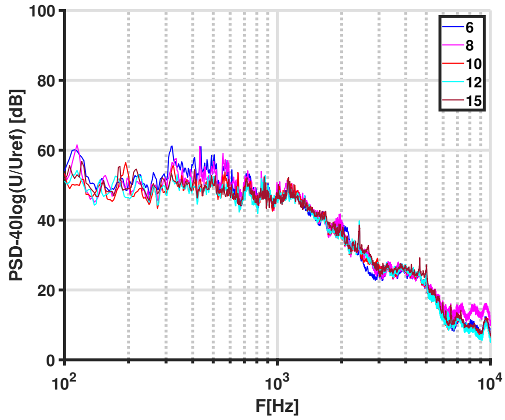

(b)

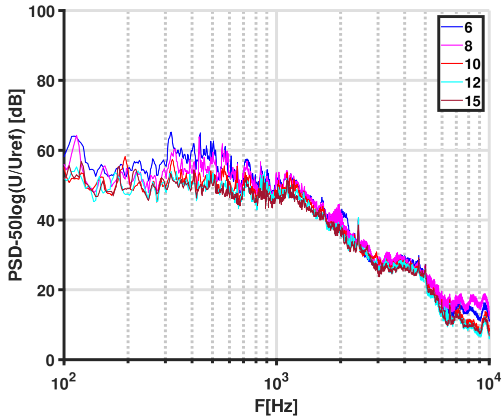

(c)

Figure 4.2.6: Scaling of PSD with different powers of wind velocity (a) wind velocity ^{3} (b) wind velocity ^{4} (c) wind velocity ^{5}.

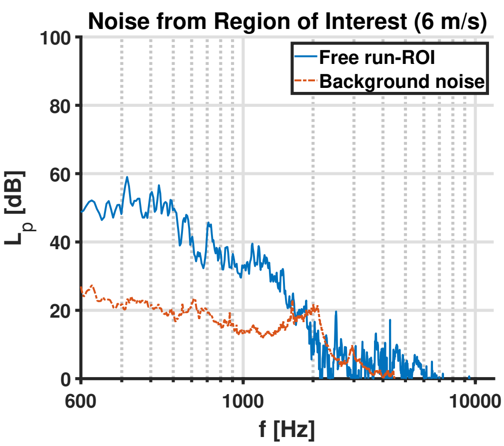

(a) Wind velocity - 6 m/s

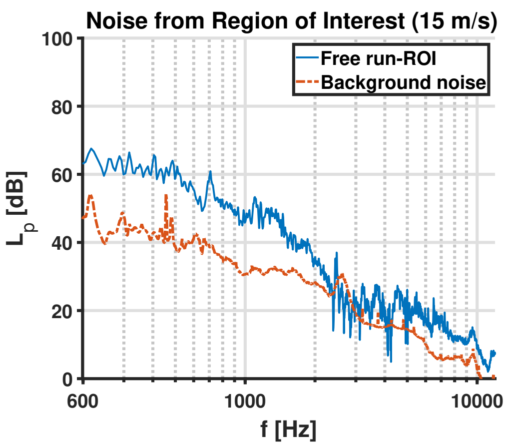

(b) Wind velocity - 15 m/s

Figure 4.2.7: Noise from rotors under no load (free run)

4.2.3.3 Noise-Source Localisation

The noise source maps for some of the cases considered are presented as Figs. 4.2.8-4.2.11. It is observed that the assembly of rotor mounting at the bottom, along with the interaction between the rotor and mounting table are very strong sources of noise, as visible in all source maps. For all three load cases (different TSR), the noise from the rotor mounting with a generator is dominant. This bias is removed by integrating the power spectrum only over the ROI. To present the general trends, the noise source plots have been averaged over the complete measurement time of 30 s and demonstrate the integrated effect of the two blades.

It was also indicated that the noise sources were frequency dependent, as illustrated in Figs. 4.2.9 - 4.2.11. The rotor sound maps were studied for a frequency range from 600 Hz to 6 kHz. However, the noise sources become strongly visible for the presented frequency range of 1.6 kHz to 4 kHz.

The wind turbine under consideration does not have a defined leading or trailing edge. However, theoretically, it is assumed that the retreating side of the blade acts as the trailing edge. For the case presented, this should be in the left half of the ROI (as the turbine was rotating clockwise in the direction of the flow). In the source maps presented in Fig. 4.2.11, one can observe asymmetry with increased noise in the outer part of the left propelling blade and not necessarily the tip. Thus, it can be said that the tip noise is not dominant in such turbines. However, this conclusion is limited to the current configuration, where the beamforming camera is positioned upstream of the rotor. Since no beamforming images were captured from the downstream side, it is challenging to draw definitive conclusions. The location of the noise source on the plots demonstrates that the retreating blade noise is dominant. As the range of dB scale is approximately 9 dB, the noise radiated by this blade is at least x-2 dB higher than the approaching blade.

An attempt has been made to find the noise source by correlating the presented source maps with PSD scaling to different powers of wind velocity. This collapse of PSD for five wind velocities (mentioned in legend in [m/s]) has been presented in Fig. 4.2.6. Some of the key aspects observed are as follows:

- For frequencies below 2000 Hz, the interaction between the blade and the plate becomes increasingly significant, as indicated by the concentrated dark red areas at the top and bottom of the rotor. Disregarding the mechanical noise source at the bottom, the noise source in the upper portion may be attributed to the flow interaction between the blade and the end plate.

- When examining the power spectrum for the frequency range between 600 Hz to 2000 Hz, the scaling exhibits an exponent of wind velocity as approximately 3 or 4.

- Within the frequency range of 600-900 Hz, the SPL demonstrates a more pronounced scaling behaviour with an exponent of wind speed of 3, correlating with rotor noise. While for higher frequencies of approximately 1000-2000 Hz, the overlap demonstrates a scaling with an exponent of 4 in relation to velocity.

- In the high-frequency domain (above 2000 Hz), where blade-generated noise predominates, the SPL exhibits scaling behaviour with exponents of 4 and 5, which are characteristic of aerodynamic noise. It should be noted here that the testing facility was not anechoic, and thus, the reflection may have contaminated the data.

Detailed analyses of the flow field around a Savonius rotor have shown the development of flow structures around the rotor [202]. The interaction between the incoming flow and the rotating blades creates a highly swirling flow, leading to the formation of shedding-vortex structures. The development of these vortices starts near the surface of the turbine blades and is subsequently shed from the tips of the blades (edges), resulting in changes in the pressure distribution both on the turbine's surface and in the surrounding flow. As a consequence, these vortices act as a noise source at high frequencies.

Similarly, these shedding vortices generate high-amplitude noise sources by inducing variations in static pressure on the blade surfaces, acting as dipole sources. This hypothesis is based on the mechanism described in [210], where investigations on the generation of Aeolian tones from a two-dimensional circular cylinder were performed. However, as the microphone array was placed upstream of the rotor for the experiments under consideration, the wake of rotor remained hidden and it was not possible to clearly record this effect.

Asymmetric patterns in the noise source have also been observed in previous studies on HAWTs in field as well as wind tunnel experiments, where it was associated with convective (Doppler) amplification and directivity of trailing edge noise [211, 212]. The impact of convective amplification was illustrated by the turbine's orientation's effect on the acoustic source distribution; when either side of the rotor plane was facing the microphone array, the source region's position shifted upward or downward, respectively. This phenomenon is quantitatively explained by variations in the blade velocity component aligned with the direction of the array. Hence, it was deduced that the irregularity in the origin of the noise depends on the location of the observer, so that if the observer is positioned on the rotor axis, the source pattern would be symmetric [212]. As the turbine under consideration is symmetrical about the central vertical axis, the directivity effect can be explained with regard to the relative angle between the microphone array and the SVAWTs rotational axis.

The change in the flow field also occurs with the change in the turbine's operating conditions. This leads to a change of flow field around the rotor, especially the outer blades and, hence, the vortex being shed, which affects the propagation of acoustic waves as well as the directivity of sources, as seen in Sections 4.2.3.1 and 4.2.3.2.

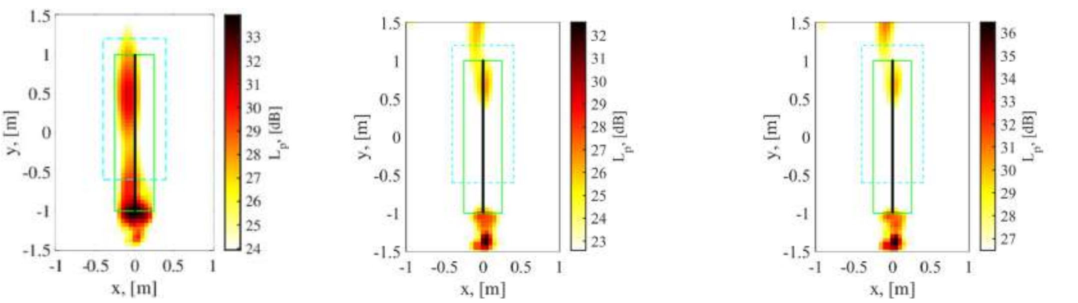

(a) Free run, TSR = 1.8 (b) Minimum TSR, TSR = 0.0 (c) Maximum C_p, TSR = 0.9

Figure 4.2.8: Noise-source localization for wind velocity 8 m/s for different loading conditions at a frequency of 4 kHz.

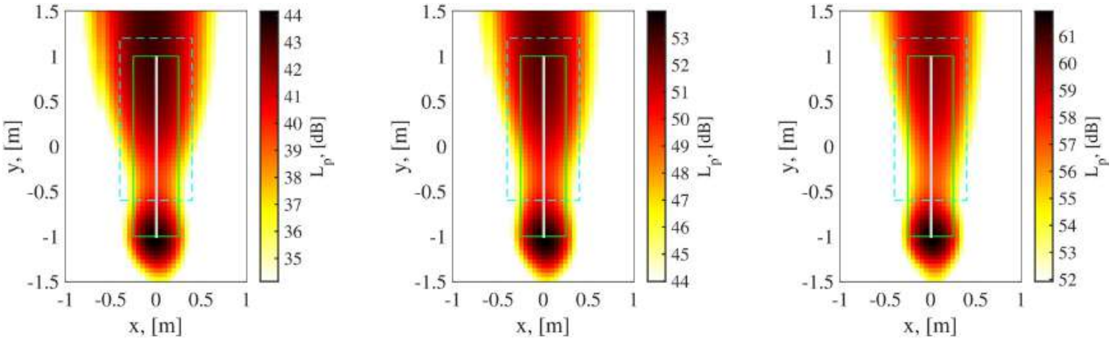

(a) (b) (c)

Figure 4.2.9: Noise-source localization for Frequency 1600 Hz at wind velocity (a)6 m/s, (b)10 m/s, (c)15 m/s (free run).

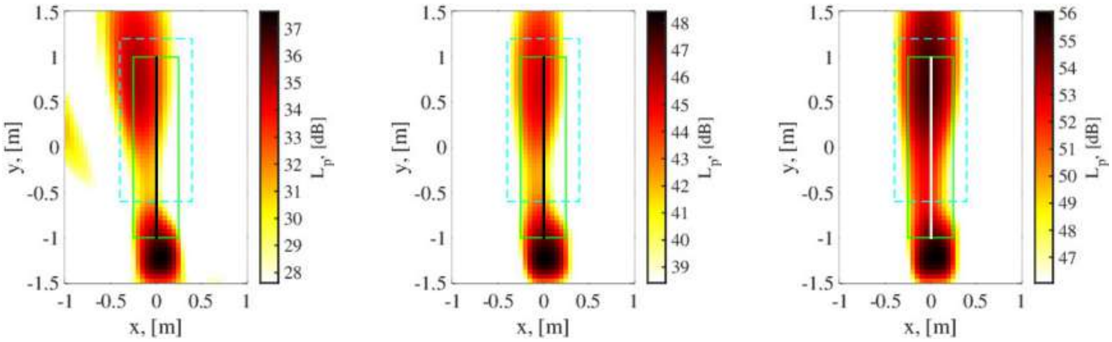

(a) (b) (c)

Figure 4.2.10: Noise-source localization for Frequency 2000 Hz at wind velocity (a)6 m/s, (b)10 m/s, (c)15 m/s (free run).

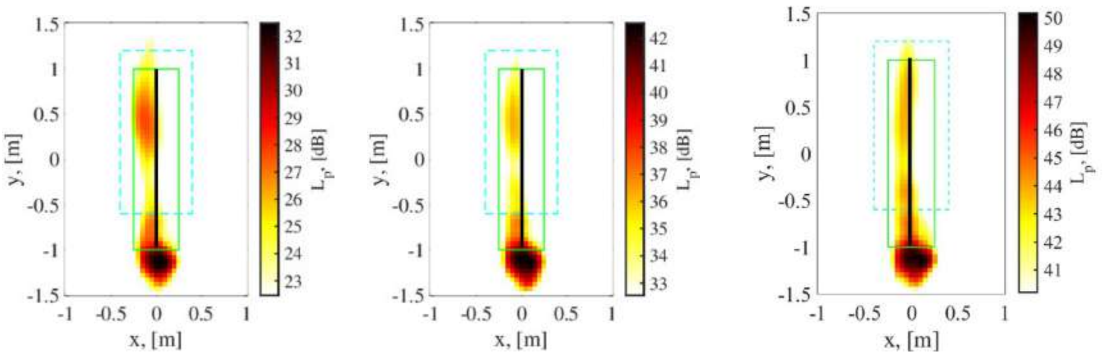

(a) (b) (c)

Figure 4.2.11: Noise-source localization for Frequency 4000 Hz at wind velocity (a)6 m/s, (b)10 m/s, (c)15 m/s (free run).

4.2.4 Conclusion

Through the conducted experiments, valuable insights have been gathered regarding the turbine's performance characteristics and noise emissions across varying operational conditions.

Initially, the study underscored the trade-off between generated noise and power output, highlighting that noise levels reach their minimum when the rotor operates at its peak efficiency point (TSR = 0.9). This observation highlights the importance of optimizing turbine performance to minimize noise emissions. Utilizing the beamforming technique, the primary noise sources were localized, while a power spectrum analysis of rotor noise was conducted over the frequency range of 600 Hz to 6 kHz. These results enhance our understanding of the acoustic phenomena associated with Savonius-type VAWTs.

Furthermore, examination of the turbine's acoustic properties under free-run conditions revealed its sensitivity to increasing wind speeds. Notably, significant noise amplification was observed when the turbine rotated freely at high TSRs. This insight allows for estimation of sound energy production when the generator is disconnected or the turbine is left to rotate freely during strong wind gusts, facilitating the development of noise mitigation strategies (future work). Additionally, a scaling relationship between wind velocity and power (3, 4, or 5) and noise level, contingent upon the noise source and frequency range, was identified and presented in Fig. 4.2.6. Lastly, the study found that, for the specific setup, rotor noise dominates background noise at frequencies up to 2 kHz, beyond which rotor noise becomes integrated within the background noise.

Part 5

ANALYSIS OF URBAN ENVIRONMENT AND WIND TURBINES

Chapter 5.1

Wind Potential Assessment: Urban environment

Comprehending the complexities of wind energy is essential for advancing renewable energy initiatives. This chapter delves into the critical role of wind characteristics in determining turbine selection and placement. Variables such as wind speed, turbulence, surface type, temperature, device height, and air density significantly influence turbine design, optimizing energy output and reducing maintenance costs.

Given the dynamic nature of wind patterns, employing optimal analysis techniques is paramount. Various probability density distributions predict wind behavior, guiding turbine installation in urban areas to maximize wind resource utilization. Precise analysis is crucial to avoid inaccuracies in wind power calculations, power generation estimates, wind load assessments, and the prediction of machinery lifespan.

This chapter evaluates wind energy potential focusing on Przywidz and Gdańsk in Poland, and four UK locations. These sites were selected due to the availability of wind data in Poland and the ongoing collaboration with a UK university within the framework of the ZEPHYR project. After evaluating wind energy potential, suitable regions for turbine installation are identified, and the appropriate turbine type for each region is determined. The flowchart depicted in Fig. 5.1.1 outlines the algorithm used to analyze measured wind data in these locations. Selecting an appropriate probability density function calculation model is crucial, requiring comparison of estimated curves to actual wind speed distribution. If dissimilarities arise, the data is recalculated using alternative equations until results align.

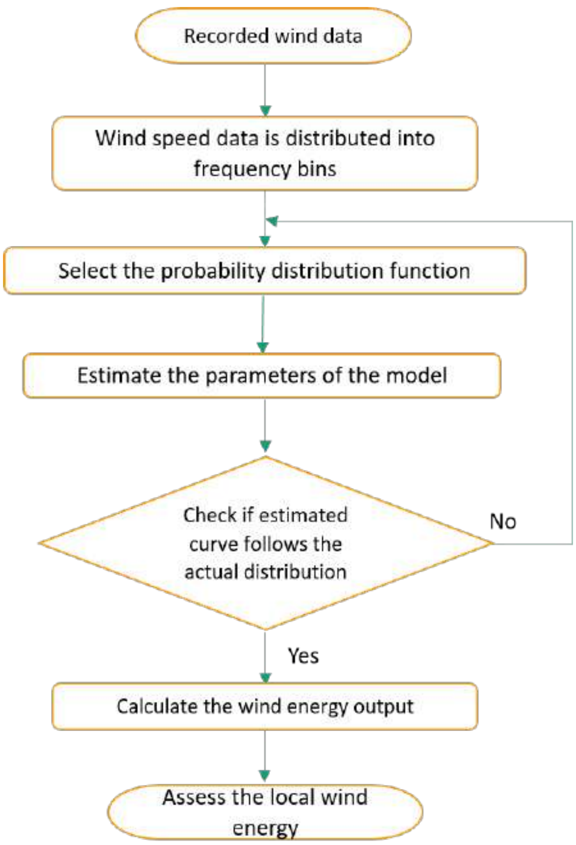

Figure 5.1.1: Algorithm followed for wind analysis

5.1.1 Study of Wind patterns in Nottingham, UK

5.1.1.1 Data Collection and Analysis

For the purpose of this study, the city of Nottingham in the county of Nottinghamshire, East midlands, England was chosen (Fig. 5.1.2). Data was collected from five weather stations positioned at the locations as shown in Fig. 5.1.3:

- Watnall- A village in the borough of Bouxton in Nottinghamshire.
- Bulwell-A market town in the City of Nottingham.
- Chaucer Building- Campus of Nottingham Trent University(NTU) in the main city.
- Clifton campus- The campus of NTU in a suburban village in the city of Nottingham.
- Sutton Bonnington- A village and civil parish lying along the valley of the River Soar in the Borough of Rushcliffe, south-west Nottinghamshire.

5.1.1.2 Type of Wind Turbine

One of the primary objectives following the assessment of optimal wind resources is the selection of an appropriate wind turbine type. Given the urban focus of this study, small VAWTs are particularly suitable due to their compact size, ability to capture wind from any direction, and lower noise levels, making them ideal for residential or small

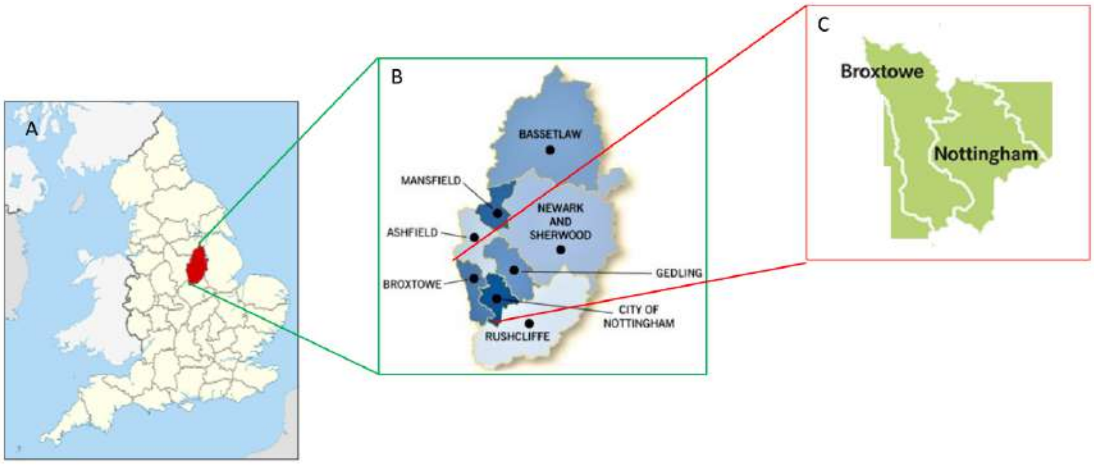

Figure 5.1.2: Area of study: (A) Nottinghamshire in black, (B) Areas in Nottinghamshire, (C) Areas under consideration.

Figure 5.1.3: Locations studied in Nottingham.

commercial use. While Savonius turbines are known for their self-starting capabilities, Darrieus turbines typically offer higher efficiency. A detailed discussion on wind turbine types and their suitability for urban environments is provided in Section 1.3.4.

A selection of commercially available specially designed small wind turbines to operate in urban environments is presented in Table 5.1.1. Power production analysis for each of these turbines for the selected location has been detailed in Section 5.1.3.

Company	Model	Diameter (m)	Tower height (m)	Blade length (m)	Swept area (m^2)	Rated power (kW)	Cut-in speed (m/s)	Type
WEPOWER	Falcon 3.4 kW	3	5.5	3.6	10.8	3.4	2.7	VAWT
WEPOWER	Falcon 5.5 kW	4	5.5	4.6	18.4	5.5	2.7	VAWT
WEPOWER	Falcon 12 kW	6	5.5	6.2	37.2	12	2.7	VAWT
Kliux Energies	Zebra Plus	3.4	6	3.05	10.37	4.9	2.5	VAWT
Interwin	Maia S	3.3	6–12 (folding)	1.65	8.5	1.8	2.8	HAWT
Interwin	Maia M	3.7	6–12 (folding)	1.85	10.8	2.3	2.5	HAWT
Interwin	Maia L	4.7	6–12 (folding)	2.35	17.4	3.3	2.3	HAWT
Quiet Revolution	QR 6	3.1	6–18 (folding)	5.1	15.81	7	1.5	VAWT
Delft University of Technology (TUD)	Turby	1.99	6–7.5 (folding)	3	5.97	3	4	VAWT
Aventa	AV-7 LoWind	12.9	18	6.45	129	6.5	2	HAWT
FinnWind	Tuule 200	5	18	2.5	19.6	—	2–2.5	HAWT

Table 5.1.1: Small industrial wind turbines - suitable for urban environments.

5.1.2 Results and Discussion

5.1.2.1 Mean Wind Speed

The mean wind speeds of the locations under consideration have been shown in Table 5.1.2. The data set includes the mean values of wind measurements done over a period of one year using 10 min averages. The mean wind speeds for two locations, i.e Sutton Bonnington- a village in the countryside and Watnall a village close to the city with a higher number of buildings are shown over a period of three years (2018-2020). One clear observation from the two is that Sutton Bonnington has a higher value of average wind speed. This may be attributed to the fact that this village has relatively lower urbanization, thus fewer buildings.

5.1.2.2 Comparison of different Probability Distribution Methods

Many different probability density estimations have been employed in various studies to statistically characterise the wind energy potential for a given data set. A detailed investigation was also performed in order to find a suitable distribution function under different conditions. Seven different distributions, namely Gamma, Weibull, Rayleigh, Log-normal, Genextreme, Gumbel and Normal were applied to the data in order to find the best probability density function for the wind potential assessment. The parameters for these distributions were calculated using MLE. Analysis was performed for two locations- Watnall and Sutton Bonnington, for three consecutive years (2018-2020). The plots showing the comparison of different distributions for a part of the data recorded over the years 2019 and 2020 are shown in Fig. 5.1.4. R^2 is used as the goodness of fit criterion, and its corresponding value to each of these distribution functions has also been detailed in the plot.

Overall, it was observed that the Rayleigh, Weibull and Gamma methods outperformed the other approaches for the different years and locations under consideration. It should also be noted here that the Rayleigh distribution produced identical results to the Weibull probability density distribution. This can be attributed to the fact that

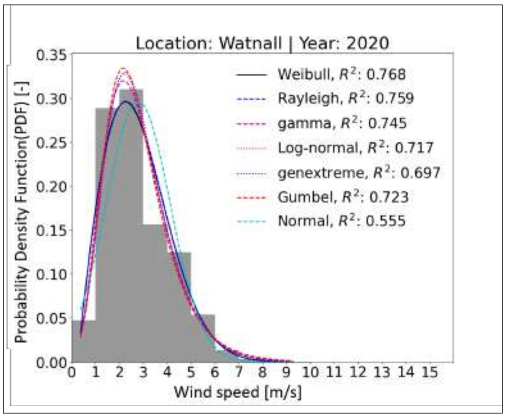

(a) Watnall, 2020

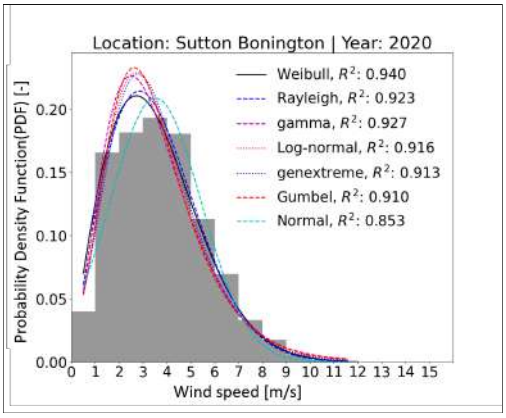

(b) Sutton-Bonnington, 2020

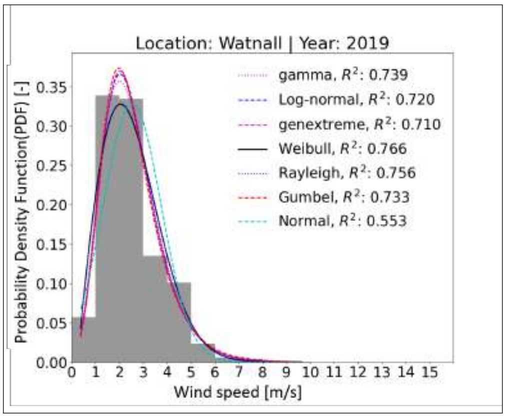

(c) Watnall, 2019

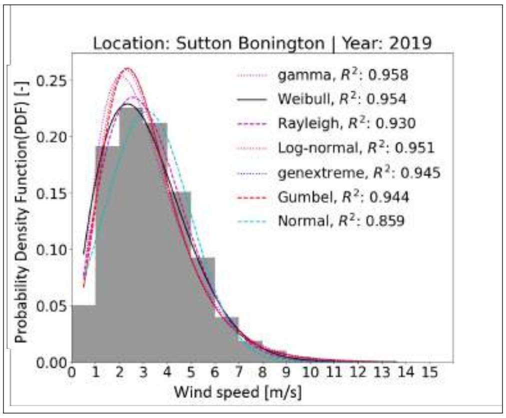

(d) Sutton-Bonnington,2019

Figure 5.1.4: Error analysis of Weibull parameters using different statistical tools for different locations and year 2019-2020.

the Rayleigh probability distribution function is a special case of the Weibull distribution when the shape factor value is '2', as observed for the study presented. The exponential or Gaussian distribution can be defined by changing the value of the shape parameter to k=1 and $k \geq 3$ respectively. The ability of the Weibull distribution to incorporate these specific probability distribution instances, suitability to investigate very high wind speeds [213], and the capability to describe the data asymmetrically about a mean value, ease of analysis make it a preferable choice for wind energy estimation as compared to the other distribution functions discussed in this paper.

Moreover, the Weibull distribution is also more flexible when compared to the gamma distribution. Thus, the Weibull probability density function was finally selected for characterizing the wind energy potential of a given data set. It was further analyzed to study the effect of the method used on predicting the shape and scale parameters of the distribution. A detailed study of the locations considered in the UK has been presented in [214].

5.1.2.3 Weibull Distribution

Different methods used for the estimation of Weibull parameters are compared in Fig. 5.1.5. The data represents the estimates calculated from a single day using 10 min average for the location Clifton campus. The best-fitting curve is given by STDM in this case. Since the sample considered for this plot is only for one day at a particular location, this result can not be generalized and requires further detailed investigation.

Thus, this plot illustrates why it is important to find the best-fitting curve in each of the cases under consideration for wind analysis.

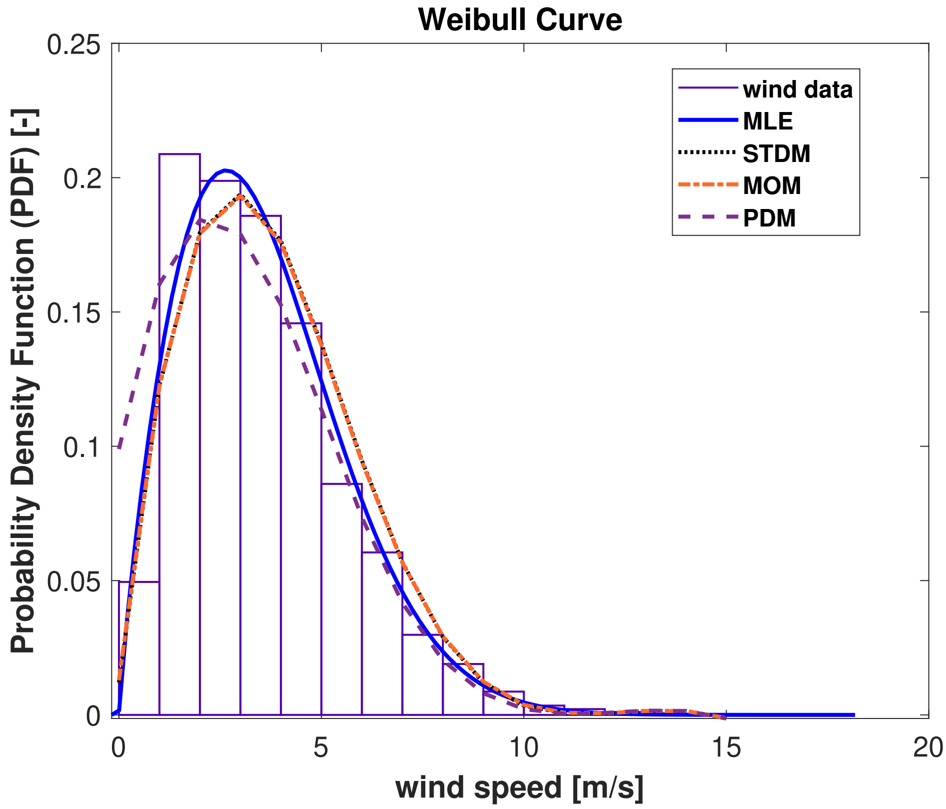

Figure 5.1.5: Weibull distribution estimation using different methods for calculating the parameters.

Table 5.1.2 presents Weibull parameters estimated using four methods-STDM, MOM, PDM, and MLE across various Nottingham locations over a one-year period (June 2020–2021). A goodness-of-fit analysis, as detailed in Section 2.1.1.5, was performed to evaluate the accuracy of each method. The preferred method for each location is highlighted in the table. Consistent with the existing literature, the results indicate that no single method universally provides the most accurate predictions across all sites, highlighting the need for the selection of site-specific methods.

Following the Weibull distribution analysis for different locations during the same year, another study considering wind data collected from suburban locations consisting of different populations and architectural buildings was performed. The k and c observed over the four years under consideration indicate that the shape factor is almost constant with a maximum variation of 4% in the case of Sutton-Bonnington and 1.3% in the case of Watnall. Over a three-year period, both Clifton Campus and Sutton Bonington exhibited similar wind distribution patterns, as indicated by consistent Weibull shape parameters. Notably, in 2019, both locations experienced a decrease in the scale parameter, reflecting a shared trend in wind speed variations.

The higher mean wind speed observed at Clifton Campus can be attributed to its denser building layout. Closely spaced buildings, with gaps smaller than their heights, can channel wind flows, leading to increased wind velocities and enhanced wind energy potential.

The Weibull probability distributions for 2018–2020, calculated using the maximum likelihood estimation, reveal distinct wind patterns at Sutton Bonington and Watnall.

Site	$\overline{v}(m/s)$	σ	**Parameters**	**STDM**	**MOM**	**PDM**	**MLE**	**Preferred method**
Clifton Campus	3.76	2.13	k	2.16	2.14	2.09	2.17	MLE
			c	3.95	3.95	3.94	3.96	
Bulwell	4.76	2.49	k	2.01	2.02	1.98	2.02	MLE
			c	5.37	5.37	5.37	5.38	
Chaucer	1.33	2.13	k	1.68	1.67	1.47	1.73	PDM
			c	1.49	1.49	1.47	1.51	
Watnall	2.63	1.06	k	2.42	2.21	3.41	2.24	PDM
			c	2.97	2.97	2.93	2.98	
Sutton Bon-nington	3.27	1.80	k	1.91	1.90	2.10	1.85	PDM
			c	3.68	3.68	3.69	3.57	

Table 5.1.2: Weibull parameters calculated using different formulas.

Sutton Bonington, characterized by open fields and sparse development, exhibits a broader wind speed distribution, indicative of greater variability and frequent low-speed winds. In contrast, Watnall, with its more developed and architecturally complex environment, shows a narrower distribution, suggesting more consistent wind speeds. These differences underscore the significant influence of local geography and built environments on wind behavior, highlighting the necessity for site-specific assessments in wind energy planning.

5.1.2.4 Wind Power Density and Energy

The energy density for the locations under consideration, over a period of one year, is as observed in Table 5.1.3. It is observed that Clifton campus gave the highest value of energy density, found by using the Maximum likelihood estimation and the least results were given by the Chaucer building using the power density method. This is directly related to the low wind speed recorded at this location. MLE nad PDM were found to be suitable for predicting the Weibull distribution parameters for the different locations under consideration.

While the values corresponding to the suburban and the village locations for the years 2018-2020 are as shown in Table 5.1.4. It should be noted that the location of Bulwell was excluded from further analysis due to contradictions with local laws. MLE was found suitable for four out of six cases as described in the table, while STDM proved to be the most useful method for only two cases. Sutton- Bonnington can be concluded as a good option when considering the wind energy availability over the three years under consideration. It can be inferred that MLE is the preferred method for most of the cases under consideration.

Site	$\overline{v}(m/s)$	Method	Energy Density(kWh/m^2/year)
Clifton Campus	3.76	MLE	418
Sutton Bonnington	3.27	MLE	354
Watnall	2.63	PDM	128
Chaucer Building	1.33	PDM	36

Table 5.1.3: Energy density production comparison of different locations in Nottingham

Site	Year	Method	Power Density (W/m^2)	Energy Density (kWh/m^2/year)
Watnall	2018	MLE	20.68	181.14
	2019	STDM	17.27	151.28
	2020	MLE	23.16	204.47
Sutton Bonnington	2018	STDM	47.80	418.76
	2019	MLE	40.45	354.31
	2020	MLE	53.47	468.37

Table 5.1.4: Power production comparison over three years.

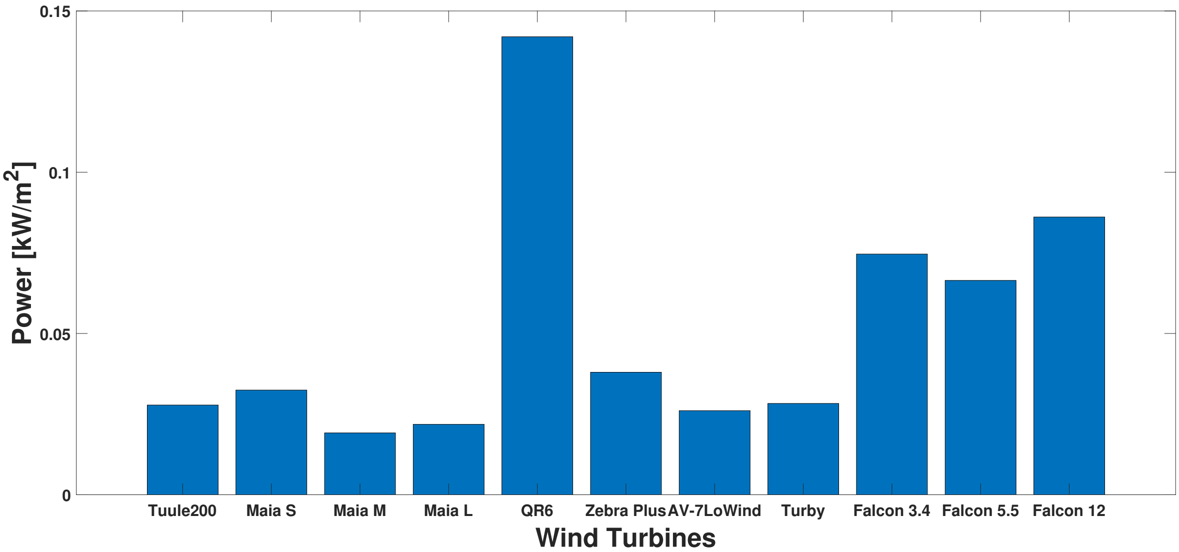

Figure 5.1.6: Variation of electrical power for various commercially available wind turbines suitable for installation in an urban environment.

5.1.3 Wind Turbine Selection

The next step of the study was to compare commercially available small wind turbines for installation in the optimal locations obtained. Results obtained in Table 5.1.3 suggest that the Clifton campus and Sutton-Bonnington are the most suitable locations. As the average wind speed at both locations is $\approx$ 3.5 m/s, the wind turbines with a minimum cut-in speed of 3 m/s were selected for maximum conversion of wind energy (see Table 5.1.1). However, due to Governmental regulations and permissions from the local authorities, the Clifton campus was selected as the final place for WT installation. In addition, installation of the turbine on the university campus offers a valuable opportunity for practical research in various fields, including medicine, engineering, and social sciences, and will promote the use of sustainable energy practices while inspiring and motivating students to participate actively in this emerging field. The results of this study may be leveraged to implement wind turbines at various locations on the campus, further promoting the utilization of green energy in everyday activities.

Fig. 5.1.6 shows the average electrical power produced (kW/m^2) for the duration of available wind data. The top-performing wind turbines in the order of power produced are QR6, Falcon- 12 kW and Falcon 3.4 kW. In addition to the highest wind power produced per unit area, QR6 is also characterised with lower cut in speed as compared to the other two turbines.

Therefore, QR6 wind turbine was selected for the current study, and a collaboration was established with the company *Quiet Revolution* to evaluate the performance of their commercial VAWT model [215]. This particular model possesses a compact and easy integration design, incorporating an aesthetically pleasing swept blade (helical shape) configuration with a unique blade tip designed to minimize noise. Additionally, the blade structure exhibits excellent aero-elastic characteristics, enabling it to harness turbulent wind conditions and mitigate vibration. The QR6 model commences operation at wind speeds as low as 1.5 m/s and includes safety cutoff features for wind speeds exceeding 20 m/s. The turbine comprises power regulation mechanisms that initiate an automatic shutdown in the event of an emergency and is designed for a life expectancy of over 30 years. The device is also equipped with an industrial programmable logic controller and is configurable to conform to grid codes in different regions worldwide. These attributes make the QR6 model a highly attractive option for installation at the designated site.

Conclusion of wind pattern study in UK.

This study assessed wind energy potential across four urban and semi-urban sites using seven PDFs: Weibull, Gamma, Rayleigh, Log-normal, Genextreme, Gumbel, and Normal. Weibull emerged as the most accurate model based on goodness-of-fit metrics. Parameter estimation via PDM and MLE yielded the best results. Sites with higher avg wind speeds and lower k values demonstrated greater wind energy potential. Clifton Campus exhibited the highest wind energy production. Given urban constraints, small VAWTs, particularly Darrieus-type, are recommended due to their high efficiency, compactness, and low noise. A decision was thus made to install a Darrieus-type vertical axis wind turbine (QR6) at the Clifton campus of Nottingham Trent University, with plans for experimental validation of predictions made through probability density estimations.

Annual variations in Weibull parameters were within a 4% error margin, indicating model reliability. While high wind energy potential is crucial, factors like noise, turbine size, public perception, and regulations must be considered. Overall, the study supports small-scale wind energy installations in urban settings, with Clifton Campus identified as a suitable site for a Darrieus-type VAWT. As the wind energy sector continues to expand, these findings provide critical insights into how wind speed data can be evaluated and leveraged to facilitate the advancement of economically viable and environmentally sustainable wind energy initiatives, particularly in urban settings where wind resources are available.

5.1.4 Study of wind patterns in Poland: Gdansk, Przywidz

5.1.4.1 Study of wind patterns at the top of a building- Gdansk

The study presented in this section of the chapter illustrates the wind patterns at wind turbine mounted at the top of the building of IMP-PAN is subjected to. This area has a high density of buildings surrounding the test location, thus, the flow is expected to be quite complex. This study was used as the basis for further wind turbine testing in real wind conditions and its comparison to the literature available from other authors.

Based on the results presented in the previous section, it is clear that the Weibull probability density function gives the most accurate results when checked against other methods discussed before. Thus, this method was selected for further analysis. A similar methodology of using different models to calculate Weibull parameters was used, followed by its ranking. Thus, The wind conditions in our test case were investigated with the above background.

The wind patterns appear to be highly irregular, particularly within urban areas. A typical example of sampling every second for 1000 samples is shown in Fig.5.1.7. It is evident that a time span of 1000 sec is very short, extending the recording time would compromise the clarity and readability of the plot.

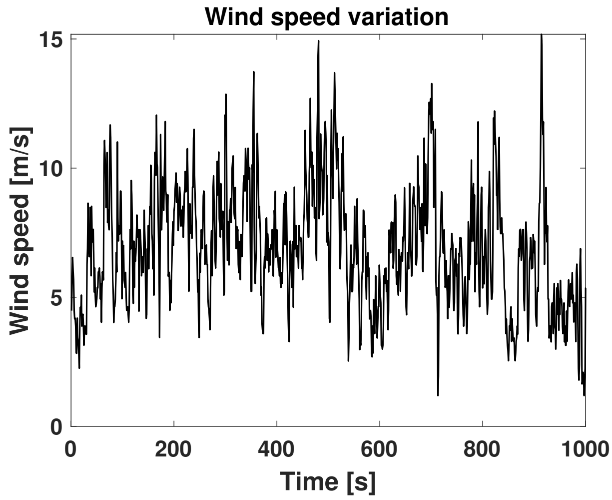

Figure 5.1.7: Wind velocity fluctuations in time

For the dataset depicted in Fig. 5.1.7, the average velocity stands at v_{av} = 6.26 m/s, with a standard deviation of SD = 2.175 m/s. This indicates a 35% fluctuation in wind speed, signifying the presence of low-velocity winds with considerable unsteadiness. Unfortunately, such challenging wind conditions are characteristic of urban environments' wind behavior.

Analysis of wind characteristics during tests

For the purpose of data analysis, different k and c values were evaluated and compared using the Root Mean Squared Error (RMSE), the Mean Absolute Percentage Error (MAPE), the analysis of variance or efficiency of the method (R^2), and the chi-square error (χ^2) values as shown in Table 5.1.5. The data set contains a one-day measurement which consisted of 65,536 sample points and was taken within a period of 18.2 hours. This data set concerned a relatively small wind flow case.

Table 5.1.5 presents the Weibull parameters computed using various methods. It is evident that the outcomes exhibit negligible discrepancies. Hence, statistical techniques are employed to determine the optimal method. Based on the calculated statistical errors, the MOM yields the most favorable results, followed by the STDM and MLE. In Fig. 5.1.5, the Weibull curve is depicted based on MOM, with all three curves overlapping.

For the specific day under consideration, the wind characteristics are described as follows:

- Shape factor 'k' – 2.44
- Scale factor 'c' – 5.48
- Average wind speed – 5.04 m/s

These wind conditions indicate low wind speeds at the location of the wind turbine tests. At such velocities, lift-driven turbines - HAWT and VAWT of the Darrieus type just start to operate.

Test Day	Shape factor	Scale factor	R^2	RMSE	χ^2	MAPE (%)
STDM	2.445	5.4837	0.955	0.0144	0.0195	0.93
MOM	2.446	5.484	0.956	0.0143	0.0191	0.92
MLE	2.429	5.488	0.953	0.0146	0.0200	0.93

Table 5.1.5: Weibull parameters and error analysis.

Turbulence intensity

Taking all the data over the 18 hours of testing period into consideration, the turbulence intensity has been determined. Typically, the turbulence intensity of wind [$TI = \frac{\sigma}{v_{av}}$] is determined from the 10-minute averaged values, which are presented in Fig. 5.1.8a. However, for the short test period analyzed in this paper, this approach is providing too few data points, and the scope of wind velocities is reduced. Therefore, Fig. 5.1.8b shows the turbulence intensity using 1-minute average values. One can observe that the mean values of wind velocity and TI are similar for these two approaches.

The values of TI correspond well to the values in article [216] for cases of wind blowing from land with a high turbulence level. This is not surprising as our wind turbine is installed on the IMP PAN building, surrounded by a heterogeneous terrain of complex structures, trees, open fields, and other buildings. The urban environment is connected with a high turbulence level of wind. Typically, the value of TI reduces with the wind velocity, as shown in Fig. 5.1.8b. One can conclude, therefore, that the location of the presented innovative wind turbine corresponds to a typical urban environment with high wind turbulence.

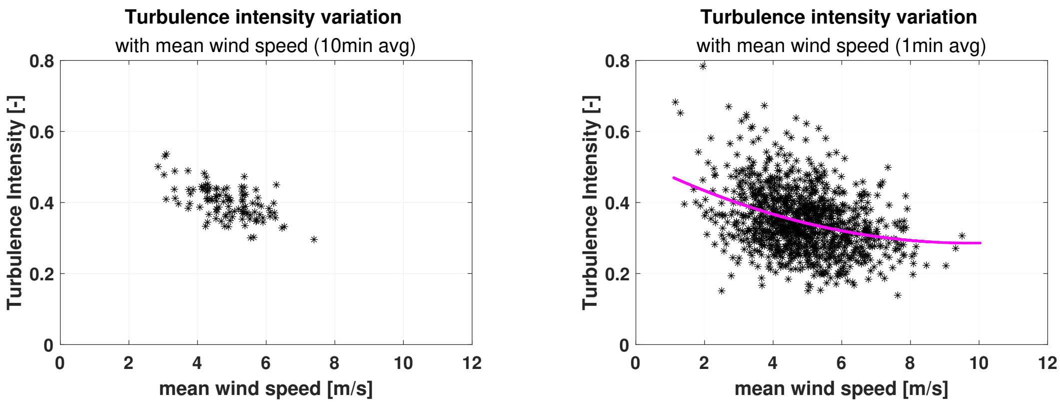

(a) 10 mins averaged (b) 1 min averaged

Figure 5.1.8: Variation of turbulence intensity

5.1.4.2 Study of wind patterns at the top of a hill- Przywidz

The study presented in this section details the wind patterns studied at the top of a hill in Przywidz. The purpose of this analysis was to understand the complexity of wind patterns in harsh winter climates, in a busy location with mountains, barren lands, and forests for later installation of a wind turbine to be tested under real weather conditions. For this purpose, two anemometers mounted at a height of 16 m (top) and 6.5 m (bottom) from the ground were used.

Similar to the previous section, a data set of 1000 samples was chosen to depict (Fig. 5.1.9) the wind speed variation recorded from both the top and bottom anemometers. The average velocity for these samples was recorded to be 5.95 m/s and 5.02 m/s from the top and bottom anemometers, respectively, with a relative difference of 18.5%. The overall average velocity for the system was found to be 5.5 m/s.

As anticipated, the wind speed recorded is low when the anemometer is situated close to the ground, as it is susceptible to wind reflections caused by surface roughness, as previously discussed in Section 1.3.1. Whereas the upper anemometer registers higher wind speeds, benefiting from being relatively unaffected from the urban ABL, as elaborated in Section 1.3.1.

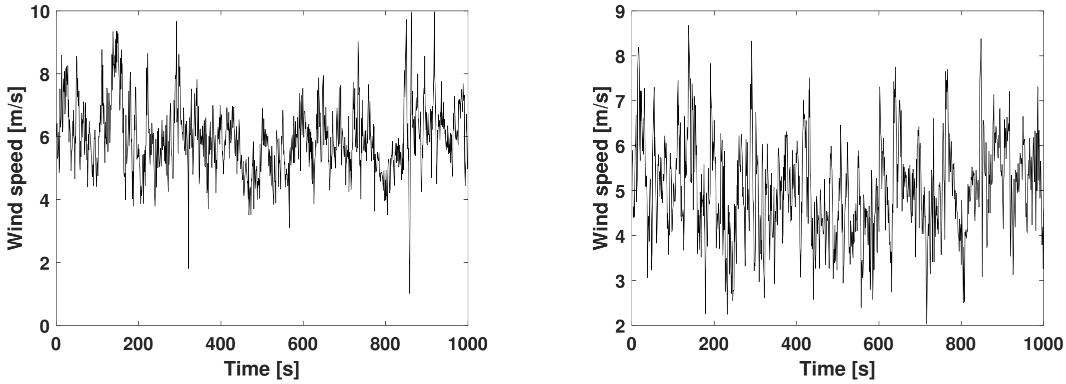

(a) Top anemometer (b) Bottom anemometer

Figure 5.1.9: A random sample of 1000 points showinf the wind speed variation at the top and bottom anemometer with time.

Analysis of wind characteristics during tests

Next, the weibull plots similar to the previous locations were plotted to study the wind potential and pattern. The data set for the results presented in this section include measurements made throughout a single day, with a total of about 65000 points. The shape and scale factor values obtained has been detailed in Table 5.1.6. As expected, 'c' is higher for the top anemometer. The value of 'k' is higher for this case, indicating that not only does the top anemometer record higher velocities, but also it is subjected to higher range of velocities. This is also visible in the weibull plots (Fig. 5.1.10).

[HTML]FFFFFF	[HTML]FFFFFF**Scale Factor**	[HTML]FFFFFF**Shape Factor**	[H
[HTML]FFFFFF***Top Anemometer***	[HTML]FFFFFF5.71	[HTML]FFFFFF4.14	[H
[HTML]FFFFFF***Bottom Anemometer***	[HTML]FFFFFF4.27	[HTML]FFFFFF3.44	[H

Table 5.1.6: Weibull parameters for the two anemometers in przywidz.

These findings imply that even though the recorded wind speed is not very high, the designated site is favorable for the installation of a drag-based wind turbine, which is ideal for such wind turbines, as explained in section. Moreover, the location is centrally located at the top of a hill, which will allow the WT to make full use of its omnidirectional property. Later, a twin-rotor wind turbine was installed at this location to analyze its efficiency in real field conditions. This has been detailed in Chapter 5.2.2.

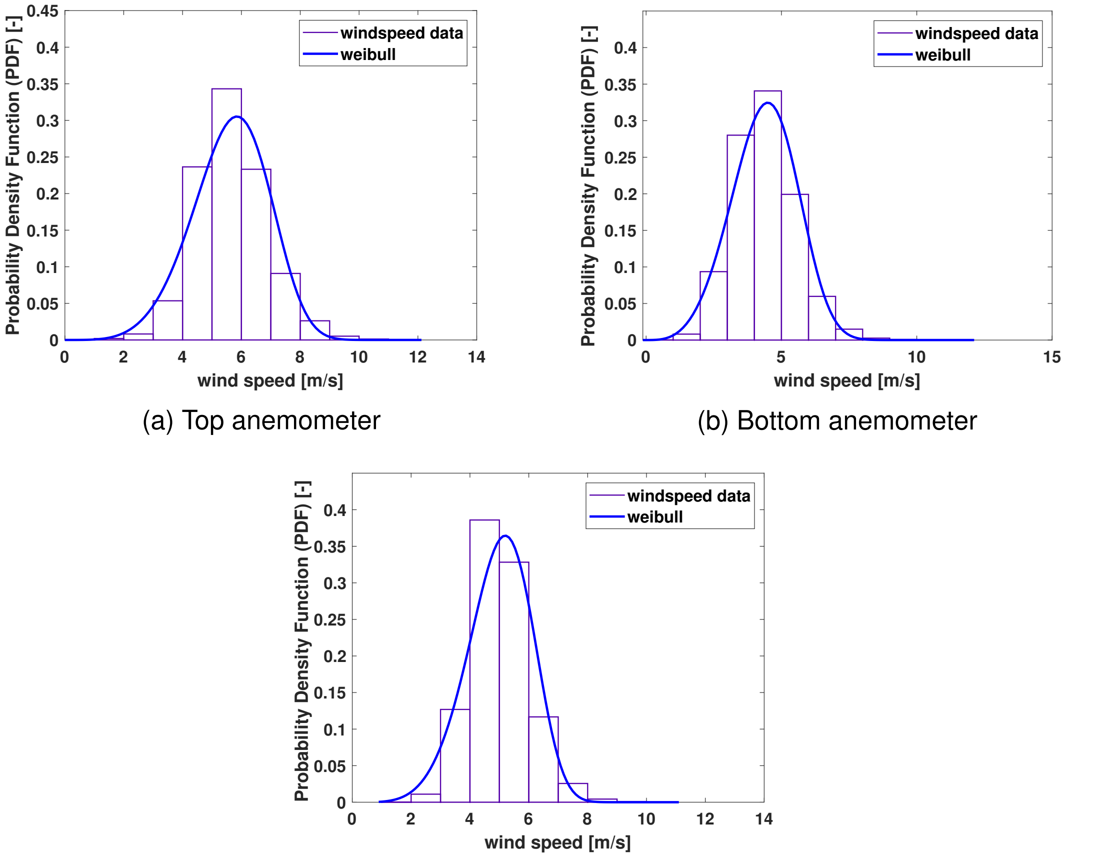

(a) Top anemometer

(b) Bottom anemometer

(c) Average anemometer

Figure 5.1.10: Weibull analysis for the two anemometers mounted at a height of 16 m (top) and 6.5 m (bottom) from the ground.

5.1.5 Conclusion: Comparative analysis of wind energy potential

This study has conducted a comprehensive assessment of wind energy potential and wind turbine siting strategies in two distinct geographical and urban contexts: four selected locations in Nottingham in the United Kingdom and selected sites in Poland. Despite differences in urban structure, topography, and wind regimes, both case studies adopted a unified methodological framework based on probabilistic modeling and statistical analysis of wind speed data. For the locations under consideration, the Weibull probability density function has consistently emerged as the most suitable model to accurately characterize wind speed distributions. Its robustness across diverse site conditions reaffirms its value as a standard tool in wind energy assessments.

The estimation of Weibull parameters k and c is a crucial step in wind energy assessment, as these parameters define the probability distribution of wind speeds and therefore strongly influence the predicted energy yield. Several estimation methods are available, as discussed above. Since each method is based on different statistical assumptions and emphasizes different properties of the dataset, they often lead to slightly different parameter values when applied to the same wind speed data. This variation does not mean that any method is unreliable; rather, it reflects the fact that real wind speed data rarely follow an exact Weibull distribution. The appropriate choice of method depends on data availability, sample size, and the objectives of the study. In practice, the best method is the one that provides the closest agreement between the modeled distribution and the observed wind speed frequencies at a given site.

The power density method and maximum likelihood estimate were identified as the most effective techniques for parameter estimation in the Nottingham study, and similar model-based parameter optimization was applied in the Polish context.

In Nottingham, four representative locations were analyzed, which included rural, semi-urban and urban environments. Results highlighted the Clifton campus of Nottingham Trent University as the most promising site, where a Darrieus-type VAWT was selected for pilot installation. The analysis demonstrated that while large-scale wind energy generation is constrained by site-specific limitations—including noise concerns, spatial restrictions, and regulatory frameworks—small-scale wind energy systems are viable and can be optimized for urban integration.

The Polish case study focused on elevated urban and semi-rural sites, specifically the IMP PAN campus roof and hilltop in Przywidz. Despite lower average wind speeds (approximately 5–6 m/s), these locations were found to be suitable for small VAWT installations due to their exposure and localized wind conditions. The study further emphasized the impact of wind turbulence and variability, particularly in urban environments, highlighting the need for context-specific turbine design and placement.

Across both regions, the following common conclusions can be drawn:

- The Weibull distribution is a reliable and adaptable tool for modeling wind speed in both urban and semi-urban settings.
- Small-scale wind energy systems, particularly VAWTs, are appropriate solutions in areas with moderate wind resources, especially where space and aesthetic considerations are critical.
- Urban turbulence and wind fluctuations significantly affect turbine performance and must be accounted for in the siting process.
- Field validation is essential to substantiate statistical predictions and improve the reliability of performance assessments.
- Non-technical factors—such as public perception, policy constraints, and environmental impact—are equally important in determining the feasibility of wind energy projects.

In conclusion, the comparative analysis demonstrates that while the wind energy potential varies across Nottingham and Poland, a shared methodological approach grounded in statistical modeling and localized analysis enables the identification of feasible, small-scale wind energy solutions in both contexts. These findings contribute to the growing body of knowledge on urban wind energy integration and offer a practical framework for future research and implementation in similar environments.

Chapter 5.2

Experimental Analysis of an Innovative Twin-Rotor Savonius Type Wind Turbine.

A key objective of this research was to evaluate the performance of the novel wind turbine in a real environment, considering the varying wind conditions. The wind characteristics during the test period were analyzed using Weibull distributions, enabling a comparison with wind turbine tests conducted by other researchers. The recorded wind speed was relatively low, around 5 m/s, and highly turbulent, which poses challenges for most wind turbines but is typical in urban settings. The turbine was installed on the roof of the IMP-PAN building.

In addition to wind conditions, the study aimed to estimate the power characteristics of the new wind turbine design. Measurements included the output of the generator, consisting of voltage and current, which facilitated the determination of the power extracted from the generator. The rotational speed of both rotors was also monitored, allowing an assessment of the power extraction algorithm's performance, which ideally operates at a TSR of approximately 1.0. The results indicated room for improvement in the power extraction algorithm. The chapter also highlights additional enhancements made to the wind turbine studied.

Furthermore, the impact of wind fluctuations on rotor behavior was analyzed, and the correlation between rotor response delay and wind gusts was determined. The discussion includes the reduction of wind velocity peaks' effects on energy production. This investigation extends to applying identical analytical procedures to a twin-rotor power plant situated atop a skiing hill.

5.2.1 Installation in Building

The twin-rotor under consideration has been designed to operate in an urban environment, where the safety of the residing population is very crucial. This rotor is also equipped with an electrical braking system to avoid any damage in the case of very high-speed winds, enabling the rotor to move freely.

This innovative prototype has been mounted on the roof of the research centre, and its configuration, together with measurement data is discussed in detail in the following sections. The illustration of its location is presented in Fig. 5.2.1, where building around the wind turbine location are in view on the city side. The objective of the presented study is to demonstrate the results of this turbine's operation performance in natural wind conditions.

Figure 5.2.1: Innovative WT prototype on the roof of IMP PAN building

This chapter explores an innovative approach to enhancing wind energy capture in urban settings through the use of guiding plates (metal sheets) positioned adjacent to the rotor. These plates direct airflow toward the rotor, thereby increasing the system's efficiency. However, this modification can impact the omnidirectional capability of traditional Savonius rotors.

To address this, a novel design that replaces the conventional single large rotor (Fig. 5.2.2a) with a configuration comprising two smaller rotors (Fig. 5.2.2b) mounted on either side of a central guiding plate, the length of which is 1.5 times the rotor diameter (D) [7]. This twin-rotor setup maintains the same projected area as the single-rotor design, facilitating direct performance comparisons.

The guiding plate, between the small rotors, stops the incoming wind. It causes the build-up of dynamic pressure from the wind on the upwind side of the turbine. This increased pressure causes the wind to accelerate over the guiding plate tips, where the air is reaching a higher velocity than the incoming wind speed. In this particular place, small rotors are implemented. Due to increased wind speed around the small rotors, the power production by these two rotors is equivalent to the power produced by the large Savonius rotor.

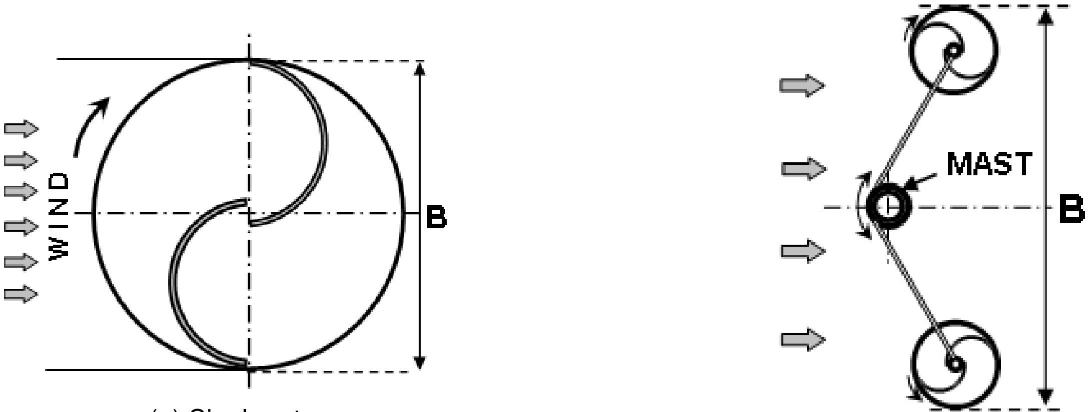

(a) Single rotor

(b) Innovative configuration

Figure 5.2.2: Savonius rotor and innovative twin rotor turbine **??**

As part of the preliminary research conducted before initiating this thesis, a significant challenge identified was the influence of rotor configuration on overall efficiency. The initial solution was characterized by the capability to change the angle between the two guiding plates between 15° - 70° , with an apex about a mast. The twin rotors consisted of 3 × 4 segment rotors, stacked vertically. A prototype was finally manufactured with the diameter of each segmented rotor as 0.25, 3m height and a width of 1.2 m in the open configuration (see Fig. 5.2.3. The idea behind the use of segmented rotors was to use them as a replacement for helical rotors to dampen the oscillatory behavior of the torque coefficient caused by this drag-type turbine [33]. Using a number of rotors in one line allows for obtaining similar effect on rotor torque variation as segmentation, by making angular off-set between one segment. In addition, the segmented design reduces the vibration of the rotor, leading to a more stable and durable structure. The segmented design provides better start-up performance as the segments can independently capture wind from different directions.

The prototype as discussed in [7] was redesigned to replace the bottom four-segment rotor with a single-stage rotor (Fig. 5.2.4) based on the experiments performed at IMP-PAN on rotor segmentation [33].

The cost of manufacturing and operation is another concern to be taken into account whilst designing a wind turbine. The innovative design, as seen in Fig. 5.2.2b details that when the setup is at an opening angle = 70°, reducing the rotor size up to 1/5 times of the traditional Savonius rotor. This leads to a huge reduction in cost, even though 2 rotors and a guiding plate combination are used.

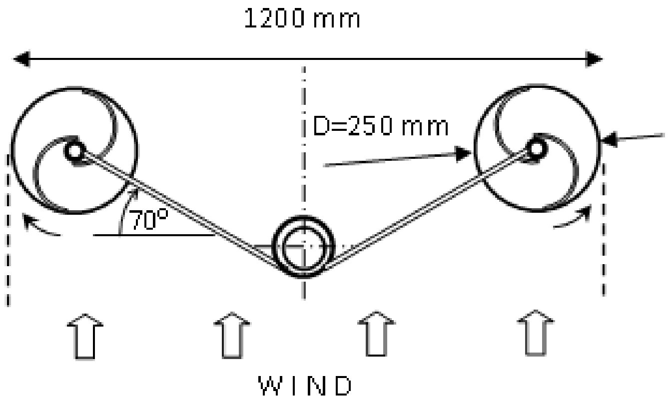

Figure 5.2.3: Test prototype dimensions [7].

The observation depicted in Fig.3.1.2 holds significant implications for practical applications. It suggests that under low wind speed conditions, utilizing single-segment rotors is recommended. However, comprehending the underlying mechanisms responsible for this phenomenon remains a formidable task, necessitating sophisticated time-resolved measurements and high-fidelity unsteady numerical simulations.

In the experimental setup of the turbine prototype utlized in this thesis, both four-segment and one-segment rotors were employed, as illustrated in Fig.5.2.4. Remarkably, these rotors successfully withstood operational conditions after a period of three years. Testing the novel rotors and the entire turbine assembly presented substantial challenges due to the unpredictable nature of wind fluctuations in urban environments. In fact, real-world open-air testing of wind turbines rarely validates the power data provided by manufacturers [216, 217].

To achieve the ultimate objective of comparing the innovative wind turbine discussed in this study with existing literature data, a comprehensive methodology was adopted to investigate the testing conditions. This approach is detailed in the following section, along with the research findings published by numerous authors.

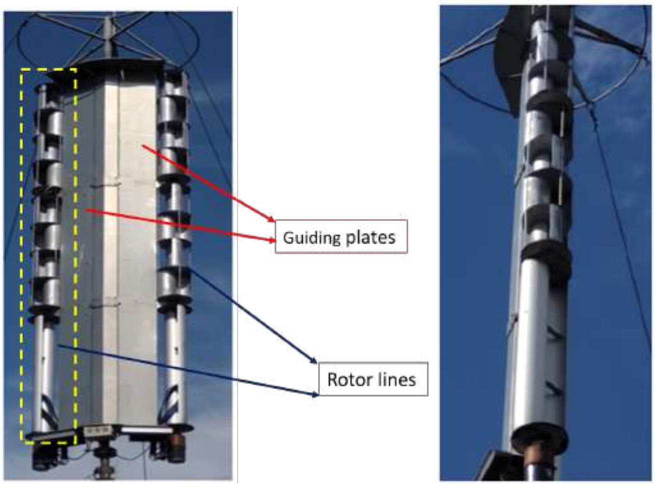

Figure 5.2.4: Updated innovative twin-rotor design

5.2.1.1 Predicted performance characteristics

As per the dimensions given in Fig. 5.2.15c, the projection area of this novel turbine is 3.6 m^2.

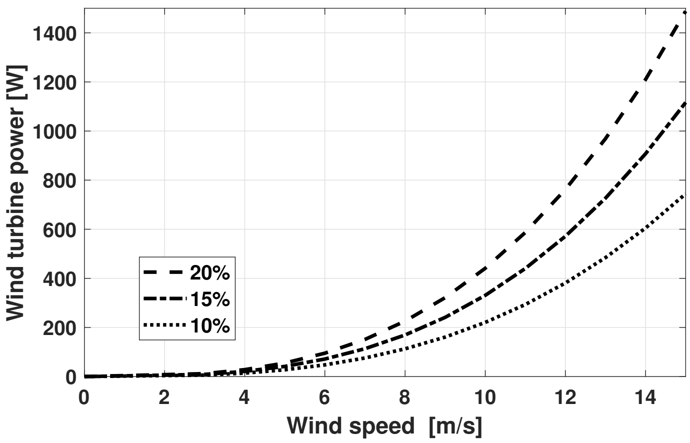

Figure 5.2.5: Power generation for chosen effectiveness and wind speeds.

Fig. 5.2.5 illustrates the expected power generation curves under different assumptions for wind turbine effectiveness (10%, 15%, or 20%). The total power presented in the figure is generated by two sets of rotors. When the wind speed is at the nominal value of 12 m/s and the effectiveness is 20%, the total power obtained is approximately 800 W. The power generated is significantly influenced by the wind turbine's effectiveness, as demonstrated.

Fig. 3.1.1b in Chapter 3.1.1 shows the typical power characteristic of the Savonius rotor as a function of $C_p = f(\text{TSR})$. Measurement of the speed of rotation and wind speed allows for calculating the TSR value. It follows from Fig. 3.1.1b that knowing the TSR value enables determining the effectiveness of power generated by the wind turbine, which is a convenient way to judge the quality of the implemented controls.

For each wind speed, one can calculate the power for TSR = 0.9, which represents the rotational speed that maximizes energy production for the Savonius rotor. This enables plotting the wind turbine power as a function of the rotor rotational speed. As a result, the power characteristics can be presented in terms of the rotor rotational speed

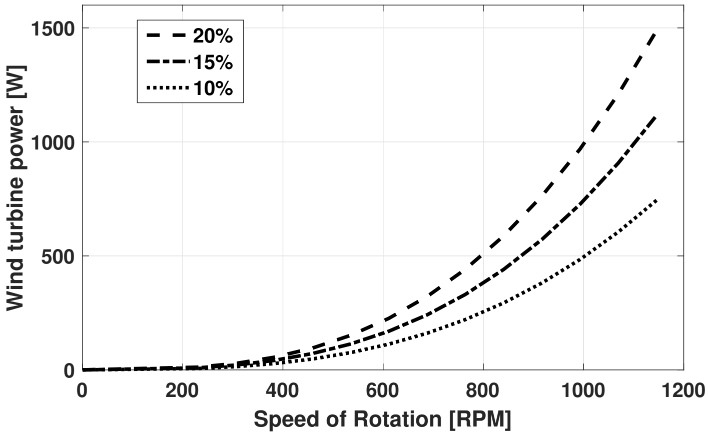

Figure 5.2.6: Wind turbine characteristics in terms of rotor speed for TSR=0.9.

in(rpm) in Fig. 5.2.6 instead of wind velocity in Fig.5.2.5. In the presented prototype, the rotors have a small diameter, resulting in relatively high rotational speeds.

Based on the numerical results presented in references [7, 218], it is anticipated that the rotor characteristics in the innovative turbine application resemble those of a single Savonius rotor. However, due to the small rotor radius, the rotational speeds are high, and the nominal power of 800 W (at 20% efficiency) is achieved at speeds exceeding 900 rpm, as seen in Fig.5.2.6. This deviation from the conventional notion that Savonius rotors are suitable for low rotational speeds is a key advantage of the innovative configuration. Substituting a large Savonius rotor with two smaller ones leads to significantly higher rotational speeds, with the increase being proportional to the ratio of the large rotor's radius to that of the small rotor (Fig. 5.2.2).

The issue of small rotational speeds in Savonius wind turbine rotors poses a challenge for selecting power generators. Slow rotation necessitates larger and heavier electrical generators. The discussed innovative solution addresses this problem by introducing higher rotational speeds, resulting in smaller and more cost-effective electrical generators. Despite the core power generators used in the prototype being relatively ineffective, with an average efficiency of approximately 70% (reaching nearly 80% under nominal conditions), the high rotational speed compensates for this limitation. The nominal speed of rotation for the generator is 1050 rpm, corresponding to a wind speed of 12 m/s and TSR = 0.9.

The data acquisition system in the prototype is situated on the wind turbine in the vicinity of the generators to avoid data transmission via the slip-ring system. Data is transmitted through a radio connection, and the produced power is dissipated into the surrounding air without being connected to any ground-level receiver. An essential feature of the system is its remotely modifiable control algorithm for the power loading of the generators, which plays a crucial role in the wind turbine's power generation quality. Various methods can be employed for the functionality of this algorithm, considering factors like wind speed measurement accessibility and adjusting the load on the rotor to achieve the prescribed rotation in the shortest time possible. However, rapid wind speed variations may hamper the effectiveness of this process. Consequently, the system must include mechanisms to handle the potential loss of wind speed measurement.

Adapting to the rapidly changing wind requires correlating the rate of wind velocity change with the response time of rotors and their load variation. Ongoing research is dedicated to refining this challenging process. The measurements presented in this chapter were obtained using a simple algorithm that increased the rotor's load as the rotational speed increased and decreased the load as the speed decreased, following a prescribed gradient of loading and de-loading based on the rotational speed. The results demonstrate the current operation of the loading process.

The measurement system captured the following data with their respective errors:

Quantity	Symbol	Error
Wind velocity	v_w [m/s]	5%
Generated voltage	U [Volt]	1%
Generated current	I [A]	2%
Speed of rotation	n [rpm]	1%

Table 5.2.1: Data captured by the measurement system and their respective errors.

The sampling frequency was 1 Hz. When combining individual measurements, the absolute uncertainty of the sum (or difference) is determined using the root sum of squares (RSS) of the individual absolute uncertainties. For the mentioned independent variables, the absolute uncertainty is 5.6% [219]. Although this is a high value, the wind velocity measurement is critical in this context.

5.2.1.2 Results and Discussion

Twin-rotor effectiveness

Field experiments were performed for the twin-rotor wind turbine as detailed above. The most important aspect for wind energy effectiveness is the speed at which this turbine is rotating.

Wind turbine control is a dynamic process in which the speed of rotation adjustment faces the dynamic variation of the wind speed. Therefore, the obtained test points form a cloud in the power-wind speed diagram. Fig. 5.2.7 shows such a measurement cloud for both generators. These diagrams show that measurements by both rotors are similar and show the limits of experienced wind speed and extracted power.

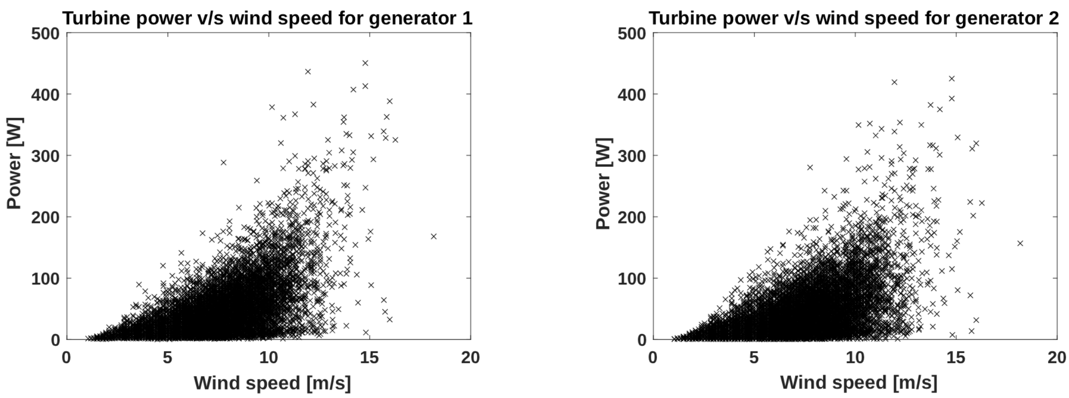

(a) Rotor 1 (b) Rotor 2

Figure 5.2.7: Measurement points of twin rotor.

The TSR variation for a random sample of 1000 points has been plotted in Fig. 5.2.8. It is observed that rotors stop from time to time, for the tested low wind speed conditions. Such moments influence the test data processing of results. These sample points at which energy is not produced are excluded from the set of data points. The TSR values calculated for each measurement point are presented in Fig. 5.2.10 with the exclusion of points where no power was produced. This reduction also means a change in measurement duration from 18.2 h down to 12.38 hr for Rotor-1 and to 12.65 hr for Rotor-2. Taking the entire set of data points into account, the averaged wind speed is v_w = 4.86 m/s. After excluding unproductive data points, the average velocity for Rotor-1 is $v_{1,av}$ = 5.57 m/s, and for Rotor-2 is $v_{2,av}$ = 5.55 m/s, respectively. The values for both rotors are quite similar, indicating a comparable effect from the exclusion of points for each rotor.

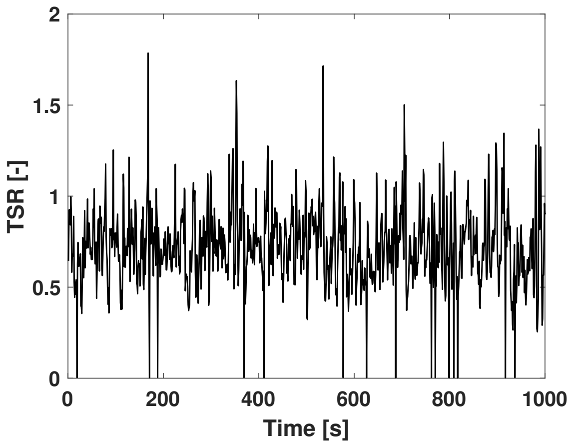

Figure 5.2.8: TSR variation with time for a particular period.

A typical characteristic of this new design is the ability to operate between a TSR range of 0.2 - 1.8 as represented in Fig. 5.2.10. An important issue is the effectiveness of the energy production by the wind turbine. As it is known the maximum power of rotors may be obtained at TSR of about 0.9. The TSR variation has been observed for the two rotors of the turbine in the following plots in Fig. 5.2.10, with average about TSR $\approx$ 0.719 and 0.751 for Rotor-1 and Rotor-2, respectively. This change in TSR values can be attributed to the difference in wind speeds and speed of rotation. The value of TSR shows the quality of energy extraction from the rotors.

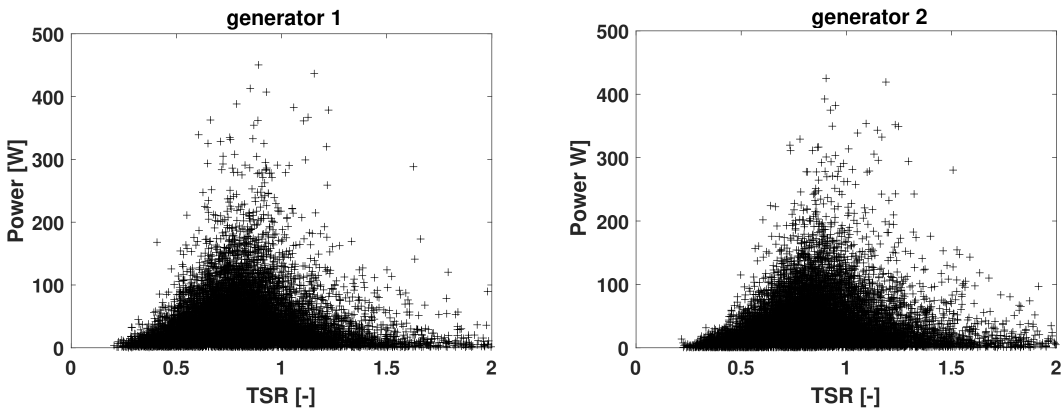

(a) Rotor 1 (b) Rotor 2

Figure 5.2.9: Generated power as a function of TSR.

Fig. 5.2.9 organizes the measurement points to demonstrate the relationship between generated power and TSR . The plot reveals the functioning of the control system. The higher density of measurement points clusters around TSR = 0.9, with an average value of approximately 0.75, as mentioned previously. This characteristic reflects the operation of the load control algorithm utilized. While the chosen test points are reasonably effective, they also suggest rotor overloading. For an appropriate algorithm, the maximum density of test points should be situated at TSR > 1.0. This proves that additional adjustments are needed to deload the system so that it can operate at a higher TSR and thus provide a higher power output.

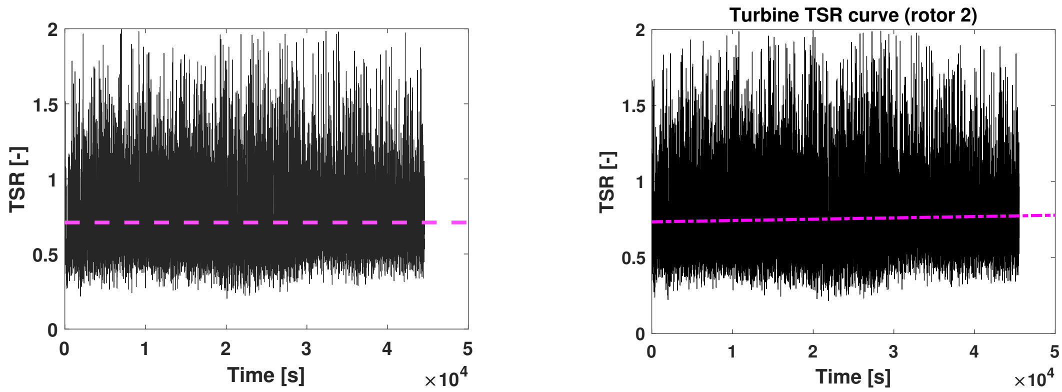

(a) Generator 1

(b) Generator 2

Figure 5.2.10: Tip Speed Ratio variation with time.

It is known that there exists a direct connection between TSR value and wind turbine effectiveness (C_p). While Fig. 3.1.1b in Chapter 3.1.1 pertains only to the typical Savonius rotor, for an innovative turbine, achieving maximum power requires TSR > 1.0. Thus, the measured TSR value at each test point serves as an indicator of wind turbine effectiveness. Fig. 5.2.11 presents plots including TSR values and effectiveness characteristics, illustrating the test points against effectiveness curves, resembling Fig. 5.2.5. The effectiveness curves ranging from 5% to 25% encompass a significant portion of the test points, reflecting the wide spectrum of wind turbine effectiveness cases resulting from the dynamic control processes involved in generator loading algorithms. This offers an opportunity to enhance the load control system by selecting points of high effectiveness. The present load control system leads to somewhat random flow cases, influenced by dynamic control processes, wind speed changes, load adjustment speed, and wind direction rotations. Finding an effective control algorithm becomes a challenging task, significantly impacting overall wind turbine effectiveness and the extent of the test points cloud. Interestingly, the indicated ranges of TSR values represented by different colors form wind turbine effectiveness bandwidths, coinciding with the shape of the effectiveness characteristics.

The cloud of points exhibits significant variability due to several factors. When rotors are accelerated from a standstill to a certain speed, low effectiveness may be observed if a gust of wind suddenly increases wind velocity and power. In this scenario, power is low at a relatively low TSR. Conversely, when the rotors rotate at high speeds, a sudden wind drop results in high TSR and power. Such occurrences can happen when rotors respond slowly to loading adjustments. A study elaborating on the response time of the prototype under consideration has been presented in the next section.

Energy produced by wind turbine

Testing wind turbines under real wind conditions poses challenges due to the wind's unsteadiness and the turbine rotors' inertia. Several authors [216, 217, 220–222] report that wind turbines in practical applications fail to achieve the effectiveness levels claimed by manufacturers. Wind turbulence significantly affects turbine performance [216, 217], with lower turbulence levels showing closer alignment to expected

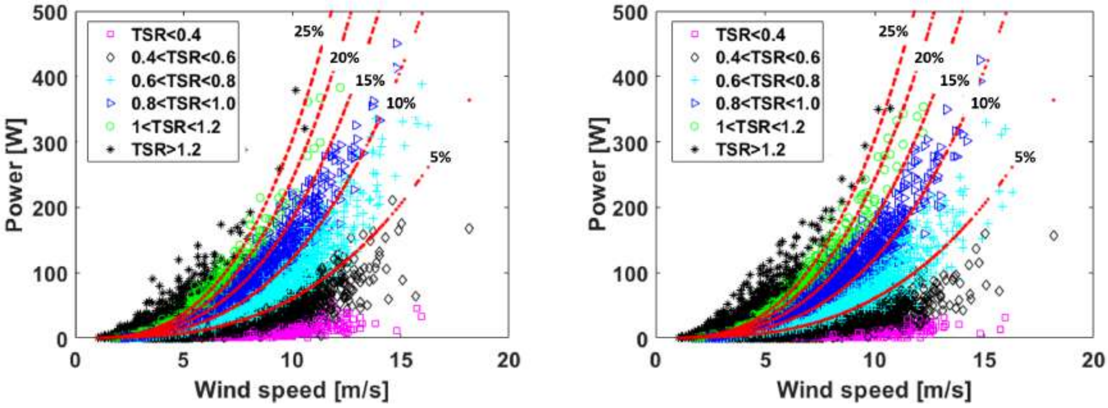

(a) Generator 1 (b) Generator 2

Figure 5.2.11: Test points against effectiveness curves with TSR marked by colors.

turbine performance.

The energy generated by the rotors relies on the output of the generator. Determining the reference wind energy, however, is not straightforward. A crucial question arises: how much energy from wind velocity peaks can the rotor utilize? In an 18.2-hour period, the energy produced by the rotor amounts to 500 Wh, while the wind energy during the same time reaches 7000 Wh. This indicates a turbine effectiveness of about 7%, which, though low, can be deemed acceptable for low wind conditions and the high turbulence intensity (TI) during the test period. Notably, the average TSR value stands at 0.75, indicating that the extracted power is less than expected. Thus, optimal adjustment of the control algorithm to improve the operating conditions and gains higher power output.

Rotor time lag analysis

The rapid fluctuations in wind frequency may impede the rotor's ability to track wind peaks [7, 216]. These wind fluctuations lead to unsteadiness in the rotor's rotational speed. However, the lightweight rotors in the innovative wind turbine, with small moments of inertia due to their compact radius, can swiftly respond to wind gusts and velocity peaks. By comparing the wind velocity signal with the rotor's 'rpm,' insights into the rotor's response to wind fluctuations can be gained.

Upon careful comparison of wind and rotor signals, a correlation between wind velocity fluctuations and rotor 'rpm' behavior is evident. However, there exists a time shift of about 3 seconds in the rotor's response. This implies that when the wind experiences a velocity peak, the rotor is delayed, missing the opportunity to harness the peak wind energy. Fig. 5.2.12 illustrates the wind velocity for the selected day (blue line), while the red line represents the tip velocity of Rotor-1. The average wind velocity on this day is denoted by $V_{AV} = 5.05$ m/s. Notably, the highest tip blade velocity peaks occur slightly after the corresponding wind velocity peaks, emphasizing the significance of exploring the correlation between these signals.

The Pearson Correlation Coefficient (PCC) was chosen for this analysis [223]. It assesses the linear dependence between random variables and is expressed by the formula:

$$r_{xy} = \frac{\sum_{i=1}^{n}(x_i - \bar{x})(y_i - \bar{y})}{\sqrt{\sum_{i=1}^{n}(x_i - \bar{x})^2}\sqrt{\sum_{i=1}^{n}(y_i - \bar{y})^2}}$$

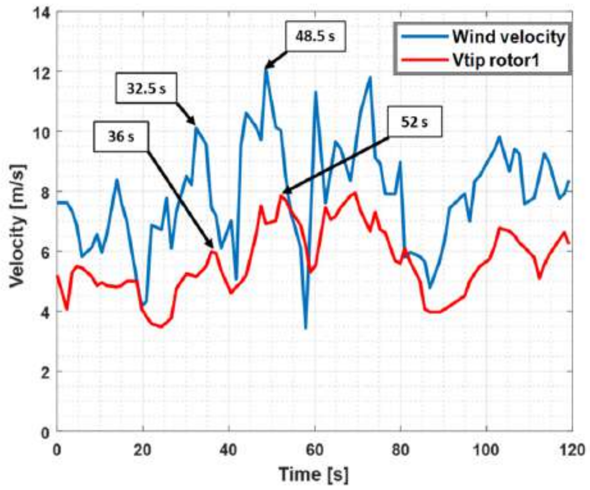

Figure 5.2.12: Relation between wind velocity and rotor-1 tip velocity.

Here, 'x' represents the wind velocity vector, while 'y' represents the velocity of the rotor blade tip, adjusted in time relative to the 'x' vector. The analysis considers data from an entire day. The correlation coefficient 'r_{xy}' varies between -1 and 1, with higher absolute values indicating a stronger linear relationship between the variables. A value of '$r_{xy} = 0$' signifies no linear relationship, '$r_{xy} = 1$' indicates an exact positive relationship, and '$r_{xy} = -1$' denotes an exact negative linear relationship. The correlation can be classified as strong, weak, or negative [224], but strict interpretations should be avoided. As a general approximation, '$r_{xy} > 0.5$' indicates a strong correlation, while '$r_{xy} < 0.5$' suggests a weak one.

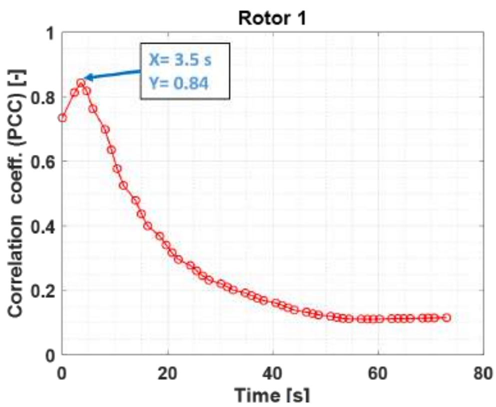

(a) Rotor 1

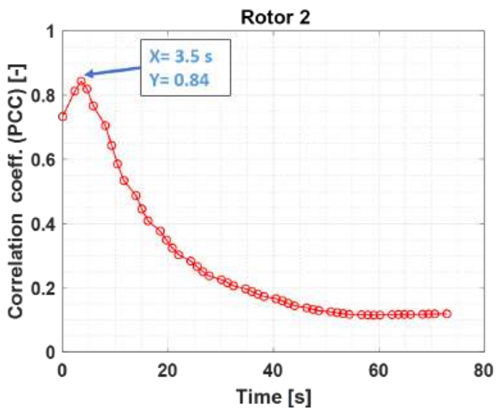

(b) Rotor 2

Figure 5.2.13: Relation between wind velocity and rotor-1 tip velocity.

The results in Fig. 5.2.13 for Rotor-1 show the highest correlation value ('$r_{xy} = 0.844$') when the time shift between signals is 3.5 seconds ('$t_{lag} = 3.5$ s'). This strong positive relationship between wind velocity ('x') and blade tip velocity ('y') confirms the correlation, albeit with a time lag of 3.5 seconds. Additionally, the plots indicate that the correlation between wind fluctuations and rotor behavior persists across a wide range of time lags, providing that rotor inertia does not heavily influence the energy transfer between wind and rotor. The plot also illustrates the correlation of time lag for wind and rotor speed for both rotors, with Rotor-1 displaying the maximum correlation at a time lag of 3.5 seconds. Similar calculations for Rotor-2 show a correlation coefficient of '$r_{xy} = 0.84$' and a time lag of '$t_{lag} = 3.5$ s,' indicating a similarity in behavior with Rotor-1.

Reducing wind fluctuations can enhance the effective reference energy harnessed by the rotors. Fig.5.2.14 illustrates this effect by reducing wind peak heights by 20% and 50%. As a result, wind turbine effectiveness increases to 8% and nearly 9%, respectively. This finding aligns with the conclusions in [216], which suggest that reducing wind turbulence fluctuations improves wind turbine effectiveness.

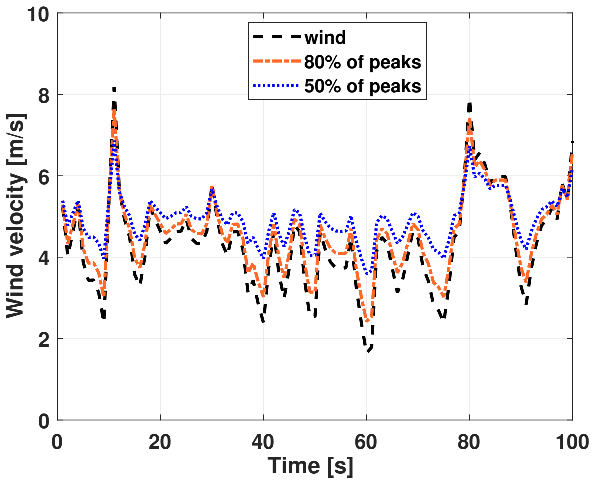

Figure 5.2.14: Reduction of wind speed peaks

The recorded energy production includes losses involved in wind turbine operation, including generator effectiveness at low rotational speeds (estimated at about 55% due to motor quality). Therefore, the wind turbine system's energy production is approximately 55% of what is delivered from the rotor.

Table 5.2.2 summarizes the obtained effectiveness of the prototype:

	Full wind	**20% of wind peaks**	**50% of wind peaks**
Energy of wind [Wh]	6722	5998	5240
Energy from generators [Wh]	494	494	494
Effectiveness including generators	7.34%	8.23%	9.42%
Rotor effectiveness	13%	15%	17%

Table 5.2.2: Energy production and effectiveness

5.2.2 Installation at countryside

Before commencing this thesis, a full-scale wind turbine power plant was developed and installed based on the innovative twin-rotor concept introduced by Dr. Doerffer and colleagues. This design aimed to enhance efficiency while reducing costs compared to traditional Savonius rotors.;

As part of the current research, a performance study was conducted to assess the effectiveness of this prototype. The following section presents the findings from this evaluation. Additionally, it outlines areas for future research and development, particularly those constrained by the project's time limitations.

5.2.2.1 The power plant

The power plant comprises three sets of twin rotors, denoted as North (N), West (W), and South (S), illustrated in Fig. 5.2.15, with each set featuring four stacked Savonius rotors at the end of guiding plates, as elaborated in Section 5.2.1. Additionally, there are two generators associated with each line of rotors—one positioned at the top and the other at the bottom. Specifically, the top generator is linked to the top two rotors in the stack, while the bottom generator is associated with the bottom two rotors. Consequently, each of the North, West, and South turbines is equipped with four generators in total. Notably, the rotor segmentation varies for each of these three sets of rotors. Subsequently, these segmented rotors were substituted with conventional single-segment Savonius rotors due to their superior performance efficiency, as analyzed and delineated in the experimental findings detailed in previous chapters.

It is important to acknowledge that the work discussed here is preliminary due to time constraints and has been analyzed at a fundamental level. Proposed modifications to data acquisition and assessment methods have been suggested but require time for implementation. Therefore, the results presented are not conclusive on their own.

The specifications of the power plant are as detailed:

Guiding Plate Angle(α): 60°

Each turbine -width (w): 2.8 m , height (h): 9.5 m

Total height of power plant (H): 16 m

Power at 12 m/s: 15 kW (3 x 5 kW) This power plant consists of two anemometers (top and bottom) as shown in Fig. 5.2.15b.

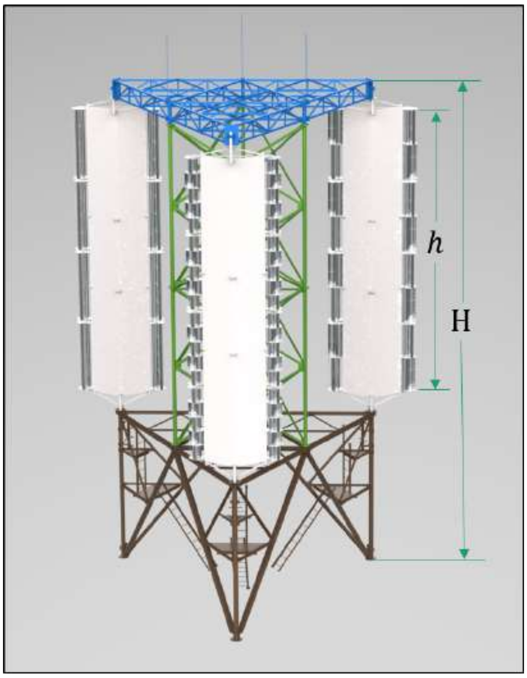

(a) Power plant CAD model

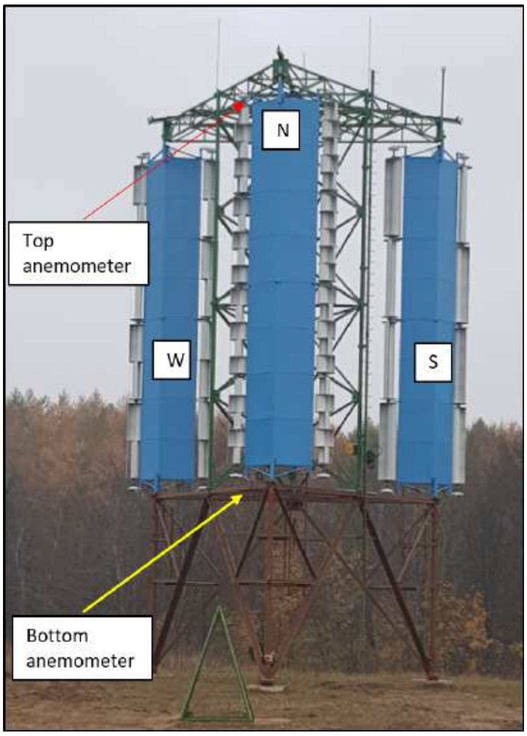

(b) Installed twin-rotor power plant.

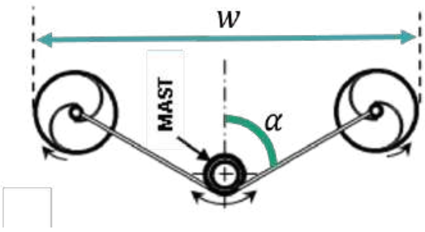

(c)

Figure 5.2.15: Prototype of Savonius type twin-rotor in Przywidz

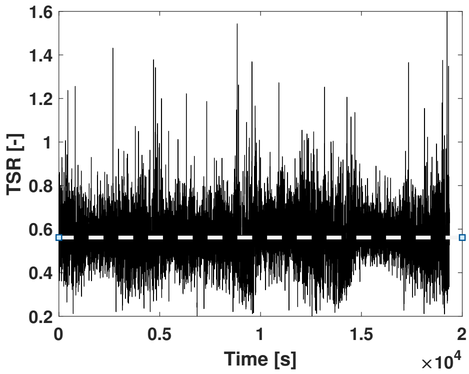

(a) North turbine

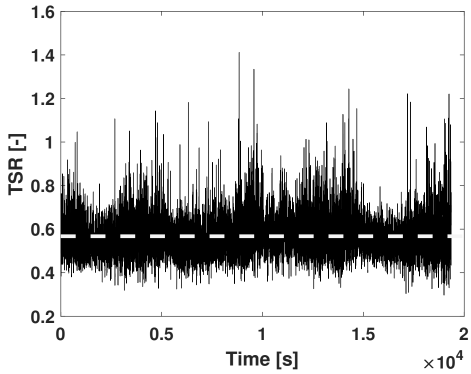

(b) South turbine

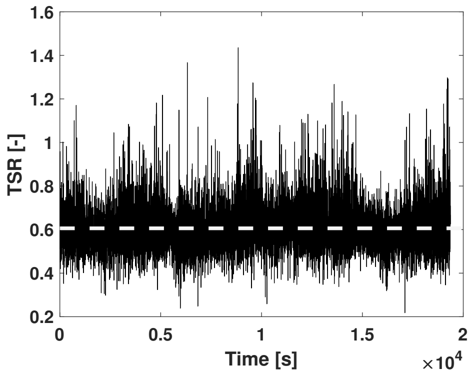

(c) West turbine

Figure 5.2.16: TSR variation as a function of time for the three wind turbine systems (a) North (b) South, (c) West.

5.2.2.2 Effectiveness of the system

The system's efficacy was assessed similar to the previous tests conducted for the twin rotor prototype on the roof. Wind turbine control entails a dynamic process involving adjustments to rotation speed to accommodate the dynamic variations in wind speed. In the case of the power plant under examination, this fluctuation is further complicated and challenging to analyze due to the differing land topography adjacent to each of the three rotors. Furthermore, the relative positioning of rotors may cause the turbines to be in the wake on the other depending on wind direction.

As presented in Section 5.2.1.1, the typical characteristic of the twin rotor is the ability to operate between a TSR range of 0.2 - 1.8 as represented in Fig. 5.2.10. As it is known, the maximum power of typical Savonius rotors may be obtained at TSR about 0.9. The TSR variation has been observed for the three turbines rotors of the turbine in the following plots in Fig. 5.2.16. However, considering the TSR values obtained for the measurement data set, the TSR range for the three cases is typically in the range of 0.3 to 1.2. This change in TSR values can be attributed to the difference in wind speeds and speed of rotation caused by the relative positioning of the wind turbines. When the wind direction originates from a particular direction, the turbine facing it experiences maximum wind velocity exposure, while the remaining turbines may be situated in its wake, depending on the wind direction.

Fig. 5.2.17 arranges the measurement points to illustrate the correlation between generated power and TSR for all three rotors. The plots exhibit notably distinct values for the turbines, as anticipated. The higher density of measurement points clusters

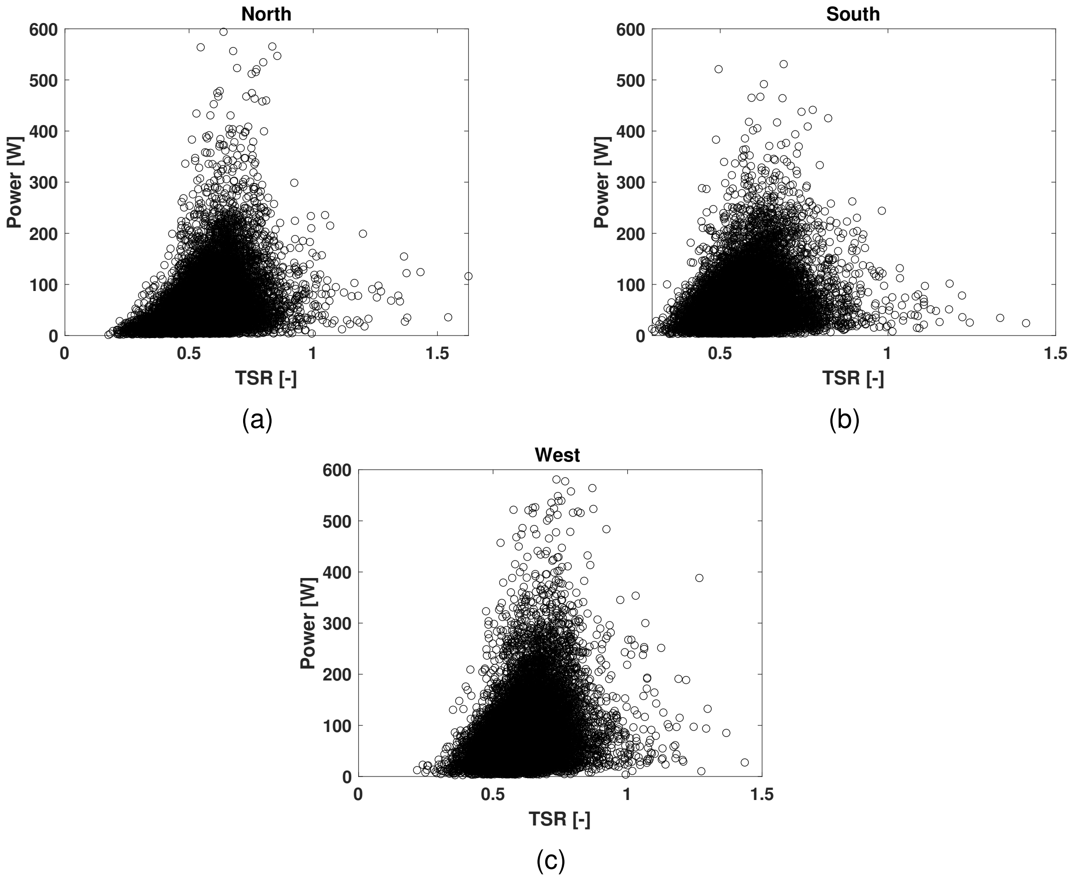

Figure 5.2.17: Power variation as a function of TSR for the three wind turbine systems (a) North (b) South, (c) West.

around TSR = 0.75, 0.65 and 0.8 for the turbines situated in North, South and West directions, respectively.

This characteristic reflects the operation of the load control algorithm utilized. While the chosen test points are reasonably effective, they also suggest rotor overloading. For an appropriate algorithm, the maximum density of test points should be situated at TSR > 1. This proves that additional adjustments are needed to deload the system so that it can operate at a higher TSR and thus provide a higher power output. Furthermore, another factor influencing the disparity in the recorded Power and TSR is contingent upon the turbine's orientation relative to the wind direction or its position in the wake of other turbines as mentioned before.

As shown in Fig. 5.2.11, similar plots have been generated for each of the three turbines in the power plant. These plots incorporate TSR values and illustrate the distribution of test points across effectiveness curves, ranging from 10% to 25%. This wide range captures various scenarios of wind turbine effectiveness, arising from the complex dynamics of generator loading algorithms. This diversity presents an opportunity to optimize the load control system by pinpointing highly effective points. However, the current load control system produces somewhat random flow patterns due to dynamic control processes, wind speed fluctuations, rapid load adjustments, and changes in wind direction.

Developing an effective control algorithm under these circumstances is a significant challenge, affecting both the overall effectiveness of the wind turbines and the distribution of test points. The variability in the data points is influenced by various factors, such as whether the turbine faces the wind directly or operates within the wake region.

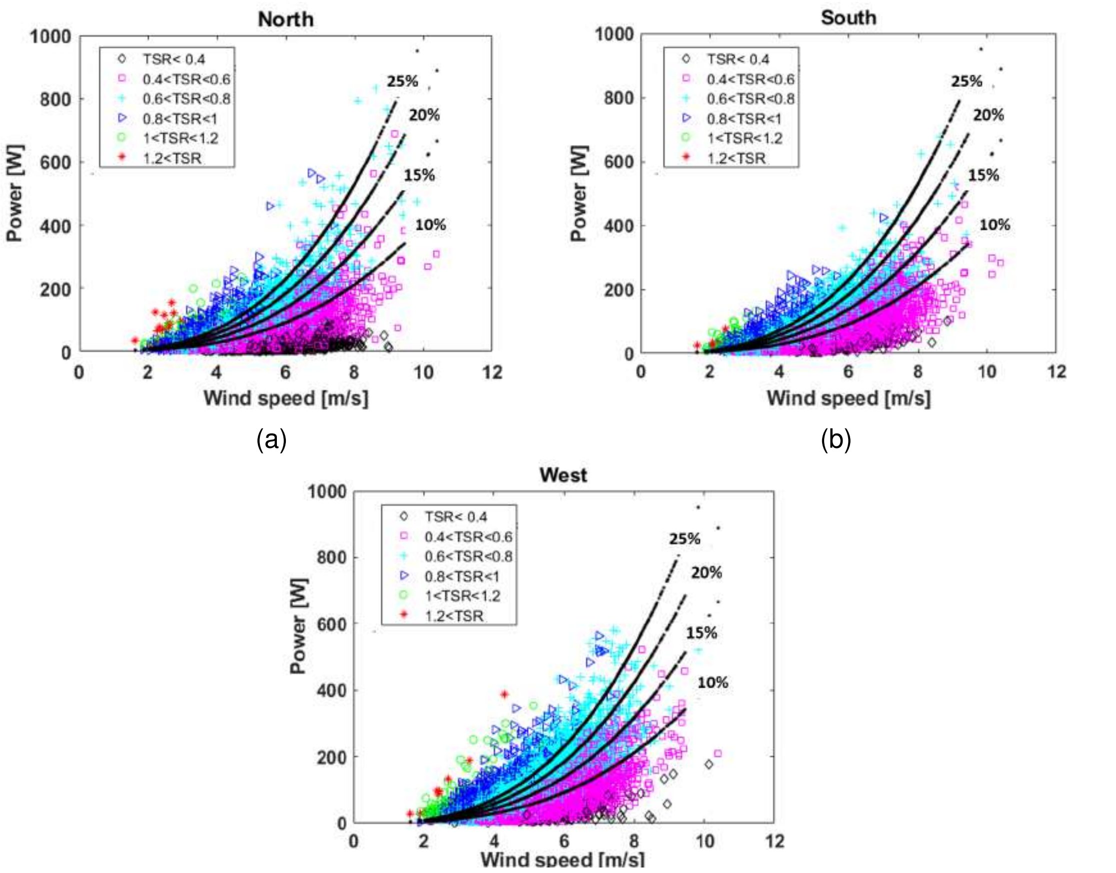

(a) (b)

(c)

Figure 5.2.18: Test points against effectiveness curves with TSR marked by colors for wind turbines(a) North (b) South, (c) West.

Additionally, the rotor's reaction time to prevailing wind speeds is crucial, as discussed further in the subsequent section.

Time lag analysis

As explained in Section 5.2.1.2, it is crucial to examine the response time of the turbine to abrupt changes in wind speed (weather gusts or sudden decline). Following the same procedure as before, the time lag was evaluate at two different velocities. In the provided findings, two lines of the northern turbine, denoted as N1 and N2, are considered. Each line comprises two vertically aligned rotors linked to a generator.

The lag results for the lower velocity of 3.5 m/s (say ws1) is presented in Figs. 5.2.19a & 5.2.19b and relatively higher velocity of 5.24 m/s (say ws2) as Figs. 5.2.19c & 5.2.19d. These velocities represent the average wind speed on two different days ($\approx$ 65k samples each day). It is observed that the time lag between rotor lines N1 & N2 is 1 second for ws1 and 3 seconds for ws2. As anticipated, the analysis of the entire day presented in Fig. 5.2.20, suggests that when the turbine encounters a sudden wind gust, the rotor mechanism takes relatively more time to adjust to the wind speed. Additionally, the plots indicate that the correlation between wind fluctuations and rotor behavior persists across a wide range of time lags, suggesting that rotor inertia does not heavily influence the energy transfer between wind and rotor.

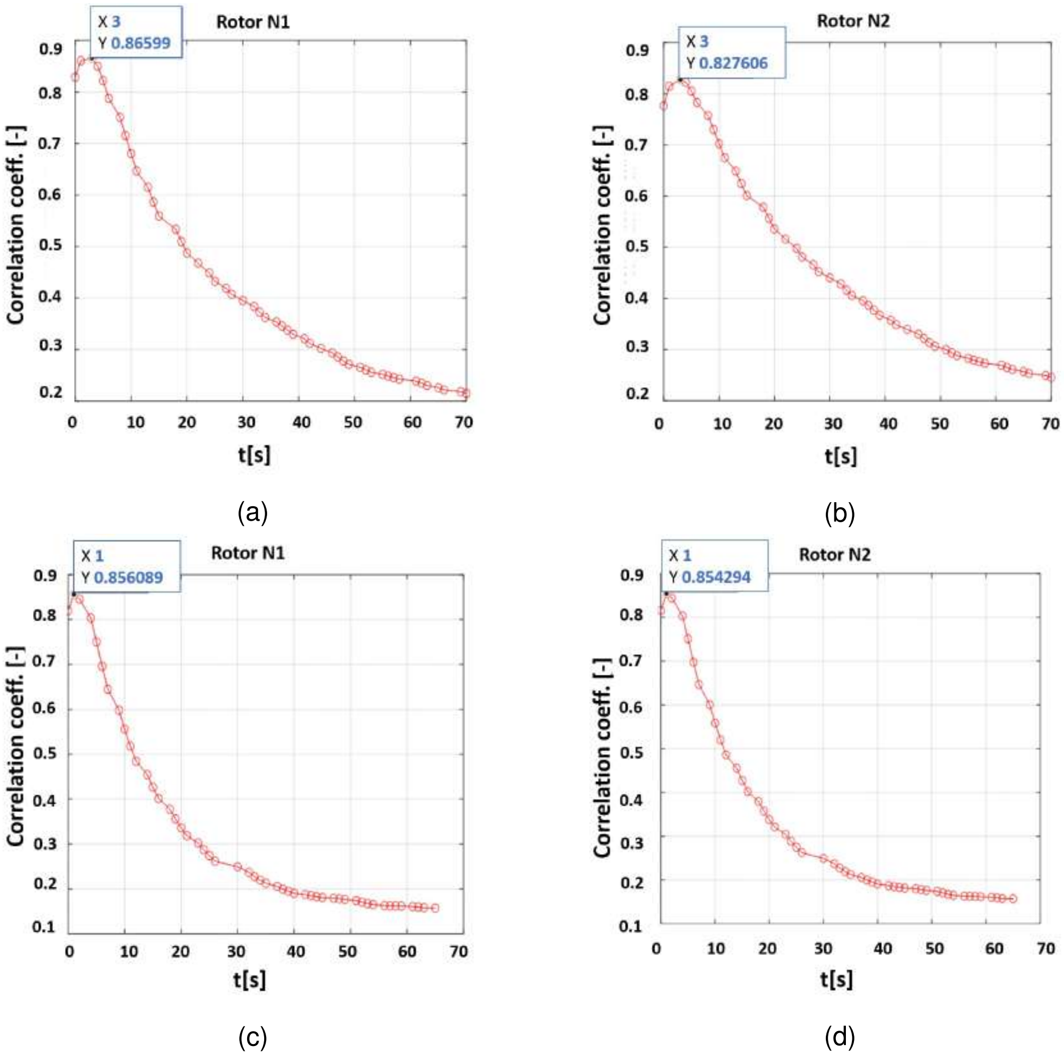

Figure 5.2.19: Time lag analysis for rotor lines N1 (a & b) 3.5 m/s, and N2 (c & d) 5.5m/s .

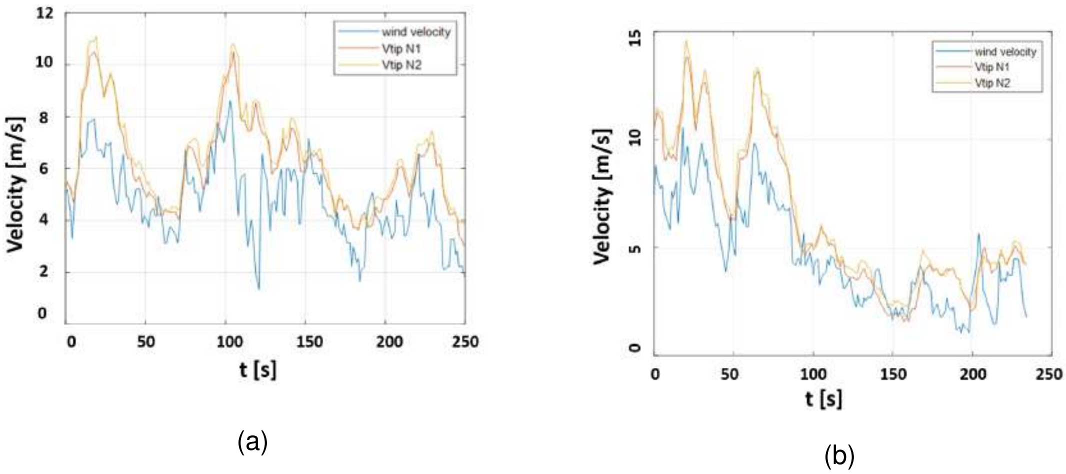

Figure 5.2.20: Delay in rotor reaction plotted over the complete range of velocity on a given day: Average wind velocity (a)3.5 m/s & (b) 5.24 m/s.

5.2.2.3 Conclusion: WT in urban environment

WT Installation in building

In a challenging urban environment, an innovative twin-rotor wind turbine underwent testing. The wind conditions were characterized by low average wind speeds of approximately 5.5 m/s and highly fluctuating winds with a TI of about 0.4. These conditions hindered achieving high wind turbine effectiveness.

Nevertheless, the investigated prototype demonstrated performance in line with expectations, showcasing excellent durability for all its components. By utilizing a simple rotor loading algorithm, the prototype achieved relatively good turbine performance. However, the average TSR value of around 0.7 indicates potential for significantly better energy production. The current rotor loading places them under considerable overload, leading to reduced rotational speed. Improved loading algorithms could elevate the rotation speed, thereby increasing power generation.

While the obtained results highlight the innovative wind turbine's promising performance, further research is required. Looking ahead, enabling remote updates to the rotor loading algorithm presents a promising avenue for future enhancements. This approach aligns with modern trends in wind turbine control systems, where adaptive and remotely configurable algorithms are increasingly employed to improve efficiency and reduce maintenance requirements.

The findings from this study lay the groundwork for developing a production-ready prototype that maintains the performance levels of a traditional Savonius rotor while significantly reducing investment costs. This advancement holds promise for more accessible and cost-effective wind energy solutions in urban environments.

WT Installation in Countryside

A preliminary assessment was conducted on a wind power plant comprising three pairs of rotors arranged to imitate a wind farm, aiming to evaluate its efficiency under real-world wind conditions. The initial findings indicate potential in the design; however, they also underscore the necessity for more extensive and detailed investigations to fully understand and optimize the system's performance. At this stage, the following conclusions can be drawn:

- Turbines facing the wind direction experience the highest wind velocity exposure, while others may be situated in their wake when the wind originates from a specific direction.
- As of the time of thesis writing, the analysis of the wind turbine system design indicates an operational range of 0.3 to 1.4, depending on which can be further improved to reach a higher TSR value of 2.
- The relationship between wind speed, power, TSR, and efficiency underscores the necessity for upgrading the loading algorithm.
- A noticeable increase in time lag occurs when the turbine is subjected to sudden wind gusts.

The analysis reveals substantial challenges in studying this particular wind turbine. Consequently, presenting data for the entire turbine as a unified entity proves challenging, necessitating an examination of each individual turbine concerning its alignment with the wind direction. During the measurement period, it was also noticed that some of the electrical components need an upgrade.

Part 6

CONCLUSION AND FUTURE WORK

Conclusion

With the global push toward renewable energy and growing concerns over environmental sustainability, urban wind energy has emerged as a promising yet underutilized resource. This thesis set out to investigate the potential and performance of SVAWTs in complex urban settings, where wind conditions are typically less favorable and infrastructure constraints are more pronounced. Through a combination of experimental studies, numerical simulations, field installations, and acoustic analyses, the research aimed to address critical gaps in the understanding and optimization of these turbines.

The investigation began with an assessment of wind potential and turbine siting across selected locations in Nottingham (UK) and Poland. Using a rigorous statistical approach, multiple probability density functions were evaluated for wind speed modeling. The Weibull distribution consistently emerged as the most accurate and reliable model. While the wind speeds at these sites were modest, they were found to be suitable for small-scale wind turbines—particularly vertical axis designs that can operate efficiently in lower wind regimes. The study highlighted not only technical viability but also contextual considerations such as noise impact, public perception, and installation constraints that must be balanced when deploying turbines in populated areas.

In parallel, a preliminary test section was manufactured, aimed at evaluating the aerodynamic performance of Savonius rotors. However, to ensure that the results accurately represented free wind conditions, it became necessary to verify whether the setup introduced boundary effects or flow constraints. Initial experiments showed that improvements were needed, prompting a series of numerical simulations, initially focused on single-segment rotors to reduce computational complexity. These simulations, particularly for configurations in which the rotor was placed close to the wind tunnel outlet, demonstrated unrealistically high efficiencies.

The test section was then upgraded to enable variation in rotor positions relative to the jet outlet, allowing a better reproduction of free-stream conditions. Subsequent experiments with both single- and five-segment rotors at multiple positions confirmed that the single-segment rotor consistently outperformed the five-segment design, with the highest efficiency at the nearest placement (0.28 m). While some simulation results aligned with experiments, discrepancies—especially in near-boundary flow behavior—revealed limitations in the CFD models and emphasized the importance of integrating more advanced simulation techniques capable of capturing flow separation and complex interactions with tunnel boundaries to better mirror real-world performance.

Noise analysis was a critical component of this research, particularly due to its relevance in urban scenarios. A comprehensive and methodical investigation was conducted to understand the acoustic behavior of Savonius-type VAWTs, particularly within the context of urban installation. The study encompassed a comparative analysis between single-segment and five-segment rotor configurations, revealing that design geometry plays a crucial role in determining noise output. The five-segment rotor, for instance, exhibited significantly lower acoustic energy as compared to the single-segment rotor. This reduction was attributed to the segmental design disrupting coherent flow structures, thereby redistributing noise energy toward higher-frequency bands that dissipate more rapidly.

Beyond overall sound level measurements, the research employed advanced acoustic diagnostics, including beamforming techniques in collaboration with TU Delft. These high-resolution measurements, combined with power spectrum analyses, enabled precise identification of noise sources and their frequency characteristics across various operating conditions.

Furthermore, the study established correlations between noise emissions and operational parameters such as TSR, rotor loading, and wind velocity. Notably, it was found that noise levels were minimized when the turbine operated near its optimal TSR, suggesting that acoustic optimization could be aligned with performance efficiency. The free-running condition—when the rotor was allowed to spin without load—resulted in substantial increases in noise output, underlining the need for effective control strategies during high wind events.

By thoroughly localizing noise sources and analyzing their relationship with rotor design and operating conditions, the study offers actionable insights for the development of quieter, high-performance VAWTs suitable for integration into noise-sensitive urban environments.

The final phase of the study focused on the development and field testing of an innovative twin-rotor Savonius wind turbine prototype under real-world urban conditions. The urban environment presented inherent challenges, characterized by relatively low average wind speeds, approximately 5.5 m/s, and a high turbulence intensity around 0.4. Despite these demanding conditions, the prototype demonstrated notable mechanical durability and operational reliability, maintaining consistent functionality throughout the testing period. While the initial performance results are encouraging, they also highlight substantial potential for enhancement. In particular, optimizing the rotor loading algorithms stands out as a critical pathway to improving energy conversion efficiency. By refining these algorithms to achieve higher tip speed ratios, the turbine's power output could be significantly increased, better aligning its performance with ideal operating parameters.

Additionally, the installation of a system featuring three twin rotors on a ski hill site provided further practical insights into the complexities of wind turbine operation in diverse environments. This installation emphasized the importance of developing adaptive control strategies capable of responding to site-specific factors such as fluctuating wind exposure, terrain influences, and operational maintenance challenges. These findings underscore that while the twin-rotor design shows promise, unlocking its full potential will require a comprehensive approach that integrates improved algorithmic control with design strategies tailored to the specific environmental and operational conditions.

Overall, the comprehensive results from experimental investigations, numerical simulations, and field testing validate the hypothesis presented in the Overview section of this thesis. The findings demonstrate that the approaches and design considerations examined throughout the research effectively address the challenges associated with integrating SVAWTs into urban environments, confirming the relevance and applicability of the proposed solutions.

Main Achievements – Contribution to the Existing Knowledge

- Conducted a comprehensive overview and comparison of wind description methods, enhancing the understanding of their suitability for evaluating wind energy potential in various environments.

- Investigated the relationship between power production and noise generation in the Savonius rotor, integrating aerodynamic performance with acoustic analysis:
  - Identified primary noise sources associated with Savonius rotor operation.
  - Demonstrated that noise emissions are reduced at conditions corresponding to maximum power output.
  - Showed a notable increase in noise levels at maximum rotational speed, which coincides with decreased power production.
- Analyzed the performance of an innovative twin-rotor Savonius wind turbine, providing practical insights into its behavior and potential within real-world conditions.

Future Work

While the research presented here offers substantial contributions, it also opens up several avenues for future exploration:

- **Noise Reduction and Acoustic Optimization:** Further investigation into alternative segmentation patterns, passive noise control measures, and sound-dampening materials could enhance urban compatibility. Additionally, integrating active control systems that adapt rotor speeds to minimize noise during peak residential hours may increase public acceptance.
- **Rotor Control and Optimization:** The twin-rotor design holds significant promise, but its full potential can only be realized with improved rotor loading algorithms. Implementing real-time control systems that dynamically adjust loading based on wind conditions can help achieve optimal performance at higher TSRs.
- **Extended Field Installations:** Real-world, long-term monitoring of multiple turbine units across various urban settings would provide more robust performance data. Such studies could also explore interactions between turbines and the built environment, including wind deflection by nearby structures.
- **Urban Integration and Design:** Future research should explore architectural integration of SVAWTs into buildings. Consideration of aesthetics, noise insulation, and structural stability will be key to facilitating mainstream adoption.
- **Data Collection and Infrastructure Upgrades:** Upgrading sensors and software systems to allow detailed data logging of turbine-specific variables (e.g., torque, RPM, wind variability) will greatly improve system diagnostics and allow for the application of machine learning techniques for predictive maintenance and efficiency tuning.

Closing Thoughts

This research establishes that, with thoughtful design, strategic placement, and continued technological refinement, Savonius-type VAWTs can offer a practical and sustainable solution for urban wind energy harvesting. A key outcome of this work is the clear identification of the appropriate rotor location within the test section to ensure power output measurements accurately reflect free-wind operation—an essential step in bridging laboratory results with real-world performance. Furthermore, the study has uncovered the significant influence of rotor structural configuration on both efficiency and noise, providing valuable guidance for design choices in noise-sensitive urban environments.

While challenges remain—particularly in further reducing acoustic emissions, enhancing efficiency, and optimizing installation strategies—the potential benefits are compelling. Urban areas, with their growing energy demands and limited space, stand to gain from compact, low-maintenance turbines capable of operating quietly and efficiently amidst complex wind conditions. The insights generated here not only advance the scientific understanding of Savonius VAWTs but also lay a solid foundation for the next generation of urban wind energy systems—systems designed to deliver clean power where it is most needed.

APPENDIX

Appendix A

Sound matrices

Numerous acoustic parameters have been formulated over time, many tailored to precisely gauge the discomfort perceived by the human auditory system. This annex provides a concise overview of the prevailing metrics commonly employed for assessing aerospace-related noise sources. Further comprehensive metrics can be referenced in the existing literature [191, 225]

A.1 Sound Pressure Level (L_p)

Sound waves arise from minor fluctuations in the pressure surrounding the barometric ambient pressure of the propagation medium. These deviations, though notably smaller than the ambient pressure, encompass a spectrum from 20 µPa (representing the auditory threshold, p_0, equating to 0 dB) to 20 Pa (marking the threshold of discomfort). While deviations beyond this range do occur, lower pressures are challenging to discern by human perception (thus not leading to disturbance), and higher pressures are not commonly encountered in practical scenarios [225].

Industrial noise exhibits significant fluctuations, evident in the oscillations recorded by the sound meter. Given the vast span of amplitudes for acoustic waves (approximately spanning 6 orders of magnitude), a logarithmic scale metric called sound pressure level (SPL or L_p)), quantified in decibels (dB), was introduced.

$$L_{\mathrm{p}} = 10\log_{10}\left(\frac{(p_z)^2}{(p_0)^2}\right) = 20\log_{10}\left((\frac{p_z}{p_0})\right) \text{ dB} \tag{A.1}$$

where, p_0 is the reference pressure (generally taken as 20 µPa) and p_z is the effective acoustic pressure given as : $p_z = \sqrt{\frac{1}{T}\int_0^T (p^2 dt)}$
To standardize the measurements, the term Equivalent SPL L_{eq} is sometimes used. It represents the steady sound pressure level that possesses the same total energy as the actual fluctuating noise over a specific period of time (T) [226].

$$L_{\mathrm{eq},T} = 10\log_{10}\left(\frac{1}{T}\int_0^T \left(\frac{(p_z(t))^2}{(p_0)^2}\right) \mathrm{d}t\right) \text{ dB} \tag{A.2}$$

In the case of multiple incoherent sound sources, the overall SPL (OSPL or $L_{p,overall}$) can be calculated by adding the L_p contributed by individual sound source logarithmically as

$$L_{\mathrm{p}} = 10\log_{10}\left(\sum_{i=1}^{M} 10^{(L_{\mathrm{p,i}})/10}\right) dB \tag{A.3}$$

A.2 Sound Levels

The human ear does not perceive sounds equally across different frequencies. To account for this varying sensitivity over the audible range, frequency weighting filters are used. These filters apply "weight" to input from discrete frequencies, contributing to the overall sound level. This enables adjustments in sound levels by increasing or decreasing them based on frequency before combining them to derive a general sound level.

The commonly used weighting types are the internationally standardized "A", "B", "C", "D"and "Z" weightings. "A" weighting considers human ear sensitivity at different sound levels, while the "C" weighting is focused on low-frequency noise during take-off (e.g., jets). Guidelines for such analyses can be found in IEC 60651.

A.2.1 A- weighted Sound Pressure Level $(L_{p,A})$

The A-weighted sound pressure level Lp_A for a certain frequency f can be calculated by adding a correction factor $\Delta L_A(f)$ for that frequency to the $Lp(f)$.

$$\Delta L_A(f) = -145.528 + 98.262 \log_{10}(f) - 19.509 \log_{10}^2(f) + 0.975 \log_{10}^3(f) \tag{A.4}$$

$L_{p,A}$ (dBA) for a certain frequency is then given as:

$$L_{p,A}(f) = L_p(f) + \Delta L_A(f) \tag{A.5}$$

The graphical representation of Eq. A.2.1 is illustrated in Fig. A.1. It can be observed that for frequencies between approximately 1 and 6 kHz $\Delta L_A > 0$, i.e., the human ear is more sensitive to these frequencies, and a penalty is applied. Outside of this range, the rest of the frequencies are reduced considerably, especially for low frequencies. In case of M no. of incoherent sources, the A-weighted OSPL (OASPL) can be calculated as Eq. A.3.

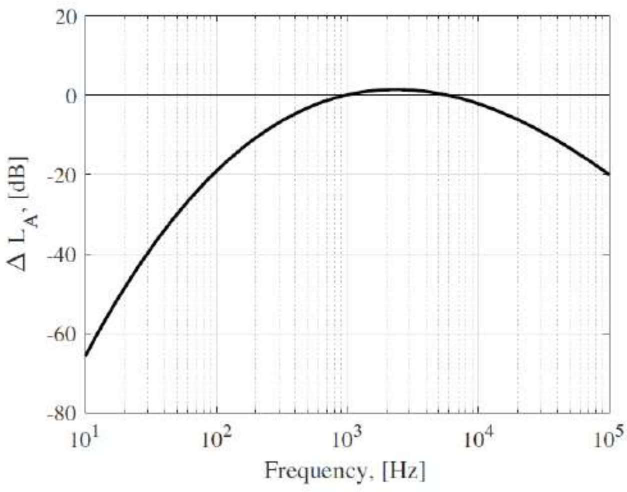

Figure A.1: A–weighting correction factor ΔL_A [155]

A.2.2 Z- weighted Sound Pressure Level

For assessing total noise exposure directly, **Z-level** sounds are particularly useful. Z-weighting filters provide a flat frequency response and represent the actual noise produced without considering human ear sensitivity (Z for zero).

Let $p_Z(t)$ denote the time-varying Z-weighted sound pressure, and p_0 represent the reference pressure (20 µPa). An analogous expression can define $L_{Ceq,T}$, the equivalent continuous C-weight level or A-weight level, by substituting the time-varying sound pressure levels with their respective A-weighted or C-weighted values. The averaged value with weighting can then be given as Eq. A.6.

$$L_{\mathrm{Zeq},T} = 10\log_{10}\left(\frac{1}{T}\sum_{i=1}^{M} T_i \times 10^{\left(L_{\mathrm{Zeq},T_i}\right)/10}\right) dB \tag{A.6}$$

The sound level in dB that has surpassed x percent of the time is represented by L_x, and consequently, the term L_{Ax} is used when discussing the A-weighted sound level (dBA). When written as $L_{Ax,tmin}$, it means that the sound level crossed the sound level x% of the time in a duration of t mins.

A.3 Sound quality metrics

Exploring the frontier of psychoacoustics, advanced sound quality metrics are presently under study for potential application in the assessment of wind turbine noise. These metrics, characterized by intricate computations, aspire to encapsulate the genuine sense of disturbance perceived by the human auditory system [227].

For decreasing influence on perceived annoyance, the most frequently employed metrics [191] include [191, 192, 227]:

- **Loudness** This pertains to the subjective perception of sound magnitude, directly correlated with the overall sound intensity
- **Roughness** characterizing the rapid fluctuations in amplitude for sounds falling within the frequency band of 15 Hz to 300 Hz.
- **Tonality** indicates the strength of discernible tonal energy within a complex sound, often unmasked.
- **Sharpness** characterizes the presence of high-frequency components in a sound
- **Fluctuation strength** refers to the perceived intensity of rapid variations or fluctuations in the amplitude of a sound over time. It captures the sensation of modulation or variation in the loudness of a sound, especially when the amplitude changes occur relatively quickly.

Given the overarching aim to distill the actually experienced annoyance into a singular measure, composite metrics such as Psychoacoustic Annoyance (PA) have been introduced, amalgamating the aforementioned four metrics.

Appendix B

Test section at IMP-PAN

B.1 Test Section

The test section, as in Politechnika Gdanska, is shown in Fig. B.1. The test section consists of three fans, mounted at the rear end, which can be regulated to obtain different wind speeds at the outlet. A provision is also made to store three rotors at the same instance. These rotors can be changed for experimental purposes with the use of an inbuilt pulley system. The main outputs of this test section include the rotational speed, wind velocity and the power characteristics of the rotor. A load-changing device is also incorporated. This takes the energy from the generator, mounted at the bottom of the rotor and puts it on a heating device. This allows for the selective operation of the rotor within the range of interest of TSR's.

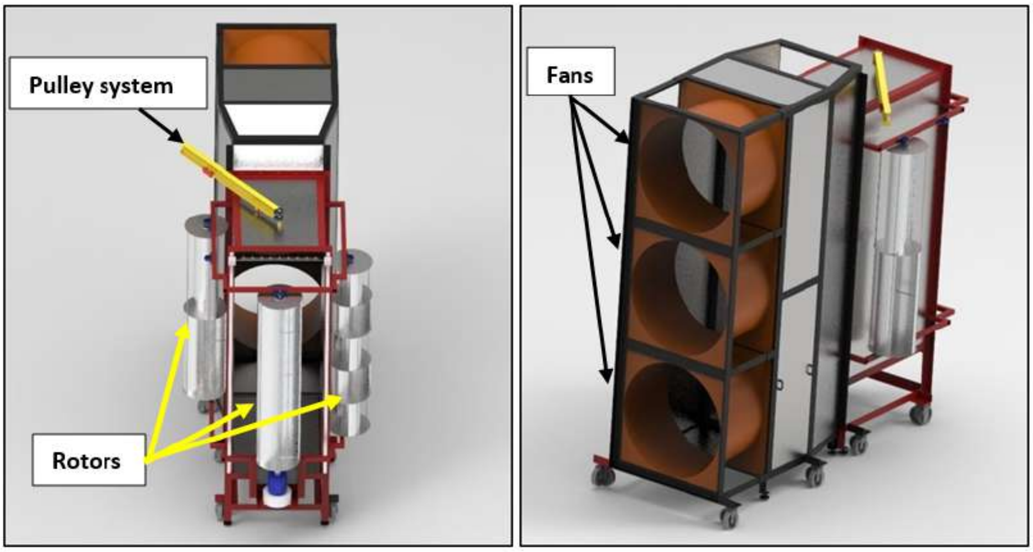

Figure B.1: Test section at IMP PAN lab.

In order to hold the rotor in position, facilitate smooth rotation and load it, the connections are made with bearings placed at either of the ends. add some pictures to show the bearings and all.

B.1.1 Flow Uniformity

The first challenge involved before making the measurements was to ensure the uniformity of flow at the test section outlet. The test section was incorporated with a

Figure B.2: Test section with different Rotors.

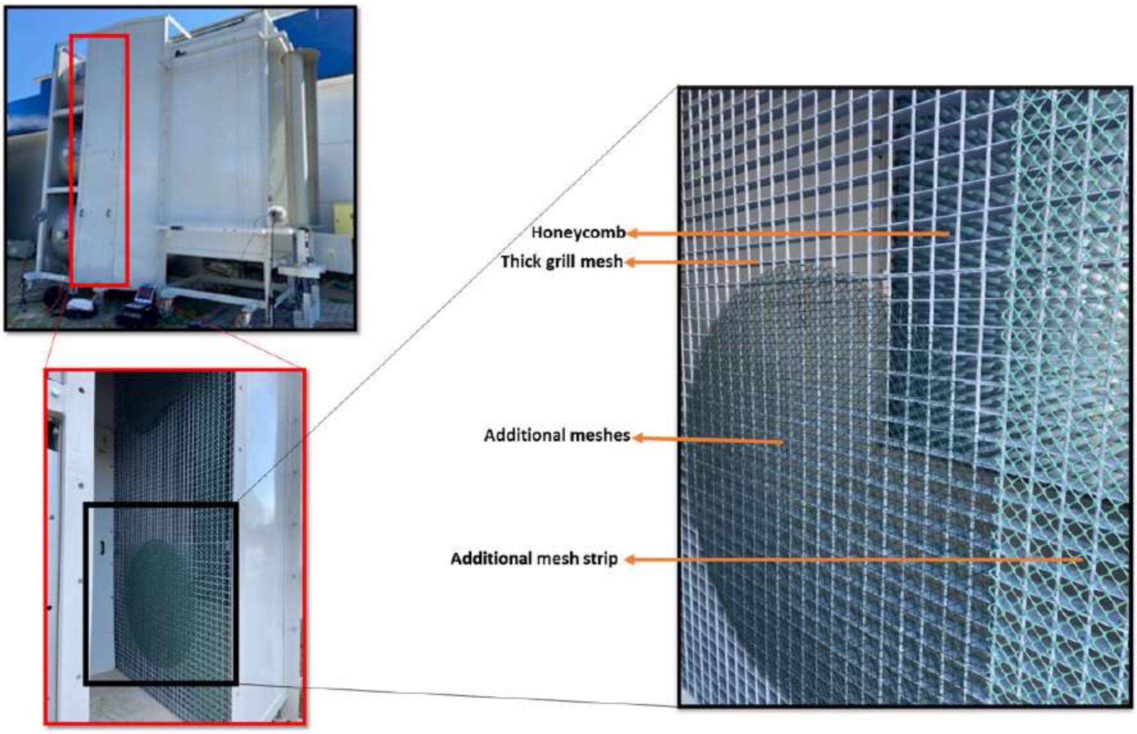

Figure B.3: Meshes inside test section for flow uniformity.

honeycomb type structure following a thick grill in order to support this requirement. However, these additions were not enough. Additional tests were conducted by adding thin meshes onto the thick grill as an attempt to obtain more uniform velocity field at the outlet.

The tests were done by employing nine Prandtl probes across the horizontal axis and taking a vertical sweep to cover the complete test section outlet. An additional fixed probe was mounted at the center of the test section to be considered as the reference.

These probes assesses the local airflow velocity by analyzing the pressure distribution surrounding it as the air movess over it. The position of these probes is seen in Fig. B.4.

Four cases with different arrangements of additional meshes were considered, and measurements were made individually for low and high wind speeds for all the cases. The high velocity refers to an approximate velocity of 12 m/s reference velocity and about 8 m/s for low wind speed. A detailed view of these meshes can be seen in Fig. B.3.

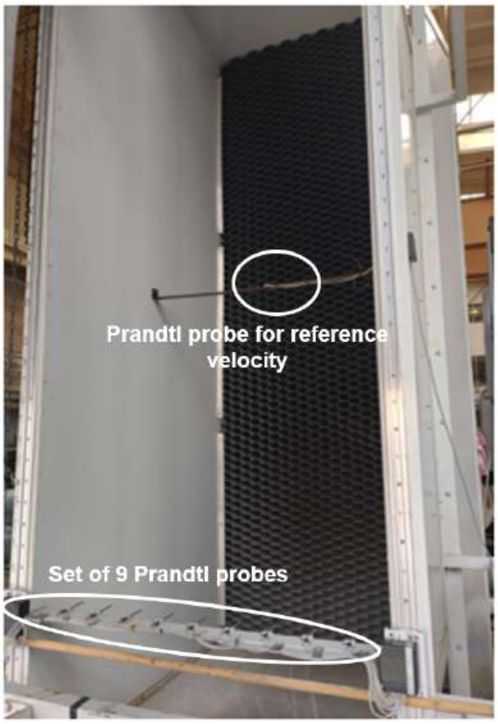

Figure B.4: Case 1

- Case 1: No additional mesh.
- Case 2: Two additional circular meshes.
- Case 3: Two circular meshes and an additional mesh strip.
- Case 4: Three circular meshes and an additional mesh strip.

The first test was done with the test section operating with no additional meshes other then the metal grill. The surface plot created from the sweep shows many spots where the difference between the wind velocities is about 6m/s. With an attempt to solve this issue, two circular meshes on the metal grill, directly in front of the three fans were placed. This decision was made as a large variation was seen mainly in this region. The results obtained for both cases discussed above displayed a higher velocity dominating on one side of the test section. This dominance can be seen on the right hand side of the surface plots. In order to address this challenge, a mesh strip was added on this side of the test section, along with the two circular meshes placed before. Considering the plots, the relative high velocity spots for the individual velocity scans, in both the high speed and low speed cases, a considerable reduction is seen on the dominating wind velocity side. However, there was still more scope of improvement, considering the central part of the plot. It was thought of to add another circular mesh to the previous case, resulting in a configuration of three circular and one mesh strip. These results looked promising at first glance on the velocity sweep plot.

In order to quantify the results obtained from case 3 and case 4, the standard deviation of the two cases was calculated, by taking the wind velocity measured by a central fixed probe as the reference. The values obtained are as presented in Table B.1 for case 3, with the reference velocity recorded as 12.985 m/s and Table B.2 for case 4 with the velocity at the central fixed probe measured as 10.527 m/s.

Even though the plots for case 3 in both the case of high wind speed and low wind speed, the tables present a different scenario. It is observed that even though the fans were operating at the same rpm, the wind velocity recorded by the reference probe was higher for case 3. Also, for further clarification, the quantification study was divided into two zones, one considering the first and the last horizontal probe values, which are affected by the side walls of the test section, and the other by removing these values. It was seen that when the area immediately next the the wall is not considered (without side points), the standard deviation was lower for case 3.

Taking into account the quantification analysis performed, it was thus concluded that the test section operating under the configuration in case 3 is more suitable for further tests to be performed using this test section.

Zone	Average	Max value	Min value	Max-Min	Standard deviation
Whole	12.349	16.142	9.098	7.044	1.319
No side points	12.504	16.142	9.787	6.355	1.242

Table B.1: Data variation with two meshes and a strip. High velocity with reference measurement in the middle of the test section = 12.985

Zone	Average	Max value	Min value	Max-Min	Standard deviation
Whole	11.503	15.111	8.941	6.170	1.257
No side points	11.568	15.111	9.365	5.746	1.302

Table B.2: Data variation with three meshes and a strip. High velocity with reference measurement in the middle of the test section = 10.527

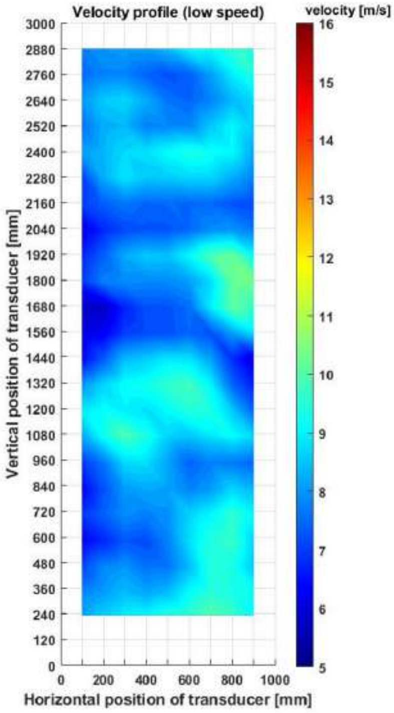

(a) Case 1

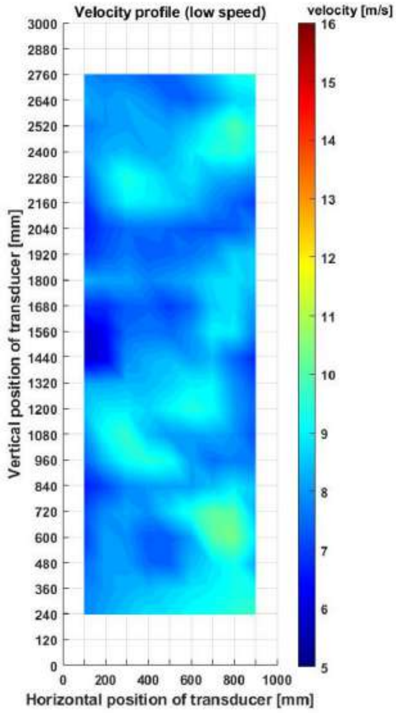

(b) Case 2

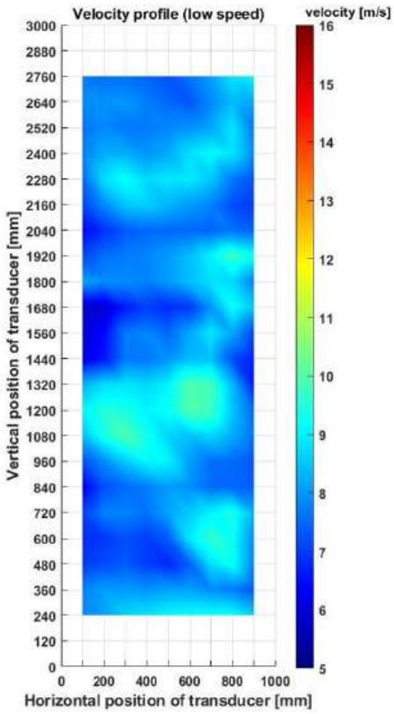

(c) Case 3

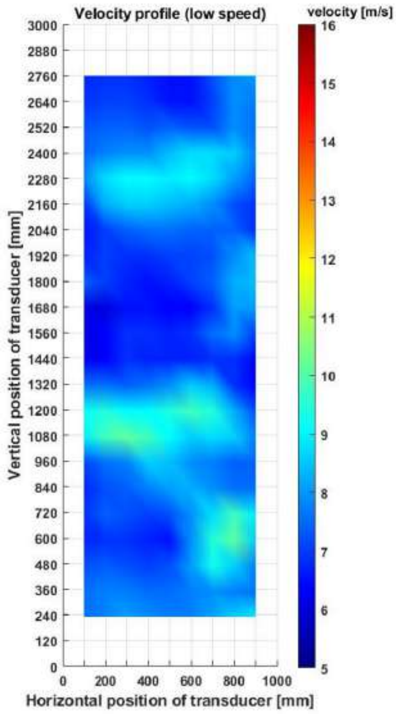

(d) Case 4

Figure B.5: Flow uniformity tests for low wind speed.

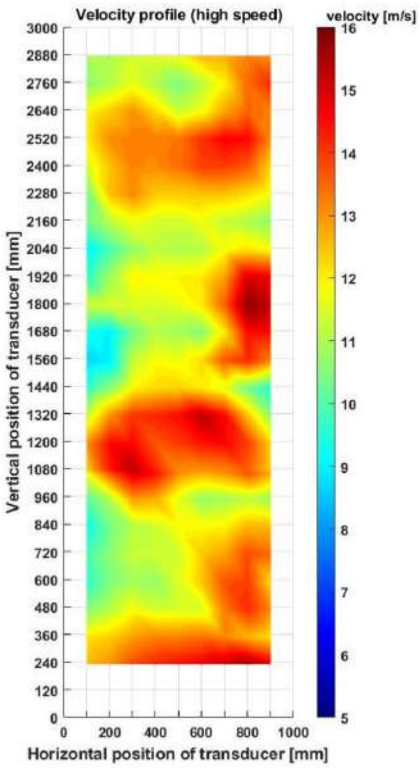

(a) Case 1

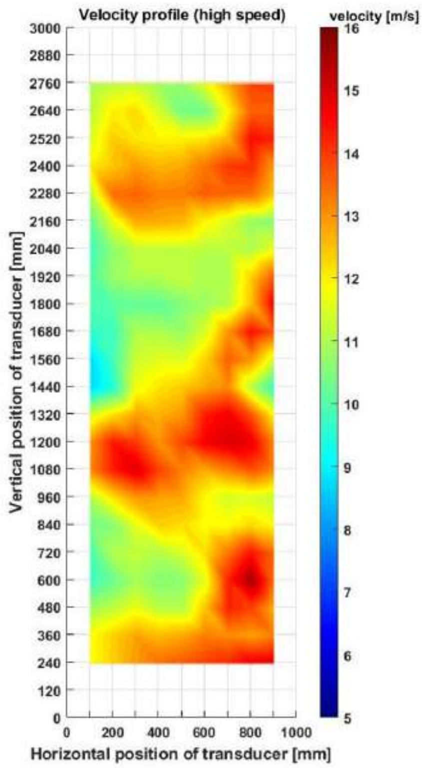

(b) Case 2

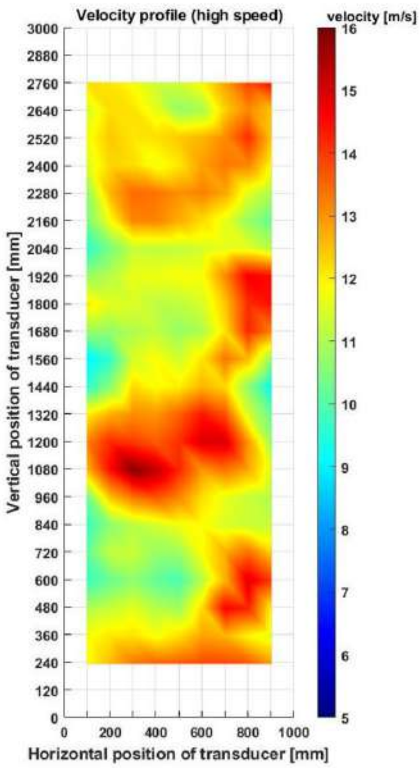

(c) Case 3

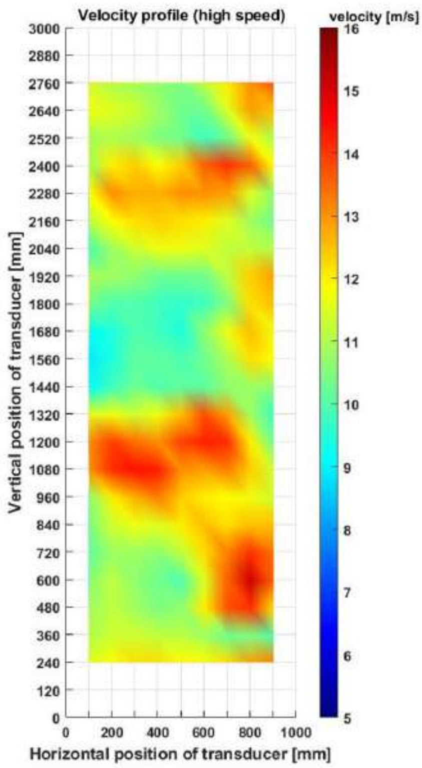

(d) Case 4

Figure B.6: Flow uniformity tests for High wind speed.

Appendix C

Supplementary material: Wind potential analysis

C.1 Additional plots for Weibull distribution 5.1.1

C.1.1 Variation of wind speed

Fig.C.1 shows the hourly variation of the wind speeds while Fig.C.2 demonstrates the average wind speed for each month. Looking into the details of the hourly wind speed averages, it can be seen that the wind speed has the leas deviation for the year 2019 for both the locations. When the complete data set of the hourly variation over the three years is taken into consideration, the average mean wind speed in the case of Sutton-Bonnington is ranging between 3 m/s to 3.6 m/s. While in the case of Watnall, this deviation ranges from 2.3 m/s to 3.2 m/s. Another interesting factor in the case of Watnall is the drop in wind speeds between 12 pm to 2 am for all the years.

The monthly wind data represented in Fig.C.2 shows a similar wind speed pattern for the two locations with a dip in the wind speeds from April to October. An interesting observation made in the case of the location Sutton-Bonnington is the sudden dip in the monthly wind speed average from 2018 to 2019-2020. As even a slight change in the surroundings of the meteorological mast, such as the addition of buildings and deforestation, can lead to a change in the local wind patterns. This change can be linked to a variation in the topography of the surrounding area. The exact factors that influenced the wind speed distribution need to be studied in more detail. The lowest wind speeds were observed for the warm months from April to September.

It is to be noted that all the calculations were performed by normalising the velocities at a height of 40 m. This height has been chosen as it is one of the most commonly used hub height when considering the installation of wind turbines. For the purpose of this study, the surface roughness (α) value has been assumed to be 0.27.

C.1.2 Weibull distribution

Fig.C.4 and Fig.C.1.2 shows the Weibull probability distribution for the years 2018-2020, calculated using the maximum likelihood estimation for the locations Sutton Bonnington and Watnall, respectively. This presents an interesting contrast of the wind patterns between a less populated and open-fielded area and a countryside that is comparatively more architecturally developed than the prior. In the case of Sutton Bonnington, maximum velocities in the range of 16 m/s are observed with a maximum probability density function value of 0.23. Whilst in the case of Watnall, the maximum velocity is restricted to 12 m/s, but a higher probability density function value of the order 0.33 is

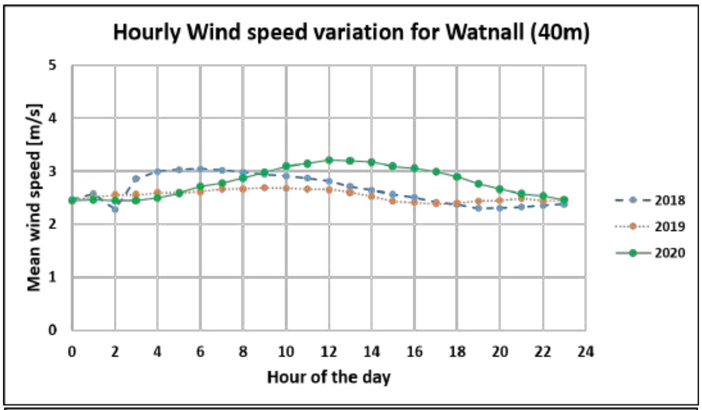

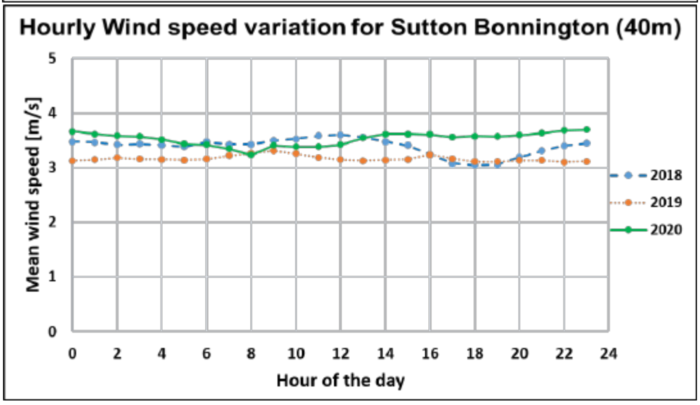

Figure C.1: Hourly wind distribution for Sutton Bonnington and Watnall areas in Nottingham.

attained.

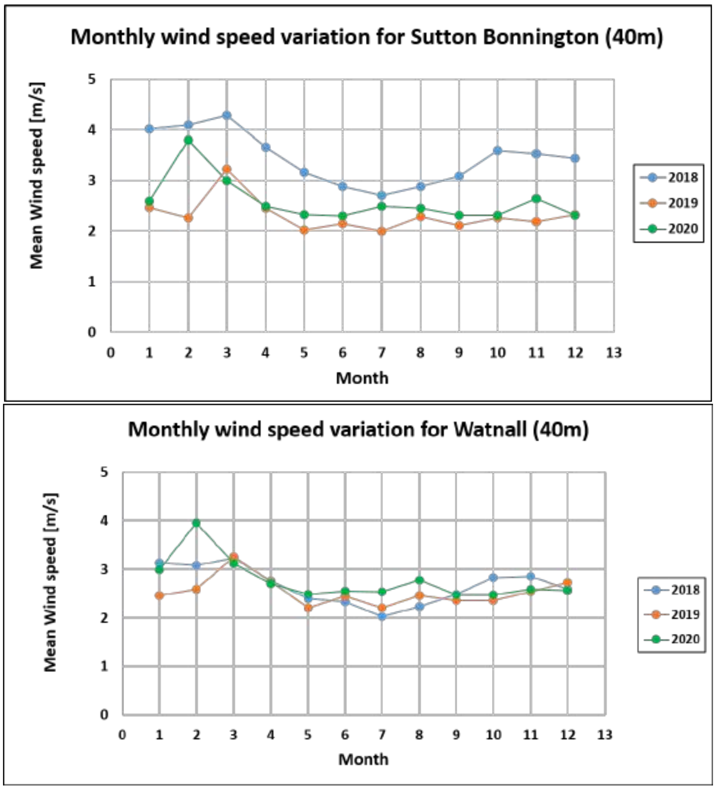

Figure C.2: Monthly wind distribution for Sutton Bonnington and Watnall areas in Nottingham.

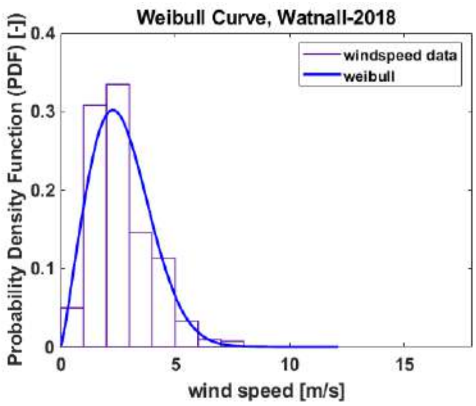

(a) Watnall,2018

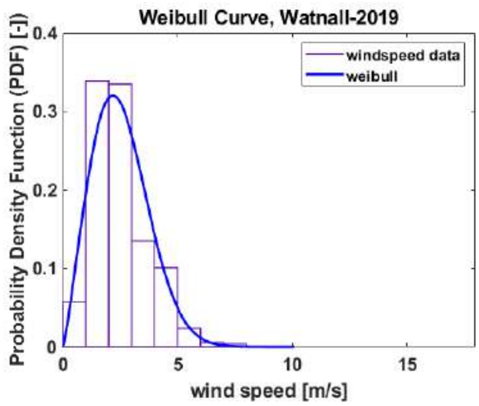

(b) Watnall,2019

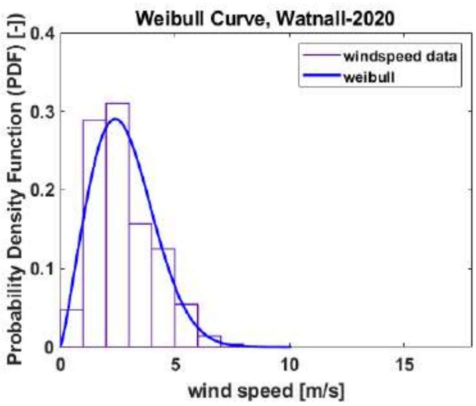

(c) Watnall,2020

Figure C.3: Weibull distribution plots: Watnall

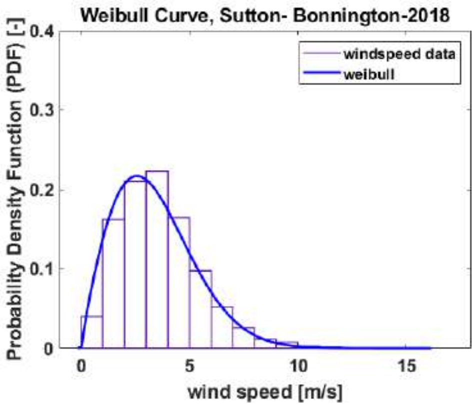

(a) Sutton-Bonnington,2018

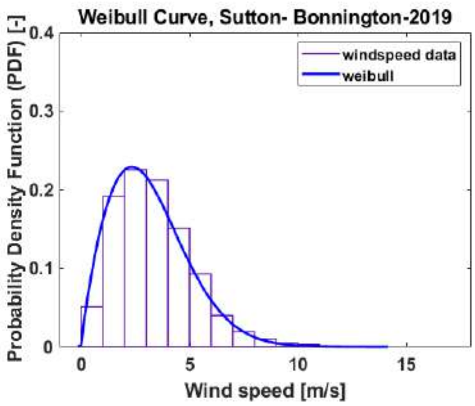

(b) Sutton-Bonnington,2019

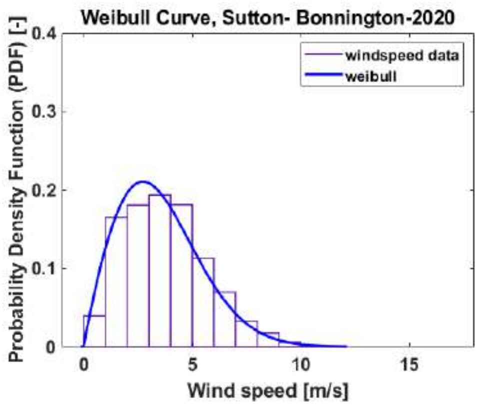

(c) Sutton-Bonnington,2020

Figure C.4: Weibull distribution plots: Sutton- Bonnington

Bibliography

[1] An-Shik Yang, Ying-Ming Su, Chih-Yung Wen, Yu-Hsuan Juan, Wei-Siang Wang, and Chiang-Ho Cheng. Estimation of wind power generation in dense urban area. *Applied Energy*, 171:213–230, 2016.

[2] Sanghyeon Kim and Cheolung Cheong. Development of low-noise drag-type vertical wind turbines. *Renewable energy*, 79:199–208, 2015.

[3] Yu-Hsuan Juan, Abdolrahim Rezaeiha, Hamid Montazeri, Bert Blocken, Chih-Yung Wen, and An-Shik Yang. Cfd assessment of wind energy potential for generic high-rise buildings in close proximity: Impact of building arrangement and height. *Applied Energy*, 321:119328, 2022. URL: https://www.sciencedirect.com/science/article/pii/S030626192200678X, doi:https://doi.org/10.1016/j.apenergy.2022.119328.

[4] Shoutu Li, Qin Chen, Ye Li, Stefan Pröbsting, Congxin Yang, Xiaobo Zheng, Yannian Yang, Weijun Zhu, Wenzhong Shen, Faming Wu, et al. Experimental investigation on noise characteristics of small scale vertical axis wind turbines in urban environments. *Renewable Energy*, 200:970–982, 2022.

[5] LV White and SJ Wakes. Permitting best use of wind resource for small wind-turbines in rural new zealand: A micro-scale cfd examination. *Energy for sustainable development*, 21:1–6, 2014.

[6] Raymond Byrne and Paul MacArtain. The 15-year operational experiences of an 850 kw peri-urban wind turbine: Lessons learned from a behind-the-meter installation in ireland. *Energy for Sustainable Development*, 70:342–360, 2022. URL: https://www.sciencedirect.com/science/article/pii/S0973082622001363, doi:https://doi.org/10.1016/j.esd.2022.08.011.

[7] Piotr Doerffer, Krzysztof Doerffer, Tomasz Ochrymiuk, and Janusz Telega. Variable size twin-rotor wind turbine. *Energies*, 12(13):2543, 2019.

[8] Yu-Hsuan Juan, Abdolrahim Rezaeiha, Hamid Montazeri, Bert Blocken, Chih-Yung Wen, and An-Shik Yang. Cfd assessment of wind energy potential for generic high-rise buildings in close proximity: Impact of building arrangement and height. *Applied Energy*, 321:119328, 2022.

[9] Davood Saeidi, Ahmad Sedaghat, Pourya Alamdari, and Ali Akbar Alemrajabi. Aerodynamic design and economical evaluation of site specific small vertical axis wind turbines. *Applied energy*, 101:765–775, 2013.

[10] Muyuan Li, Yanbo Shen, Jinfeng Yao, Dong Ye, Jing Fan, and Ian Simmonds. An assessment of observed wind speed and wind power density over china for 1980–2021. *Wind Energy*, 25(12):2052–2070, 2022.

[11] CG Justus, WR Hargraves, and Ali Yalcin. Nationwide assessment of potential output from wind-powered generators. *Journal of Applied Meteorology (1962-1982)*, pages 673–678, 1976.

[12] Erik Möllerström, Fredric Ottermo, Anders Goude, Sandra Eriksson, Jonny Hylander, and Hans Bernhoff. Turbulence influence on wind energy extraction for a medium size vertical axis wind turbine. *Wind Energy*, 19(11):1963–1973, 2016.

[13] Atul Gautam, Vilas Warudkar, and JL Bhagoria. A comparative analysis of wind characteristics for distinct terrains of india. *Sustainable Energy Technologies and Assessments*, 52:102089, 2022.

[14] Ziyang Xu, Jing Wei, Shijie Zhang, Zhirou Liu, Xiangqian Chen, Qiang Yan, and Jianpeng Guo. A state-of-the-art review of the vibration and noise of wind turbine drivetrains. *Sustainable Energy Technologies and Assessments*, 48:101629, 2021.

[15] Rahman Saidur, Nasrudin A Rahim, Monirul Rafiqu Islam, and Khalid H Solangi. Environmental impact of wind energy. *Renewable and sustainable energy reviews*, 15(5):2423–2430, 2011.

[16] Paula Ferreira, Fátima Lima, Fernando Ribeiro, and Filipa Vieira. A mixed-method approach for the assessment of local community perception towards wind farms. *Sustainable Energy Technologies and Assessments*, 33:44–52, 2019.

[17] Mojtaba Nedaei, Ehsanolah Assareh, and Philip R. Walsh. A comprehensive evaluation of the wind resource characteristics to investigate the short term penetration of regional wind power based on different probability statistical methods. *Renewable Energy*, 128:362–374, 2018. URL: https://www.sciencedirect.com/science/article/pii/S0960148118305986, doi:https://doi.org/10.1016/j.renene.2018.05.077.

[18] T Li, Y Hayashi, Y Hara, and K Suzuki. Wind tunnel test on a three stage out phase savonius rotor. In *Proceedings of European Wind Energy Conference and Exhibition*, 2004.

[19] Zhendong Zhang, Hui Qin, Yongqi Liu, Liqiang Yao, Xiang Yu, Jiantao Lu, Zhiqiang Jiang, and Zhongkai Feng. Wind speed forecasting based on quantile regression minimal gated memory network and kernel density estimation. *Energy conversion and management*, 196:1395–1409, 2019.

[20] Abul Kalam Azad, Mohammad Golam Rasul, and Talal Yusaf. Statistical diagnosis of the best weibull methods for wind power assessment for agricultural applications. *Energies*, 7(5):3056–3085, 2014. URL: https://www.mdpi.com/1996-1073/7/5/3056.

[21] Pascalin Tiam Kapen, Marinette Jeutho Gouajio, and David Yemélé. Analysis and efficient comparison of ten numerical methods in estimating weibull parameters for wind energy potential: Application to the city of bafoussam, cameroon. *Renewable Energy*, 159:1188–1198, 2020.

[22] Narayanan Natarajan, Mangottiri Vasudevan, and Shafiqur Rehman. Evaluation of suitability of wind speed probability distribution models: a case study from tamil nadu, india. *Environmental Science and Pollution Research*, 29(57):85855–85868, 2022.

[23] Abhisek Banerjee. Performance and flow analysis of an elliptic bladed savonius-style wind turbine. *Journal of Renewable and Sustainable Energy*, 11(3), 2019.

[24] Joao Vicente Akwa, Horacio Antonio Vielmo, and Adriane Prisco Petry. A review on the performance of savonius wind turbines. *Renewable and sustainable energy reviews*, 16(5):3054–3064, 2012.

[25] Louis Angelo Danao, Jonathan Edwards, Okeoghene Eboibi, and Robert Howell. A numerical investigation into the influence of unsteady wind on the performance and aerodynamics of a vertical axis wind turbine. *Applied Energy*, 116:111–124, 2014.

[26] Zhun Fan, Shan Li, Zhiteng Gao, Lijun Zhang, Xiaobo Zheng, Weijun Zhu, Wenzhong Shen, Mikael Sjöholm, Torben Krogh Mikkelsen, Tongguang Wang, et al. On the importance of wind turbine wake boundary to wind energy and environmental impact. *Energy Conversion and Management*, 277:116664, 2023.

[27] Flower Turbines. `https://www.flowerturbines.com/`. Accessed: March 27, 2024.

[28] New World Wind - WindTree. `https://www.newworldwind.com/windtree`. Accessed: March 27, 2024.

[29] IBIS Power- Ingewikkelde duurzaamheidsproblematiek in vastgoed, mooi en makkelijk opgelost. `https://www.ibispower.eu/powernest`. Accessed: March 27, 2024.

[30] Muhammad Mahmood Aslam Bhutta, Nasir Hayat, Ahmed Uzair Farooq, Zain Ali, Sh Rehan Jamil, and Zahid Hussain. Vertical axis wind turbine–a review of various configurations and design techniques. *Renewable and Sustainable Energy Reviews*, 16(4):1926–1939, 2012.

[31] S Roy. Ducoin a. *Unsteady analysis on the instantaneous forces and moment arms acting on a novel savonius-style wind turbine Energy Convers. Manage*, 121:281–296, 2016.

[32] Krzysztof Sobczak. Numerical investigations of an influence of the aspect ratio on the savonius rotor performance. *Journal of Physics: Conference Series*, 1101:012034, 10 2018. `doi:10.1088/1742-6596/1101/1/012034`.

[33] Krzysztof Doerffer, Janusz Telega, Piotr Doerffer, Paulina Hercel, and Andrzej Tomporowski. Dependence of power characteristics on savonius rotor segmentation. *Energies*, 14(10):2912, 2021.

[34] Shivangi Sachar, Piotr Doerffer, Pawel Flaszynski, Jozef Kotus, Krzysztof Doerffer, and Joanna Grzelak. Correlation between the generated noise and effectiveness for a vertical axis savonius type rotor. In *AIAA SCITECH 2023 Forum*, page 0611, 2023. `doi:10.2514/6.2023-0611`.

[35] Chen Jian, Jan Kumbernuss, Zhang Linhua, Lu Lin, and Yang Hongxing. Influence of phase-shift and overlap ratio on savonius wind turbine's performance. *Journal of Solar Energy Engineering*, 134(1):011016, 12 2011. `doi:10.1115/1.4004980`.

[36] Tsutomu Hayashi, Yan Li, Yutaka Hara, and Katsuya Suzuki. Wind tunnel tests on a three-stage out-phase savonius rotor, jsme int. ser. b: Spec. *Issue Exp. Mech. Heat. Fluid Flow*, 48(1):9–16, 2005.

[37] Placide Jaohindy, Sean McTavish, François Garde, and Alain Bastide. An analysis of the transient forces acting on savonius rotors with different aspect ratios. *Renewable Energy*, 55:286–295, 2013.

[38] Krzysztof Sobczak. Numerical investigations of an influence of the aspect ratio on the savonius rotor performance. In *Journal of Physics: Conference Series*, volume 1101, page 012034. IOP Publishing, 2018.

[39] Saha UK Roy S. Review of experimental investigations into the design, performance and optimization of the savonius rotor. *Proc IMechE Part A: Journal of Power Energy*, 227(4):528–42, 2013.

[40] Prabhu SV Kamoji MA, Kedare SB. Performance tests on helical savonius rotors. *Renew Energy*, 34(3):521–9, 2009.

[41] V. D'Alessandro, S Montelpare, R. Ricci, and A. Secchiaroli. Unsteady aerodynamics of a savonius wind rotor: a new computational approach for the simulation of energy performance. *Energy*, 35:3349–63, 2010.

[42] N.H. Mahmoud, A.A El-Haroun, Wahba E., and M.H. Nasef. An experimental study on improvement of savonius rotor performance. *Alexandria Engineering Journal, Alexandria University*, 51:19–25, August 2012.

[43] Robert E. Sheldahl, Bennie Francis Blackwell, and Louis Victor Feltz. Wind tunnel performance data for two- and three-bucket savonius rotors. *Journal of Energy*, 2:160–164, 1978.

[44] Mohammed Hadi Ali et al. Experimental comparison study for savonius wind turbine of two & three blades at low wind speed. *International Journal of Modern Engineering Research (IJMER)*, 3(5):2978–2986, 2013.

[45] Ida Bagus Alit, Rudy Sutanto, I Made Mara, and Mirmanto Mirmanto. Effect of concentrator, blade diameter and blade number on the savonius wind turbine performance. *Asian Journal of Applied Sciences*, 5(2), Apr. 2017. URL: `https://www.ajouronline.com/index.php/AJAS/article/view/4610`, `doi:10.24203/ajas.v5i2.4610`.

[46] M Anbarsooz. Aerodynamic performance of helical savonius wind rotors with 30° and 45° twist angles: Experimental and numerical studies. *Proceedings of the Institution of Mechanical Engineers, Part A: Journal of Power and Energy*, 230(6):523–534, 2016. `arXiv:https://doi.org/10.1177/0957650916648828`, `doi:10.1177/0957650916648828`.

[47] Vimal Patel, Ganapathi Bhat, TI Eldho, and SV Prabhu. Influence of overlap ratio and aspect ratio on the performance of savonius hydrokinetic turbine. *International Journal of Energy Research*, 41(6):829–844, 2017.

[48] J-L Menet. A double-step savonius rotor for local production of electricity: a design study. *Renewable energy*, 29(11):1843–1862, 2004.

[49] UK Saha, S Thotla, and D Maity. Optimum design configuration of savonius rotor through wind tunnel experiments. *Journal of Wind Engineering and Industrial Aerodynamics*, 96(8-9):1359–1375, 2008.

[50] Y Teff-Seker, O Berger-Tal, Y Lehnardt, and N Teschner. Noise pollution from wind turbines and its effects on wildlife: A cross-national analysis of current policies and planning regulations. *Renewable and Sustainable Energy Reviews*, 168:112801, 2022.

[51] Chun-Hsiang Chiu, Shih-Chun Candice Lung, Nathan Chen, Jing-Shiang Hwang, and Ming-Chien Mark Tsou. Effects of low-frequency noise from wind turbines on heart rate variability in healthy individuals. *Scientific reports*, 11(1):17817, 2021.

[52] Honnavalli N Kumara, S Babu, G Babu Rao, Santanu Mahato, Malyasri Bhattacharya, Nitin Venkatesh Ranga Rao, D Tamiliniyan, Harif Parengal, D Deepak, Athira Balakrishnan, et al. Responses of birds and mammals to long-established wind farms in india. *Scientific reports*, 12(1):1339, 2022.

[53] Wolfgang Babisch et al. Traffic noise and cardiovascular disease: epidemiological review and synthesis. *Noise and health*, 2(8):9, 2000.

[54] Willy Passchier-Vermeer and Wim F Passchier. Noise exposure and public health. *Environmental health perspectives*, 108(suppl 1):123–131, 2000.

[55] Gösta Leon Bluhm, Niklas Berglind, Emma Nordling, and Mats Rosenlund. Road traffic noise and hypertension. *Occupational and environmental medicine*, 64(2):122–126, 2007.

[56] Erik Möllerström, Sebastian Larsson, Fredric Ottermo, Jonny Hylander, and Lars Bååth. Noise propagation from a vertical axis wind turbine. In *inter. noise 2014, 43rd International Congress on Noise Control Engineering, Melbourne, Australia, November 16-19, 2014*. Australian Acoustical Society, 2014.

[57] Amgad Dessoky, Thorsten Lutz, Galih Bangga, and Ewald Krämer. Computational studies on darrieus vawt noise mechanisms employing a high order ddes model. *Renewable Energy*, 143:404–425, 2019. URL: https://www.sciencedirect.com/science/article/pii/S0960148119306160, doi:https://doi.org/10.1016/j.renene.2019.04.133.

[58] M.H. Mohamed. Aero-acoustics noise evaluation of h-rotor darrieus wind turbines. *Energy*, 65:596–604, 2014. URL: https://www.sciencedirect.com/science/article/pii/S0360544213009936, doi:https://doi.org/10.1016/j.energy.2013.11.031.

[59] Stefan Oerlemans and Peter Fuglsang. Stefan oerlemans, peter fuglsang siemens wind power - ewea, 2012. URL: https://www.ewea.org/events/workshops/wp-content/uploads/2012/12/EWEA-Noise-Workshop-Oxford-2012-1-1-Stefan-Oerlemans.pdf.

[60] Ganesh Vijayakumar, James Brasseur, Adam Lavely, Michael Kinzel, Eric Paterson, Matthew Churchfield, and Patrick Moriarty. Considerations in coupling les of the atmosphere to cfd around wind turbines. In *50th AIAA Aerospace Sciences Meeting including the New Horizons Forum and Aerospace Exposition*, page 817, 2012.

[61] Min-Soo Jeong, Sang-Woo Kim, In Lee, Seung-Jae Yoo, and Kwang Chun Park. Investigation of wake effects on aeroelastic responses of horizontal-axis windturbines. *AIAA journal*, 52(6):1133–1144, 2014.

[62] Horia Dumitrescu, Vladimir Cardos, Alexandru Dumitrache, and Florin Frunzulica. Low-frequency noise prediction of vertical axis wind turbines. *Proceedings of the Romanian Academy*, 11(1):47–54, 2010.

[63] Akiyoshi Iida, Akisato Mizuno, and Keiko Fukudome. Numerical simulation of aerodynamic noise radiated form vertical axis wind turbines. In *Proceedings of the 18 International Congress on Acoustics*, 2004.

[64] TurbineGenerator.org. Evolution of wind turbines – infographic. https://www.turbinegenerator.org/evolution-wind-turbines-infographic/, April 2015. Accessed: 2025-09-12.

[65] Willy Tjiu, Tjukup Marnoto, Sohif Mat, Mohd Hafidz Ruslan, and Kamaruzzaman Sopian. Darrieus vertical axis wind turbine for power generation i: Assessment of darrieus vawt configurations. *Renewable Energy*, 75:50–67, 2015. URL: https://www.sciencedirect.com/science/article/pii/S096014811400603X, doi:https://doi.org/10.1016/j.renene.2014.09.038.

[66] Ben F Blackwell, Louis V Feltz, and Robert E Sheldahl. *Wind tunnel performance data for two-and three-bucket Savonius rotors*. Sandia Laboratories Springfield, VA, USA, 1977.

[67] C. Srinivasan, G. Ajithkumar, S. Arul, G. Arulprasath, and T.M. Dharunbabu. Design of combined savonius-darrieus wind turbine. *IOSR Journal of Mechanical and Civil Engineering*, 14:201–214, 2017. doi:10.9790/1684-1402056070.

[68] Tetsuya Wakui, Yoshiaki Tanzawa, Takumi Hashizume, and Toshio Nagao. Hybrid configuration of darrieus and savonius rotors for stand-alone wind turbine-generator systems. *Electrical Engineering in Japan*, 150:13 – 22, 03 2005. doi:10.1002/eej.20071.

[69] Heesoo Shin, Mario Rüttgers, and Sangseung Lee. Neural networks for improving wind power efficiency: A review. *Fluids*, 7(12):367, 2022. doi:https://doi.org/10.3390/fluids7120367.

[70] Jan van der Tempel. *Design of Support Structures for Offshore Wind Turbines*. PhD thesis, Delft University of Technology, Delft, The Netherlands, 2006. Offshore Engineering report 2006.OE.009; DUWIND report 2006.029. URL: https://repository.tudelft.nl/islandora/object/uuid:dc4bb40e-51bb-4d2c-bc1f-fbe0bb5ef39a.

[71] The Engineering ToolBox, 2003. URL: https://www.engineeringtoolbox.com/air-altitude-temperature-d_461.html.

[72] energy fundamentals. Physics of wind turbine. URL: https://home.uni-leipzig.de/energy/energy-fundamentals/15.htm.

[73] Magdalena R. V. Sta. Maria and Mark Z. Jacobson. Investigating the effect of large wind farms on energy in the atmosphere. *Energies*, 2(4):816–838, 2009. URL: https://www.mdpi.com/1996-1073/2/4/816, doi:10.3390/en20400816.

[74] O.A. Ajayi. Application of automotive alternators in small wind turbines, Jan 1970. URL: http://resolver.tudelft.nl/uuid:60a3ca0e-25f0-4892-ae52-300dcb4443ab.

[75] Chen L Ng E, Yuan C. Improving the wind environment in high-density cities by understanding urban morphology and surface roughness: a study in hong kong. *Landsc Urban Plan.*, 101:59–74, 2011.

[76] TR Oke. Initial guidance to obtain representative meteorological observations at urban sites. *World Meteorological Organization Geneva*, 81, 2004.

[77] J Wieringa. New revision of davenport roughness classification. *Proceedings of 3EACWE.Eindhoven, The Netherlands;2001.p.285–92.*, 2001.

[78] H Lettau. Note on aerodynamic roughness-parameter estimation on the basis of roughness-element description. *Journal of Appl Meteorol.*, 8:828–32, 1969.

[79] Edwards I Raupach M, Thom A. A wind-tunnel study of turbulent flow close to regularly arrayed rough surfaces. *Bound-LayerMeteorol.*, 18:373–97, 1980.

[80] Edwards I Raupach M, Thom A. A wind-tunnel study of turbulent flow close to regularly arrayed rough surfaces. *Bound-LayerMeteorol.*, 18:373–97, 1980.

[81] Lowry WP Spronken-Smith RA, Oke TR. Advection and the surface energy balance across an irrigated urban park. *International Journal Climatol.*, 20:1033–47, 2000.

[82] Stefan Emeis. *Wind Energy Meteorology*, volume 2 of *Atmospheric Physics for Wind Power Generation*. Springer International Publishing, Belgium, 2018.

[83] Scott B Capps, Alex Hall, and Mimi Hughes. Sensitivity of southern california wind energy to turbine characteristics. *Wind Energy*, 17(1):141–159, 2014. URL: `https://dx.doi.org/10.1002/we.1570`.

[84] Ivana Pobočíková, Zuzana Sedliačková, and Mária Michalková. Application of four probability distributions for wind speed modeling. *Procedia Engineering*, 192:713–718, 2017. 12th international scientific conference of young scientists on sustainable, modern and safe transport. URL: `https://www.sciencedirect.com/science/article/pii/S1877705817326693`, `doi:https://doi.org/10.1016/j.proeng.2017.06.123`.

[85] Ali Naci Celik. A statistical analysis of wind power density based on the weibull and rayleigh models at the southern region of turkey. *Renewable Energy*, 29(4):593–604, 2004. URL: `https://www.sciencedirect.com/science/article/pii/S0960148103002775`, `doi:https://doi.org/10.1016/j.renene.2003.07.002`.

[86] Giwhyun Lee, Yu Ding, Le Xie, and Marc G Genton. A kernel plus method for quantifying wind turbine performance upgrades. *Wind Energy*, 18(7):1207–1219, 2015.

[87] Adriano Zambom and Ronaldo Dias. A review of kernel density estimation with applications to econometrics. 5, 12 2012.

[88] Matthew Patrick and Yue Jia. Kernel density adaptive random testing. pages 1–10, 04 2015. `doi:10.1109/ICSTW.2015.7107451`.

[89] Peng Chen, Chaoshun Li, and Xiaoyuan Zhang. Degradation trend prediction of pumped storage unit based on a novel performance degradation index and gru-attention model. *Sustainable Energy Technologies and Assessments*, 54:102807, 2022.

[90] Qinkai Han, Fanman Meng, Tao Hu, and Fulei Chu. Non-parametric hybrid models for wind speed forecasting. *Energy Conversion and Management*, 148:554–568, 2017. URL: https://www.sciencedirect.com/science/article/pii/S0196890417305654, doi:https://doi.org/10.1016/j.enconman.2017.06.021.

[91] Markus Gross, Vanesa Magar, and Alfredo Peña. Evaluation of orography and roughness model inputs and deep neural network regression for wind speed predictions. *Wind Energy*, 25(12):2036–2051, 2022.

[92] Lei Hua, Chu Zhang, Tian Peng, Chunlei Ji, and Muhammad Shahzad Nazir. Integrated framework of extreme learning machine (elm) based on improved atom search optimization for short-term wind speed prediction. *Energy Conversion and Management*, 252:115102, 2022.

[93] Joseph P. Hennessey. Some aspects of wind power statistics. *Journal of Applied Meteorology and Climatology*, 16(2):119 – 128, 1977. URL: https://journals.ametsoc.org/view/journals/apme/16/2/1520-0450_1977_016_0119_saowps_2_0_co_2.xml, doi:10.1175/1520-0450(1977)016<0119:SAOWPS>2.0.CO;2.

[94] SA Ahmed and HO Mahammed. A statistical analysis of wind power density based on the weibull and ralyeigh models of “penjwen region” sulaimani/iraq. *Jordan Journal of Mechanical and Industrial Engineering*, 6(2):135–140, 2012.

[95] H Zeng. Integration of renewable energy with urban design: based on the examples of the solar photovoltaics and micro wind turbines. *Massachusetts Institute of Technology*, page available at http://dspace.mit.edu/handle/ 1721.1/69461., 2011.

[96] H. Riegler. Hawt versus vawt. *Refocus*, 4:44–46, 07 2003. doi:10.1016/S1471-0846(03)00433-5.

[97] Samuel Perkin, Deon Garrett, and Pall Jensson. Optimal wind turbine selection methodology: A case-study for búrfell, iceland. *Renewable Energy*, 75:165–172, 2015. URL: https://www.sciencedirect.com/science/article/pii/S0960148114006089, doi:https://doi.org/10.1016/j.renene.2014.09.043.

[98] Deveci Tech. Enlil wind, 2025. Accessed: 2025-06-05. URL: https://enlilwind.com/.

[99] Ara Ibrahim, Abdullah Fadhil, Zhalin Khalil, and Rawa Azad. Design project report engr-491&492: Highway vertical axis wind turbines with vortex generators, 02 2019.

[100] Alex Wilson. The folly of building-integrated wind. *Environmental Building News*, 18(15):1–15, 2009.

[101] J. Park, H. Jung, S. Lee, and J. Park. A new building-integrated wind turbine system utilizing the building. *Energies.*, 8 (10):11846–11870, 2015.

[102] Josiah Mortimer. Elephant & castle tower block turbines barely move because of how loud they are. *MyLondon*, March 2022. Accessed: 2025-05-12. URL: https://www.mylondon.news/news/south-london-news/elephant-castles-iconic-strata-tower-23551686.

[103] B Shahizare, N Nik-Ghazali, WT Chong, S Tabatabaeikia, Nima Izadyar, and Alireza Esmaeilzadeh. Novel investigation of the different omni-direction-guide-vane angles effects on the urban vertical axis wind turbine output power via three-dimensional numerical simulation. *Energy Conversion and Management*, 117:206–217, 2016.

[104] Rakesh Kumar, Kaamran Raahemifar, and Alan S. Fung. A critical review of vertical axis wind turbines for urban applications. *Renewable and Sustainable Energy Reviews*, 89:281–291, 2018. URL: https://www.sciencedirect.com/science/article/pii/S1364032118301254, doi:https://doi.org/10.1016/j.rser.2018.03.033.

[105] Sandra Eriksson, Hans Bernhoff, and Mats Leijon. Evaluation of different turbine concepts for wind power. *renewable and sustainable energy reviews*, 12(5):1419–1434, 2008.

[106] Shubham Shubham, Nigel Wright, Francesco Avallone, and Anton Ianakiev. Aerodynamic and aeroacoustic investigation of vertical axis wind turbines with different number of blades using mid-fidelity and high-fidelity methods. In *AIAA AVIATION 2023 Forum*, page 3642, 2023.

[107] Matthias Kinzel, Quinn Mulligan, and John O Dabiri. Energy exchange in an array of vertical-axis wind turbines. *Journal of Turbulence*, 13(1):N38, 2012.

[108] John O Dabiri. Potential order-of-magnitude enhancement of wind farm power density via counter-rotating vertical-axis wind turbine arrays. *Journal of renewable and sustainable energy*, 3(4):043104, 2011.

[109] R. Mereu, D. Federici, G. Ferrari, P. Schito, and F. Inzoli. Parametric numerical study of savonius wind turbine interaction in a linear array. *Renewable Energy*, 113:1320–1332, 2017. URL: https://www.sciencedirect.com/science/article/pii/S0960148117305980, doi:https://doi.org/10.1016/j.renene.2017.06.094.

[110] Belkacem Belabes, Abdelkader Youcefi, and Marius Paraschivoiu. Numerical investigation of savonius wind turbine farms. *Journal of Renewable and Sustainable Energy*, 8(5):053302, 2016. arXiv:https://doi.org/10.1063/1.4963688, doi:10.1063/1.4963688.

[111] Colin H Hansen, Con J Doolan, and Kristy L Hansen. *Wind farm noise: measurement, assessment, and control*. John Wiley & Sons, 2017.

[112] Henrik Møller and Christian Sejer Pedersen. Low-frequency noise from large wind turbines. *The Journal of the Acoustical Society of America*, 129(6):3727–3744, 2011. arXiv:https://doi.org/10.1121/1.3543957, doi:10.1121/1.3543957.

[113] Farhad Forouharmajda, Hadi Asadya, Mariana Alves Pereirab, Adrian Fuentec, and Siamak Pourabdiana. Is enough attention paid to the health effects of low-frequency noise in today's society? *International Journal of Preventive Medicine*, 13:162, 2022.

[114] Sophia K. Chiu, Scott E. Brueck, Douglas M. Wiegand, Hannah L. Free, and Hannah Echt. Evaluation of low-frequency noise, infrasound, and health symptoms at an administrative building and men's shelter: A case study. *Seminars*

in Hearing, 44(04):503–520, June 2023. URL: http://dx.doi.org/10.1055/s-0043-1769497, doi:10.1055/s-0043-1769497.

[115] Henk ME Miedema and Henk Vos. Exposure-response relationships for transportation noise. *The Journal of the Acoustical Society of America*, 104(6):3432–3445, 1998.

[116] Peng Liang, Jiangjing Li, Zenglei Li, Jing Wei, Jing Li, Shenghao Zhang, Shenglong Xu, Zhaohui Liu, and Jin Wang. Effect of low-frequency noise exposure on cognitive function: a systematic review and meta-analysis. *BMC Public Health*, 24(1):125, 2024.

[117] Yoshiyasu Takefuji. Understanding environmental noise: Transmission, attenuation, resonance and health implications. *Green Technologies and Sustainability*, 3(3):100215, 2025. URL: https://www.sciencedirect.com/science/article/pii/S2949736125000491, doi:https://doi.org/10.1016/j.grets.2025.100215.

[118] Maria Alzira Cavacas, Vitor Tavares, Maria João Oliveira, Pedro Oliveira, Ana Sezinando, and José Martins dos Santos. Effects of industrial noise on circumpulpar dentin-a field emission scanning electron microscopy and energy dispersive spectroscopy analysis. *International journal of clinical and experimental pathology*, 6(12):2697, 2013.

[119] José João Baltazar Mendes, Pedro Miguel Antunes Oliveira, José Américo Almeida de Brito, Artur Manuel Perez Neves Águas, and José António Mesquita Martins Dos Santos. Noise rich in low frequency components, a new comorbidity for periodontal disease? an experimental study. *Journal of Indian Society of Periodontology*, 18(4):503–507, 2014.

[120] Birgitta Berglund, Peter Hassmén, and raymond Soames Job. Sources and effects of low-frequency noise. *The Journal of the Acoustical Society of America*, 99:2985–3002, 06 1996. doi:10.1121/1.414863.

[121] Geoff Leventhall, Peter Pelmear, and Stephen Benton. A review of published research on low frequency noise and its effects. Defra Report EPG 1/2/50, Department for Environment, Food and Rural Affairs (Defra), London, UK, 2003. URL: https://www.researchgate.net/publication/237245317_A_Review_of_Published_Research_on_Low_Frequency_Noise_and_its_Effects.

[122] Eja Pedersen, Frits van den Berg, R.H. Bakker, and Jelte Bouma. Response to noise from modern wind farms in the netherlands. *The Journal of the Acoustical Society of America*, 126:634–43, 09 2009. doi:10.1121/1.3160293.

[123] Eja Pedersen and Kerstin Persson Waye. Wind turbine noise, annoyance and self-reported health and well-being in different living environments. *Occupational and environmental medicine*, 64:480–6, 08 2007. doi:10.1136/oem.2006.031039.

[124] G.P. van den Berg. Effects of the wind profile at night on wind turbine sound. *Journal of Sound and Vibration*, 277(4):955–970, 2004. URL: https://www.sciencedirect.com/science/article/pii/S0022460X03012197, doi:https://doi.org/10.1016/j.jsv.2003.09.050.

[125] John L Davy, Kym Burgemeister, and David Hillman. Wind turbine sound limits: Current status and recommendations based on mitigating noise annoyance. *Applied acoustics*, 140:288–295, 2018.

[126] P Gallo, L Fredianelli, Diego Palazzuoli, Gaetano Licitra, and Francesco Fidecaro. A procedure for the assessment of wind turbine noise. *Applied Acoustics*, 114:213–217, 2016.

[127] WR Graham and CE Pearson. Noise from a model-scale vertical-axis wind turbine. *AIAA Journal*, 60(1):224–235, 2022.

[128] Harvey H Hubbard and Kevin P Shepherd. Aeroacoustics of large wind turbines. *The Journal of the Acoustical Society of America*, 89(6):2495–2508, 1991.

[129] G Guidati, J Ostertag, and S Wagner. Prediction and reduction of wind turbine noise-an overview of research activities in europe. In *2000 ASME Wind Energy Symposium*, page 42, 2000.

[130] Stefan Oerlemans and Beatriz Méndez López. Acoustic array measurements on a full scale wind turbine. In *11th AIAA/CEAS aeroacoustics conference*, page 2963, 2005.

[131] Thomas F Brooks, D Stuart Pope, and Michael A Marcolini. Airfoil self-noise and prediction. Technical report, 1989.

[132] WCP van der Velden. *Computational aeroacoustic approaches for wind turbine blade noise prediction*. PhD thesis, Delft University of Technology, 2017.

[133] Christina Ekrem Dimmen. Quantification of aeroacoustic noise sources from wind turbines. Master's thesis, The University of Bergen, 2022.

[134] Nicole A Pettingill, Nikolas S Zawodny, Christopher Thurman, and Leonard V Lopes. Acoustic and performance characteristics of an ideally twisted rotor in hover. In *AIAA Scitech 2021 Forum*, page 1928, 2021.

[135] C.A. Arce León. *A study on the near-surface flow and acoustic emissions of trailing*. PhD thesis, 2017. doi:10.4233/UUID:EE9B5495-FDE2-4BB1-807D-E7547F2A393D.

[136] K. S. Murthy and O. P. Rahi. Estimation of weibull parameters using graphical method for wind energy applications. *2014 Eighteenth National Power Systems Conference (NPSC)*, 2014. doi:10.1109/npsc.2014.7103858.

[137] Kasra Mohammadi and Ali Mostafaeipour. Using different methods for comprehensive study of wind turbine utilization in zarrineh, iran. *Energy Conversion and Management*, 65:463–470, 2013. doi:10.1016/j.enconman.2012.09.004.

[138] Karl Pearson. Method of moments and method of maximum likelihood. *Biometrika*, 28(1/2):34–59, 1936. URL: http://www.jstor.org/stable/2334123.

[139] C. G. Justus and Amir Mikhail. Height variation of wind speed and wind distributions statistics. *Geophysical Research Letters*, 3(5):261–264, 1976. URL: https://agupubs.onlinelibrary.wiley.com/doi/abs/10.1029/GL003i005p00261, arXiv:https://agupubs.onlinelibrary.wiley.com/doi/pdf/10.1029/GL003i005p00261, doi:https://doi.org/10.1029/GL003i005p00261.

[140] Seyit A. Akdağ and Ali Dinler. A new method to estimate weibull parameters for wind energy applications. *Energy Conversion and Management*, 50(7):1761–1766, 2009. URL: https://www.sciencedirect.com/science/article/pii/S0196890409000934, doi:https://doi.org/10.1016/j.enconman.2009.03.020.

[141] Ronald A Fisher. Frequency distribution of the values of the correlation coefficient in samples from an indefinitely large population. *Biometrika*, 10(4):507–521, 1915.

[142] MJM Stevens and PT Smulders. The estimation of the parameters of the weibull wind speed distribution for wind energy utilization purposes. *Wind engineering*, pages 132–145, 1979.

[143] Tian Pau Chang. Performance comparison of six numerical methods in estimating weibull parameters for wind energy application. *Applied Energy*, 88(1):272–282, 2011. URL: https://www.sciencedirect.com/science/article/pii/S0306261910002321, doi:https://doi.org/10.1016/j.apenergy.2010.06.018.

[144] M.R. Islam, R. Saidur, and N.A. Rahim. Assessment of wind energy potentiality at kudat and labuan, malaysia using weibull distribution function. *Energy*, 36(2):985–992, 2011. URL: https://www.sciencedirect.com/science/article/pii/S0360544210007012, doi:https://doi.org/10.1016/j.energy.2010.12.011.

[145] Qblade - next generation wind turbine simulation. https://qblade.org/, Sep 2022.

[146] Rmse: Root mean square error. https://www.statisticshowto.com/probability-and-statistics/regression-analysis/rmse-root-mean-square-error/. Accessed: March 27, 2022.

[147] Yeliz Mert Kantar and Ilhan Usta. Analysis of the upper-truncated weibull distribution for wind speed. *Energy conversion and management*, 96:81–88, 2015.

[148] Jami Hossain, Suman Sharma, and VVN Kishore. Multi-peak gaussian fit applicability to wind speed distribution. *Renewable and Sustainable Energy Reviews*, 34:483–490, 2014.

[149] Mary McHugh. The chi-square test of independence. *Biochemia medica*, 23:143–9, 06 2013. doi:10.11613/BM.2013.018.

[150] Florian R Menter. Improved two-equation k-omega turbulence models for aerodynamic flows. Technical report, 1992.

[151] Florian R Menter. Two-equation eddy-viscosity turbulence models for engineering applications. *AIAA journal*, 32(8):1598–1605, 1994.

[152] Thomas J Mueller. *Aeroacoustic measurements*. Springer Science & Business Media, 2002.

[153] Don H Johnson. Array signal processing. *concepts and techniques*, 1993.

[154] Barry D Van Veen and Kevin M Buckley. Beamforming: A versatile approach to spatial filtering. *IEEE assp magazine*, 5(2):4–24, 1988.

[155] R. Merino Martinez. *Microphone arrays for imaging of aerospace noise sources*. PhD thesis, 2018. doi:10.4233/UUID:A3231EA9-1380-44F4-9A93-DBBD9A26F1D6.

[156] Stefan Oerlemans. Detection of aeroacoustic sound sources on aircraft and wind turbines. 2009.

[157] Thomas Padois, Franck Sgard, Olivier Doutres, and Alain Berry. Acoustic source localization using a polyhedral microphone array and an improved generalized cross-correlation technique. *Journal of Sound and Vibration*, 386:82–99, 2017.

[158] Thomas Padois, Olivier Doutres, Franck Sgard, and Alain Berry. Time domain localization technique with sparsity constraint for imaging acoustic sources. *Mechanical Systems and Signal Processing*, 94:85–93, 2017.

[159] Robert Dougherty. Advanced time-domain beamforming techniques. In *10th AIAA/CEAS Aeroacoustics Conference*, page 2955, 2004.

[160] P Sijtsma. Beamforming on moving sources. 2006.

[161] Pieter Sijtsma. Clean based on spatial source coherence. *International journal of aeroacoustics*, 6(4):357–374, 2007.

[162] Ennes Sarradj. A fast signal subspace approach for the determination of absolute levels from phased microphone array measurements. *Journal of Sound and Vibration*, 329(9):1553–1569, 2010.

[163] E Sarradj, C Schulze, and A Zeibig. Identification of noise source mechanisms using orthogonal beamforming. *Noise and vibration: emerging methods*, 2005.

[164] A. G. Olabi, Tabbi Wilberforce, Khaled Elsaid, Tareq Salameh, Enas Taha Sayed, Khaled Saleh Husain, and Mohammad Ali Abdelkareem. Selection guidelines for wind energy technologies. *Energies*, 14(11):3244, 2021. doi:10.3390/en14113244.

[165] Robert P Dougherty. Functional beamforming for aeroacoustic source distributions. In *20th AIAA/CEAS aeroacoustics conference*, page 3066, 2014.

[166] Thomas F Brooks and William M Humphreys. A deconvolution approach for the mapping of acoustic sources (damas) determined from phased microphone arrays. *Journal of sound and vibration*, 294(4-5):856–879, 2006.

[167] Otis Lamont Frost. An algorithm for linearly constrained adaptive array processing. *Proceedings of the IEEE*, 60(8):926–935, 1972.

[168] Henry Cox, Robertm Zeskind, and Markm Owen. Robust adaptive beamforming. *IEEE Transactions on Acoustics, Speech, and Signal Processing*, 35(10):1365–1376, 1987.

[169] Carroll Mason Sparrow. On spectroscopic resolving power. *Astrophysical Journal, vol. 44, p. 76*, 44:76, 1916.

[170] Pieter Sijtsma. Phased array beamforming applied to wind tunnel and fly-over tests. 2010.

[171] Ennes Sarradj. Three-dimensional acoustic source mapping with different beamforming steering vector formulations. *Advances in Acoustics and Vibration*, 2012, 2012.

[172] Thomas Ahlefeldt, Carsten Spehr, Tobias Berkefeld, Alessandro Di Marco, and Lorenzo Burghignoli. A tomographic directivity approach to frequency domain beamforming. In *2018 AIAA/CEAS Aeroacoustics Conference*, page 2808, 2018.

[173] Yu Liu, Alexander R Quayle, Ann P Dowling, and Pieter Sijtsma. Beamforming correction for dipole measurement using two-dimensional microphone arrays. *The Journal of the Acoustical Society of America*, 124(1):182–191, 2008.

[174] Stewart Glegg and William Devenport. *Aeroacoustics of low Mach number flows: fundamentals, analysis, and measurement*. Academic Press, 2017.

[175] GP Howell, AJ Bradley, MA McCormick, and JD Brown. De-dopplerization and acoustic imaging of aircraft flyover noise measurements. *Journal of Sound and Vibration*, 105(1):151–167, 1986.

[176] Jørgen Hald. Removal of incoherent noise from an averaged cross-spectral matrix. *The journal of the acoustical society of America*, 142(2):846–854, 2017.

[177] Daniel Ernst, Carsten Spehr, and Tobias Berkefeld. Decorrelation of acoustic wave propagation through the shear layer in open jet wind tunnel. In *21st AIAA/CEAS aeroacoustics conference*, page 2976, 2015.

[178] Roberto Merino-Martınez, Pieter Sijtsma, and Mirjam Snellen. Inverse integration method for distributed sound sources. In *Proceedings of the 7th Berlin Beamforming Conference (BeBeC), Berlin, Germany*, pages 5–6, 2018.

[179] Rahim Hassanzadeh and Milad Mohammadnejad. Effects of inward and outward overlap ratios on the two-blade savonius type of vertical axis wind turbine performance. *International Journal of Green Energy*, 16(15):1485–1496, 2019. URL: https://www.tandfonline.com/doi/full/10.1080/15435075.2019.1671420, doi:10.1080/15435075.2019.1671420.

[180] Tania Rus, Lucian Florin Rus, Dana Adriana Ilutiu-Varvara, Roxana Mare, Ancuta Abrudan, and Florin Domnita. Experimental investigation on the influence of overlap ratio on savonius turbines performance. *International Journal of Renewable Energy Research (IJRER)*, 10(3):7764–7772, 2020. URL: https://www.ijrer.ijrer.org/index.php/ijrer/article/view/7764.

[181] Author(s) Unknown. Numerical and experimental study on the effect of overlap on savonius wind turbine. *ResearchGate*, 2023. Accessed on [Date]. URL: https://www.researchgate.net/publication/370756501.

[182] M. Ebrahimpour, R. Shafaghat, R. Alamian, and M. S. Shadloo. Power performance analysis based on savonius wind turbine blade design and layout optimization through rotor wake flow analysis. *Energies*, 15(24):9500, 2022. URL: https://www.mdpi.com/1996-1073/15/24/9500, doi:10.3390/en15249500.

[183] V.J. Modi, N.J. Roth, and M.S.U.K. Fernando. Optimum-configuration studies and prototype design of a wind-energy-operated irrigation system. *Journal of Wind Engineering and Industrial Aerodynamics*, 16(1):85–96, 1984. URL: https://www.sciencedirect.com/science/article/pii/0167610584900503, doi:https://doi.org/10.1016/0167-6105(84)90050-3.

[184] Sukanta Roy and Antoine Ducoin. Unsteady analysis on the instantaneous forces and moment arms acting on a novel savonius-style wind turbine. *Energy Conversion and Management*, 121:281–296, 2016.

[185] Krzysztof Sobczak. Numerical investigations of an influence of the aspect ratio on the savonius rotor performance. In *Journal of Physics: Conference Series*, volume 1101, page 012034. IOP Publishing, 2018. doi::10.1088/1742-6596/1101/1/012034.

[186] Ishmail B Celik, Urmila Ghia, Patrick J Roache, and Christopher J Freitas. Procedure for estimation and reporting of uncertainty due to discretization in cfd applications. *Journal of fluids Engineering-Transactions of the ASME*, 130(7), 2008.

[187] KR Cooper et al. Closed-test-section wind tunnel blockage corrections for road vehicles. *SAE SP-1176, Warrendale*, 1996.

[188] Ann Hyvärinen. Investigation of blockage correction methods forfull-scale wind tunnel testing of trucks, 2015.

[189] Houigab Jeong, Seungho Lee, and Soon-Duck Kwon. Blockage corrections for wind tunnel tests conducted on a darrieus wind turbine. *Journal of Wind Engineering and Industrial Aerodynamics*, 179:229–239, 2018.

[190] Shivangi Sachar, Piotr Doerffer, Paweł Flaszyński, Jozef Kotus, Krzysztof Doerffer, Joanna Grzelak, and Michał Piotrowicz. Aeroacoustic effect of savonius rotor segmentation. *Archives of Acoustics*, 2025. doi:10.24425/aoa.2025.153665.

[191] Abhishek Kumar Sahai, Dick Simons, and Eike Stumpf. Consideration of aircraft noise annoyance during conceptual aircraft design. Technical report, Lehrstuhl und Institut für Luft-und Raumfahrtsysteme (ILR), 2016.

[192] Jens Blauert. *Communication acoustics*, volume 2. Springer, 2005.

[193] Tigran Mkhoyan, Coen De Visser, and Roeland De Breuker. Adaptive real-time clustering method for dynamic visual tracking of very flexible wings. 01 2020. doi:10.2514/6.2020-2250.

[194] Nakash Nazeer, Xuerui Wang, and Roger M Groves. Sensing, actuation, and control of the smartx prototype morphing wing in the wind tunnel. In *Actuators*, volume 10, page 107. MDPI, 2021.

[195] CAE Software und Systems GmbH - Bionic M-112 Acoustic Camera. https://www.cae-systems.de/en/products/acoustic-camera-sound-source-localization/bionic-m-112.html. Accessed: March 27, 2023.

[196] Mariusz Siedlecki. Urban-rural wind speed differences in lodz. *University of Lodz*, 2002.

[197] Roberto Merino-Martinez. *Microphone arrays for imaging of aerospace noise sources*. PhD thesis, 11 2018. doi:10.4233/uuid:a3231ea9-1380-44f4-9a93-dbbd9a26f1d6.

[198] Carlos Arce León, Roberto Merino-Martínez, Daniele Ragni, Francesco Avallone, and Mirjam Snellen. Boundary layer characterization and acoustic measurements of flow-aligned trailing edge serrations. *Experiments in fluids*, 57:1–22, 2016.

[199] Francesco Avallone, Wouter C van der Velden, Roberto Merino Martinez, and Daniele Ragni. Near-wall pressure fluctuations over noise reduction add-ons. In *23rd AIAA/CEAS aeroacoustics conference*, page 4171, 2017.

[200] Stefan Oerlemans and Pieter Sijtsma. Acoustic array measurements of a 1: 10.6 scaled airbus a340 model. In *10th AIAA/CEAS Aeroacoustics Conference*, page 2924, 2004.

[201] Thomas Brooks and William Humphreys, Jr. Effect of directional array size on the measurement of airframe noise components. In *5th AIAA/CEAS Aeroacoustics Conference and Exhibit*, page 1958, 1999.

[202] Sanghyeon Kim and Cheolung Cheong. Development of low-noise drag-type vertical wind turbines. *Renewable energy*, 79:199–208, 2015.

[203] Werner M Dobrzynski. Airframe noise–landing gear noise. *Encyclopedia of Aerospace Engineering*, 2010.

[204] Newby Curle. The influence of solid boundaries upon aerodynamic sound. *Proceedings of the Royal Society of London. Series A. Mathematical and Physical Sciences*, 231(1187):505–514, 1955.

[205] Roy K Amiet. Noise due to turbulent flow past a trailing edge. *Journal of sound and vibration*, 47(3):387–393, 1976.

[206] Alan Powell. On the aerodynamic noise of a rigid flat plate moving at zero incidence. *The Journal of the Acoustical Society of America*, 31(12):1649–1653, 1959.

[207] MPJ Sanders, CH Venner, and LD de Santana. Slat noise measurements in open-jet, hard-wall and hybrid wind tunnel test sections. *Journal of Sound and Vibration*, 546:117420, 2023.

[208] Stefan Oerlemans and Paul Migliore. Aeroacoustic wind tunnel tests of wind turbine airfoils. In *10th AIAA/CEAS aeroacoustics conference*, page 3042, 2004.

[209] Stefan Oerlemans. Wind tunnel aeroacoustic tests of six airfoils for use on small wind turbines; period of performance: August 23, 2002 through march 31, 2004. Technical report, National Renewable Energy Lab.(NREL), Golden, CO (United States), 2004.

[210] Cheolung Cheong, Phillip Joseph, Yonghwan Park, and Soogab Lee. Computation of aeolian tone from a circular cylinder using source models. *Applied Acoustics*, 69(2):110–126, 2008.

[211] J. G. Schepers, S. Oerlemans, G. Guidati, and S. Wagner. Experimental demonstration of wind turbine noise reduction through optimized airfoil shape and trailing-edge serrations. NLR Technical Report NLR-TP-2001-324, National Aerospace Laboratory NLR, Amsterdam, The Netherlands, 2001. URL: `https://resolver.tudelft.nl/uuid:48fca1b2-36a5-4c2c-bf35-da04d371e3ec`.

[212] Stefan Oerlemans, Pieter Sijtsma, and B Méndez López. Location and quantification of noise sources on a wind turbine. *Journal of sound and vibration*, 299(4-5):869–883, 2007.

[213] Janardan Rohatgi, Alex Araújo, and Ana Rosa Primo. Extreme wind speeds and their prediction for wind turbines. *Wind Engineering*, 37(6):595–603, 2013. arXiv:https://doi.org/10.1260/0309-524X.37.6.595, doi:10.1260/0309-524X.37.6.595.

[214] Shivangi Sachar, Shubham Shubham, Piotr Doerffer, Anton Ianakiev, and Paweł Flaszyński. Wind speed probabilistic forecast based wind turbine selection and siting for urban environment. *IET Renewable Power Generation*, 18(15):3285–3300, 2024. doi:10.1049/rpg2.13132.

[215] QuiteRevolution. Vertical axis wind turbines the qr6 helical vawt, 2020. URL: https://www.quietrevolution.com/products/.

[216] Luisa C Pagnini, Massimiliano Burlando, and Maria Pia Repetto. Experimental power curve of small-size wind turbines in turbulent urban environment. *Applied Energy*, 154:112–121, 2015.

[217] Luisa Pagnini, Giuseppe Piccardo, and Maria Pia Repetto. Full scale behavior of a small size vertical axis wind turbine. *Renewable Energy*, 127:41–55, 2018.

[218] Alessandro Chiappalone. *Studio di una turbina eolica innovativa ad asse verticale*. PhD thesis, Tesi di Laurea Magistrale. Università degli Studi di Genova, Scuola Politecnica, 2016.

[219] S Rabinowich. *Measurement errors and uncertainties: theory and practice*. Springer Science & Business Media, 2005.

[220] Ahmed S Saad, Ibrahim I El-Sharkawy, Shinichi Ookawara, and Mahmoud Ahmed. Performance enhancement of twisted-bladed savonius vertical axis wind turbines. *Energy Conversion and Management*, 209:112673, 2020.

[221] S Rolland, W Newton, AJ Williams, TN Croft, DT Gethin, and M Cross. Simulations technique for the design of a vertical axis wind turbine device with experimental validation. *Applied Energy*, 111:1195–1203, 2013.

[222] SA Rolland, M Thatcher, W Newton, AJ Williams, TN Croft, DT Gethin, and M Cross. Benchmark experiments for simulations of a vertical axis wind turbine. *Applied energy*, 111:1183–1194, 2013.

[223] HE Soper, AW Young, BM Cave, A Lee, and Karl Pearson. A cooperative study. on the distribution of the correlation coefficient in small samples. appendix to the papers of 'student'and ra fisher. *Biometrika*, 11:328–413, 1917.

[224] Jacob Cohen. Statistical power analysis for the behavioral sciences. hoboken. *NJ: Routledge. doi*, 10:9780203771587, 2013.

[225] Gerrit JJ Ruijgrok. *Elements of aviation acoustics*. Delft University Press, 1993.

[226] Colin Hansen. Fundamentals of acoustics. *American Journal of Physics - AMER J PHYS*, 19, 01 1951.

[227] Shashikant R More. *Aircraft noise characteristics and metrics*. Purdue University, 2010.